Effects of Firn Ventilation on Geochemistry of Polar Snow

Thomas A. Neumann

A dissertation submitted in partial fulfillment of
the requirements for the degree of

Doctor of Philosophy

University of Washington

2003

Program Authorized to Offer Degree: Department of Earth and Space Sciences

University of Washington

Graduate School

This is to certify that I have examined this copy of a doctoral dissertation by

Thomas A. Neumann

and have found that it is complete and satisfactory in all respects,
and that any and all revisions required by the final
examining committee have been made.

Chair of Supervisory Committee:

_____

Edwin D. Waddington

Reading Committee:

_____

Howard B. Conway

_____

Charles F. Raymond

_____

Eric J. Steig

_____

Edwin D. Waddington

Date: _____

In presenting this dissertation in partial fulfillment of the requirements for the Doctoral degree at the University of Washington, I agree that the Library shall make its copies freely available for inspection. I further agree that extensive copying of this dissertation is allowable only for scholarly purposes, consistent with "fair use" as prescribed in the U.S. Copyright Law. Requests for copying or reproduction of this dissertation may be referred to University Microfilms, 1490 Eisenhower Place, P.O. Box 975, Ann Arbor, MI 48106, to whom the author has granted "the right to reproduce and sell (a) copies of the manuscript in microform and/or (b) printed copies of the manuscript made from microform."

Signature_____

Date_____

University of Washington

Abstract

Effects of Firn Ventilation on Geochemistry of Polar Snow

by Thomas A. Neumann

Chair of Supervisory Committee:

Professor Edwin D. Waddington
Department of Earth and Space Sciences

The effects of air motion in firn on geochemical species is examined. Stable isotope data from Taylor Mouth, Antarctica are compared with data from nearby Taylor Dome and are found to be significantly different. Three possible reasons for the difference between these two records are presented: (1) the standard stable isotope - surface temperature relationship, (2) mixing precipitation from several sources and (3) post-depositional isotopic change.

A two-dimensional model to estimate condensation and sublimation rates of water in firn based on firn-ventilation theory is presented. This model is used to investigate preservation characteristics of chemical species in snow and quantify the effects of post-depositional water-vapor motion. Results demonstrate the sensitivity of sublimation and condensation rates in the firn to hand-to-hand diffusion, grain size, wind speed and temperature.

The sensitivity of stable isotope ratios to firn ventilation quantify what other investigators have suggested: isotopic exchange in the upper few meters is more rapid than can be explained by existing models, isotopic equilibration with atmospheric

vapor is an important component of isotopic exchange and ventilation enhances exchange by creating regions of relatively rapid sublimation and condensation in the firn.

The concentration of irreversibly deposited species (e.g. non-sea-salt-sulfate) is decreased by condensation in pore spaces and increased by sublimation of surrounding ice grains. Results suggest that concentration changes induced by firn ventilation are on the order of 3%, making it unlikely that this effect can be detected in field data.

The concentration of reversibly-deposited species in snow (e.g. H_2O_2) is generally decreased by sublimation of the surrounding ice grain. Condensation increases the diffusion path from the grain interior to the surface and can scavenge species which exist as trace gasses from pore-space air. Results suggest that firn ventilation has little effect on H_2O_2 concentration in firn, but may be more important to the preservation of other reversibly-deposited species.

In summary, results show that firn-ventilation induced water vapor motion is a key component of isotopic change in the firn, and may be important for reversibly-deposited geochemical species; but is probably not important for irreversibly-deposited geochemical species.

TABLE OF CONTENTS

List of Figures v

List of Tables ix

Chapter 1: Introduction 1

1.1 Background 1

1.2 Motivation and Goals 2

1.3 Synopsis/Organization 2

Chapter 2: Non-Climate Influences on Stable Isotopes at Taylor Mouth, Antarctica 5

2.1 Summary 5

2.2 Introduction 6

2.3 Comparison of Taylor Dome and Taylor Mouth Isotope Records . . . 7

2.4 Isotope-Temperature Relation 9

2.5 Mixing of Snow From Different Sources 11

2.6 Post-Depositional Isotopic Enrichment 14

2.6.1 Model Description 15

2.6.2 Discussion of Assumptions 18

2.6.3 Model Application 21

2.7 Discussion 25

2.8 Conclusions 28

Chapter 3: Vapor Motion in the Firn **35**

3.1 Summary . . . 35
3.2 Introduction . . . 36
3.3 Air Flow Field . . . 38
3.4 Heat Flow . . . 41
3.5 Vapor Flow . . . 42
3.6 Boundary Conditions . . . 44
3.7 Model Verification . . . 46
3.7.1 Flow-Field Continuity . . . 46
3.7.2 Energy Conservation . . . 47
3.7.3 Numerical Tests . . . 49
3.8 Application . . . 56
3.8.1 Winter Conditions . . . 56
3.8.2 Summer Conditions . . . 68
3.8.3 Seasonal Comparison . . . 77
3.8.4 Response Time . . . 78
3.8.5 Influence of Grain Size . . . 79
3.8.6 Comparison With Field Data . . . 83
3.8.7 Cumulative Effects . . . 86
3.8.8 Overview of Modeling Results . . . 89
3.9 Limitations/Improvements . . . 89
3.10 Summary and Conclusions . . . 93

Chapter 4: Effects of Firn Ventilation on Isotopic Exchange **96**

4.1 Summary . . . 96
4.2 Introduction . . . 97
4.3 Model For Post-depositional Stable Isotopic Change . . . 98

4.4 Results . . . 105
4.4.1 Simplified Diffusion Model . . . 106
4.4.2 Ventilation - Summer . . . 107
4.4.3 Ventilation - Winter . . . 111
4.5 Discussion . . . 112
4.6 Conclusions . . . 116

Chapter 5: Effects of Ventilation on Irreversibly-Deposited Species **127**

5.1 Summary . . . 127
5.2 Introduction . . . 127
5.3 Model Details . . . 129
5.4 Results and Discussion . . . 131
5.4.1 Seasonal Cycles . . . 131
5.4.2 Daily Cycles . . . 132
5.4.3 Hand-to-Hand Diffusion . . . 134
5.4.4 Cumulative Effects . . . 136
5.5 Conclusions . . . 137

Chapter 6: Effects of Ventilation on Reversibly-Deposited Species **144**

6.1 Summary . . . 144
6.2 Introduction . . . 144
6.3 Model Details . . . 146
6.4 Results . . . 151
6.5 Discussion . . . 154
6.6 Conclusions . . . 157

Chapter 7: Conclusion and Summary **164**

7.1 Vapor Motion in Firn . . . 164

7.2 Implications for Geochemistry 167
7.2.1 Stable Isotopes 167
7.2.2 Irreversibly-Deposited Species 168
7.2.3 Reversibly-Deposited Species 169
7.3 Future Research 170
7.3.1 An Inverse Problem 171

Bibliography **174**

Appendix A: Analytic Model for Post-Depositional Isotopic Change **185**

Appendix B: Energy-Conservation Model **188**
B.1 Mass and Energy Conservation in Firn 188
B.2 Discretization Technique 192

Appendix C: Derivation of Partitioning Function **200**

Appendix D: Vapor Transport Model **206**

Appendix E: Transfer of water between phases **212**

Appendix F: Isotopic Conservation in Pore Space Vapor **216**

Appendix G: Effects of Isotopic Equilibration on Ice Grains **219**

LIST OF FIGURES

2.1 Taylor Dome study area. 29
2.2 Surface elevation of Taylor Mouth area. 30
2.3 The Taylor Dome and Taylor Mouth isotope records. 31
2.4 Filtered Taylor Mouth isotope record. 32
2.5 Isotopic change in idealized snow sample. 33
2.6 Accumulation rate along the Taylor Mouth flowline. 34

3.1 Schematic of outflow boundary condition. 45
3.2 Near-surface horizontal and vertical air-flow velocities. 51
3.3 Contours of temperature field T calculated using parameters of Albert (2002). 53
3.4 Contours of mass-exchange rate calculated using parameters of Albert (2002). 54
3.5 Near-surface horizontal and vertical air-flow velocities for winter conditions with strong winds. 57
3.6 Contours of temperature field T calculated for conditions typical of Antarctic winter with strong winds. 59
3.7 Contours of mass-exchange rate calculated for conditions typical of Antarctic winter with strong winds. 61
3.8 Contours of cumulative mass exchange during Antarctic winter under windy conditions. 62

3.9 Difference between winter temperature fields calculated with moderate and strong winds. 64
3.10 Contours of mass-exchange rate calculated for conditions typical of Antarctic winter with moderate winds. 67
3.11 Contours of temperature field T calculated for conditions typical of Antarctic summer with strong winds. 70
3.12 Contours of mass-exchange rate calculated for conditions typical of Antarctic summer with strong winds. 72
3.13 Contours of cumulative mass exchange during Antarctic summer under windy conditions. 73
3.14 Difference between summer temperature fields calculated with moderate and strong winds. 74
3.15 Contours of mass-exchange rate calculated for conditions typical of Antarctic summer with moderate winds. 76
3.16 Idealized response time of firn to step change in temperature. 79
3.17 Mass-exchange rate as a function of depth for three different values of ice-grain diameter. 80
3.18 Mass-exchange rate as a function of ice-grain diameter. 82

4.1 Effective isotopic diffusivity as a function of k. 118
4.2 Near-surface air-flow velocity vectors with strong winds. 119
4.3 Near-surface firn temperature in summer with strong winds. 120
4.4 Near-surface sublimation and condensation rate in Antarctic summer with strong winds. 121
4.5 Isotopic change in regions of air inflow. 122
4.6 Model prediction of pore-space vapor composition in regions of air inflow. 123

4.7 Model prediction of isotopic change and δ_v in regions of air inflow under reduced wind speed. 124
4.8 Isotopic change in regions of air outflow. 125
4.9 Model prediction of pore-space vapor composition in regions of air outflow. 126

5.1 Near-surface air-flow velocity vectors with strong winds. 139
5.2 Cumulative daily mass-transfer of water as a result of diurnal surface temperature changes. 140
5.3 Change in Peclet number as a result of enhanced water vapor diffusivity. 141
5.4 Comparison of cumulative daily condensation with difference water vapor diffusivity. 142
5.5 Cumulative change in firn mass as a result of diurnal surface temperature changes. 143

6.1 Sensitivity of model for reversible species to grain discretization. . . . 159
6.2 Temperature and water condensation/sublimation rate time series used in model for reversible species. 160
6.3 Predicted changes in H_2O_2 with no sublimation/condensation effects. 161
6.4 Predicted changes in grain radius and H_2O_2 with sublimation/condensation effects. 162
6.5 Predicted changes in grain radius and H_2O_2 with sublimation/condensation effects over summer season. 163

B.1 Locations of control-volume centers and interfaces in energy conservation model. 199

C.1 Grid used for one-dimensional steady-state model. 202

D.1 Location of control-volume centers and interfaces in vapor transport model. 211

E.1 Several published estimates of saturation vapor pressure over ice. . . 213

LIST OF TABLES

3.1 Summary of condensation and sublimation in firn results. 88

ACKNOWLEDGMENTS

This dissertation and the work presented represented by it would not have been possible without the help and support of several people. In particular, I'd like to thank my adviser, Ed Waddington, for his support and encouragement over the past several years. He has spent countless hours and late nights discussing many aspects of both my research and many other topics. Through these discussions, he has helped me to clarify my thoughts and better understand several aspects of glaciology. In addition, I am fortunate to have had the opportunity to work with Howard Conway, Charlie Raymond, and Eric Steig in a number of different contexts. Their continued support, enthusiasm, and insight have been greatly appreciated. I have also benefitted from the keen insight (and wit) of Al Rasmussen over the past few years. I also would like to thank Nadine Nereson and Tony Gades for reading through drafts of this dissertation; I benefitted greatly from their comments and suggestions. I am grateful for several discussions with Alan Rempel, which helped me to clarify many of the ideas presented in Chapter 4 and Appendix F.

I would also like to offer my gratitude to my fellow students at the University of Washington who have made the last seven years much more enjoyable. In particular, I would especially like to thank Bob Hawley for his unfailing support and good humor, and discussions on countless topics, both science related and otherwise, and keen insight on the wonder that is the 1966 Dodge Dart; and Throstur Thorsteinsson for many enjoyable tennis matches and discussions

over the years.

On a personal note, I would like to thank my wife Maureen for her continued patience and support, and without whom this work would not have been possible. She has made the last few years would have not been nearly so interesting and enjoyable. This work also would not have been possible without the support of Kofi who has kept me company while writing. I also thank the rest of my friends and family for their love and support over the years.

This work was financially supported by U.S. National Science Foundation grant NSF-OPP 0196085 to and University of Washington Royalty Research Fund grant RRF-2503 to Ed Waddington.

Chapter 1

INTRODUCTION

1.1 Background

The concentrations of aerosols, dust, and other species in polar snow record different aspects of climate at the time the snow was deposited (Legrand and Mayewski, 1997). The stable isotopic ratios of the water molecules in snow grains record information about the temperature at which the snow formed; the concentration of hydrogen peroxide (H_2O_2) in snow is used as proxy for the oxidizing capacity of the atmosphere; the concentration of sulfur aerosol particles in snow provide information about the energy balance of the atmosphere in which the snow was formed. Near-surface polar snow contains information about modern climate conditions at the site where the snow is collected. Similarly, ice recovered from deep ice cores contains information about past climates at the site of deposition.

Understanding how climate information from the atmosphere is incorporated into the ice is the forward problem in ice core paleoclimate studies. The inverse problem addresses the question in the reverse order: What can be determined about paleoclimate, based on geochemical records from ice cores? In order to relate measured ice core chemistry to past climates, we need to understand both the forward problem and the inverse problem. The forward problem can be separated into three main steps: (1) transportation of geochemical species to the polar regions, (2) transfer of these species to the ice sheet surface and (3) preservation of geochemistry in the snow after deposition.

This dissertation focuses on the third step: the preservation of different chemical species in firn. The goal is to understand how initial concentrations of impurities in snow have changed since they were deposited initially to the time that the ice is recovered from a core. This work focuses on changes in the upper few meters of the snowpack that are caused by firn ventilation (e.g. Waddington and others, 1996). The term firn ventilation refers to the forced air flow through snow as a result of wind blowing over the wavy snow surface.

1.2 Motivation and Goals

Observations of post-depositional chemical change (e.g. Grootes and Steig, 1992; McConnell and others, 1998; Wagnon and others, 1999) and extensive theoretical work on firn ventilation (e.g. Gjessing, 1977; Clarke and others, 1987; Colbeck, 1989; Waddington and others, 1996; Colbeck, 1997; Albert, 2002) demonstrate that significant post-depositional redistribution of water and trace constituents is possible in the firn. Current models of post-depositional chemical change in snow either neglects the effects of firn-ventilation driven water vapor redistribution (e.g. McConnell and others, 1998) or treats the effects qualitatively (e.g. Waddington and others, 2002). The goal of this dissertation is to develop a quantitative model for the condensation and sublimation of water in firn based on firn-ventilation theory. I use this model to investigate modern preservation of different chemical species in polar snow and present a quantitative model of the effects of post-depositional water-vapor motion on different geochemical species in snow and determine the extent to which firn ventilation can cause measurable changes in the geochemistry of polar snow.

1.3 Synopsis/Organization

Chemical measurements on snow or ice cores are usually made in terms of the concentration of a particular impurity, i.e. the ratio of the amount of an impurity to

an amount of ice. Therefore a change in chemical concentration can be caused by a change in the amount of chemical present, and/or a change in the amount of ice present. Through time, impurities deposited at the surface become buried by further accumulation of snow. In order to understand how the concentration of an impurity can change with depth, it is important to understand the mobility of both water vapor and chemical species with depth in the snowpack. Here I study both components.

Chemical impurities in polar snow are broadly classified into two main groups (e.g. Waddington and others, 1996); irreversibly-deposited (which are relatively immobile after deposition to the surface) and reversibly-deposited (which cycle between the atmosphere and snow after deposition) species. In addition, the stable isotopic composition of the ice matrix itself is of interest to ice core geochemists. An analysis of the effects of firn ventilation on each of these geochemical species is presented.

Chapter 2 examines the disparity between $\delta^{18}O$ records from two ice cores collected from Taylor Dome, Antarctica. I discuss possible reasons for the differences in the records and present a new model for post-depositional isotopic change. Chapter 3 presents a 2-D model for water vapor motion in the firn. I compare this model with an existing model (Albert, 2002) and use it to estimate sublimation and condensation rates in the firn for a variety of environmental conditions. The model suggests that air in firn pore spaces will always be nearly saturated (relative humidity = 1). The degree to which the relative humidity $\neq 1$ drives mass exchange between phases. Chapter 4 presents a new 2-D model for isotopic change in the firn, using the sublimation and condensation rates generated in Chapter 3. I compare the results of my model with existing models (Cuffey and Steig, 1998; Johnsen and others, 2000) and demonstrate that firn ventilation is an important component of isotopic exchange in the firn, as equilibration with atmospheric water vapor, sublimation and condensation are all significant processes in isotopic diffusion in firn. Chapter 5 examines the effect of firn ventilation on the concentration of irreversibly-deposited species in firn, using non-sea-salt (nss-) sulphate as a proxy for the behavior of other irreversibly deposited

species. I also investigate the effects of enhanced water vapor diffusivity (hand-to-hand diffusion) in snow on the vapor-motion model (Chapter 3) and on concentrations of nss-sulphate. Results suggest that the concentration changes induced by firn ventilation are much smaller than the annual variability of nss-sulphate in surface snow. Chapter 6 uses H_2O_2 as representative of other reversibly-deposited species, and I discuss the sensitivity of H_2O_2 concentration in firn to ventilation. This analysis suggests that firn ventilation is of secondary importance to H_2O_2 concentration, but it may be more important to the preservation of other reversibly-deposited species. Chapter 7 summarizes the results of this dissertation and suggests future directions for research on the geochemistry of snow. Some of the development necessary for completeness is presented as appendices.

Chapter 2

NON-CLIMATE INFLUENCES ON STABLE ISOTOPES AT TAYLOR MOUTH, ANTARCTICA

Material from the first half of this chapter was presented under the title 'From the dome to the flank: Relating two stable isotope records' as a poster at the American Geophysical Union 2000 Fall Meeting with co-authors E.D. Waddington, H.P. Marshall (both University of Washington), D.L. Morse (University of Texas) and P.M. Grootes (Leibniz Labor für Alterbestimmung und Isotopenforschung, Christian-Albrechts-Universität). Material from the second half of this chapter was presented under the title 'Post-depositional changes in stable isotope ratios' as an invited talk at the American Geophysical Union 2001 Spring Meeting.

2.1 Summary

The late Holocene trends in $\delta^{18}O$ differ significantly between the Taylor Dome and Taylor Mouth ice cores. Assuming that the Taylor Dome core records the local climate signal leaves three possible causes for the observed differences: (1) Ice at depth at Taylor Mouth originates at higher and colder elevations; the trend in the Taylor Mouth core may be due to a standard $\delta^{18}O$ - surface temperature relationship. (2) Taylor Mouth, unlike Taylor Dome, may receive precipitation from multiple sources with distinct isotopic compositions. (3) Taylor Mouth is a low accumulation rate area; the isotopic record may be affected by vapor motion and post-depositional isotope enrichment in the firn. Modelling firn pore-space vapor as a combination of vapor from the atmosphere and vapor from sublimating ice grains, we conclude that post-depositional processes can modify $\delta^{18}O$ values by several ‰ in areas of low accumulation rate. Attributing the entire difference to process (1) requires an unrealistically large $\delta^{18}O$ - surface temperature slope. It is not likely that the observed difference between the Taylor Dome and Taylor Mouth isotope records are caused by

this effect. Additional field sampling strategies for isotopes could differentiate between possibilities (2) and (3).

2.2 Introduction

Taylor Dome (Fig. 2.1) is an ice dome located inland of the Transantarctic Mountains in south Victoria Land, East Antarctica. An ice core to bedrock was collected from near the summit of Taylor Dome in 1994 (Grootes and others,1994). This core has provided a 150 kyr stable isotope record (Steig and others, 2000; Grootes and others, 2001) and an atmospheric CO_2 record for the past 60 kyr (Indermuhle and others, 2000). Several short ($\leq$100 m) firn cores were also collected in order to assess the spatial variability of climate and climate signal preservation in the area. One of these cores was collected approximately 30 kilometers NE of the main core site, at the head of Taylor Valley (Fig. 2.1), a site we refer to as Taylor Mouth. Assuming the ice geometry has not changed significantly, ice at the Taylor Mouth core site originates along a flowline from a saddle approximately 12 km to the north west (Fig. 2.2).

The north side of Taylor Dome receives less than 4 cm ice equivalent accumulation per year (Morse and others, 1999). Consequently, the Taylor Mouth core, although only 100 m long, provides an isotope record spanning 2100 years (Neumann and others, in preparation). Neumann and others (in preparation) generated a depth-age scale for the Taylor Mouth core which allows us to compare the Taylor Mouth isotope record with the Taylor Dome core. Although the two cores were collected only 40 km apart (Fig. 2.1), the Taylor Mouth and Taylor Dome isotope records show different trends in the Holocene, Taylor Mouth becoming less negative towards the present, Taylor Dome becoming more negative (Fig. 2.3).

In this paper, we explore three possible causes for the observed differences between the two cores: (1) Since the ice at depth in the Taylor Mouth core originates at progressively higher elevations with lower mean annual surface temperatures, the trend in

the Taylor Mouth core may be due to spatial temperature variation following a standard δ^{18}O - surface temperature relationship (Dansgaard and others, 1973; Jouzel and others, 1997) rather than temporal change. (2) The Taylor Mouth area may receive varying percentages of precipitation from multiple sources with distinct isotopic compositions. Precipitation could come from storms passing over Taylor Dome, or storms penetrating up Taylor Valley (Fig. 2.1), or snow blown from the polar plateau by the prevailing katabatic wind. Precipitation arriving at Taylor Mouth could be a mix of precipitation from these various source regions. (3) Wind-driven ventilation of the firn near Taylor Mouth could modify stable isotope ratios. Firn ventilation can cause vapor redistribution in the firn. Isotope ratios can then be modified by sublimation and condensation in the firn, resulting in the loss of light isotopes. This process can be important in low accumulation rate areas like Taylor Mouth, where snow remains near the surface for several years (Waddington and others, 2002). We present a model to examine how air flow through firn could modify the stable isotope ratios prior to deep burial. We find that the δ^{18}O - surface temperature relation slope needed to match observation with only process (1) is unrealistically large. We show that either option (2) or (3) could be responsible for the observed trend in the Taylor Mouth δ^{18}O record. We identify field measurements that could be used in the future to discriminate between these two possibilities.

2.3 Comparison of Taylor Dome and Taylor Mouth Isotope Records

We have measured oxygen isotope ratios δ^{18}O in the Taylor Mouth core. Using the depth-age model of Neumann and others (in preparation), we can convert the measured $\delta^{18}O(z)$ into a temporal record $\delta^{18}O(t)$. We compare the Taylor Mouth isotope record with the Taylor Dome stable isotope record, which was collected nearby (Fig. 2.1). The oxygen isotope records for both cores were measured at the University of Washington Quaternary Isotope Laboratory; details of the measurement procedure

vapor cools at the lapse rate; this cooling results in condensation, and the condensate precipitates. Stable isotopes of oxygen and hydrogen fractionate upon condensation, causing the remaining vapor to preferentially lose heavy isotopes. Continued cooling of moisture results in progressively more negative δ^{18}O of precipitation. In Antarctica, precipitation is believed to form just above the inversion layer (Robin, 1977). Consequently, the δ^{18}O of precipitation is often used as a proxy for temperature at the inversion layer. Mean annual surface temperature is linearly related to the temperature at the inversion layer (Jouzel and Merlivat, 1984). In this way, the δ^{18}O of precipitation can be linearly related to mean annual surface temperature. This spatial correlation becomes stronger as the range of surface temperatures spanned becomes greater. Sites that receive precipitation as a result of orographically-induced cooling of storm systems may therefore be expected to have a linear relationship between annual average δ^{18}O values and mean annual temperature (Dansgaard and others, 1973). Since the ice in the Taylor Mouth core was originally deposited over a range of elevation (Fig. 2.2), we might expect the stable isotope record to include this elevation effect.

In order to investigate an elevation influence on δ^{18}O at Taylor Mouth (process 1), we first need to remove the temporal changes. By subtracting the trend of the Taylor Dome Holocene record (Fig. 2.3), which we assume reflects only changing climate in the area, we remove the temporal climate signal from the Taylor Mouth record. This correction accentuates the trend in the Taylor Mouth record. The residual trend shown in Figure 2.4 must be due to processes other than climate change.

We use the same particle paths that provided ages for the Taylor Mouth core (Neumann and others, in preparation) to calculate the elevation at the point of origin for ice at any depth in the core. These origin sites span 100 meters vertically. Measured 10 meter firn temperatures at the two points marked by stars in Figure 2.2 indicate a surface temperature lapse rate of -2°C per 100 meters of elevation along the Taylor Mouth flowline. This lapse rate together with the corrected δ^{18}O trend in

the core yields a temperature-isotope relationship of:

$$\delta^{18}\mathrm{O} = 2.59\, T_\mathrm{s} + 56.9\ , \tag{2.1}$$

where T_s is the mean annual surface temperature measured in degrees Celsius. In this analysis, we have made the critical assumption that the present slope of the δ^{18}O - T_s relationship has been constant during the past 2100 years. Although Jouzel and others (1997) discuss several factors that can change this slope with time, we assume that this relationship has been stable over the period spanned by the Taylor Mouth core.

The slope of Equation (2.1) is significantly higher than other values reported for East Antarctica. Dansgaard and others (1973) report a slope of 0.76‰ per °C over a large range of surface temperatures in East Antarctica. However, the variation in both surface temperature and surface δ^{18}O values at Taylor Mouth is small compared with the range of values used by Dansgaard and others (1973), so the coefficients in Equation (2.1) are very poorly constrained. Dansgaard (1964) calculated a maximum theoretical slope of 0.95 for entirely orographically-driven precipitation. Consequently, it is unlikely that the entire trend in the residual of the Taylor Mouth ice core (Fig. 2.4) is due to advection by down-slope ice flow and a causal δ^{18}O - T_s relationship.

2.5 Mixing of Snow From Different Sources

Most of the precipitation at Taylor Dome arrives from the south, with only a small contribution from the north (Morse and others, 1998). Since the dominant wind direction at the Taylor Mouth core site is downslope off Taylor Dome (Fig. 2.2), it is likely that some of the precipitation arriving at Taylor Mouth could be delivered by storms passing over the dome. This snow could have a slightly lighter δ^{18}O value than the summit snow, if the storm continued to precipitate as it moved toward Taylor Mouth. Precipitation could also be wind-blown from the Dome or the polar

plateau, and would have the isotopic signature of the source area. In either of these cases, the δ^{18}O of the snow delivered to Taylor Mouth would not have a causal linear relationship with T_s at Taylor Mouth.

We might also assume that some precipitation arrives by normal orographic processes in air masses arriving upslope from Taylor Valley, and that this snow, which may have a normal δ^{18}O - T_s relationship, is mixed in varying proportions with spatially uniform δ^{18}O snow from Taylor Dome or the polar plateau. If the amount of Dome or plateau snow delivered to the Taylor Mouth area decreases with distance from the plateau, we can create a mixing model to represent the spatial distribution of deposited snow. In the simplest version of this model, the amount of constant δ^{18}O snow from the plateau decreases linearly along the flowline. We further assume that the isotopic content $\delta^{18}O_{valley}$ of the orographic precipitation from Taylor Valley storms is related to surface temperature by the typical relation for East Antarctica (Dansgaard and others, 1973):

$$\delta^{18}\mathrm{O}_{\mathrm{valley}}(x) = 0.76\, T_s(x) - 10\ . \tag{2.2}$$

We can then set limits on the isotopic value of the incoming snow from the plateau, and on the mixing ratio along the flow line. We define $\psi(x)$ as the fraction of snow transported from the polar plateau as a function of x, $\delta^{18}\mathrm{O}_{\mathrm{plateau}}$ as the bulk isotopic value of that snow (treated as a constant), $\delta^{18}\mathrm{O}_{\mathrm{core}}$ as the stable isotope record from the core after removing the temporal climate signal from the Taylor Dome core (Fig. 2.4), and $\delta^{18}\mathrm{O}_{\mathrm{valley}}(x)$ as the isotopic content of snow delivered up Taylor Valley. We can represent the mixing of snow from these two sources (up-valley and plateau) by:

$$\delta^{18}\mathrm{O}_{\mathrm{core}} = (1-\psi(x))\ \delta^{18}\mathrm{O}_{\mathrm{valley}}(x) + \psi(x)\ \delta^{18}\mathrm{O}_{\mathrm{plateau}}\ . \tag{2.3}$$

In this way, we describe the Taylor Mouth record as a combination of orographic precipitation in storms from Taylor Valley, and wind-blown surface snow from the plateau. For a given $\delta^{18}O_{plateau}$ and measured $\delta^{18}O_{core}$, we vary the mixing ratio $\psi(x)$ to find a $\delta^{18}O_{valley}(x)$ that most closely matches the $\delta^{18}O_{core}$ profile assuming

the Dansgaard and others (1973) relationship (Equation (2.2)). Snow from Taylor Dome has an average δ^{18}O of -40‰. Using this analysis, we find that snow from the summit of Taylor Dome cannot produce a $\delta^{18}O_{valley}(x)$ similar to Equation (2.2), regardless of the mixing ratio $\psi(x)$. Any input snow that is isotopically heavier than the minimum Taylor Mouth values (δ^{18}O = -41.5‰) will increase the slope of the relationship between δ^{18}O and T_s for up-valley precipitation. Measurements of δ^{18}O from snow pits west of the Taylor Dome core site have average values of -45‰. By using $\delta^{18}O_{plateau}$ = -45‰, we can produce a $\delta^{18}O_{valley}(x)$ profile consistent with Equation (2.2) if $\psi(x)$ varies linearly from 0.45 at the upstream end of the flowline to 0.0 at the core site.

This analysis assumes that the precipitation at Taylor Mouth arrives continually throughout the year. However, we know that precipitation is episodic (McConnell and others, 1997a; van der Veen and others, 1999), and that δ^{18}O values of precipitation reflect the season of deposition (Steig and others, 1994). Equation (2.3) uses annual average δ^{18}O values, rather than seasonally weighted δ^{18}O values. If snow is blown to Taylor Mouth from the plateau or Taylor Dome predominantly in one season, Equation (2.3) will not reflect this. For example, winter precipitation at Taylor Dome typically has δ^{18}O = -45‰ (Grootes and Steig, 1992), similar to the annual average δ^{18}O of the plateau. Using this analysis, we are unable to distinguish between mixing snow from the plateau throughout the year or mixing snow from Taylor Dome only in winter.

This simple mixing model illustrates two points about the Taylor Mouth isotope record. First, if the snow deposited upstream of Taylor Mouth includes a sizable contribution of isotopically heavy snow from Taylor Dome (δ^{18}O = -40.5‰) then an up-valley contribution of snow must have a very steep δ^{18}O - T_s relationship. Second, a contribution of blown snow from the colder polar plateau (δ^{18}O = -45‰) implies that any up-valley precipitation must have a lower slope δ^{18}O - T_s relationship, closer to what is seen elsewhere in the East Antarctic. We can explain the observed trend

in the Taylor Mouth isotope record with this mixing model if the source area for the blown snow has a more negative $\delta^{18}O$ value than the minimum Taylor Mouth values ($\delta^{18}O$ = -41.5‰).

2.6 *Post-Depositional Isotopic Enrichment*

Alternatively, the observed differences between the Taylor Mouth and Taylor Dome stable isotope records may be a result of post-depositional isotopic change at Taylor Mouth (process 3). Isotopic ratios may be modified by water vapor movement in the firn. It has been observed that ice core geochemistry can be complicated by sublimation and redeposition of water within the upper meters of the snow pack (McConnell and others, 1998; Wagnon and others, 1999). The effects of water vapor movement are intensified in low accumulation rate areas, where snow remains exposed to near-surface ventilation effects for several years (Waddington and others, 1996; Waddington and others, 2002). Wind-driven ventilation acts to increase the rate of water vapor motion in the firn. The strong spatial gradient of accumulation rate across Taylor Dome (Morse and others, 1999) creates an ideal environment to investigate the effects of ventilation on stable isotopes.

Grootes and Steig (1992) measured $\delta^{18}O$ in the upper two meters at sites on a 10 kilometer grid on Taylor Dome. The average isotopic values change from -42.7‰ along the south side of the dome where the accumulation rate is highest, to -41‰ at the summit, to -39.2‰ along the north side of the dome where the accumulation rate is lowest. Air movement through the firn can cause sublimation and redeposition of water vapor within the firn; one commonly observed result is depth hoar. As noted by several authors (e.g. Vimeux and others, 2001), the phase changes associated with the formation of depth hoar will cause isotopic changes in the firn. By investigating fractionation processes in the firn, and estimating sublimation and redeposition rates, we explore the importance of firn ventilation on stable isotope

ratios in low accumulation rate areas such as Taylor Mouth and the north side of Taylor Dome.

2.6.1 Model Description

Water vapor sublimates from ice with negligible isotopic fractionation, i.e. $\delta^{18}O_{vapor} = \delta^{18}O_{ice}$ (Friedman and others, 1991). However, as vapor recondenses, the heavier isotope ^{18}O is redeposited preferentially. Since the redeposited ice is isotopically heavier than the vapor from which it condenses, the remaining vapor is depleted in the heavy isotope. If we consider this as a Rayleigh process, we can quantify how the $\delta^{18}O$ of the remaining vapor and the condensate change as a function of the amount of vapor remaining. In a Rayleigh process, the condensate forms at isotopic equilibrium with the vapor, and is immediately removed from the vapor after condensation. Following Dansgaard (1961):

$$R_v = R_{vo}\,\beta^{\alpha-1} \tag{2.4}$$

$$R_c = R_{vo}\,\frac{1-\beta^{\alpha}}{1-\beta}\,, \tag{2.5}$$

where R_v is the stable isotope ratio in the vapor, R_{vo} is its initial value, α is the temperature-dependent fractionation coefficient which determines how heavy and light isotopes are partitioned between the vapor and condensed phases, β is the fraction of vapor that does not condense in the firn (i.e. remaining fraction of the vapor phase), and R_c is the stable isotope ratio of the total condensate. (See Appendix A for details.) We construct an analytical model of $\delta^{18}O$ changes in a mass of firn as a result of air flow through the firn using the above relations.

Massey (1995) studied the isotopic composition of water vapor above the snowpack-air interface at Summit, Greenland. The $\delta^{18}O$ of the atmospheric water vapor ($\delta^{18}O$ = -45‰) was approximately in isotopic equilibrium (Criss, 1999) with the average $\delta^{18}O$ of the snowpack ($\delta^{18}O$ = -30‰). Massey (1995) experimented with forcing this

atmospheric vapor through 2 m of firn. By comparing the $\delta^{18}O$ of the atmospheric vapor with the $\delta^{18}O$ of the vapor that had been pumped through the snowpack, Massey found that the pumped vapor was a mixture of atmospheric vapor, and vapor sublimated directly from the average snow grains.

Following this result, we model the pore-space vapor as a mix of vapor with the $\delta^{18}O$ of atmospheric vapor (which is in isotopic equilibrium with the snow) and vapor with the $\delta^{18}O$ of vapor sublimated from the snowpack. We assume that the air in the snowpack pore space is always at saturation vapor density. The total mass m_v of the vapor in the pore space is then constant (number concentration of moles $\times$ pore space volume $\times$ molar mass of water).

We let τ specify the characteristic residence time for air in firn. We define $\mathcal{R}$ as the fractional rate at which the remaining mass of firn sublimates. The fraction of the firn that sublimates per characteristic time is then $\mathcal{R}\tau$. We again let β specify the fraction of the pore-space vapor m_v that is lost to the atmosphere. The fraction $(1-\beta)$ of the pore-space vapor is therefore redeposited (condensed) in the firn. The fraction of the pore-space vapor that is derived from sublimating snow grains is determined by the relative humidity RH of the atmosphere. If the relative humidity of the incoming air is near saturation, the fraction of the pore-space vapor that comes from sublimating snow grains is small. Conversely, if the RH of the incoming air is small, the fraction of pore-space vapor from sublimating snow grains is large. Consequently, the fraction of the firn the sublimates per characteristic time $\mathcal{R}\tau$ is limited by the RH of the air entering the firn.

Values of $\mathcal{R}$ are determined by the vapor density of air entering the firn, the saturation vapor density (determined by firn temperature) and the pore space volume of the firn (determined by firn porosity). We assume that the time required for the pore-space air to reach saturation vapor density is small relative to the characteristic time τ, an assumption discussed in Section 2.6.2. This means that we assume that the air in the pore spaces is always at saturation vapor density.

Using these parameters, we can calculate how the net solid mass of firn m_f changes as a function of time, how the isotopic content of the condensate $\delta^{18}O_c$ changes as a function of time, and how the bulk isotopic content of the remaining firn $\delta^{18}O_f$ changes.

We normalize both mass terms (net mass of solid firn m_f and total mass of vapor in pore space m_v) by a reference mass $m_o = 1\text{kg}$ in order to express the changes as per kg of snow (see Appendix A for details):

$$m_f(t) = \frac{(1-\beta)\, m_v}{\mathcal{R}\,\tau} + \left(m_f(0) - \frac{(1-\beta)\, m_v}{\mathcal{R}\,\tau} \right) \exp\left(-\mathcal{R}t\right) \tag{2.6}$$

$$\delta^{18}O_c(t) = \left(1000 + \delta^{18}O_{vo}(t)\right) F - 1000 \tag{2.7}$$

$$\delta^{18}O_f(t) = \frac{Fb - 1000}{Fa - 1} + \left(\delta^{18}O_f(0) - \frac{Fb - 1000}{Fa - 1} \right) \times \ldots \exp\left((1 - Fa)(\ln(m_f(t)) + \mathcal{R}t)\right) , \tag{2.8}$$

where

$$\delta^{18}O_{vo}(t) = (1 - RH)\, \delta^{18}O_f(t) + RH \left(\frac{\delta^{18}O_f(t)}{\alpha} + 1000 \left(\frac{1}{\alpha} - 1 \right) \right) \tag{2.9}$$

$$F = \left(\frac{1 - \beta^{\alpha}}{1 - \beta} \right) \tag{2.10}$$

$$a = (1 - RH) + \frac{RH}{\alpha} \tag{2.11}$$

$$b = 1000\, RH\, (\frac{1}{\alpha} - 1) + 1000\,, \tag{2.12}$$

and $\delta^{18}O_{vo}(t)$ is the isotopic composition of the pore-space vapor. a, b, and F are constants and the factor of 1000 arises from the definition of the $\delta^{18}O$ scale (e.g. Paterson, 1994, p. 380). β is the fraction of vapor that does not recondense in the firn, as defined above, and α is the equilibrium isotopic fractionation coefficient. Although we derived this model for $\delta^{18}O$, we can also predict changes of δD in the firn by using the isotopic fractionation coefficient α appropriate for deuterium.

2.6.2 Discussion of Assumptions

First, we assumed that vapor condensation proceeds as a Rayleigh process. Jouzel and Merlivat (1984) also explored an isotopic kinetic effect that can modify the Rayleigh process in condensation. Since the heavy and light isotopes of water have different masses, their diffusivities in air differ by about 3% (Merlivat, 1978). This modifies the equilibrium fractionation coefficient α. This kinetic effect is a function of the relative humidity of the air mass, and a coefficient that depends on the size and geometry of the condensing crystals. This effect is critically important in clouds, where the relative humidity (RH) can be as high as 1.3. In the snowpack, where relative humidity is very close to 1, this additional fractionation factor modifies the equilibrium fractionation coefficient by at most 4%. Given the wide range of possible values of other parameters, this is a secondary effect.

Second, we assume that the average isotopic content of the vapor sublimated from the firn equals the average isotopic content of the firn, i.e. the water in the remaining snow grain is continually well-mixed. There are a number of processes that act to isotopically homogenize grains in the snowpack. Whillans and Grootes (1985) examined isotopic diffusion through solid ice grains. They found that the diffusion time scale for isotopic perturbations within the grain to decay to half amplitude was:

$$\tau_{1/2} = 0.057 \frac{l^2}{D_{\text{ice}}}, \tag{2.13}$$

where l is the path length from the interior of the grain to the air-ice interface, D_{ice} is the temperature-dependent diffusivity of stable isotopes in ice, and the factor of 0.057 arises because an ice grain is three dimensional. In summer at Taylor Dome, temperatures are typically -20°C. For a spherical grain of radius 0.25 mm, this diffusion time scale is about 20 days. In the winter, when the temperature is much lower, the diffusion time scale is about 100 days.

In addition, grain metamorphism will homogenize the remaining mass isotopically, as smaller grains are consumed and incorporated into larger grains. There are a

number of processes that lead to grain metamorphism; here we discuss two of them. (1) The differences in the radius of curvature of snow grains result in local differences in saturation vapor pressure. Small grains have a large radius of curvature and an associated high saturation vapor pressure over their surface. They are consumed by larger grains which have a small radius of curvature and a lower vapor pressure. At -40°C (the mean annual temperature at Taylor Dome), the time scale for radius of curvature metamorphism (Colbeck, 1980) ranges from 20 minutes for small grains (radius = 1 μm) to decades for large grains (radius = 1 mm). (2) In addition, temperature gradients in the snow will also cause vapor pressure gradients, which lead to grain metamorphism (Colbeck, 1983a). At -40°C and a temperature gradient of 5°C per meter, the time scale for grain consumption varies from 18 hours for small grains (radius = 1 μm) to 2 years for large grains (radius = 1 mm).

Clearly, diffusion within the grains acts to homogenize the grains isotopically more quickly than the above grain metamorphism processes for an average grain size of 100 μm. We treat the grains as isotopically well-mixed, an assumption that may be valid only in the summer season.

Third, we assume that α, $\mathcal{R}$, RH and β are constant with respect to time. In practice, the fractionation coefficient α is an exponential function of temperature which changes throughout the year. For the 30°C temperature range at Taylor Dome, α varies from 1.014 to 1.018 (Whillans and Grootes, 1985); in our model we use a value of 1.016, which corresponds to about -40°C.

$\mathcal{R}$ and β vary with the relative humidity RH of the air entering the snowpack. In general, the relative humidity of air just above the snowpack is not known. When air enters with a high relative humidity, the firn sublimation rate $\mathcal{R}$ will be low, since the air cannot hold more vapor. Conversely, air entering with low relative humidity will result in a higher value for $\mathcal{R}$, since the air mass approaches equilibrium saturation vapor density as it moves through the firn. In Chapter 3, I demonstrate that the time required for pore space air to reach saturation density is much smaller than the

residence time τ of air in the firn. Massey (1995) found that at Summit, Greenland, in the summer of 1990, the isotopic mixing ratio between vapor from the atmosphere and vapor from sublimating snow grains was between 0.5 and 0.25. This suggests that the atmospheric relative humidity at the time of the study was between 0.5 and 0.75. Recent measurements of relative humidity at South Pole (S. Warren, personal communication) also fall in this range.

Our model also assumes that the firn is isothermal. Since saturation vapor density is a function of temperature, the temperature profile of the firn is important. A model that accounts for variable temperature and the associated variation in saturation vapor density along a trajectory, such as the model described by Albert and McGilvary (1992), will be an important component of the full solution of the effect of air movement on $\delta^{18}O$ values in firn.

This analysis does not include a full treatment of other physical processes in the firn, such as mass-transfer rates from the ice crystals to the vapor, or air flow rates through the firn. The residence time τ of air in the firn depends on the physical properties of the firn such as surface microtopography and permeability (Waddington and others, 1996). These properties may change throughout the year, leading to variations in τ. Our model uses a constant τ. The ratio of the characteristic time for the mass transfer to the characteristic residence time of air in firn will determine to what extent saturation vapor density is reached as air moves through firn, and whether isotopic equilibrium is reached between the vapor in the pore space and in the surrounding snow grains. Consequently, better understanding of the time scale for mass transfer from ice grains to vapor will be another important part of the full solution. This analysis assumes that the air in the pore spaces is always saturated, and that the pore-space vapor leaves the firn before reaching isotopic equilibrium with the snow grains.

2.6.3 Model Application

To estimate an upper limit for $\mathcal{R}$, the fractional rate of snow mass sublimation, we consider the end member case where all the pore-space vapor originates from sublimated ice grains. We first estimate the saturation vapor density in the pore space using the Clausius-Clapeyron equation (Appendix E):

$$\rho_v^{sat} = \rho_{v_0} \exp\left(C\left(\frac{1}{T_0} - \frac{1}{T}\right)\right) , \tag{2.14}$$

where ρ_{v_0} and T_0 are reference vapor density and temperature (usually taken at the triple point), T is absolute temperature and $C = 6145$K is a constant. This formulation ignores the vapor density dependence on radius of curvature of snow grains. However, for average grain sizes in snow ($r = 100$ μm to 1000 μm), the bulk temperature dominates the local saturation vapor density (Colbeck, 1982).

Surface snow at Taylor Dome has porosity of the order 0.5 to 0.6 m^3 of void space per m^3 of snow. For the range of porosities and saturation vapor densities that we expect, the total mass of vapor in the pore spaces will be around 10^{-4} kg of vapor per cubic meter of snow, or about 10^{-6} kg of vapor per kg of snow. This sets an upper limit on the fraction $\mathcal{R}\tau$ of the firn that can be sublimated per characteristic time τ.

Another key parameter in this analysis is the characteristic residence time τ for vapor in the firn. Based on the ventilation modelling of Colbeck (1989) and Waddington and others (1996), we expect that residence times in the upper 50 cm of firn will be of the order 10 seconds. These estimates result in an upper estimate of $\mathcal{R}$ (i.e. $\mathcal{R}_{max}$ on the order of $10^{-7}s^{-1}$).

Since air entering the firn already contains water vapor, the above estimate for $\mathcal{R}$ is an upper bound. In fact, incoming air will also have some initial isotopic composition, which then mixes with vapor sublimated from the firn, as discussed above. Although RH and $\mathcal{R}$ are independent parameters in our equations, physically we can link these parameters. If we assume that saturation vapor density in the firn cannot be exceeded, then $\mathcal{R} = (1 - RH) \times \mathcal{R}_{max}$. For example, for $RH = 0$, we assume that all pore-space

vapor is due to sublimating ice grains and $\mathcal{R}$ takes its maximum value.

The parameter β, which defines the fraction of vapor lost to the atmosphere, is also poorly known. Air may exit the snow pack with some degree of either under- or super-saturation relative to the temperature of the snow. Albert and McGilvary (1992) demonstrated that for moderate air flow speeds, air can exit firn with some super-saturation (order of 1%). By using a range of β, we can study a range of both under- and super-saturation of air leaving the firn. In this model, as β goes to zero, the relative humidity of air leaving the firn goes to zero, and all pore-space vapor is condensed in the firn.

Figure 2.5 uses Equation (2.8) to calculate the isotopic change in the remaining firn after one year, for various $(\mathcal{R}, \beta)$ combinations. The horizontal axis represents a range of mass vaporization rates from a minimum of $\mathcal{R} = 0$ (no sublimation) to $\mathcal{R}_{max}$ (all pore-space vapor due to sublimation). The vertical axis represents a range of possible β values, from a minimum of 0 (no vapor is lost to the atmosphere - all vapor is condensed in the firn) to a maximum of 1 (all vapor lost to atmosphere - no vapor is condensed in firn).

We verify that this model behaves as expected for a few end-member cases. For $\beta = 1$, all pore-space vapor is lost to the atmosphere, and no vapor is condensed in the snowpack. Since there is no condensation, and therefore no isotopic fractionation, we expect that the average δ^{18}O value of the snowpack will not change, regardless of the mass vaporization rate $\mathcal{R}$. As Figure 2.5 shows, along the horizontal line $\beta = 1$, our model predicts that there is no change in δ^{18}O of the firn.

If all the pore-space vapor is derived from sublimating snow grains, $\mathcal{R} = \mathcal{R}_{\text{max}}$. If all of this vapor is recondensed in the snow pack ($\beta = 0$), we again expect that the average δ^{18}O value of the snow will not change. This situation occurs in the lower right corner of Figure 2.5. As expected, the model predicts no change in δ^{18}O .

Finally, if no snow sublimates ($\mathcal{R} = 0$), and undersaturated air leaves ($\beta < 1$), then atmospheric vapor is deposited in the snow. Atmospheric vapor is assumed to

be in equilibrium with the snow, and therefore to be more negative than the snow. This situation, while not likely to be widespread in nature, would lead to a decrease in the bulk δ^{18}O of the firn, as seen in the lower left corner of Figure 2.5.

Figure 2.5 allows us to explore many different environmental scenarios. For example, if the relative humidity of air exiting the snowpack is approximately equal to the relative humidity of air entering the snowpack, solutions are found along the diagonal from the upper left corner to the lower right corner. Furthermore, we anticipate that atmospheric relative humidity RH will be greater than 50%, which corresponds to $\beta > 0.5$. Figure 2.5 shows that, for a range of β, after one year the average isotopic content of the snowpack could change by a few tenths of 1‰. Even for very low $\mathcal{R} = 0.1\ \mathcal{R}_{\text{max}} = 10^{-8}$ (corresponding to $RH = 0.9$), our model predicts a change of 0.05‰ after 1 year. For $\mathcal{R} = 0.3\ \mathcal{R}_{\text{max}} = 3 \times 10^{-8}$ (corresponding to $RH = 0.7$), our model predicts a change of 0.2‰ after 1 year. At Taylor Mouth, the net accumulation rate is low, as shown in the upper panel of Figure 2.6. Firn remains near the surface for $\sim$ 5 years or longer near the core site. Even though the post-depositional isotopic change proceeds slowly, the total offset could be as much as a few permil at Taylor Mouth.

We expect the effects of this process to scale inversely with accumulation rate. High accumulation rates bury surface snow before post-depositional isotope fractionation can modify the δ^{18}O values of the deposited snow. Conversely, low accumulation rates allow snow to remain near the surface and open to the effects of this process for several years.

The accumulation rate along the Taylor Mouth flowline (see upper panel of Fig. 2.6) varies from a low of $\sim$ 5 cm ice equivalent per year near the core site, to a high of $\sim$ 12 cm per year at 3200 m along the flow line. Consequently, we expect the effects of post-depositional modification to vary along the flow line. The general effect of this process is to remove the lighter isotope preferentially. Isotope values in the firn become heavier (less negative) through time.

By comparing the surface origin sites of ice in the Taylor Mouth core with the accumulation rate along the flow line (see lower panel of Fig. 2.6), we can predict how the effects of this process may change with increasing depth in the core. Ice that originated near the core site, where the accumulation rate is low, experienced the largest post-depositional modification. Ice originating near the core site may have been a few permil more negative when first deposited. Conversely, ice from deeper in the core originated farther up the flowline where the accumulation rate is higher, and therefore experienced less post-depositional modification. Since the effect of this modification is to make δ^{18}O values heavier, the surface snow along the flow line may have had a more uniform stable isotope distribution originally.

We can explain some of the residual trend in the Taylor Mouth δ^{18}O record (Fig. 2.4) with this model of post-depositional isotopic enrichment. Based upon our calculations, it is relatively easy to change the isotopic composition of surface snow by several permil prior to deep burial at Taylor Mouth. The sign of the change will depend on poorly-constrained knowledge, such as the relative humidity of the atmosphere above the snow surface and the isotopic composition of water vapor in the atmosphere. As shown in Figure 2.5, it is possible to either enrich or deplete the firn of heavy isotopes. If the firn temperature is lower than the air temperature, we may expect air leaving the firn to be under-saturated relative to the air, due to the temperature sensitivity of saturation vapor density (Equation 2.14). This situation may result in a net transport of atmospheric vapor into the firn, and a corresponding decrease in the δ^{18}O value of the firn. Conversely, if the firn is warmer than the atmosphere, air may leave the firn with some degree of supersaturation. The net result of this situation may be to remove water vapor from the firn into the atmosphere, and enrich the remaining firn in heavy isotopes.

In order to make a quantitative prediction about post-depositional changes in near-surface snow, the firn evolution model should be coupled with models for other physical processes. Modelling the temperature of the firn as a function of depth and

time of year, and better understanding of the time scale for transfer of water molecules from the solid to the vapor phase will both be important. By using our equations with a 2-D model which solves the coupled equations of energy conservation and water vapor movement (such as that of Albert and McGilvary, 1992 and Albert, 2002) we will be better able to predict the pattern of post-depositional isotopic change with depth in the snowpack.

This model can be used to interpret the measurements of Grootes and Steig (1992) mentioned above. Our model suggests that isotope profiles from low accumulation rate areas (such as the north side of Taylor Dome) will show isotopic enrichment relative to higher accumulation rate areas. Other investigators have shown similar results. Satake and Kawada (1997) used measurements of δD and δ^{18}O to estimate heavy isotopic enrichment as a result of depth hoar formation in East Queen Maud Land, Antarctica. They assumed that vapor from sublimating snow grains always forms at isotopic equilibrium with the snow grains. Assuming an initial isotopic composition of the snow, Satake and Kawada (1997) used a Rayleigh model to determine that as much as 35% of precipitation was sublimated prior to deep burial, leading to an isotopic enrichment of 6‰ for δ^{18}O and 50‰ for δD . The study site has a low accumulation rate, with snow remaining near-surface for as long as 40 years. Our more detailed model supports the findings of Satake and Kawada (1997), and further demonstrates the importance of understanding post-depositional changes in low accumulation rate areas.

2.7 Discussion

We have presented three options for explaining the residual trend in the Taylor Mouth stable isotope measurements (Fig. 2.4). Although deeper ice in the Taylor Mouth core originates at higher elevation and lower mean annual temperature, it is unlikely that the entire trend is due to a causal δ^{18}O - T_s relationship. The slope of the required

relation is too large, and down-slope storm paths from the south should not be expected to follow the standard relation (2.2), which was derived for orographic lifting. It is possible to explain the Taylor Mouth measurements if the precipitation at Taylor Mouth is a mix of orographic precipitation from storms travelling up Taylor Valley and surface snow blown from the polar plateau. Alternatively, post-depositional isotopic change can explain the residual trend in the Taylor Mouth isotope record.

Further measurements may make it possible to differentiate between mixing of precipitation from different sources, and post-depositional isotopic change. The effects of post-depositional isotopic change should increase with decreasing accumulation rate. Ice at the bottom of the Taylor Mouth core (100 m depth) originates on the surface in an area of relatively high accumulation rate (Fig. 2.6). Of all the ice in the core, snow deposited at this point along the Taylor Mouth flowline should be modified least by post-depositional change. Upstream of this point, accumulation rate decreases toward the nearby topographic saddle (Fig. 2.2). Snow deposited close to the saddle where accumulation rate is low may have experienced more post-depositional modification and therefore have a heavier isotopic signature, compared with snow deposited farther downstream, where the accumulation rate is higher. The dotted curve in Figure 2.6c shows the predicted variation in δ^{18}O along the flow line if the variations seen in the core are due entirely to post-depositional changes. Snowpit samples collected from below the ventilated zone along the length of flowline would then show heavy values near the saddle, lighter values in the higher accumulation rate area (Fig. 2.6), and heavy values close to the core site. This prediction could also be confirmed by samples from a longer core from the Taylor Mouth site.

Alternatively, if precipitation at Taylor Mouth is a mix of snow from different sources, we expect surface isotopic values to become progressively lighter upstream close to the saddle. Surface snow collected along the flowline would then progress from isotopically light snow near the saddle (reflecting a polar plateau source) to isotopically heavy snow (reflecting an up-valley component to precipitation at Taylor

Mouth), as shown by the dashed curve in Figure 2.6c. By collecting snow samples near the up-stream saddle, we could differentiate between this mixing model and post-depositional isotopic change. Isotopically heavy values would suggest that post-depositional processes are active, while isotopically light values would suggest that some redistribution of snow from the nearby plateau occurs.

A second way to discriminate between these two possibilities is to study deuterium excess. The deuterium excess (d) in precipitation is defined as (Dansgaard, 1964):

$$d = \delta\,\mathrm{D} - 8\,\delta^{18}\mathrm{O}\,. \tag{2.15}$$

Deuterium excess variations in polar snow can be used as a proxy for variations in evaporation temperature and relative humidity at the moisture source (Ciais and others, 1995).

If precipitation at Taylor Mouth is mixed, snow arriving from the polar plateau is likely to have a different moisture source than precipitation arriving up-valley. Consequently, Taylor Mouth precipitation might have two distinct deuterium excess components reflecting the two distinct moisture sources. If this is the case, the deuterium excess of surface snow along the flowline should vary from d values characteristic of surface snow on the polar plateau to d values consistent with precipitation arriving up Taylor Valley. Surface measurements of d could be used to determine if there are separate moisture sources for precipitation at Taylor Mouth.

Deuterium excess measurements may also enhance studies of post-depositional change. If spatial and temporal variations in δ^{18}O or δD of precipitation at a site are larger than the predicted post-depositional change of a few permil, the effects of post-depositional change may be indistinguishable from variations in initial stable isotope ratios through time. However, the natural variation in deuterium excess in precipitation is $\sim$ only 20% of the variation of either 8 δ^{18}O or δD (Vimeux and others, 2001). We can use our model of post-depositional isotopic change to predict changes in deuterium excess, in addition to δ^{18}O or δD individually. Using deuterium

excess may be a more robust way to predict the effects of post-depositional isotopic change. Our model predicts that d values may change by a few tenths of 1‰ per year; leading to a change of a few ‰ in d in areas with low accumulation rate.

2.8 Conclusions

Interpretation of the stable isotope record from the Taylor Mouth ice core is non-unique with the available data. However, we can comment on several possible complicating factors. The record is probably affected by precipitation arriving from multiple sources, including snow blown from Taylor Dome or from the plateau surface inland of Taylor Dome, snow precipitated from storms passing over the summit of Taylor Dome, and snowfall from storms coming upslope from Taylor Valley. Only the last of these might be expected to show a causal $\delta^{18}O$ - T_s relationship. The record may also be influenced by post-depositional modification of the stable isotopes by near-surface ventilation. We predict a post-depositional enrichment trend opposite to the trend in accumulation rate. Further measurements of stable isotope ratios at the surface along the flow line to the core site would help to differentiate between these possibilities. The large accumulation rate gradient across Taylor Dome makes it an attractive site for further study of post-depositional geochemical changes. Studies of spatial climate patterns using ice cores (e.g. ITASE) may help to address these issues by sampling over a large spatial distance, but in low accumulation rate areas, increased spatial sampling will be of value only if post-depositional processes are better understood.

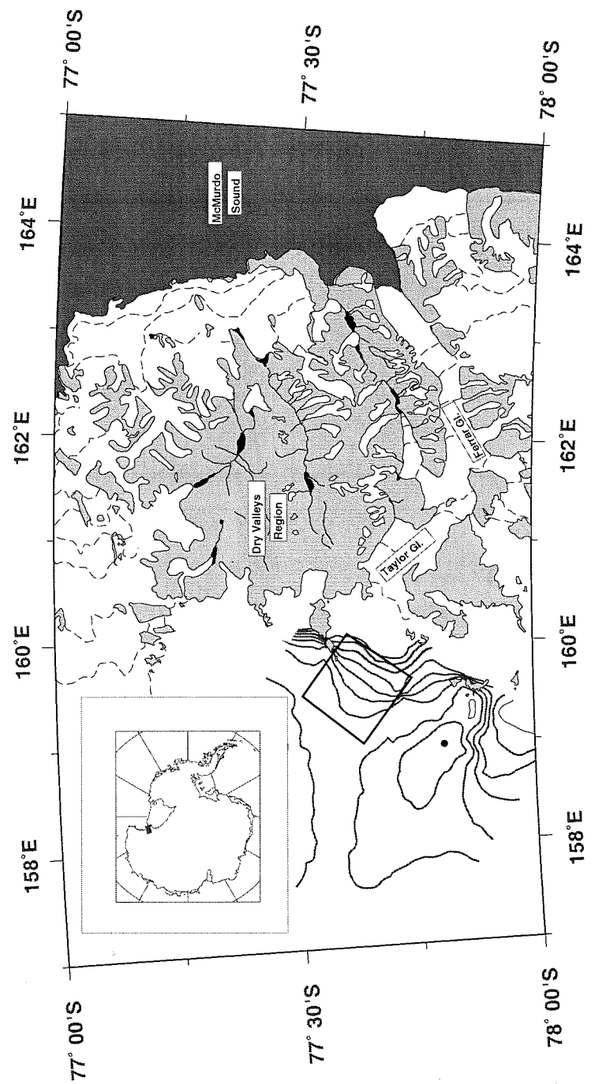


Figure 2.1: Location of Taylor Dome study area. Solid dot marks location of 554 m Taylor Dome ice core, at elevation 2425 m. Surface elevation contour interval is 50 m. Box denotes Taylor Mouth study site, shown in more detail in Figure 2.2

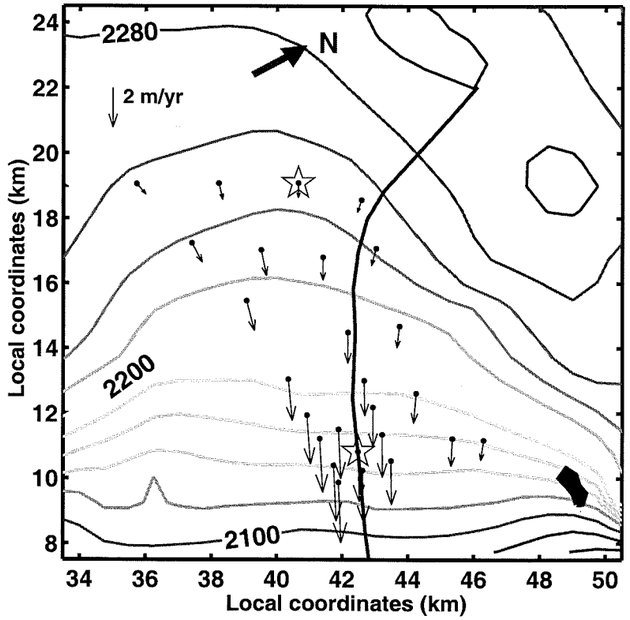


Figure 2.2: Surface elevation of Taylor Mouth area. Local coordinate system is described by Morse and others (in preparation). Poles in strain grid (dots) were surveyed in successive seasons to derive surface ice flow velocities. The flow line through the core site is inferred from these measurements. Stars mark locations of 10-meter firn temperature measurements. Core site is located at (42.5 km, 11 km). Shaded area in lower right is a nunatak.

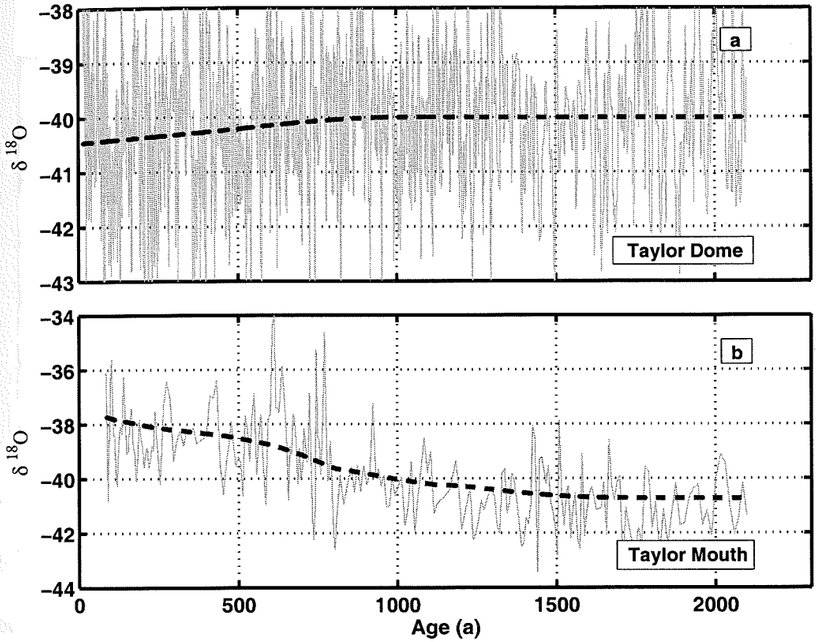


Figure 2.3: The Taylor Dome and Taylor Mouth δ^{18} O records. The Taylor Dome record (upper) is plotted on the "st9810" time scale Steig and others,1998. The Taylor Mouth record is plotted on the time scale of Neumann and others (in preparation). The dashed lines show the time series after low-pass filtering with a cut-off at 1500 years.

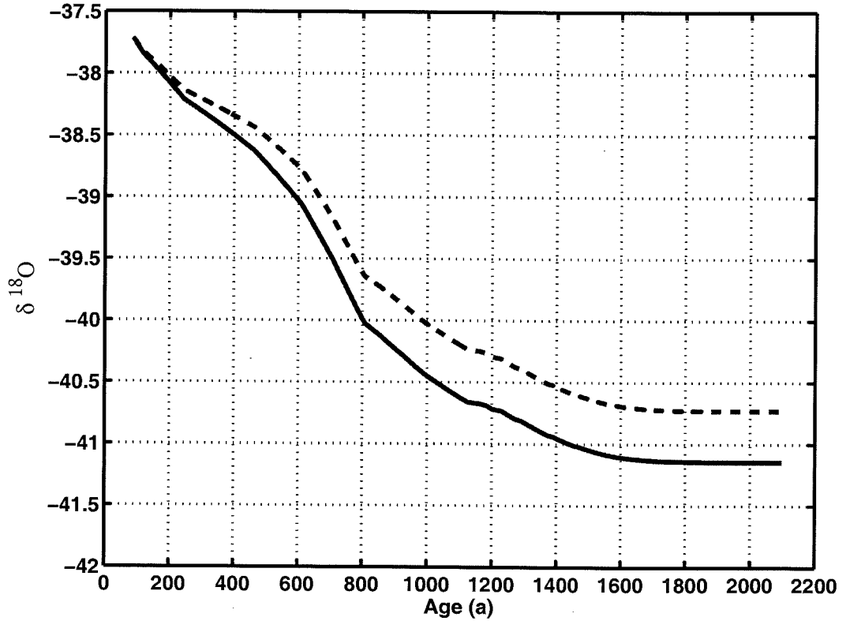


Figure 2.4: The dashed line is the low-pass filtered Taylor Mouth isotope record. The solid line shows the Taylor Mouth isotope record after removing the local climate trend, represented by the Taylor Dome record (Fig. 2.3).

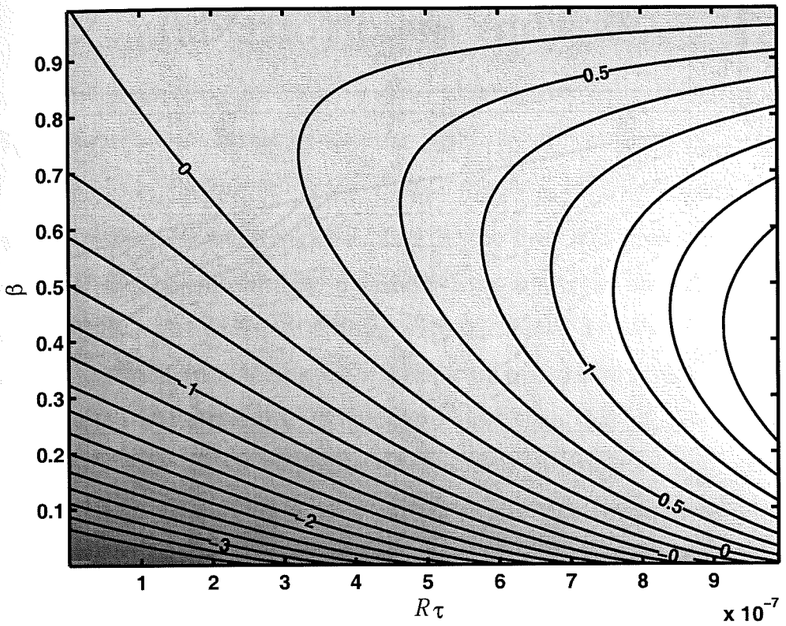


Figure 2.5: The change in the bulk isotopic content of an idealized mass of snow in units of permil after one year for a range of β (fraction of vapor leaving the firn) and $\mathcal{R}\tau$ (fraction of firn sublimated in time τ). Contour interval is 0.25 ‰ . Our models show that it is possible to either enrich or deplete heavy isotopes in the firn. Additional environmental information at a site, such as the temperature of the firn as a function of depth and time of year, make it possible to use this model to predict the pattern of post-depositional change.

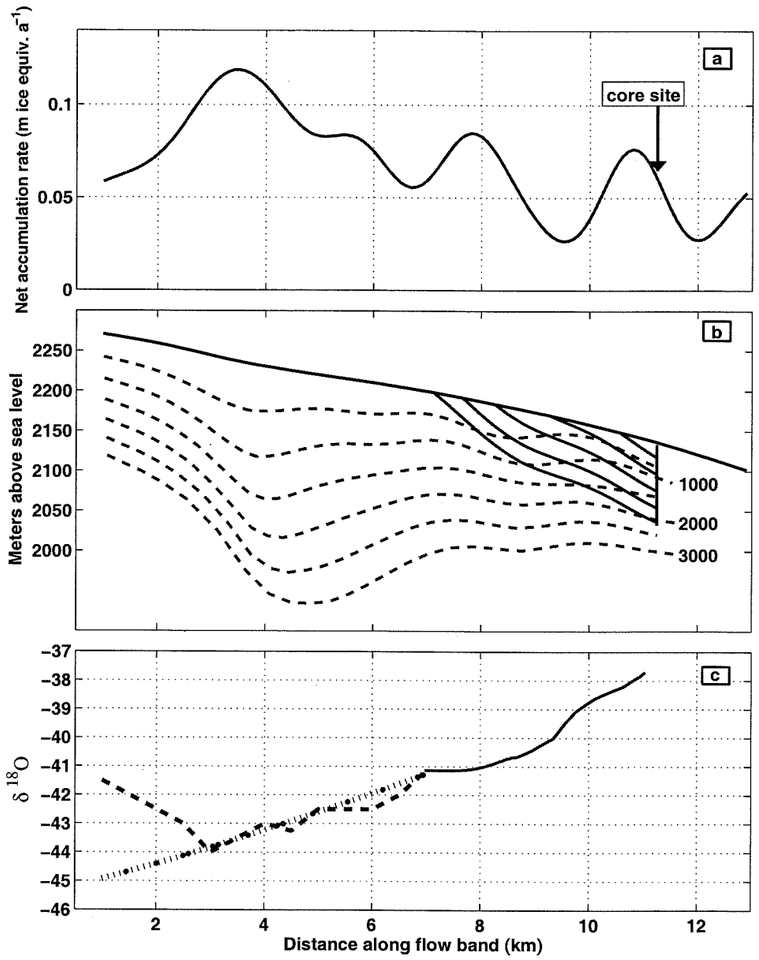


Figure 2.6: (a) Net accumulation rate as a function of distance along the Taylor Mouth flow line inferred using inversion procedure described in (Neumann and others, in preparation). (b) Isochrones and particle paths to the core site. (c) δ^{18}O below the ventilation zone along the flow line. Solid line shows values tracked from core site using ice flow model. Dotted curve shows best fit if variation is due entirely to mixing of plateau snow (with fixed δ^{18}O) and orographic precipitation from Taylor Valley (δ^{18}O linearly related to surface temperature). Dashed curve shows best fit if variation is due to post-depositional change that scales with accumulation rate. As accumulation rate decreases upstream of $x = 3.5$km, post-depositional processes lead to enrichment.

Chapter 3

VAPOR MOTION IN THE FIRN

3.1 Summary

I describe my model for water-vapor motion in the firn, and present the relevant equations and boundary conditions. I present both analytical and numerical tests and compare this model with results from a similar model by Albert (2002), which has been applied at a specific site with specific environmental conditions. In this chapter, I develop a computationally simpler model than that of Albert (2002) in order to examine water-vapor motion in the firn for a variety of environmental conditions, rather than specific values at a particular site. This new model is used to verify prior results and highlight possible problems with earlier work. I use my model to estimate subsurface mass-exchange (sublimation and condensation) rates on the Antarctic Plateau. I explore the effect of (a) changes in environmental conditions (wind speed and grain size) and (b) the numerical procedure (particularly choices of grid size and time step) on modeled mass-exchange rates in the firn. I use the model to estimate surface sublimation rates and compare these with published measurements and other models, and show that my results compare favorably. In order to make predictions about a specific site, observations such as measurements of ice grain size, surface topography, and variations of surface temperature, wind speed and atmospheric relative humidity through time are necessary. In conclusion, I describe future modifications that may generate improved surface mass exchange estimates, and I highlight some of the general results of this model.

3.2 Introduction

It has long been recognized that redistribution of water vapor below the snow surface occurs in polar environments (e.g. Gow, 1965) and this process is important in many different contexts. The effects of water-vapor motion are most readily observed in snow pits: low-density depth hoar layers are found below the surface, while at the surface, higher-density wind-packed slabs are often found, especially in low accumulation rate environments. Water-vapor motion is an important aspect of grain growth in firn and snow metamorphism in general (de Quervain, 1973; Colbeck, 1983a). It is also an important component of snow geochemistry. Sublimation at depth in the firn releases volatile species (McConnell and others, 1998; Wagnon and others, 1999), promoting equilibration with atmospheric concentration. Most models of isotopic diffusion in the firn (Cuffey and Steig, 1998; Johnsen and others, 2000) assume that isotopic ratios are modified through diffusion of water vapor along temperature gradients in the firn. Other models of isotopic change require knowledge of mass exchange rate explicitly (Neumann, 2001). Sublimation at the snow surface can also be an important component of both the mass balance and the surface energy balance (Bintanja, 2001). An improved understanding of the mechanisms and magnitudes of water-vapor motion in the firn would be useful in all of these considerations.

Past work on water-vapor motion in firn has focused on the impact of firn microstructure and the layered nature of snow on vapor transport properties (Albert and others, 1996; Davis and others, 1996) and air flow through firn (ventilation) (Colbeck, 1989; Waddington and others, 1996; Colbeck, 1997). For example, the presence of a low-permeability surface windpack can reduce overall ventilation rates in the subsurface, yet the presence of high-permeability buried layers can cause flow channeling, or increased flow in buried hoar layers (Albert, 1996). Prior models of water-vapor motion in firn (Albert, 1996; Albert and McGilvary, 1992; Albert, 2002) demonstrate the relevant equations, parameters, and conditions where we expect significant water-vapor motion in the firn.

This chapter describes my model for tracking vapor motion through firn in two dimensions. Air flow over a specified snow surface topography generates pressure fluctuations along the snow surface. For specified values of firn permeability and porosity, the two-dimensional air flow through the firn is calculated using Darcy's Law (Equation (3.5)). This air flow field is required to satisfy the continuity equation (Equation (3.6)) and is used as input to numerical models for heat flow and water vapor flow in the firn. The heat and vapor flow models (Equations (3.7) and (3.8)) are coupled through phase changes of water between the solid and vapor phases (sublimation and condensation). The mass exchange (Equation (3.9)) impacts the energy balance in the firn through latent heat effects, and it also changes the local vapor density. The primary model outputs are the time-dependent temperature distribution and the vapor flow divergence, which shows locations of sublimation and condensation.

The model physics is similar to that in other vapor-motion models (e.g. Albert, 1996; Albert, 2002). This model is different in that I use the control-volume technique (Patankar, 1982), whereas Albert (2002) uses the finite-element method; I use a different method of calculating air-flow velocities (Section 3.3); I use a different method of calculating saturation vapor density in the firn (Appendix E) and I make several different simplifying assumptions.

The ratio τ_d / τ_r is a Damkohler number $\mathcal{D}$ (e.g. Conklin and others, 1993) that estimates the extent to which the pore spaces in the firn are expected to reach saturation vapor density, where τ_r is the residence time for air in the pore space and τ_d is the characteristic time for vapor diffusion in a typical pore. If $\tau_d > \tau_r$, pore spaces in the firn will always be saturated; if $\tau_d < \tau_r$, air will be advected through the pore spaces before reaching saturation. Using typical values of the vapor diffusivity in air and pore size, I estimate τ_d as 0.1 s; typical values of the sub-surface air flow through the firn suggest that τ_r as 0.1 s. The ratio τ_d / $\tau_r = \mathcal{D}$ is ~ 1 and suggests that pore space air will be near saturation, but may be slightly above or below. Model results

presented below confirm this and suggest that the relative humidity in the firn differs from 1 by less that 0.1 %. This analysis also suggest that firn could change from a regime dominate by $\mathcal{D} \leq 1$ to a regime dominated by $\mathcal{D} \geq 1$ throughout the year as wind speed and temperature change.

This model is the foundation for the following chapters where I examine the impact of subsurface vapor motion on snow geochemistry. The three main components of the model (air flow, heat flow and vapor flow) plus the appropriate boundary conditions are described in the following sections. I then test the model against several analytical and numerical results. I use the model to estimate the pattern and magnitude of subsurface water-vapor motion on the Antarctic Plateau during the winter and summer with both strong wind (10 m s^{-1}) and moderate wind (5 m s^{-1}). I also investigate the importance of grain size in the model, and compare model results with published estimates of subsurface mass exchange and measurements of surface sublimation rate.

3.3 Air Flow Field

In both the heat-flow model and the vapor-flow model, I calculate the two-dimensional air-flow velocity field $\vec{\mathbf{u}}$ in a vertical slice of firn, following the method of Colbeck (1989) and Waddington and others (1996). I used a coordinate system where x is positive to the right, y is positive down, u is the air-flow velocity in the positive x direction, and v is air-flow velocity in the positive y direction (Fig. B.1). I assume that the snow surface topography is sinusoidal, with specified amplitude h and wavelength λ. Since firn is a porous and permeable medium, steady air flow over the sinusoidal topography can induce significant air flow through firn, as noted by Gjessing (1977). For steady air flow, and for uniform porosity ϕ and permeability K, the two-dimensional subsurface pressure field can be calculated using the Laplace equation:

$$\nabla^2 p(x,y) = 0\,, \tag{3.1}$$

where $p(x,y)$ is the pressure field. Assuming sinusoidal surface topography on the snow, variation of pressure along the surface is (Colbeck, 1989):

$$p(x,0) = p_0 \cos\left(\frac{2\pi x}{\lambda}\right)\,, \tag{3.2}$$

where λ is the bump wavelength and p_0 is the magnitude of the pressure variation along the snow surface and is given by (Colbeck, 1989; Waddington and others, 1996):

$$p_0 = C\rho_{\text{air}} U_{10}^2 \frac{h}{\lambda}\,, \tag{3.3}$$

where ρ_{air} is the density of air, U_{10} is the wind speed at 10 meters above the snow surface and h is the bump height. C is a proportionality constant between the pressure drop across a dune on the surface and the aspect ratio of the dunes and is $\simeq 3$. The two-dimensional subsurface air-pressure field is (Colbeck, 1989):

$$p(x,y) = p_0\, \mathrm{e}^{-2\pi y/\lambda} \cos\left(\frac{2\pi x}{\lambda}\right). \tag{3.4}$$

The volumetric air flux density $(\mathcal{Q}_x, \mathcal{Q}_y)$ is calculated from the pressure field and Darcy's Law, and is given by (Waddington and others, 1996):

$$(\mathcal{Q}_x, \mathcal{Q}_y) = \frac{2\pi K p_0}{\lambda\, \mu\, \phi}\, \mathrm{e}^{-2\pi y/\lambda} \left(\sin\left(\frac{2\pi x}{\lambda}\right), \cos\left(\frac{2\pi x}{\lambda}\right)\right)\,, \tag{3.5}$$

where μ is the viscosity of air. The subsurface air flux density decreases exponentially with depth with e-folding depth $\lambda/2\pi$. The surface topography in the polar regions exhibits roughness at a variety of length scales (Gow, 1965). Waddington and others (1996) demonstrated that microtopography (h between 1 and 10 cm, λ between 50 cm and 3 m) is the most effective way to induce large air flux through snow. Microtopography will typically lead to subsurface air-flow velocities with e-folding scales ≤ 50 cm. Because of these findings, it is reasonable to expect that advection will be important only in the upper 2 meters of the firn, below which air-flow velocities are negligibly small for most surface topographies. I use the Darcy velocities $(\mathcal{Q}_x, \mathcal{Q}_y)$ as the sub-surface air-flow velocities $\vec{\mathbf{u}} = (u, v)$ in my model.

Other models of vapor motion in the firn (e.g. Albert, 2002) numerically calculate the air-flow field using Darcy's Law. Albert and others (2000) measured the

two-dimensional permeability tensor K_{ij} at Siple Dome, Antarctica. Using these permeability measurements and measurements of the pressure drop due to air flow over surface topography, Albert (2002) numerically calculated the subsurface air-flow field $\vec{\mathbf{u}}$ in the snow. I found that the air-flow velocities calculated using the method of Colbeck (1989) and Waddington and others (1996), which uses a constant permeability and calculated pressure variation along the snow surface, are within the uncertainty of the more elaborate calculation of Albert (2002). As a result, I have used the method of Colbeck (1989) and Waddington and others (1996) in my model of vapor motion in firn.

The subsurface air-flow field $\vec{\mathbf{u}}$ calculated following the methods of Colbeck (1989) and Waddington and others (1996) satisfies the continuity equation:

$$\frac{\partial}{\partial t}\left(\phi\rho_{\mathrm{a}}\right) + \nabla\cdot\left(\phi\rho_{\mathrm{a}}\vec{\mathbf{u}}\right) = 0\,, \tag{3.6}$$

where the air density rho_{a} is held constant. The extent to which my discrtization of $\vec{\mathbf{u}}$ satisfies Equation (3.6) under a variety of grid sizes and time steps used in my model is described in Section 3.7.1.

McConnell and others (1998) calculated subsurface air-flow velocities using the method of Albert (1996) for several different permeability distributions at South Pole. Their calculations demonstrated that the subsurface air-flow velocity can vary by up to 2 orders of magnitude depending on the microstructure (permeability and porosity) of the firn. In particular, the low permeability wind-packed surface layer, which typically form in winter and spring, substantially reduce subsurface air-flow velocities. As stated above, my model uses uniform firn microstructure for all times of the year. Consequently, the subsurface air-flow velocities presented here may be too large for some sites. If this model is to be applied at a particular site, the firn microstructure should be measured and the method of Albert (1996) should be used to estimate the subsurface air flow velocity.

3.4 Heat Flow

My model for conservation of energy in the firn tracks energy flow as a result of heat conduction, the advection of sensible heat due to air flow through the firn (ventilation) and latent heat release or uptake due to the condensation of water vapor or sublimation of snow grains in the firn.

There are additional energy terms that one may include in this type of model. The additional kinetic energy introduced by air moving through the firn is several orders of magnitude smaller than the other terms, and is not considered in this analysis. I assume that the accumulation of snow transports a negligible amount of heat. Benfield (1951) studied the advection of heat by accumulating snow and found that this is a first order effect for large accumulation rates ($\sim$ 8 m yr^{-1}). However, when accumulation rate is less than 1 m yr^{-1}, snow accumulation has a negligible impact on the energy balance of the firn. In this dissertation, I apply this model to conditions typical of the Antarctic Plateau, which has accumulation rates $\ll$ 1 m yr^{-1}, and so I assume that sensible heat is carried by the moving air only.

In Appendix B, I derive the following expression for the two-dimensional time-dependent temperature T of the firn from a statement of energy conservation in the firn:

$$\frac{\partial}{\partial t}\left[T\left(\phi\left(\rho c_{\mathrm{p}}\right)_{\mathrm{a}} + \left(1-\phi\right)\left(\rho c_{\mathrm{p}}\right)_{\mathrm{i}}\right)\right] + \nabla\cdot\left(\phi\left(T\rho c_{\mathrm{p}}\right)_{\mathrm{a}}\vec{\mathbf{u}}\right) - \nabla\cdot\left(K\nabla T\right) - Q = 0\,, \tag{3.7}$$

where ρ is the density, c_{p} is the specific heat capacity, ϕ is the porosity of the firn, $\vec{\mathbf{u}}$ is the air flow velocity (u, v) and K is a bulk effective thermal conductivity of the firn and accounts for heat conduction through the ice-air-water vapor mixture. The subscripts a and i refer to *air* and *ice*, respectively. Q represents the energy contribution per unit volume due to phase changes of water between ice and vapor. Q is calculated as $Q = LS$, where L is the latent heat release per mass for the phase change, and S is the mass of water changing phase per unit time per unit volume

(mass-exchange rate). S is calculated in the vapor-transport model described below (Section 3.5). Consequently, the energy-conservation model and the vapor-transport model are linked through the source term S.

Equation (3.7) and (3.6) are solved simultaneously for the time-dependent firn temperature $T(x, y, t)$ using the control-volume technique of Patankar (1982) using software I have written to use with the MATLAB[1] package. The discretization and solution technique used are presented in Appendix B.

3.5 Vapor Flow

My model for vapor transport in the firn closely follows other published models (Albert and McGilvary, 1992; Albert, 2002). Water vapor diffuses through the pore spaces in the firn as a result of temperature gradients, which cause vapor pressure gradients in the firn. Water vapor can also be advected by air flow through firn as a result of surface-pressure variations (e.g. Colbeck, 1989).

Water vapor can be added to the pore space through the sublimation of surrounding ice grains, or removed through condensation onto neighboring ice grains. Throughout this work, sublimation refers only to the transfer of water from the solid to the vapor phase; condensation refers to the transfer of water from the vapor to the solid phase; and mass exchange refers to both the sublimation and condensation rates. Mass exchange is driven by a mismatch between local vapor density ρ_v and local saturation vapor density ρ_{sat}. For example, if $\rho_v < \rho_{\text{sat}}$, some of the surrounding ice grains will sublimate to increase ρ_v toward the equilibrium value ρ_{sat}.

I assume that ρ_{sat} is determined only by temperature. In reality, one may also consider the radius of curvature of the ice grains, but for radii larger than about 1 μm, the temperature effect dominates (Colbeck, 1983a). I present my model for calculating ρ_{sat} in Appendix E. In Appendix D, I express the changes in vapor density

[1]MATLAB$^{\text{TM}}$ is a registered trademark of The Math Works, Inc. 3 Apple Hill Drive, Natick, MA 01760-2098, 508-647-7000

ρ_v based on water mass conservation in the pore space, as in Albert and McGilvary (1992):

$$\frac{\partial}{\partial t}\rho_v + \nabla \cdot (\rho_v \vec{\mathbf{u}}) - \nabla \cdot (\kappa \nabla \rho_v) - S = 0 \,, \tag{3.8}$$

where $\vec{\mathbf{u}}$ describes the air-flow field (u, v) and κ is the diffusivity of water vapor in the firn. The source term S accounts for the mass of water changing phase per unit time per unit volume (mass exchange), and couples the vapor-transport model to the energy-conservation model, as described above. The mass exchange rate S is driven by the difference between local vapor density, and local saturation vapor density and is calculated as (Appendix E):

$$S = h_{\text{m}} a_{\text{s}} \left(\rho_v^{\text{sat}} - \rho_v \right) \tag{3.9}$$

where h_{m} is the mass exchange coefficient, and a_{s} is the surface area to volume ratio for snow of a given density. For a given volume of snow, a larger a_{s} will produce a larger mass exchange rate. a_{s} is determined by the snow grain radius. This model assumes a uniform grain size and parameterizes a_{s} by using an effective diameter for grains. The mass-exchange rate S is sensitive to choice of effective grain size, as discussed in Section 3.8.5 below. The model presented here uses a single value for the mass exchange coefficient h_{m}. In fact, this coefficient is likely also a function of the pore size as well as a kinematic term defining the rate at which water molecules can change phase. The average pore size will also influence the subsurface air flux. In this model, average pore size has been parameterized through the bulk porosity of the firn, and the single value used for h_{m} implicitly assumes a single value for the mean pore size.

The air-flow field (u, v) is required to satisfy the continuity equation (Equation (3.6)). Equations (3.8), (3.9) and (3.6) are solved simultaneously for the time-dependent vapor density in the firn pore space $\rho_v(x, y, t)$ using the control-volume technique of Patankar (1982). The discretization and solution techniques are presented in Appendix D.

3.6 Boundary Conditions

I solved for the time-dependent vapor density and temperature on a rectangular two-dimensional grid. The principle boundary conditions are:

- **Left and right** In the energy-conservation model (Equation (3.7)), I insulate the right and left boundaries, such that there is no heat flux into or out of the solution space. This is equivalent to a Neumann boundary condition (Trim, 1990), where $\nabla T = 0$. I also use Neumann no-flux boundary conditions for the left and right boundaries in the vapor-transport model (Equation (3.8)). The locations of the left and right boundaries coincide with locations where the horizontal air flow velocity is zero. At these locations, there is no heat or vapor flow due to model symmetry as a result of the periodic surface topography.

- **Basal** Along the basal edge in the energy-conservation model, I assume a constant geothermal heat flux q_{geo}. This is another form of a Neumann boundary condition. In the vapor-transport model, I assume that there is no vapor flux across the basal boundary.

- **Upper** The upper boundary condition for air flow (Equation (3.2)) is applied along a flat surface at y =0 as in Colbeck (1989), rather than along the actual wavy surface topography. Cunningham and Waddington (1993) studied this approximation and found that the method used by Colbeck (1989) to determine volumetric air flux retains the essential physics of the problem as long as the aspect ratio h/λ of the surface topography is much less than 1. All surface topographies used in this dissertation have aspect ratios much less than 1.

  Along the upper edge of the solution space, there are regions of both air inflow and air outflow, corresponding to the air-pressure variations across the snow surface (Equation (3.2)). Over the regions of air inflow, I use a Dirichlet (Trim,

1990) boundary condition and prescribe the temperature T_{in} and vapor density ρ_{vin} along the upper row of grid cells based on the temperature and vapor density of the atmosphere. The upper boundary condition can be changed through time, as the atmospheric surface temperature and vapor density change. This upper boundary condition assumes that the atmosphere acts as an infinite reservoir of heat and water vapor.

Over the regions of air outflow, I specify the temperature gradient and vapor density gradient at the snow surface (a Neumann boundary condition). This gradient is defined by the corresponding gradient in the grid cells just below the snow surface. This procedure extrapolates the temperature and vapor density

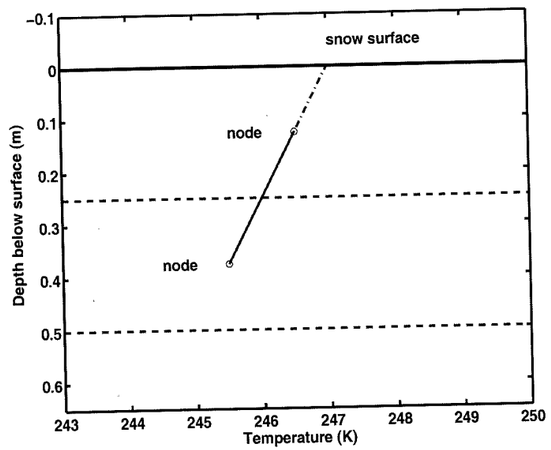


Figure 3.1: Schematic of boundary condition used in regions of air outflow. Solid horizontal line indicates snow surface, dashed lines indicate grid cell interfaces and open circles are grid centers where temperature and vapor density are calculated. Temperature gradient between two nodes nearest the surface (solid line) is extrapolated to determine temperature gradient at the snow surface (dash-dot line). A similar extrapolation is used to determine the vapor density gradient at the snow surface.

gradients from the uppermost two nodes to the last half grid cells bordering the surface (Fig. 3.1). This boundary condition changes with time, as the temperature and vapor density gradient near the upper surface change. Consequently, the temperature and vapor density fields at the snow surface are not calculated independently, but are extrapolated based on the gradient of temperature and vapor density between the upper two rows of grid cells.

To close the set of equations, the model also requires an initial condition for both the temperature and vapor density pattern in the firn. The initial conditions depend upon the context in which the model is to be used. Several scenarios are described below.

3.7 Model Verification

I used a number of tests (both analytical and numerical) in order to verify that my model for vapor transport in the firn works as expected. Since it is not possible to test all components of the model simultaneously against an analytical solution, I tested each component individually. I then compared the output of the entire model with other published results from similar models (e.g. Albert and McGilvary, 1992; Albert, 2002). My model compares favorably with other models, and highlights some possible problems with earlier work.

3.7.1 Flow-Field Continuity

In order to test whether my specified air-flow field (u, v) satisfied the continuity equation, I calculated the total air flux across each boundary. Adding the fluxes into and out of each control volume allowed me to calculate to what degree the flow field satisfied the continuity equation. I used a surface topography of $h = 10$ cm, $\lambda = 3$ m and $U_{10} = 10$ m s^{-1}, which generated a maximum surface air velocity of 0.11 m s^{-1}. For equidimensional control volumes of 1 cm on a side, a maximum error of 1.4×10^{-4} m^2 s^{-1} occurred near the surface, where flow velocities were greatest. Decreasing the control volume size to 1 mm on a side decreased the maximum error to 1.4×10^{-6} m^2 s^{-1}. I was able to continue to decrease the maximum error by decreasing the dimensions of the control volumes.

During the model applications described in Section 3.8, I have generally used a grid spacing of 10 cm horizontally and 1 cm vertically. With this grid size (and bump height $h = 10$ cm and wavelength $\lambda = 3$ m) I calculated a maximum error of 4×10^{-5} m^2 s^{-1}. This grid size was an acceptable compromise between computational efficiency and solution accuracy. The maximum near-surface air-flow velocity in the following applications is 1×10^{-2} m s^{-1}, which represents a maximum flux of 1×10^{-3} m^2 s^{-1}. Using this grid size and surface topography, the maximum error in air flux is ~ 4 %, which is acceptably small.

3.7.2 Energy Conservation

I tested the energy-conservation model stability and the stability of my parameterization of the boundary conditions with a steady-state test. By running the energy-conservation model with surface topography as described above and a uniform initial temperature field, I determined to what extent the model conserves energy. The temperature of the inflowing air was equal to the initial firn temperature. Under a variety of time steps and grid spacing, the temperature range in the 2-D model ($T_{\max} - T_{\min}$) increased over the first ~ 1000 iterations to a steady value of at most 1×10^{-10} K, an acceptably small temperature deviation. Based on this result, I assumed that energy was neither created nor destroyed as a result of my parameterization of the boundary conditions.

I tested the heat conduction aspect of the energy-conservation model by setting the air-flow velocity to zero, eliminating latent heat release from phase changes and imposing a temperature variation at the firn surface which was sinusoidal in time. This allowed me to compare the energy-conservation model with the well-known analytical

solution to propagation of seasonal temperature changes in firn, given by Paterson (1994, p.206):

$$T(y,t) = T_S \, e^{\left(-y\sqrt{\omega/2k}\right)} \sin\left(\omega t - y\sqrt{\omega/2k}\right) , \tag{3.10}$$

where t is time, y is the vertical coordinate, k is the thermal diffusivity in firn, T_S is the amplitude of the seasonal cycle and $\omega/2\pi$ is the frequency. Using a time step of 1 day, a forcing period ω of one year, and a 10 cm grid spacing down to 75 m, the maximum error in my model was 0.022 K. I can reduce this error by either decreasing the time step, or the size of the control volumes. This result demonstrated that the heat conduction aspect of my energy-conservation model was working properly.

By making a few modifications to the model set-up, I tested the energy-conservation model with advection and diffusion against the analytical solution for steady, one-dimensional heat conduction with vertical advection, given by Paterson (1994, p. 218):

$$T(y) = \bar{T}_S + \frac{\sqrt{\pi}}{2} \, l \left(\frac{dT}{dy}\right)_B \left(\mathrm{erf}\left(\frac{y}{l}\right) - \mathrm{erf}\left(\frac{h}{l}\right)\right) , \tag{3.11}$$

where $\bar{T}_S$ is the surface temperature (constant in time), the geothermal heat flux is $\left(\frac{dT}{dy}\right)_B$, h is the ice thickness, k is the thermal diffusivity, c is the vertical advection velocity (accumulation rate), erf is the error function and l is given by $l^2 = \sqrt{2kh/c}$. In order to compare my model to this analytical solution, I eliminated the latent heat effects from phase changes, assumed that the air-flow velocity was zero, set the porosity of the firn to 0 (i.e. solid ice) and assumed that the vertical velocity is given by $-by/h$. I also assumed that sensible heat is carried by the *ice*, rather than the air. These changes were made in defining the values of constants in the model, and no substantial changes were made to the energy conservation algorithm.

Using a time step of 10 years, and a vertical grid spacing of 10 cm, I started the model with a uniform temperature distribution and a geothermal heat flux of 75 mW/m^2. Through time, my modeled temperature profile approached the analytical solution. After 10,000 model years, the error was 0.1 K; after 60,000 years, the

error had dropped to 0.008 K. After 100,000 years, the error between the analytical and modeled temperature profile was 0.001 K. From this test, I concluded that the advective and diffusive parts of the energy-conservation model were behaving as expected.

From the three tests described above, I concluded that the energy-conservation model was working as expected. The desired level of accuracy in the model can be achieved by refining the time step, the grid size or by running the model for a long period of time. All of these are familiar trade-offs in numerical modeling. The algorithm for the vapor-transport model described above is nearly identical to the algorithm for the energy-conservation model. Since there are no analytical tests possible for vapor transport through a porous media (such as firn), I relied on the above tests of the energy conservation algorithm to demonstrate the stability and reliability of the vapor-transport algorithm.

3.7.3 Numerical Tests

Albert and McGilvary (1992) I tested my model for vapor transport in the firn against published results from a similar numerical model (Albert and McGilvary, 1992; henceforth A&M). A&M uses the finite-element method to solve many of the same equations outlined above. The main differences between my model and the model of A&M are in the solution technique, the method of calculating air-flow velocities (Section 3.3) in the firn and the method of calculating saturation vapor density (Appendix E).

A&M use their model to calculate the thermal effects of forced air flow and vapor transport through a cylinder of snow. They compare the model results with laboratory measurements of temperature in a snow sample and relative humidity at the outflow end of the snow sample.

Before attempting to fully model forced air flow through a snow cylinder, they present several simplified calculations designed to test different aspects of the model:

heat conduction only, heat conduction with advection, heat conduction with advection and phase changes. I was able to match the model results of A&M in all cases to within 0.1 K, which is the resolution of the published figures. I inferred slight differences in the values of several constants between my model and that of A&M. For example, with small reasonable adjustments to values for the heat capacity of moist air and the vapor pressure at the triple point of water, I was able to match all of the results presented in A&M.

Figure 6 of A&M show calculated vapor density and relative humidity along the length of the snow sample. This calculation uses a specified temperature at both ends of the snow sample, and a specified relative humidity at the upstream end. Their model shows a marked decrease in relative humidity at the outlet end of the snow sample, suggesting that local saturation vapor density was not reached before the air exited the snow sample. By increasing the effective particle diameter by an order of magnitude (to 3 mm), I matched the value of their relative humidity at the outlet, but not the slope of the relative humidity curve near the outlet. The particle diameter affects the surface area to volume ratio, which is an important component of the algorithm to calculate the mass of water changing phase per unit time in the model (Appendix E). There are several other possible explanations for the mismatch between my model calculations and those presented in Figure 6 of A&M, such as differences in the grid size, the time step, differences in other model parameters or interpolation scheme. Among these possible explanations, differences in other model parameters is the most likely cause; although A&M defined many of the constants used in the model, others were not defined.

Albert 2002 I was able to do a more comprehensive test by comparing my full model estimates of mass exchange rate and pattern in the firn (including advection, diffusion and phase changes) against those of Albert (2002). Albert (2002) used the same numerical scheme as A&M to calculate temperature and vapor density changes (finite-element method). The study also used the measured firn permeability tensor

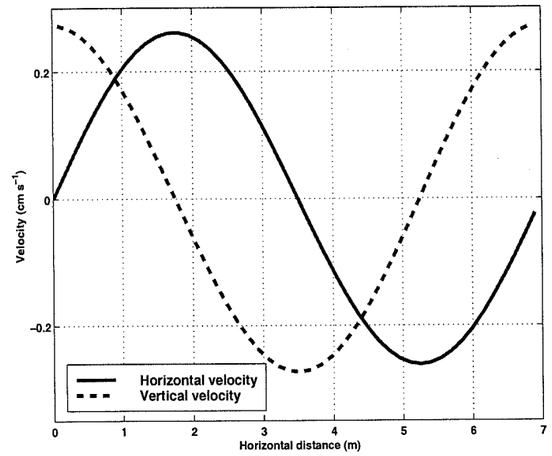


Figure 3.2: Near-surface air-flow velocities for $\lambda = 7$ m, $h = 17$ cm, and 10-meter wind speed = 8.25 m s^{-1}. Horizontal and vertical velocities were calculated following the method of Colbeck (1989) and Waddington and others (1996), as described in Section 3.3. Horizontal velocities are positive to the right; vertical velocities are positive down. The surface topography parameters (λ and h) were tuned to produce the same pressure drop (5 Pa) over surface bumps used by Albert (2002). Air flows into the firn (vertical velocity is positive) on the intervals $x = 0$:1.75 m and 5.25:7 m. Air flows out of the firn (vertical velocity is negative) between $x = 1.75$ and 5.25 m. Since I use a constant permeability, the magnitude of the velocities decrease exponentially with depth with an e-folding scale of $\lambda/2\pi$ (Equation (3.5)).

from Siple Dome of Albert and others (2000) when calculating the subsurface air-flow velocities (Section 3.3).

My model uses a simpler solution technique than the model of Albert (2002), a simplified approach to calculating sub-surface air flow rates, and a different method for calculating saturation vapor density in the firn. I expected that my mass exchange rate and pattern would be somewhat different, since I used an isotropic permeability, rather than an anistropic permeability. This difference in permeability will primarily affect the subsurface air-flow velocity. By tuning the height and 10-meter wind speed

in my model (bump height = 17 cm, bump wavelength = 7 m, 10-meter wind speed = 8.25 m s^{-1}), I was able to generate a pressure variation of 5 Pa across the upper surface, which is the value measured by Albert (2002) at Siple Dome, Antarctica. I used the methods described above in Section 3.3 to determine the subsurface air-flow velocity, and found that my laterally-averaged air-flow velocities are within the error bars of the air flow calculations presented in Albert (2002). There could be potentially large differences between my air-flow velocities and those of Albert (2002), since areas of high or low permeability will create areas of larger or smaller velocities at depth. The near-surface air-flow velocities that I calculated are shown in Figure (3.2). These surface velocities are the same as those used by Albert (2002).

In the following comparisons with Albert (2002), I used a horizontal and vertical grid spacing of 10 cm, a time step of 15 seconds and the boundary conditions described in Section 3.6. Air flowing into the firn had a prescribed temperature T = -5^{-5} C, and relative humidity = 1.

My calculated temperature field (Fig. 3.3) is similar to the temperature field shown in Figure 3 of Albert (2002). In regions of air inflow (Fig. 3.2; x = 0:1.75 m and 5.3 m to 7 m), the temperature field was dominated by the downward advection of relatively warm air. This advection resulted in a nearly isothermal region in the upper 50 cm of the firn. In regions of air outflow (Fig. 3.2; x = 1.75:5.3 m), the near-surface temperature was dominated by the upward advection of relatively cold air from below, and the diffusion of heat from the adjacent warm regions. Below about 5 m depth, advection was no longer important, the temperature field was dominated by conduction, and the isotherms were parallel. My calculated near-surface horizontal gradients in temperature were somewhat larger than those presented in Albert (2002). This could be a manifestation of differences in the thermal constants used in the two models (not all of which were defined in Albert (2002)), more vigorous air-flow velocities in my model, or differences in calculating the latent heat effects (see Appendix E). Qualitatively, the models predicted similar temperature fields; quantitatively, there

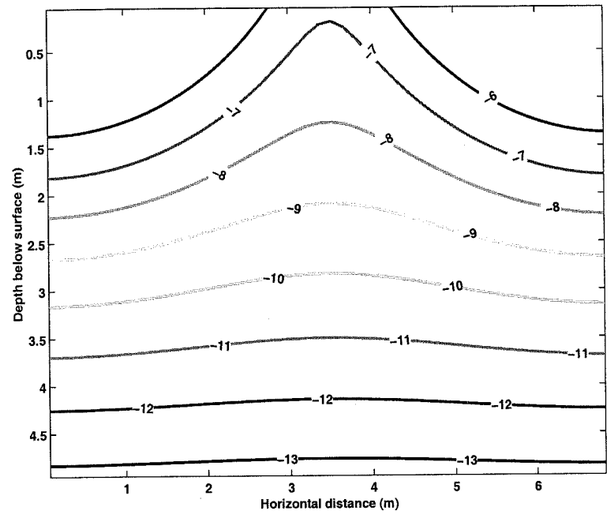


Figure 3.3: Contours of temperature field $T(x, y)$, given in °C, calculated using parameters of Albert (2002). I solved for $T(x, y)$ on a grid of x = 0:0.1:7 m and y = 0:0.1:10 m, although only the upper 5 m are shown here. Below 5 m, advection was no longer important and $T(x, y)$ is dominated by conduction, which resulted in parallel isotherms. Air flowing into the firn (Fig. 3.2) had constant temperature $T(x, 0)$ = -5 C. The left and right margins were insulated, and a constant heat flux was imposed along the base in order to match the temperature gradient presented in Albert (2002).

were significant differences. High resolution temperature measurements of the firn in the vicinity of surface topography, although difficult, would help further refine these temperature models.

I also compared my calculated subsurface sublimation rates (Fig. 3.4) with the subsurface sublimation rates plotted in Figure 4 of Albert (2002). These two figures are qualitatively similar. In regions of air inflow (Fig. 3.2; air enters the firn between x = 0:1.75 m and 5.3 m to 6.8 m along the snow surface, where x is the lateral spatial coordinate. This notation is used through this work to denote regions where air enters the firn and leaves the firn.), there was little sublimation or condensation in the upper

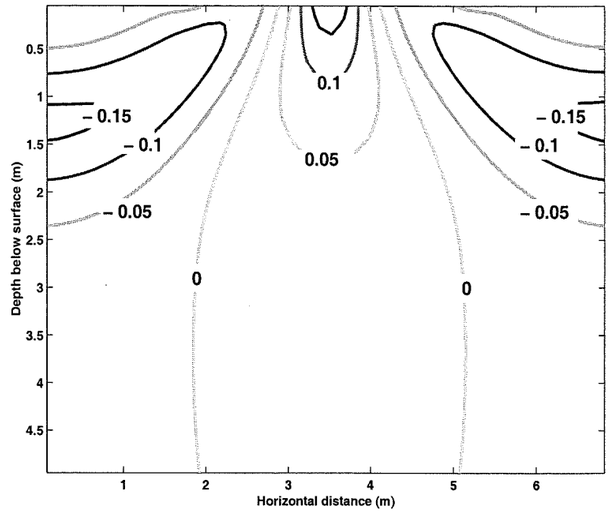


Figure 3.4: Contours of mass exchange rate (given in 10^{-6} kg m^{-3} s^{-1}) calculated using parameters of Albert (2002). Contour interval is 0.05 $\times$ 10^{-6} kg m^{-3} s^{-1}. Positive values indicate sublimation, negative values indicate condensation. I solved for the mass exchange rate on a grid of x = 0:0.1:7 m and y = 0:0.1:10 m, although only the upper 5 m are shown here. Air flowing into the firn was saturated (i.e. relative humidity = 1). The left and right margins were insulated (no vapor flux), as was the basal boundary.

25 cm as a result of the nearly isothermal temperature profile. Below this near-surface region, warm and moist air was advected into cooler and drier regions, resulting in local super-saturation. Consequently, water vapor condensed onto neighboring snow grains. I found that the locus of condensation was at ~1 m depth in regions of air inflow. Figure 4 of Albert (2002) shows similar features. Since the spatial temperature gradients were not as pronounced in Albert (2002) and there was no large near-surface isothermal zone, the locus of condensation was closer to the surface (centered at ~40 cm depth). Similarly, my model predicted significant condensation down to ~2 m, while Figure 4 of Albert (2002) shows no significant phase change beneath 1.25 m.

Figure (Fig. 3.4) shows that in regions of air outflow (Fig. 3.2; located between x = 1.75:5.3 m), my model predicted a small region of sublimation (located between x = 3 m and x = 4 m), where cold and dry air from the firn interior was advected through relatively warm near-surface layers. On the edges of this sublimation area, there were two adjacent areas of condensation (x = 1.5:3 m and x = 4:5.3 m). This was the result of horizontal advection from the warm and nearly isothermal areas in regions of air inflow to colder and drier areas dominated by airflow out of the firn. This horizontal advection created a region of local super-saturation, and consequently, condensation. In contrast, the model of Albert (2002) has much smaller horizontal temperature gradients, possibly as a result of differences in the value used for the thermal conductivity of the firn, or the total time the model was run. Consequently, regions of air outflow in Albert (2002) are entirely dominated by sublimation, as cold and dry air from the firn interior is advected into warmer near surface layers.

Qualitatively, the pattern of sublimation and condensation generated by the model matches the published results of Albert (2002). The differences in the pattern can again be attributed to either differences in the thermal constants used in the two models, to the calculated velocity fields or to the way the source terms were calculated. Quantitatively, there are significant but explainable differences in the absolute values of sublimation and condensation rate predicted by the two models. Albert (2002) predicts maximum rates of 0.050 kg m^{-3} s^{-1}, which are unrealistically large by several orders of magnitude (0.050 kg m^{-3} s^{-1} results in a mass exchange of 5 kg m^{-3} every 2 minutes). My model predicted maximum rates of 1.5 $\times$ 10^{-}7 kg m^{-3} s^{-1}, which are similar to values suggested by others (e.g. Bintanja, 2001; van den Broeke and others, 1997; Section 3.8.6). The unrealistically large values reported by Albert (2002) are most likely typographical error.

The above tests have demonstrated that my model agrees with a number of analytical models, and reproduces several published numerical results. Air flow in my model satisfies the continuity equation and satisfies analytical tests for stability, heat

conduction and heat advection and conduction. My model also reproduces the major results of both Albert and McGilvary (1992) and Albert (2002). My model uses a simpler solution technique than the model of Albert (2002), a simplified approach to calculating sub-surface air flow rates, and a different method for calculating saturation vapor density in the firn. With confidence and insight gained from the above tests, I now use the model to predict sublimation and condensation rates in the firn under several environmental conditions.

3.8 Application

Using the above models for conservation of energy and vapor motion in the firn, I calculated the fields of temperature T and mass exchange S for winter and summer, under both strong and moderate winds, and for several grain sizes.

3.8.1 Winter Conditions

Winter temperature profiles in firn are characterized by cold surface temperatures and warmer temperatures at depth. For calculating the temperature and mass exchange fields, I began with an initial estimate of firn temperature based on Equation (3.10). At this point I neglect advection to establish an approximate starting point. I used environmental parameters typical of the Antarctic plateau in winter: -40 C mean annual temperature, -50 C minimum winter temperature, bump height h = 10 cm, bump wavelength λ = 3 m and a 1 mm grain size.

I conducted two series of simulations: one with high winds (10 m wind speed = 10 m s^{-1}; amplitude of pressure variation along the surface topography (pressure drop) of 10 Pa) and another with moderate winds (5 m s^{-1}; amplitude of pressure variation along the surface topography of 2.5 Pa). Benson (1971) studied a 7 year record of mean monthly wind speed at Byrd Station, Antarctica and found that wind speed during all 84 months studied was between 5 and 10 m s^{-1}. Observations from the

Climate Monitoring and Diagnostics Lab (CMDL) South Pole weather station are generally lower than the values at Byrd, but are also within these limits. In both strong and moderate wind scenarios, I used a horizontal grid spacing of 10 cm, and a constant vertical grid spacing of 1 cm. I assumed that air flowing into the firn had a constant temperature T = -50 C, and an atmospheric relative humidity of 95%.

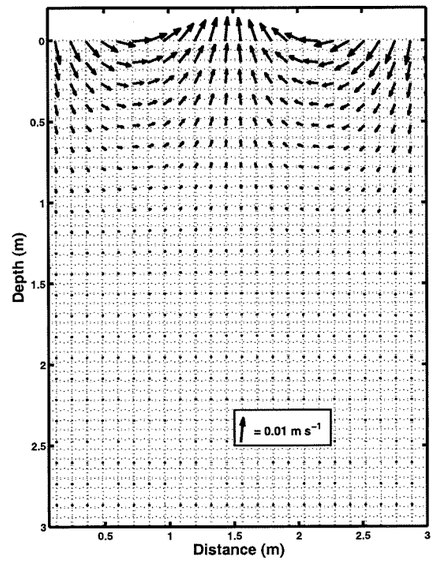


Figure 3.5: Near-surface air-flow velocities for winter conditions with strong winds. Horizontal and vertical velocities were calculated following the method of Colbeck (1989) and Waddington and others (1996), as described in Section 3.3. Horizontal velocities are positive to the right; vertical velocities are positive down. This simulation used surface topography parameters λ = 3 m and h = 10 cm with 10 meter wind speed U_10 of 10 m s^{-1} which generated a pressure drop at the surface of 10 Pa. Air enters the firn (vertical velocity is positive) on the intervals x = 0:0.75 m and 2.25:3 m. Air flows out of the firn (vertical velocity is negative) between x = 0.75 and 2.25 m. Since I use a constant permeability, the magnitude of the velocities decrease exponentially with depth with an e-folding scale of $\lambda/2\pi$ (Equation (3.5))

Strong winds: In the strong wind case, the maximum air-flow velocities into the firn were 0.97 cm s^{-1}, which lead me to choose a time step of 1 second. The air-flow velocities are shown in Figure (3.5). The e-folding depth, given this microtopography, is $\sim$ 50 cm. Since the left- and right-hand edges are insulated and a constant heat flux is imposed along the base, the firn loses heat to the atmosphere as time progresses. I ran the model until transients in the near-surface temperature and mass exchange fields had died out, which took around 10^6 model seconds (approximately 11.5 model days). Beyond this point, changes in the temperature field were due primarily to thermal diffusion below the near-surface ventilated zone. I accepted this as an equilibrated solution which approximated the temperature and mass exchange fields in the firn at midwinter.

The upper 3 m of the temperature field is shown in Figure 3.6. The near-surface temperature field is dominated by advection. Regions of inflowing air are nearly isothermal in the upper $\sim$40 cm, as a result of the advection of cold air from the atmosphere into the firn. In regions of outflowing air, relatively warm air from at depth in the firn is carried towards the surface. Between the regions of strong vertical advection, horizontal advection carries cold air laterally from regions of air inflow to regions of air outflow, creating the sinusoidal pattern of the near-surface isotherms. Below about 2.5 m depth, advection is less important, and the temperature field is dominated by conduction, resulting in parallel isotherms.

The upper 3 m of the mass exchange field is shown in Figure 3.7. Since the air in the atmosphere is undersaturated, there is rapid sublimation in the near-surface control volumes in regions of inflowing air. Since my grid size was too coarse to resolve the details of this strong sublimation, I conducted a separate high-resolution calculation of this (essentially) surface sublimation phenomenon. I found that the incoming under-saturated air reached saturation vapor density in the upper 1 cm, and sublimation rates were typically 2×10^{-6} kg m^{-3} s^{-1} in the upper cm. The quantifies what the Damkohler number (ratio of characteristic time for vapor diffusion

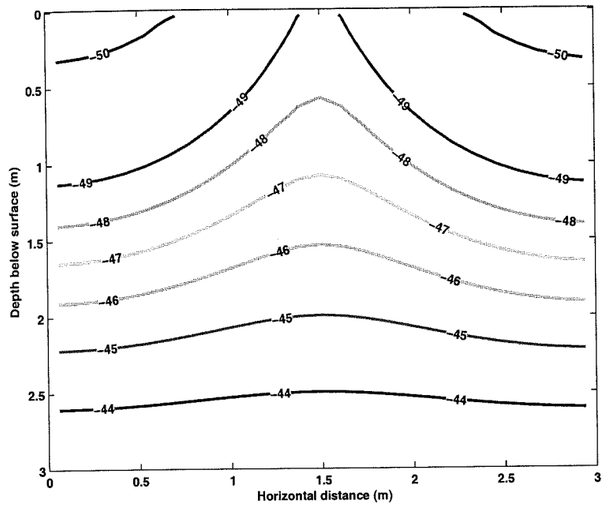


Figure 3.6: Contours of temperature field $T(x, y)$, in °C, calculated for conditions typical of Antarctic winter. I solved for $T(x, y)$ on a grid of x = 0:0.10:3 m and y = 0:0.01:5 m, although only the upper 3 m are shown here. Below 2.5 m, advection is no longer important and $T(x, y)$ is dominated by conduction, which results in parallel isotherms. Air flowing into the firn (Fig. 3.5) has constant temperature $T(x, 0)$ = -50 C. The left and right margins are insulated, and a constant heat flux is imposed along the base.

in a pore and residence time of air in a pore) presented above suggests; that air in pore spaces should always be near saturation. Mass exchange between the pore space air and surrounding snow grains keep the relative humidity close to 1. In regions of air outflow, there is no near-surface sublimation, as the air leaving the firn is slightly supersaturated, as a result of advection from the (relatively) warm firn interior.

Below the upper 1 cm in regions of air inflow (x = 0: 0.75 m and 2.25: 3 m; Fig. 3.5), there is very little mass exchange in the near-surface isothermal zone (upper $\sim$ 40 cm). Below $\sim$ 40 cm, cold dry air from the atmosphere is advected into increasingly warmer regions (Fig. 3.6). A mismatch between the vapor density of the inflowing

air and the local saturation vapor density develops (purely a function of temperature (Appendix E)), resulting in sublimation. For this model run, the maximum sublimation rate in regions of inflowing air ($\sim 8.2 \times 10^{-9}$ kg m^{-3} s^{-1}) was centered at 1 m depth. Below this, air-flow velocities and temperature gradients decrease, and large differences between the vapor density of the air and local saturation vapor density do not develop. All advection-driven mass exchange is found in the upper 1.75 m of the firn, where air-flow velocities are significant. Below this depth, the only mass exchange results from diffusion of water vapor along temperature gradients in the firn, and is several orders of magnitude smaller than advection-driven mass exchange.

The horizontal advection of cold and dry air from regions dominated by air inflow to warmer regions dominated by air outflow curves the locus of large sublimation rate (Fig. 3.7). The horizontal air flow extends the size of the region characterized by inflowing air into areas warmed by vertical air flow from depth towards the surface. This is a general result seen in many of the model results presented here: the horizontal advection of air, coupled with lateral temperature gradients, result in an increase in the size of the region characteristic of inflowing air. In the case of winter conditions, the result is a larger than expected region of sublimation; in summer, the result is a larger than expected region of condensation.

In regions of air outflow (x = 0.75: 2.25 m; Fig. 3.5), warm air from the firn interior is advected towards the surface. Condensation results, as the local vapor density in the outflowing air exceeds the local saturation vapor density of the cooler near-surface firn. The maximum condensation rate (-2 $\times$ 10^{-8} kg m^{-3} s^{-1}) is centered on the region of greatest vertical velocity (x = 1.5 m). All near-surface condensation is concentrated in a relatively narrow region from x = 1.3 m to 1.7 m due to the horizontal advection of cold dry air from regions of air inflow, as noted above.

By assuming that these environmental conditions persist for much of the winter, I estimated the total mass exchange in the firn during the winter season. I assumed that this temperature pattern and wind speed persist for the coldest 2 months of the

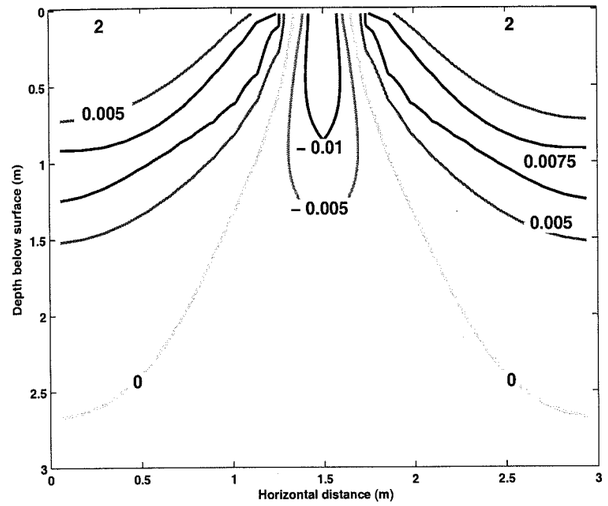


Figure 3.7: Contours of mass exchange rate (given in 10^{-6} kg m^{-3} s^{-1}) calculated using environmental conditions typical in Antarctic winter with strong winds (10 m s^{-1}). Contours of 0, $\pm$0.005, 0.075 and -0.01 $\times$ 10^{-6} kg m^{-3} s^{-1} are plotted. Positive values indicate sublimation, negative values indicate condensation. Strong near-surface sublimation is a result of under-saturated air flowing into the firn (initial relative humidity = 0.95). I solved for the mass exchange rate on a grid of x = 0:0.12:3 m and y = 0:0.01:5 m, although only the upper 3 m are shown here. The left and right margins were insulated (no vapor flux), as was the basal boundary.

year. The resulting total mass exchange field is shown in Figure (3.8). The maximum sublimation is at the surface in regions of air inflow. Over the course of the winter (60 days), the total sublimation in the near-surface layers is $\sim$ 10 kg m^{-3}. Most of the sublimation is in the upper 1 cm, as noted above. Beneath this near-surface layer, mass exchange rates are much more modest, and the cumulative values for sublimation (or condensation) rarely exceed $\sim$ 0.07 kg m^{-3}.

As noted above, the air leaving the firn is slightly supersaturated (relative humidity = 1.00001) as a result of air flow from the warm interior towards the cooler surface.

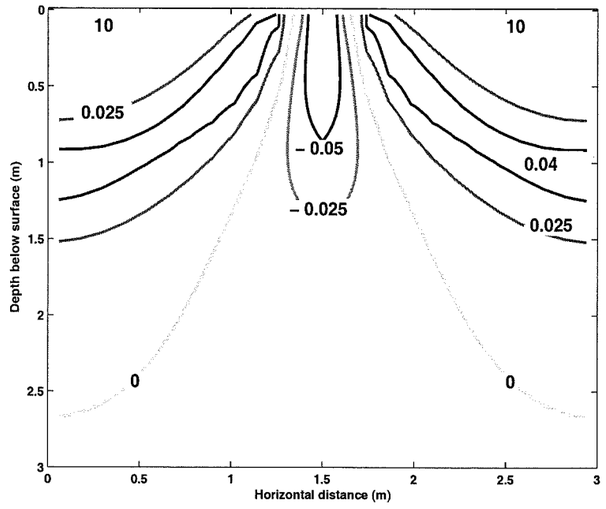


Figure 3.8: Contours of cumulative mass exchange (given in kg m^{-3}) calculated using environmental conditions typical in Antarctic winter with strong winds (10 m s^{-1}). Contours of 0, ± 0.025, 0.04 and -0.05 kg m^{-3} are plotted. Positive values indicate sublimation, negative values indicate condensation. Strong near-surface sublimation is a result of under-saturated air flowing into the firn (initial relative humidity = 0.95). I assumed that the environmental parameters used in this section persist for 60 days.

This also suggests that the Damkohler number for firn is $\sim$1, as suggested above. This supersaturation, coupled with the 95% relative humidity of the ambient atmosphere, results in a net transport of water vapor to the atmosphere as a result of air flow through the firn. I calculated the net mass of water vapor lost to the atmosphere per unit time ($\mathcal{M}$) as:

$$\mathcal{M} = \langle \rho_v(\text{out}) v(\text{out}) \rangle_{area} + \langle \rho_v(\text{in}) v(\text{out}) \rangle_{area} , \tag{3.12}$$

where:

$$\rho_v(\text{in}) = \rho_v(\text{atm}) \text{ and} \tag{3.13}$$

$$v(\text{out}) = -v(\text{in}) \tag{3.14}$$

where $\langle \ldots \rangle_{\text{area}}$ denotes an average value per unit of surface area, v is the vertical velocity, ρ_v is the vapor density and the indices *in* and *out* refer to areas of air *inflow* and *outflow* respectively. I found that for this combination of surface topography, temperature gradient and mass exchange coefficients, there was a net mass exchange of 6.2×10^{-8} kg m^{-1} s^{-1}, which corresponds to a mass flux of approximately 0.6 g per day as a result of air moving through the firn per square meter.

To further test the model, I repeated the above calculations using both coarser and finer grid spacing in both the x and y directions. For the model run described above, I used a 10 cm spacing in x, and 1 cm spacing in y. I will refer to this model run as the medium resolution case. For comparison, I generated a high resolution case (5 cm spacing in x and 0.5 cm in y) and a low resolution case (15 cm spacing in both x and y). I linearly interpolated the results of these three models onto a regular grid and compared the calculated $T(x, y)$ and mass exchange fields.

I found that, after 5000 model seconds, the three models predict the same temperature field to within 8×10^{-3} K. After 1e4 model seconds, the disagreement between the three models had fallen to 4×10^{-3} K. The medium and high resolution cases show even less disagreement, a maximum of 2×10^{-4} K. Based on these calculations, I assumed that the grid spacing has a minimal effect on $T(x, y)$.

For the mass exchange field, the results showed more variability. The patterns are all similar, and resemble Figure (3.7). Contours of constant sublimation are displaced by up to 10 cm between the three models. In general, the medium and high resolution cases agree to within 4 cm (or less), while the low resolution case shows greater disagreement. Based on this analysis, I accepted the medium resolution case as a reasonable proxy for the higher resolution (and presumably more accurate) case. Further tests with different grid spacing would help to illuminate the dependence of the predicted mass-exchange field on grid spacing. In the present study, I used the medium resolution case for all subsequent work, unless otherwise noted. Consequently, the mass-exchange rates presented in the following sections are not exact, as described

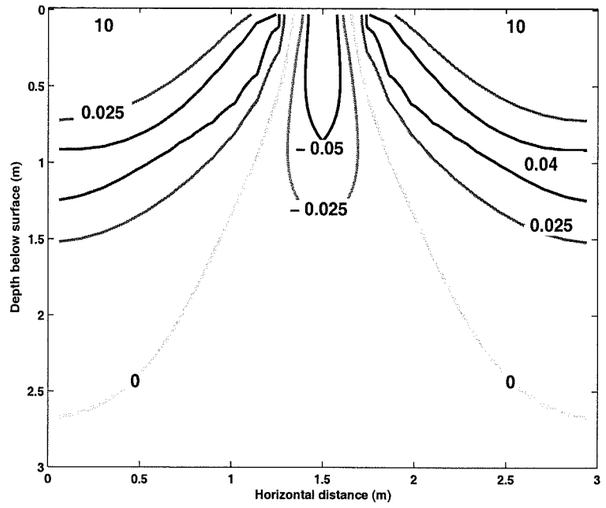


Figure 3.8: Contours of cumulative mass exchange (given in kg m^{-3}) calculated using environmental conditions typical in Antarctic winter with strong winds (10 m s^{-1}). Contours of 0, $\pm$0.025, 0.04 and -0.05 kg m^{-3} are plotted. Positive values indicate sublimation, negative values indicate condensation. Strong near-surface sublimation is a result of under-saturated air flowing into the firn (initial relative humidity = 0.95). I assumed that the environmental parameters used in this section persist for 60 days.

This also suggests that the Damkohler number for firn is $\sim$1, as suggested above. This supersaturation, coupled with the 95% relative humidity of the ambient atmosphere, results in a net transport of water vapor to the atmosphere as a result of air flow through the firn. I calculated the net mass of water vapor lost to the atmosphere per unit time ($\mathcal{M}$) as:

$$\mathcal{M} = \langle \rho_v(\text{out}) v(\text{out}) \rangle_{area} + \langle \rho_v(\text{in}) v(\text{out}) \rangle_{area} \, , \tag{3.12}$$

where:

$$\rho_v(\text{in}) = \rho_v(\text{atm}) \text{ and} \tag{3.13}$$

$$v(\text{out}) = -v(\text{in}) \tag{3.14}$$

where $\langle \ldots \rangle_{\text{area}}$ denotes an average value per unit of surface area, v is the vertical velocity, ρ_v is the vapor density and the indices *in* and *out* refer to areas of air *inflow* and *outflow* respectively. I found that for this combination of surface topography, temperature gradient and mass exchange coefficients, there was a net mass exchange of 6.2×10^{-8} kg m^{-1} s^{-1}, which corresponds to a mass flux of approximately 0.6 g per day as a result of air moving through the firn per square meter.

To further test the model, I repeated the above calculations using both coarser and finer grid spacing in both the x and y directions. For the model run described above, I used a 10 cm spacing in x, and 1 cm spacing in y. I will refer to this model run as the medium resolution case. For comparison, I generated a high resolution case (5 cm spacing in x and 0.5 cm in y) and a low resolution case (15 cm spacing in both x and y). I linearly interpolated the results of these three models onto a regular grid and compared the calculated $T(x, y)$ and mass exchange fields.

I found that, after 5000 model seconds, the three models predict the same temperature field to within 8×10^{-3} K. After 1e4 model seconds, the disagreement between the three models had fallen to 4×10^{-3} K. The medium and high resolution cases show even less disagreement, a maximum of 2×10^{-4} K. Based on these calculations, I assumed that the grid spacing has a minimal effect on $T(x, y)$.

For the mass exchange field, the results showed more variability. The patterns are all similar, and resemble Figure (3.7). Contours of constant sublimation are displaced by up to 10 cm between the three models. In general, the medium and high resolution cases agree to within 4 cm (or less), while the low resolution case shows greater disagreement. Based on this analysis, I accepted the medium resolution case as a reasonable proxy for the higher resolution (and presumably more accurate) case. Further tests with different grid spacing would help to illuminate the dependence of the predicted mass-exchange field on grid spacing. In the present study, I used the medium resolution case for all subsequent work, unless otherwise noted. Consequently, the mass-exchange rates presented in the following sections are not exact, as described

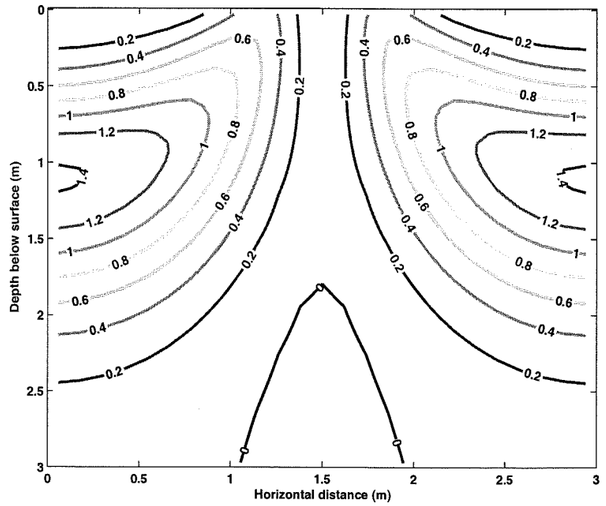


Figure 3.9: Difference between winter temperature fields calculated with moderate wind and strong wind, given in K. Positive values denote regions where the moderate wind case is warmer. Contour interval is 0.2 K.

above.

Moderate winds: In the moderate wind case, I used the same surface topography and boundary conditions as above, but assumed a 10 m wind speed of 5 m s^{-1}, which generated an amplitude of pressure variation along the surface topography of 2.5 Pa. This generated a maximum surface air-flow velocity of 0.3 cm s^{-1}. The pattern of surface air-flow velocities and e-folding depth are the same as shown in Figure 3.5; only the magnitude is different. I ran the moderate wind case for 1×10^6 model seconds, as in the strong wind case described above. I assumed that after 1×10^6 model seconds, initial transients had decayed, and subsequent changes were primarily due to thermal diffusion. I used this as an acceptable estimate of the temperature and mass exchange fields in the midwinter firn.

The temperature pattern is qualitatively similar to the strong wind case (Fig. 3.6), although with some important differences. The differences are a result of the lower advective velocities (and consequently lower Peclet number) in the moderate wind case. Figure (3.9) shows the difference between the temperature fields with 10 m wind speed of 5 m s^{-1} (moderate wind case) and 10 m wind speed of 10 m s^{-1} (strong wind case). Positive values denote regions where the moderate wind case is warmer, negative values denote regions which are cooler in the moderate wind case. The total difference between the two cases will also be a function of total model time elapsed. Since the left- and right-hand edges are insulated and a constant heat flux is imposed at the base, the overall result of air flow in the in firn is to transfer heat to the atmosphere. Due to the larger advective velocities, the strong-wind case transfers heat more readily than the moderate wind case. However, it is useful to compare how the two temperature patterns differ after a fixed elapsed time (1×10^6 model seconds).

Near the surface (upper 15 cm) in regions dominated by air inflow (x = 0: 0.75 m and 2.25: 3 m; Fig. 3.5), there is little difference between the two cases; advection generates a nearly isothermal near-surface zone. Below this isothermal zone, the firn is warmer by up to 1.4 K in the moderate wind case compared to the strong wind case, as result of the smaller vertical velocity. The difference in $T(x, y)$ is largest at $\sim$ 1.2 m depth. Figure (3.9) also shows that areas immediately surrounding regions of air inflow are warmer under moderate winds as a result of the decreased importance of horizontal advection of cold air from the inflow regions. Regions of air outflow (x = 0.75: 2.25 m; Fig. 3.5) show similar $T(x, y)$ in both the moderate and strong wind cases (difference less than 0.2 K). Even though strong winds carry heat from the firn interior more readily than the moderate wind case (which would make the strong wind scenario warmer), the lateral advection of cold air cools the regions of air outflow, such that there is little difference in $T(x, y)$ in the two scenarios.

The upper 3 m of the mass exchange field is shown in Figure (3.10). The pattern is similar to that calculated for strong wind (Fig. 3.7). In regions of air inflow (x =

0: 0.75 m and 2.25: 3 m; Fig. 3.5), there is a locus of sublimation at depth as a result of the advection of cold dry air from the surface into the interior of the firn. In the strong wind case, the locus of sublimation was centered at 1 m depth, and reached a maximum value of $\sim 8.2 \times 10^{-9}$ kg m^{-3} s^{-1}. Under moderate winds, the locus of maximum sublimation is closer to the surface (at 50 cm depth) as a result of the smaller vertical velocity. The maximum sublimation rate is also smaller by 35%, as a result of the smaller vertical velocity combined with a smaller temperature gradient. In general, since local saturation vapor density is a function of temperature (Appendix E), and temperature gradients in the firn are smaller under moderate wind conditions than with strong wind, vapor density and saturation vapor density differences (and by extension, mass-exchange rates) are smaller under moderate wind than under strong wind.

As in the strong wind case, the advection of under-saturated air from the atmosphere into the firn in regions of air inflow produces rapid sublimation in the upper few cm. I found that the incoming under-saturated air reached saturation vapor density in the upper 1 cm in both the strong and moderate wind case. The sublimation rates were lower in the moderate wind case, typically 5×10^{-9} kg m^{-3} s-1. In regions of air outflow, there is no near-surface sublimation, since the air leaving the firn is lightly supersaturated due to advection from the warmer interior of the firn, as was seen in the strong wind case.

The differences in the lateral extent of sublimation between the moderate wind case (Fig. 3.10) and strong wind case (Fig. 3.7) are also a result of smaller air-flow velocities along with a smaller temperature gradient. In the strong wind case, large horizontal air-flow velocities extend the region of sublimation into areas dominated by air flow from depth towards the surface. This horizontal advection resulted in a relatively narrow region (0.4 m) of firn dominated by outflowing warm air (Fig. 3.7). Under moderate winds, the width of the region dominated by air outflow is wider (65 cm) as a result of the smaller horizontal air-flow velocities. With no horizontal

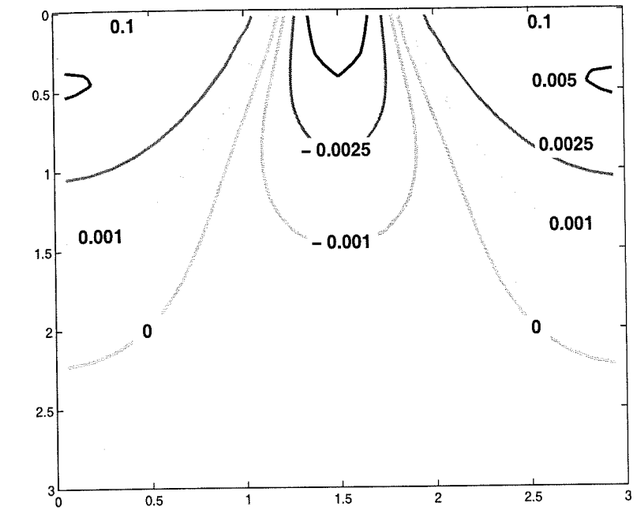


Figure 3.10: Contours of mass-exchange rate (given in 10^{-6} kg m^{-3} s^{-1}) calculated using environmental conditions typical in Antarctic winter with moderate winds (5 m s^{-1}). Contours denote lines of 0, ± 0.001, ± 0.0025 and $\pm 0.005 \times 10^{-6}$ kg m^{-3} s^{-1} mass exchange rate. Positive values indicate sublimation, negative values indicate condensation. Strong near-surface sublimation is a result of under-saturated air flowing into the firn (initial relative humidity = 0.95). I solved for the mass exchange rate on a grid of x = 0:0.12:3 m and y = 0:0.01:5 m , although only the upper 3 m are shown here. The left and right margins were insulated (no vapor flux), as was the basal boundary.

air flow, I expect that only diffusion through the firn would redistribute water vapor laterally, and the width of the region dominated by air outflow would take a maximum value ($\sim$ 1.5 m, or half the wavelength of the surface topography).

In the regions dominated by air outflow (x = 0.75: 2.25 m; Fig. 3.5), warm air from the firn interior is advected towards the surface, resulting in condensation. Since the horizontal air-flow velocities are lower in the moderate wind case, the size of the vapor condensation region is larger than in the strong wind case, as discussed above. The air leaving the firn is moving more slowly and the temperature gradients

are smaller in regions of air outflow in the moderate wind case. Consequently, the magnitude of the condensation rates in the moderate wind case are smaller than those of the strong wind case by 35%. The air exits the firn with an even smaller degree of supersaturation than seen in the strong wind case, and the total mass of water transferred to the atmosphere is similarly diminished.

This comparison between moderate winds and strong winds highlights a general result of this model of water-vapor motion in firn. When all other environmental parameters are kept equal, smaller air-flow velocities produce smaller mass exchange rates in the firn. With small air-flow velocities, only a fraction of the air in a given volume is replaced in each time step. Consequently, the local saturation vapor density remains close to the saturation value, and large mass exchange rates do not develop. In the end member case of no air flow, regardless of initial vapor density, air in the firn pore space would quickly reach saturation values everywhere. Water vapor would be transported only through diffusion, and mass-exchange rates would be very low. In the other end member case of large subsurface air-flow velocity, all of the air in a given volume would be replaced in a given time step. Depending on the vapor density gradient, grid size and time step, very large mass exchange rates could be achieved. The subsurface air-flow velocity is determined by surface topography and wind speed, as described in Section 3.3. Consequently, knowledge of these parameters at a site is necessary in order to estimate the subsurface mass exchange rate.

3.8.2 Summer Conditions

Summer temperature profiles in the firn are characterized by a warm surface temperature and colder temperature at depth. For calculating the temperature and mass exchange fields, I began with an initial estimate of mid-summer firn temperature based on Equation (3.10), with a seasonal temperature cycle of ± 20 degrees. Although this equation does not consider advection, I used it as an approximate starting point. I used environmental values typical of the Antarctic plateau in summer: -40 C mean annual temperature, -20 C maximum summer temperature, bump height $h = 10$ cm, bump wavelength $\lambda = 3$ m and a 1 mm grain size.

I again conducted two series of simulations: one with high winds (10 m wind speed $= 10\ \mathrm{m\,s^{-1}}$; surface pressure drop of 10 Pa) and another with moderate winds ($5\ \mathrm{m\,s^{-1}}$; surface pressure drop of 2.5 Pa). In both instances, I used a horizontal grid spacing of 10 cm, and a uniform vertical grid spacing of 1 cm. I assumed that air flowing into the firn had a constant temperature T = -20 C, and an atmospheric relative humidity of 80%. There are few measurements of relative humidity in the Antarctic interior, as a result of the difficulty of accurately measuring very low vapor densities. The value I chose for the summer simulation is based on unpublished observations by S. Hudson and M. Town (2001) in late summer at South Pole (S. Warren, pers. comm.).

Strong winds: The surface air-flow velocities are the same as depicted in Figure (3.5). The maximum surface velocities were 0.97 cm $\mathrm{s^{-1}}$, which lead me to choose a time step of 1 second. The e-folding depth of the velocity field, given this microtopography, is $\sim$ 50 cm as in the other cases presented here.

Since the left- and right-hand edges are insulated and a constant heat flux is imposed along the base, the summer firn gains heat from the atmosphere as time progresses in the model. I ran the model until transients in the near-surface temperature and mass exchange fields had died out, which took around 1×10^6 model seconds (approximately 11.5 model days). Beyond this point, changes in the temperature field were due primarily to thermal diffusion below the near-surface ventilated zone. I accepted this as an equilibrated solution which approximated the temperature and mass exchange fields in the firn at midsummer.

The upper 3 m of the temperature field is shown in Figure (3.11), and has features similar to the winter high velocity temperature field shown in Figure (3.6). Regions of inflowing air are nearly isothermal in the upper $\sim$ 50 cm, as a result of the advection of warm air from the atmosphere into the firn. In regions of outflowing air, relatively cold air from at depth in the firn is carried towards the surface. The effect of horizontal

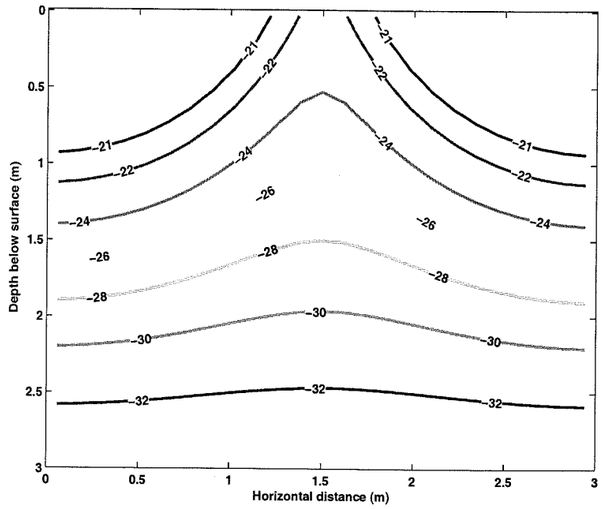


Figure 3.11: Contours of temperature field $T(x, y)$, in °C, calculated for conditions typical of Antarctic summer. I solved for $T(x, y)$ on a grid of x = 0:0.12:3 m and y = 0:0.01:5 m, although only the upper 3 m are shown here. Below 2.5 m, advection is less important and $T(x, y)$ is dominated by conduction, resulting in parallel isotherms. Air flowing into the firn (Fig. 3.5) has constant temperature $T(x, 0)$ = -20 C. The left and right margins are insulated, and a constant heat flux is imposed along the base.

advection between cold and warm regions is to create the sinusoidal pattern of the near-surface isotherms. Below about 2.5 m depth, advection is less important, and the temperature field is dominated by conduction, resulting in parallel isotherms.

The upper 3 m of the mass exchange field is shown in Figure 3.12. Since the air in the atmosphere is under-saturated and the Damkohler number for firn is ~1, there is rapid sublimation in the grid cells nearest to the surface in regions of inflowing air. I again conducted a separate high-resolution calculation of the near-surface sublimation rate. I found that the incoming under-saturated air reached saturation vapor density in the upper 1 cm, as in the winter model. Sublimation rates were much larger in the summer case, typically 6.5 $\times$ 10^{-4} kg m^{-3} s−1 in the upper 1 cm, as a result of the

low atmospheric relative humidity.

Below the upper 1 cm in regions of air inflow (x = 0: 0.75 m and 2.25: 3 m; Fig. 3.5), there is very little mass exchange in the near-surface isothermal zone (upper ~ 50 cm). Below ~ 50 cm, warm moist air is advected into increasingly cooler and drier regions (Fig. 3.11), and condensation results. For this model run, the maximum condensation rate beneath inflowing air (~ -2.5 $\times$ 10^{-7} kg m^{-3} s^{-1}) was centered at 1 m depth. Below this, air-flow velocities and temperature gradients decrease, and the condensation rate decreases. Significant advection-driven mass exchange is found in the upper 2.5 m of the firn, deeper than was found in the winter scenarios presented above. Below this depth, much slower mass exchange results from diffusion of water vapor along temperature gradients.

The horizontal advection of warm and moist air from regions dominated by air inflow to colder regions dominated by air outflow curves the locus of large condensation rate into the semi-circular pattern shown in Figure 3.12. This modification of the mass exchange field as a result of horizontal air flow is similar to that seen in the winter scenarios presented above. In the case of winter conditions, the result is a larger-than-expected region of sublimation; in summer, the result is a larger-than-expected region of condensation.

In regions of air outflow (x = 0.75: 2.25 m; Fig. 3.5), cold dry air from the firn interior is advected towards the surface, resulting in sublimation. The maximum sublimation rate (2 $\times$ 10^{-7} kg m^{-3} s^{-1}) is centered on the region of greatest vertical velocity (x = 1.5 m). All near-surface sublimation is concentrated in a relatively small region from x = 1.3 m to 1.7 m as a result of the horizontal advection of warm moist air from regions of air inflow, as noted above.

By assuming that these environmental conditions persist for much of the summer, I estimated the total mass exchange in the firn during the summer season. I assumed that this temperature pattern and wind speed were representative of the warmest 2 months of the year. The total mass-exchange field is shown in Figure 3.13. The

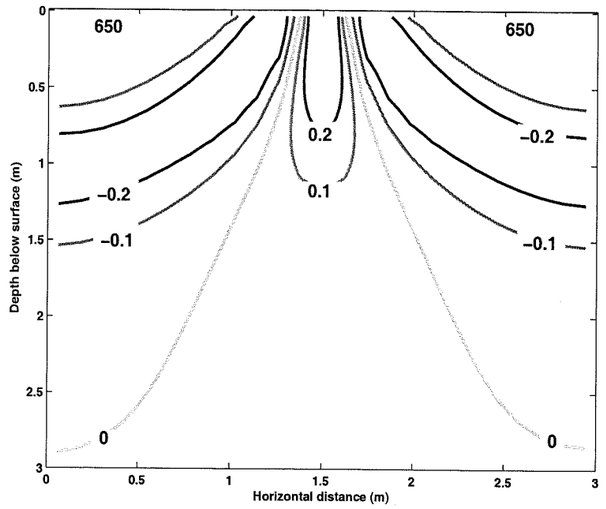


Figure 3.12: Contours of mass-exchange rate (given in 10^{-6} kg m^{-3} s^{-1}) calculated using environmental conditions typical in Antarctic summer with strong winds (10 m s^{-1}). Contours of 0, $\pm$0.1 and $\pm$0.2 $\times$ 10^{-6} kg m^{-3} s^{-1} are plotted. Positive values indicate sublimation, negative values indicate condensation. Strong near-surface sublimation is a result of under-saturated air flowing into the firn (initial relative humidity = 0.80). I solved for the mass exchange rate on a grid of x = 0:0.12:3 m and y = 0:0.01:5 m, although only the upper 3 m are shown here. The left and right margins were insulated (no vapor flux), as was the basal boundary.

maximum total sublimation is at the surface (upper 1 cm) in regions of air inflow. Over the course of the summer (60 days), the total sublimation near the surface is $\sim$ 3250 kg m^{-3}, a very large value. If correct, as much as 7 cm of the snow surface could be converted to water vapor during the summer season for snow with a density of 450 kg m^{-3}. This is comparable to the summer mean (7 year average) accumulation rate at the South Pole reported by McConnell and others (1997a), suggesting that the summer surface elevation change would be more modest. This model for water-vapor motion in the firn does not take into account either accumulation of fresh snow at

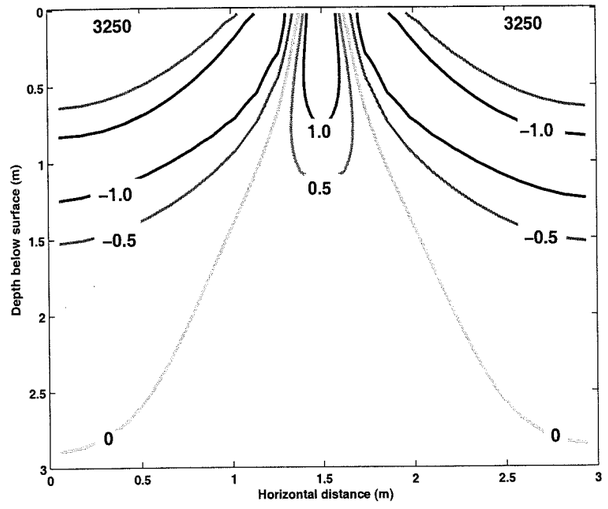


Figure 3.13: Contours of cumulative mass exchange (given in kg m^{-3}) calculated using environmental conditions typical in Antarctic summer with strong winds (10 m s^{-1}). Contours of 0, $\pm$0.5 and $\pm$ 1 kg m^{-3} are plotted. Positive values indicate sublimation, negative values indicate condensation. Strong near-surface sublimation is a result of under-saturated air flowing into the firn (initial relative humidity = 0.80). I assumed that the environmental parameters used in this section persist for 60 days.

the surface, or net lowering of the surface through sublimation, and has limited value in studying surface sublimation (Section 3.9). Beneath this near-surface layer, mass exchange rates are much more modest, and the cumulative values for sublimation (or condensation) rarely exceed $\sim$ 1 kg m^{-3}.

The air leaving the firn is essentially saturated as a result of sublimation of snow grains as the air leaves the firn. This saturation, coupled with the 80% relative humidity of the ambient atmosphere, results in a net transport of water vapor to the atmosphere due to air flow through the firn. I calculated the net mass of water vapor lost to the atmosphere per unit time ($\mathcal{M}$; Equation (3.12)) during the summer season. For this combination of surface topography, temperature gradient and mass

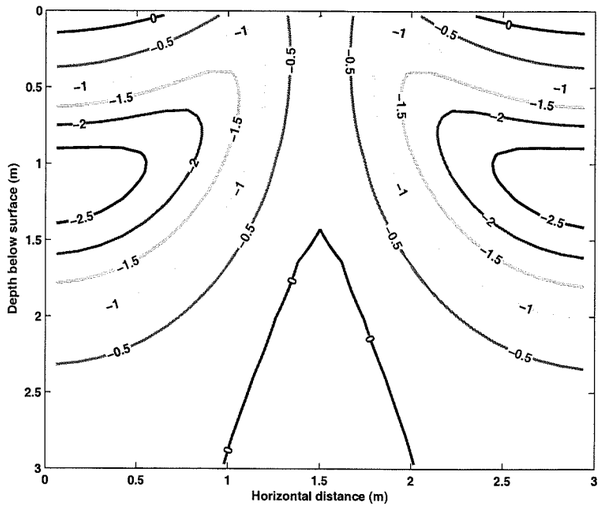


Figure 3.14: Difference between summer temperature fields calculated with moderate wind and strong wind, given in K. Negative values indicate that the moderate wind case is cooler throughout the model. Contours of 0.5 K are plotted.

exchange coefficients, there was a net mass exchange of 1.6 $\times$ 10^{-8} kg m^{-2} s^{-1} to the atmosphere, which corresponds to a mass flux of approximately 1.4 g m^{-2} per day as a result of air flowing out of the firn.

Moderate winds: In the moderate wind case for summer, I used the same surface topography and boundary conditions as in the winter moderate wind case. Again, since the left- and right-hand edges are insulated and a constant heat flux is imposed along the base, the point at which the model is 'equilibrated' is somewhat arbitrary. I again ran the model for 1 $\times$ 10^6 model seconds, at which point, transients in the temperature and mass exchange fields had run their course.

The temperature pattern is qualitatively similar to the strong wind case (Fig. 3.11), although with some important differences. The differences are primarily due to the lower advective velocities (and consequently lower Peclet number) in the moderate

wind case. Figure (3.14) shows the difference between the temperature fields with moderate wind and with strong wind. Negative values indicate that the firn is cooler in the moderate wind case. Near the surface (upper 15 cm) in regions dominated by air inflow (x = 0: 0.75 m and 2.25: 3 m; Fig. 3.5), there is little difference between the two cases. Below this near-surface zone, the firn is cooler by up to 2.5 K in the moderate wind case compared to the strong wind case, as result of the smaller vertical velocity. The difference in $T(x, y)$ is largest in a region centered at $\sim$ 1.25 m depth. Figure (3.14) also shows that areas immediately surrounding regions of air inflow are cooler under moderate winds as a result of the decreased importance of horizontal advection of warm air from the inflow regions. Regions of air outflow (x = 0.75: 2.25 m; Fig. 3.5) show similar $T(x, y)$ in both the moderate and strong wind cases (difference less than 0.5 K). Even though in the strong wind case, cool air from at depth is advected more readily than the moderate wind case (which would make the strong wind scenario cooler), the lateral advection of warm air warms the regions of air outflow, such that there is little difference in $T(x, y)$ in the two scenarios in regions of air outflow. There is little difference in the temperature fields below 3 m.

The upper 3 m of the mass-exchange field is shown in Figure (3.15). The pattern is similar to that calculated for strong wind (Fig. 3.12). In regions of air inflow (x = 0: 0.75 m and 2.25: 3 m; Fig. 3.5), there is a locus of condensation at depth as a result of the advection of warm moist air from the surface into the interior. In the strong wind case, the locus of condensation was centered at 1 m depth, and reached a maximum value of $\sim$ -2.5 $\times$ 10^{-7} kg m^{-3} s^{-1}. Under moderate winds, the locus of maximum sublimation is closer to the surface (at 45 cm depth) as a result of the smaller vertical velocity. The maximum sublimation rate is smaller by 30%, as a result of the smaller vertical velocity combined with a smaller temperature gradient. Since local saturation vapor density is a function of temperature, and temperature gradients in the firn are smaller under moderate wind conditions than with strong wind, saturation vapor pressure differences (and by extension, mass exchange rates)

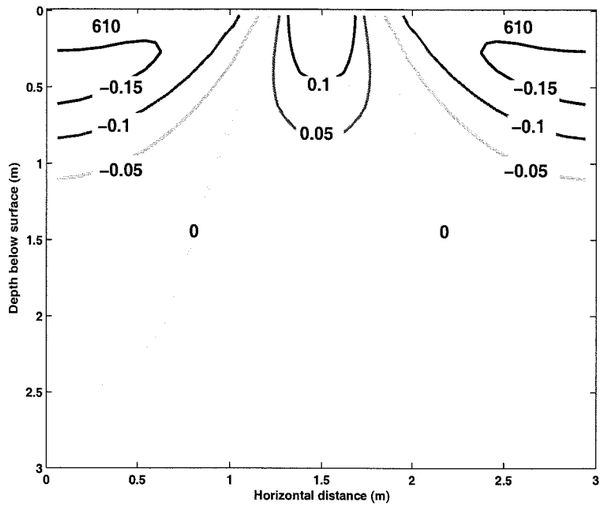


Figure 3.15: Contours of mass-exchange rate (given in 10^{-6} kg m^{-3} s^{-1}) calculated using environmental conditions typical in Antarctic summer with moderate winds (5 m s^{-1}). Contours denote 0, ± 0.05, ± 0.1 and 0.15×10^{-6} kg m^{-3} s^{-1}. Positive values indicate sublimation, negative values indicate condensation. Strong near-surface sublimation results from flow of under-saturated air into the firn (initial relative humidity = 0.80). I solved for the mass exchange rate on a grid of x = 0:0.12:3 m and y = 0:0.01:5 m , although only the upper 3 m are shown here. The left and right margins were insulated (no vapor flux), as was the basal boundary.

are smaller under moderate wind than under strong wind.

As in the strong wind case, the advection of under-saturated air from the atmosphere into the firn in regions of air inflow produces rapid sublimation in the upper few cm. I found that the incoming under-saturated air reached saturation vapor density in the upper 1 cm in both the strong and moderate wind case. The sublimation rates were lower in the moderate wind case, typically 6.1×10^{-4} kg m^{-3} s^{-1}. In regions of air outflow, there is a region of near-surface sublimation, since the air leaving the firn is moving from colder to warmer regions, as was seen in the strong wind case.

The comparison between moderate winds and strong winds for summer conditions mirrors the results found for winter conditions: when all other environmental parameters are kept equal, smaller air-flow velocities produce smaller mass exchange rates in the firn. With small air-flow velocities, only a fraction of the air in a given volume is replaced in each time step. Consequently, the local saturation vapor density remains close to the saturation value, and large mass exchange rates do not develop.

3.8.3 Seasonal Comparison

The comparison between mass exchange rates during winter conditions and during summer conditions is also useful. During winter, the surface is colder than at depth; consequently, the model predicts sublimation in regions of inflowing air, and condensation in regions of outflowing air. In summer, the situation is reversed. The firn is cooler at depth and warmer at the surface; this leads to condensation in regions of inflowing air and sublimation in regions of outflowing air, as described above.

As a result of the non-linearity of water vapor pressure over ice (Equation (E.1)), mass-exchange rates are up to two orders of magnitude larger in the summer than the winter. This suggests that winter-time mass exchange can largely be ignored when studying water-vapor motion on annual time scales or longer. The disparity between winter and summer sublimation rates was also noted by van den Broeke (1997) in a mass-balance model for Antarctica.

For both winter and summer scenarios, I used the same surface topography, and the same surface wind speed. Albert and Hawley (2002) noted seasonal changes in both surface roughness and wind speed at Summit, Greenland. Surface topography reached a maximum amplitude in late winter, as was found by Gow (1965) at the South Pole. In addition, strong winds (greater than 10 m s^{-1}) were more frequent during the winter. If these observations are true in general, these two factors lead to enhanced subsurface air-flow velocities in the winter months. This difference in ventilation rate would reduce the disparity between winter and summer mass exchange rates, but

mass exchange rates will still be larger in summer as a result of the much higher vapor pressures in summer. For example, the model predicts that mass-exchange rates in summer with moderate winds (5 m s^{-1}) are a factor of 8 or more greater than mass-exchange rates in winter with strong winds (10 m s^{-1}). This suggests that winter-time mass exchange can generally be ignored on annual timescales or longer.

3.8.4 Response Time

I examined the idealized response time of firn to a step change in temperature at the snow surface. For this simulation, I used a uniform initial temperature distribution and measured the characteristic response time τ of the firn (time required for the firn to experience 1 - e^{-1} of the total change). I used the same surface micro topography as above (h = 0.1m, λ = 3m) with strong winds (10 meter wind speed = 10 m s^{-1}). Consequently, the air-flow field is the same as was used in the simulations of strong winds in winter and summer described above, and is shown in Figure (3.5).

Figure (3.16) shows the response time in hours as for the upper 1.5m of the firn. Temperature changes of a week or shorter will primarily influence regions of air inflow. Advection from at depth in the firn in air outflow regions buffers the firn temperature, making these areas less sensitive to short-term fluctuations. Daily temperature cycles are primarily important in the upper 50 cm of regions of air inflow, as discussed further in Chapter 5. The model predicts that very short term temperature fluctuations (on the scale of hours) will influence only the uppermost 20cm of the firn. Synoptic scale systems lasting $\sim$ 1 week may influence as much as the upper 1.25m of the firn. The simulation was run for 5 model days (limited by computation time) and does not estimate the response time to lower frequency temperature changes, such as seasonal temperature cycles.

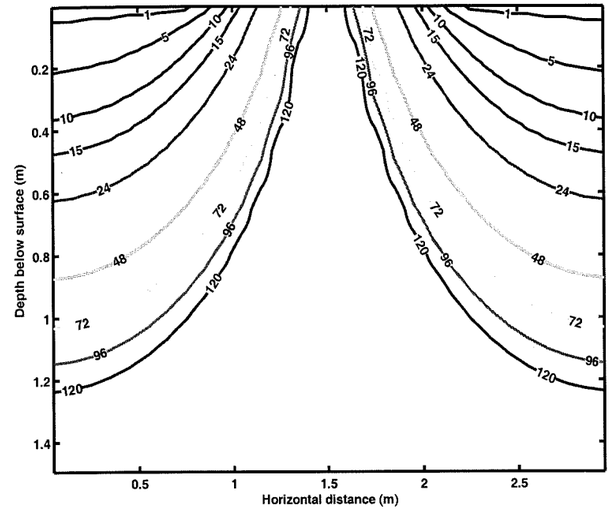


Figure 3.16: Idealized response time τ (hours) of firn to a step change in temperature at the firn surface. Response time τ calculated as time required for firn temperature to experience $1 - e^{-1}$ of the total change. Response time calculation is limited by computation time, the simulation runs approximately in real-time. Simulation used an initially uniform firn temperature and air flow as in Figure (3.5) (bump height h = 0.1m, bump wavelength λ = 3m). Regions of air inflow respond rapidly (τ < 24 hours), while regions of air outflow are buffered by advection from the firn interior.

3.8.5 Influence of Grain Size

One aspect of the model that has not yet been discussed is the effect of grain size on mass-exchange rate. The model assumes that all ice grains in the firn have the same surface area to volume ratio. For a given volume, a larger surface area in the firn will produce a larger mass exchange rate (Equation (3.9)). This model parameterizes the surface area to volume ratio through an effective diameter for ice grains. Published measurements of the grain size of near-surface Antarctic snow vary from 3 mm (Taylor, 1971) to 65 μm (Grenfell and others, 1994). An extensive study of snow pits by

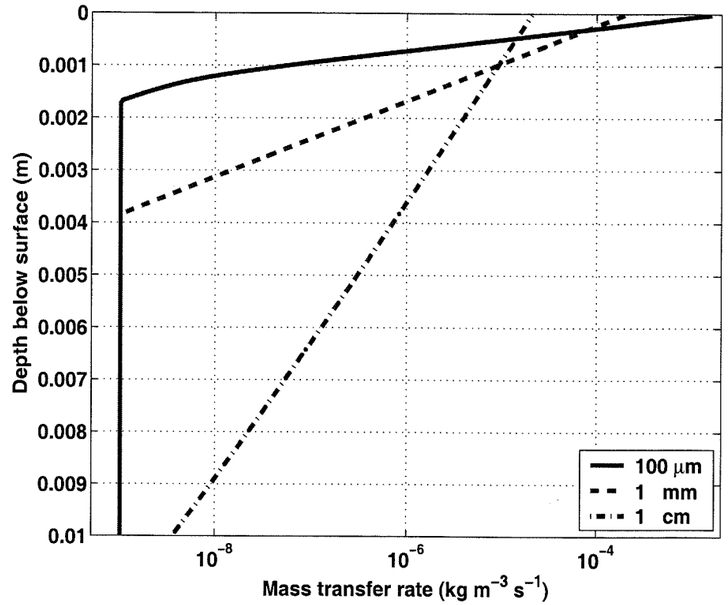


Figure 3.17: Mass exchange rate (given in kg m^{-3} s^{-1}) calculated for 3 different values of the ice grain diameter. I used a vertical grid of 0.5 mm, and a time step of 0.01 seconds, along with a surface pressure drop of 10 Pa. In some cases, the grain size used exceeds the vertical grid resolution. Although not a physically plausible scenario, mathematically it poses no difficulty and helps to illuminate the role that grain size plays in determining the mass exchange rate. The smallest grain size (100 μm) has largest mass exchange rate at the surface, and reaches saturation vapor density by 2 mm depth. The 100 μm grains also show the smallest average mass exchange rate in the upper 1 cm. Larger grain sizes have smaller mass exchange rates in the upper few mm, and take longer to reach saturation vapor density, although have higher average mass exchange rates in the upper 1 cm.

Picciotto and others (1971) in Queen Maud Land, East Antarctica, showed variable grain diameter due to several grain growth processes (described by Yosida and others, 1955 and Colbeck, 1983a) from $\sim$ 1 mm at the surface to $\sim$ 2 mm at 1 meter depth. All of my calculations presented above used a constant diameter of 1 mm, which

seems to be the mean of the published estimates that I found.

In order to study the affect of grain size on mass exchange rate, I used a vertical grid resolution of 0.5 mm and a time step of 0.01 seconds. I used the temperature pattern associated with strong air flow during winter presented above (Fig. 3.6). Air entered the firn with a relative humidity of 80 %. I calculated the mass exchange rate as a function of depth in the region of maximum air flow into the firn for three different grain sizes, shown in Figure (3.17). In some cases, the grain size used exceeds the vertical grid resolution. Although not a geometrically plausible scenario, mathematically it poses no difficulty and helps to illuminate the role of grain size in determining the mass exchange rate. With 100 μm grains, the model predicted a mass exchange rate that was large at the surface, but decreased rapidly with depth. It is apparent that incoming air quickly reaches saturation vapor pressure, and remains near saturation vapor pressure below the upper 2 mm. With 1 mm grains, the initial mass exchange rate is somewhat smaller, and incoming air takes longer to reach local saturation vapor pressure. Using 1 cm grains, the initial mass exchange rate is lower yet, and air does not appear to reach local saturation vapor pressure in the upper 1 cm.

Although near-surface mass-exchange rates are higher with smaller grains, mean mass-exchange rates are larger with larger grains. As shown in Figure (3.17), the mean mass-exchange rate over the upper 1 mm is highest for the 1 cm grains. Larger grain sizes result in slower instantaneous mass exchange rates, and allow a disequilibrium between the local saturation vapor pressure and the saturation vapor pressure of the air to persist. This results in larger spatially-averaged mass exchange rates. For smaller grain sizes, the local vapor pressure remains close to saturation values, and large mass exchange rates do not develop. Figure (3.18) is a plot of mass exchange rate as a function of grain size in a region of air inflow at a depth of 18 cm below the surface. I used a grid size of 10 cm in x and 1 cm in y for all results plotted in Figure (3.18). The larger grid size acts as a filter, averaging mass exchange over the

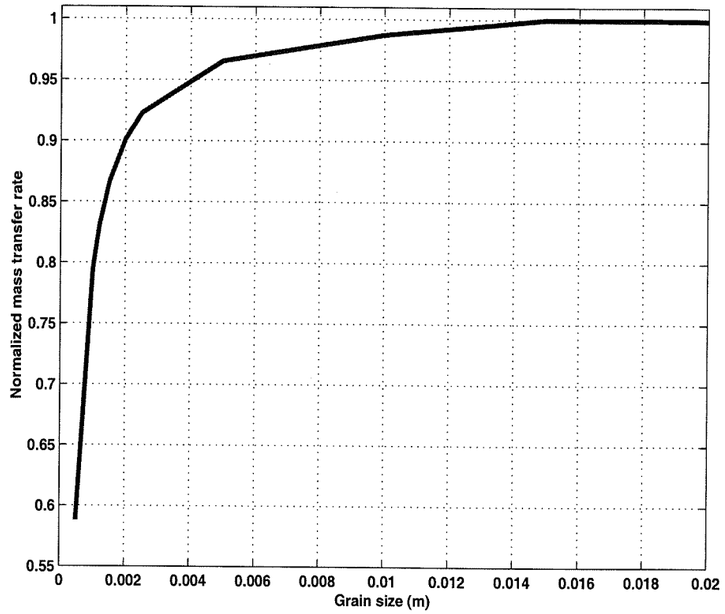


Figure 3.18: Normalized mass exchange rate calculated for different values of the effective particle diameter. I used a vertical grid of 6 mm, and a time step of 1 second, along with a surface pressure drop of 10 Pa. Small grain sizes have large instantaneous mass exchange rates (Fig. 3.17), and quickly reach local saturation vapor density. Consequently, small grain sizes have smaller mass-exchange rates when averaged over a typical grid cell ($\sim$ 1 cm). Larger grain sizes show larger average mass-exchange rates since they allow a disequilibrium between the local saturation vapor pressure and the saturation vapor pressure of the air to persist.

depth interval of the control volume. All mass-exchange rates in Figure (3.18) are normalized to the mass exchange rate using 2 cm grains. The average mass-exchange rate for 500 μm grains is 40% less than the average mass exchange rate for 2 cm grains. These results qualitatively confirm what we expect to find: larger grains lead to larger average mass-exchange rates in the firn. This result is due to the linear dependence of mass-exchange rate on the surface area to volume ratio of grains in the

function I used to calculate mass transfer (Equation (3.9) Appendix E).

These results also point to the importance of the mass-exchange coefficient in Equation (E.2) of Appendix E. As described above, changes in grain size influence the mass-exchange rate through the surface area to volume ratio of the ice grains. Although the interaction between snow and water vapor has been studied in a number of different contexts, the mass-exchange coefficient has not been well-studied. This critical parameter determines how fast water vapor in contact with snow will reach saturation vapor density. In both this model and that of Albert (2002), the mass-exchange coefficient is based on the work of Chu and others (1953). Future work will focus on measuring this parameter in the lab for a variety of grain sizes and air flow velocities.

3.8.6 Comparison With Field Data

There are no field measurements of subsurface water-vapor motion to compare with my model results, but there are a limited number of measurements of surface sublimation rate. Although my model is not designed for determining surface sublimation rates, it can be used if the relative humidity of the atmosphere is known. Using relative humidity = 0.80 and snow density = 450 kg m^{-3}, this model predicted a sublimation of $\sim$ 7 cm snow from the surface during the summer season. In this section, I compare this estimate with other estimates (observation- and model-based estimates) of surface sublimation rate from the Antarctic interior.

Weller (1969) calculated the surface energy balance at Plateau Station based on measurements of incoming solar radiation and estimates of sensible heat fluxes from the firn. By using a parameterization of sensible and latent heat flux (Bowen ratio), Weller (1969) partitioned the residual energy between sensible transfer from the atmosphere and latent heat release by sublimating snow. This method resulted in estimated sublimation rates of 1 mm per day on sloped faces, and essentially zero sublimation over horizontal snow faces. The difference in sublimation rate between

sloping and flat surfaces results in a net flattening (deflation) of the snow surface. Gow (1965) speculated that this mechanism was responsible for the observed deflation of sastrugi during the summer season at South Pole. Extrapolating the daily sublimation estimates of Weller (1969) over the whole summer season produces a surface lowering of $\sim$ 6 cm, similar to my estimate.

Fujii and Kusunoki (1982) developed a model for surface sublimation or condensation based on eddy diffusion theory, and the difference between vapor pressure at the surface and at 2 meters above the surface at Mizuho Station, Antarctica. The summer atmospheric conditions at Mizuho Station are similar to the windy summer scenario presented above. The diffusive model of Fujii and Kusunoki (1982) showed good agreement with measurements of surface elevation changes at snow stakes. The mean daily sublimation rate during the 1977-78 summer was 0.06 g cm^{-2}. The estimated sublimation rate presented above for windy summer conditions in regions of air inflow was 6.5×10^{-4} kg m^{-3} s^{-1} in the upper 1 cm. This result converts to a daily sublimation rate of 0.06 g cm^{-2}. It should be noted that sublimated vapor in Fujii and Kusunoki (1982) was lost to the atmosphere, while in my model it is advected into the firn. This suggests that (a) surface sublimation as a result of air flow into the firn was not significant during the 1977-78 season at Mizuho Station (possibly due to low surface permeability) and (b) the difference between surface vapor pressure and vapor pressure at 2 m can generate large sublimation rates in windy conditions. Although the direction of the vapor flux differs between my model and that of Fujii and Kusunoki (1982), it is encouraging that the vapor fluxes are of comparable magnitude.

van den Broeke (1997) estimated sublimation rates over Antarctica using a global circulation model. Sublimation in the model was driven by the relative humidity in the lowest atmospheric model layer, and the wind velocity in that model layer. The largest sublimation rates were found in summer in the coastal regions when dry air from the interior descends to lower and warmer elevations. In the interior, the model

predicts sublimation rates of 5 to 10 mm water equivalent per year (1 to 2 cm of snow per year). van den Broeke suggested that the model likely overestimates sublimation rates in the interior because errors in the sea ice parameterization effectively lower the atmospheric relative humidity. However the model results compared well against the limited number of existing observations of surface sublimation rate (mostly from coastal sites).

Bintanja (2001) compared the importance of surface sublimation and snowdrift sublimation through measurements of the surface energy balance in East Antarctica (elevation 1200 m.a.s.l.). This study inferred the latent heat release at the snow surface as a function of time from measurements of relative humidity, other measured components of the surface energy balance and estimates of the friction velocity. He found that surface sublimation during the study period accounted for a latent heat release of 1.2 cm of water equivalent (2.5 cm of snow) during the summer season.

By using a rayleigh-distillation model for stable isotope exchange at the snow surface, Satake and Kawada (1997) inferred that sublimation removed 30-35% of accumulated snow at a site near Mizuho Station. Since the average accumulation rate at Mizuho station is $\sim$ 12 cm of snow per year, sublimation could remove as much as 4 cm of snow per year.

The disagreement between my estimate of near surface sublimation (based on the atmospheric relative humidity and mass-exchange theory) and other estimates (including several based on radiative transfer) could be due to several different causes. For example, my model assumes that both the air-flow velocity and atmospheric relative humidity are constant in time. In fact, surface wind variations cause variation in the subsurface air-flow velocity. Further, measurements by Bintanja (2001) showed that, during periods of very light winds, the near surface relative humidity essentially reached the saturation point, eliminating the vapor pressure difference that drives surface sublimation. Although the atmospheric relative humidity and the wind speed are generally independent, during periods of light wind they are strongly correlated.

My model estimates of the surface sublimation rate (and associated surface lowering) compare favorably with other published estimates and measurements.

3.8.7 Cumulative Effects

This model predicts subsurface water-vapor motion assuming that the surface topography is stationary; firn microstructure, wind speed and surface temperature do not change with time; and no snow accumulates at the surface. In order to determine the cumulative mass exchange experienced by a parcel of firn over several seasons, it is necessary to reconsider these three assumptions, as they can influence the pattern and magnitude of the subsurface mass exchange rate and the time a parcel of firn is exposed to rapid mass exchange.

Topographic surface perturbations (such as sastrugi) cause surface pressure perturbations in the presence of wind, which drives air flow through the firn (Section 3.3). The locations of the topographic perturbations determine regions of inflowing and outflowing air. Consequently, variations in sastrugi location from year to year will cause the location of inflowing and outflowing air to vary. A parcel of snow may be affected by sublimation one summer (as a result of outflowing air), and by condensation the next (as a result of inflowing air). In this case, the net cumulative subsurface mass exchange over several years would be more difficult to calculate than if the surface bumps were stationary in time. Gow (1965) showed that bump amplitudes increase during winter at South Pole, and decrease in summer. Weller (1969) showed that the deflation is due to enhanced solar radiation on the sloping bump faces, which results in sublimation, and therefore sastrugi deflation. This process tends to level the surface during the summer months. Albert and Hawley (2002) measured changes in bump amplitude, bump wavelength and wind speed throughout a single year at Summit, Greenland, and showed that these variables vary seasonally. Seasonal variation in surface topography and wind speed will vary the magnitude of subsurface air flow. However, it is not yet known how sastrugi locations vary through time. This is a

potentially important consideration in determining the long-term effects of subsurface mass exchange, and warrants further study.

In this model for vapor motion in firn, I have assumed that the firn microstructure (density, porosity and permeability) does not change with time. Albert and Shultz (2002) showed that firn microstructure at Summit is generally similar from one year to the next, but the details show some changes over time. It is clear that snow grain metamorphism (e.g. Yosida and others, 1955; Colbeck, 1983a) causes water-vapor redistribution in firn, and that grain metamorphism is responsible for changes in firn microstructure. A quantitative understanding of the relationship between water-vapor motion in firn and changes in firn permeability, grain size, density and porosity is lacking. Studies such as Gow (1969) and Albert and Shultz (2002) improve our understanding of how these parameters vary with depth, and how they can be parameterized as functions of depth. McConnell and others (1998) presented results of air-flow modeling for several wind speeds with a buried low-permeability layer. Ultimately, it may be possible to model the development of firn microstructure physically using models for mass and energy conservation at both the grain-scale (1 mm) and sastrugi-scale (1 m), although this level of model sophistication is still in the future.

Through time, surface snow will be buried and advected downward as a result of ongoing snow accumulation at the surface. Based on the above model results, most ventilation-driven mass exchange is confined to the upper 1.5 m. In areas with large accumulation rate, snow will be advected through this region in a single season. On the polar plateau however, typical accumulation rates are $\sim$ 10 cm snow per year. In this case, snow could spend as much as 10 years in regions with rapid mass exchange. As a parcel of firn is advected down through the upper 2 meters, it may pass through zones of both condensation as well as sublimation. In order to determine the cumulative water-vapor motion experienced by a parcel of firn, the magnitude as well as the timing of the precipitation is important.

If we assume that surface bumps form in the same place from year to year, firn microstructure does not change with time and the accumulation rate is constant, we can estimate the cumulative subsurface mass exchange experienced by a parcel of firn. Under regions of air inflow during the summer with strong winds, the average mass exchange rate is -1.7 $\times$ 10^{-7} kg m^{-3} s^{-1} between 0.5 m and 1.5 m depth (Fig. 3.12). Note that a negative mass exchange rate in the model reflects condensation, or a local increase in mass. If the accumulation rate is 10 cm snow per m^2 per year, a 10 cm thick parcel of firn will take 10 years to pass through this zone of rapid mass exchange (neglecting firn compaction processes). The total mass exchange experienced by the parcel of firn is then 0.05 kg per year, if winter mass exchange is neglected. Over 10 years, the parcel increases in mass by 0.5 kg. If the average snow density is 450 km m^{-3}, this additional mass represents a mass increase of only 1%, a very modest change. It is evident from numerous field studies (e.g., Taylor, 1971) that snow density varies with depth by much more than the 1% that this model accounts for. This is no particularly surprising, since other processes such as grain metamorphism and mechanical compaction also change firn density.

Table 3.1: Summary of condensation and sublimation in firn results. Mass-exchange rates expressed in kg m^{-3} s^{-1}. All results for 1 mm grain size. Note that the patterns of sublimation and condensation are reversed in winter and summer. Regions of air inflow exhibit sublimation in winter and condensation in summer.

Season	Wind Speed	Max. Sub. Rate (Depth)	Max. Cond. Rate (Depth)
Winter	10 m s^{-1}	8.2 $\times$ 10^{-9} (1 m)	-2 $\times$ 10^{-8} (0 m)
	5 m s^{-1}	5 $\times$ 10^{-9} (0.5 m)	-8 $\times$ 10^{-9} (0 m)
Summer	10 m s^{-1}	2 $\times$ 10^{-7} (0 m)	-2.5 $\times$ 10^{-7} (1 m)
	5 m s^{-1}	1.2 $\times$ 10^{-7} (0 m)	-1.5 $\times$ 10^{-7} (0.45 m)

3.8.8 Overview of Modeling Results

Table 3.1 summarizes the results of the modeling presented above. In general, sublimation and condensation in the firn result from temperature gradients in the firn coupled with air flow through the firn. Summer mass-exchange rates are larger than winter rates, and as wind speed increases the depth to maximum mass-exchange rates increases. Although not specific to any one location, the above calculations present estimates of sublimation and condensation rates in antarctic firn during summer and winter, under both strong and moderate winds. The results above also demonstrate the sensitivity of condensation and sublimation rate to mean grain size, and point to the need for better measurements of the mass-exchange coefficient. The agreement of my estimates for surface sublimation rate and other published estimates is encouraging, but it should be stressed that my model was not designed to estimate surface sublimation rates, and the results should be treated with caution.

3.9 Limitations/Improvements

This model is well-suited for estimating subsurface mass exchange rates in the firn. In constructing the model and generating the mass exchange rate estimates presented above, I have made a number of assumptions in order to simplify the calculation and consequently, the interpretation of the model output. As a result, the model is appropriate for generating initial estimates of water-vapor motion, but is not appropriate for detailed analysis of a specific site. In order to study a specific site, a number of simple modifications to the model are required:

- Time dependence of firn microstructure. As noted above, in order to determine the cumulative effects of water-vapor motion in the firn, it is important to consider how firn microstructure (e.g. porosity, density, permeability, pore size) changes with time. Changes in microstructure will primarily affect the ventilation velocities.

- Spatial variability of permeability. The permeability of the firn can vary over short spatial scales, as shown by Albert and others (2000). The microstructure and layered nature of the snow and firn can have important effects on the vapor-transport properties in firn (Albert et al., 1996; Davis et al., 1996). The presence of a low-permeability surface windpack can reduce overall ventilation rates in the subsurface, yet the presence of high-permeability buried layers can cause flow channeling, or increased flow in buried hoar layers (Albert, 1996; Colbeck, 1997; McConnell and others, 1998). To use the model to determine mass exchange rates at a specific site, measurements of the permeability tensor K_{ij} should be made, and Darcy's Law should be solved numerically to determine the volumetric air flux in the firn, as in Albert (2002). As discussed in Section 3.3, the analytical expression I used to determine the subsurface flow velocity replicates the results of the more complicated calculation of Albert (2002) for firn conditions at Siple Dome, Antarctica. Other sites could have a significantly different permeability structure such that the analytical expression is a poor estimator of actual subsurface air-flow velocity.

- Grain size. It is apparent from Section 3.8.5 that the grain size is an important component in the mass exchange calculation. It has been shown by many investigators (e.g. Gow, 1969) that grain size generally increases with depth, as a result of firn metamorphism. Consequently, the model should be modified to reflect the variation of effective grain size as a function of depth measured at a given site.

- Inter-particle-vapor flow. Saturation vapor density over ice varies as a function of the radius of curvature of the ice surface (Colbeck, 1980). Consequently, water vapor is transferred from small grains (with large curvature and high vapor densities) to larger grains (with smaller curvature and low vapor densities) as the firn ages. As a result, average grain size increases with depth in the firn and the

number density of grains (number of snow grains per unit volume) decreases with depth (e.g. Gow, 1969). The magnitude of the vapor flux associated with grain growth should be related to the size distribution of new snow and the microstructure of the snow, in particular the average pore size. Sturm and Benson (1997) estimated the inter-particle water vapor flux in a seasonal snowpack by observing the change in the number of grains and the average size of the snow grains through time. They found that the magnitude of the inter-particle vapor flux was more than an order of magnitude smaller than the water vapor fluxes due to temperature gradients in the snow. The model presented here captures the water vapor flux due to temperature gradients in the snow, but neglects the water vapor flow induced by snow grain metamorphism.

- Surface topography. As discussed by Gow (1965) and Weller (1969), the amplitude of the surface topography responsible for subsurface air flow changes markedly throughout the year. Albert and Hawley (2002) also showed that the dominant wavelength of surface topography can change throughout the year. Although subsurface mass exchange rates are largest in summer for a fixed topography, the change of bump height and amplitude through the summer at a site should be considered.

- Wind speed at the surface. This analysis has used a constant wind speed at 10 m height of either 10 m s^{-1} (for strong wind scenarios) or 5 m s^{-1} (for moderate wind scenarios). Although wind speed at a site is often uniform (e.g. Benson, 1971), there can be large variations on short time scales. This model for water-vapor motion in firn should be modified to use wind speed observations at a particular site, when available.

- Surface temperature and relative humidity. The model assumes that atmospheric temperature and relative humidity are constant. Temperature in the

polar regions shows a strong daily cycle during the summer months, when mass exchange rates are largest. Measurements of near-surface relative humidity are more difficult, but existing data (e.g. Bintanja, 2001) suggest that it is tied to wind speed, and can vary on hourly time scales. The vapor-transport model should be modified to incorporate estimates of diurnal temperature variation, as well as any data on atmospheric relative humidity that exist at the site.

- Hand-to-hand diffusion. The model results presented here neglect the possibility of increased vapor diffusivity κ and mass exchange as a result of the so-called hand-to-hand diffusion (Yosida and others, 1955; Colbeck, 1993). The difference in thermal conductivity between air and ice leads to an unequal partitioning of the macro-scale temperature gradient in firn. Since the thermal conductivity of air is smaller than that of ice, temperature gradients across pore spaces are large, leading to larger than expected vapor-pressure differences across pore spaces. The large vapor-pressure gradient results in faster vapor diffusion through pore spaces. The high thermal conductivity of ice allows vapor to be absorbed on one side of an ice grain and vapor to be released on the opposite side (hence the term 'hand-to-hand'). Colbeck (1993) presented a particle-to-particle model and summarized other studies (e.g. Yosida and others, 1955) and showed that vapor may diffuse through snow up to 5 times faster than through air, depending on the ice-grain geometry in the snow. The vapor model presented here does not use an enhanced water vapor diffusivity. The diffusivity of water vapor in firn is equal to the diffusivity of water vapor in air, scaled by the firn density, as in Whillans and Grootes (1985). The implications of hand-to-hand diffusion are further analyzed in Chapter 5.

The model presented here can easily be modified to make use of additional information available at a specific site. The results provide an initial estimate of the expected magnitude of sub-surface sublimation and condensation rates in Antarctic

firn. In the following chapters I use the mass-exchange rates generated above to study the impact of firn ventilation on geochemical species in the firn. The results presented in this dissertation should be taken as an initial estimate of the importance of firn ventilation on snow geochemistry, rather than as a prediction for a particular site.

As noted above, the model is not well-suited to predict surface vapor exchange with the atmosphere. Radiative transfer theory can be used to model the surface energy balance (e.g. Clow, 1987) and calculate near-surface mass exchange. But these methods are not able to determine mass exchange rates as a function of depth. It is possible to combine these two approaches to produce a complete model of energy conservation and water-vapor motion in the upper few meters of the firn. Explicitly accounting for both short- and long-wave radiative fluxes in this model of water motion in firn would require modifying both the upper boundary condition (Section 3.6) and the way the source term is calculated (Appendix E). Explicitly adding the surface energy balance terms to this model would also require knowledge of several other environmental parameters such as optical depth of snow and scattering coefficients if the model is to be applied at a specific site.

3.10 Summary and Conclusions

Using conservation of mass and energy I constructed a model of water-vapor motion in the firn that resembles the model of Albert (2002). However, as discussed above, my model uses a different solution technique, a different method of calculating air-flow velocities (Section 3.3) in the firn, a different method of calculating saturation vapor density (Appendix E), and makes a number of other simplifying assumptions. My model includes water vapor diffusion along vapor pressure gradients as well as the advection of water vapor by air flow through the firn. Subsurface air-flow velocity was calculated using the methods of Colbeck (1989) and Waddington and others (1996). Analysis of results demonstrate the following:

- Large subsurface mass exchange rates are found where temperature gradients are large, usually around 1 m depth. Air flowing into the firn reaches local saturation vapor pressure in the upper 1 cm of the firn. Consequently, atmospheric relative humidity has a negligible effect on mass exchange rates below the uppermost cm. The primary importance of firn ventilation is to alter temperature gradients in the firn, rather than to carry large (or small) vapor pressures from the atmosphere into the firn.

- In general, mass exchange rates are much larger during summer than winter. This is primarily due to the strong temperature dependence of water vapor pressure over ice (Equation (E.1)). Consequently, winter exchange can be neglected when studying the cumulative effects of subsurface water-vapor motion on time scales longer than 1 year.

- The mass exchange rate is strongly influenced by the mean size of snow grains in the firn. Large grains have lower instantaneous mass exchange rates, which allows differences between local vapor pressure and saturation vapor pressure to persist. This results in larger mean mass exchange rates for larger grains. Small grains have a larger surface area per m^{-3} of firn than large grains, allowing for more rapid mass exchange and cause air in firn pore spaces to essentially always be saturated.

- The model results presented here are estimates for environmental conditions typical on the Antarctic plateau. In order to apply the model to a specific site, the model should be adapted to make use of measurements of surface temperature, wind speed, surface topography, accumulation rate, grain size as a function of depth and the two-dimensional permeability.

- Firn microstructure is an important aspect of sub-surface water vapor transfer

that has not been examined in detail in this thesis. In particular, the coupling between snow grain metamorphism and firn ventilation should be studied in more detail. The inter-particle water vapor flux due to snow grain metamorphism is a potentially important part of post-depositional geochemical change. Initial estimates based on the change in the number density and size distribution of snow grains as a function of depth suggest that water vapor flow due to grain metamorphism contribution is much smaller than the water vapor flow due to firn ventilation. However, grain metamorphism will also cause changes in firn microstructure that will in turn affect firn ventilation. In particular the permeability, porosity (and average pore size) and density of the firn all may change as a result of grain metamorphism. When using the model presented here, care should be taken to insure that values of average grain size, porosity, density and permeability are all self-consistent. A more complete model should allow the firn microstructure to change through time as a result of grain metamorphism.

The following chapters use the model of subsurface water-vapor motion presented above to assess the effects of firn ventilation on snow geochemistry. The next chapter examines changes in stable isotope ratios in snow as a result of subsurface water-vapor motion, and following chapters explore changes in irreversibly- and reversibly-deposited species.

Chapter 4

EFFECTS OF FIRN VENTILATION ON ISOTOPIC EXCHANGE

Material from this chapter was presented under the title 'A two-dimensional model of post-depositional changes in stable isotope ratios in polar firn' at the American Geophysical Union 2002 Fall Meeting with co-author E.D. Waddington (University of Washington)

4.1 Summary

A new model to calculate isotopic diffusion in the upper few meters of firn is presented. The model tracks the isotopic composition of both the solid ice matrix and the pore-space vapor through time in a two-dimensional section. Stable isotopes in the vapor phase move through the firn as a result of diffusion along concentration gradients and advection due to firn ventilation. Ventilation carries atmospheric water vapor into the firn where it mixes with existing pore-space vapor. The model uses a function for equilibration between pore-space vapor and the surrounding snow grains, unlike other models that assume the two phases are in equilibrium. The model also calculates the isotopic effects of ventilation-driven sublimation and condensation in the firn. Model predictions of isotopic diffusion in firn compare favorably with existing diffusion models, although it likely underestimates effective diffusivity. Model results quantify what other investigators have suggested: isotopic diffusion in the upper few meters is more rapid than can be explained by the Whillans and Grootes (1985) model; isotopic equilibration with atmospheric vapor is an important component of post-depositional isotopic change; and ventilation enhances isotopic exchange by creating regions of relatively rapid sublimation and condensation in the firn.

4.2 Introduction

Stable isotope ratios recorded in polar snow can be related to the condensation temperature of the original snow grains (Dansgaard, 1964, Jouzel and others, 1997). Variations in temperature are recorded in successive layers of snow as variations in the stable isotopic ratios of the snow. Through time, isotopic diffusion modifies the isotope profile in snow and destroys high-frequency information. Recent work has focused on reconstructing the original isotopic ratios in snow from the diffused records collected in the field (e.g. Cuffey and Steig, 1998; Bolzan and Pohjola, 2000). Reconstructing the original records requires an understanding of the processes involved in isotopic diffusion.

Prior work on stable isotope diffusion in firn (e.g. Whillans and Grootes, 1985) recognized that diffusion through the vapor phase is the most important process in redistributing isotopes in the firn. In order to predict isotopic changes in snow as a result of diffusion through the vapor phase, prior studies have generally assumed that the pore-space vapor and the surrounding snow grains are in isotopic equilibrium. This assumption allows for an analytical model of isotopic diffusion in the firn, originally presented by Johnsen (1977) and simplified by Whillans and Grootes (1985). Other studies (e.g., Cuffey and Steig, 1997; Johnsen and others, 2000) have modified this model, but have not substantially changed the theory of Whillans and Grootes (1985). Results of these models show broad agreement with observations of isotopic profiles in firn, but do not illustrate the underlying physical processes.

Rather than parameterizing isotopic changes in the firn, my new model is a step towards a physically-based time-dependent model of stable isotopic change in firn. The model tracks the evolution of the isotopic composition of both the pore-space vapor and the firn in a two-dimensional cross-section of the firn. Isotopes are redistributed in the firn as a result of: (a) advection of atmospheric vapor (with a specified isotopic composition) as a result of forced air flow through the firn (ventilation or wind

pumping; Clarke and others, 1987), (b) transport (diffusion) along isotopic gradients in the pore-space vapor, (c) isotopic equilibration between vapor and solid and (d) sublimation and condensation in the firn. Throughout this work, 'condensation' refers to the vapor $\rightarrow$ solid phase change, and 'sublimation' refers to the reverse process solid $\rightarrow$ vapor.

A key difference between this model and prior work is in how isotopes are exchanged between phases. Prior work has assumed that pore-space vapor and surrounding snow grains are in isotopic equilibrium; this model allows for isotopic equilibration between the phases through time, but does not assume that equilibrium is reached.

4.3 Model For Post-depositional Stable Isotopic Change

Changes in stable isotope ratios are tracked in a two dimensional slice of firn through time. Unlike earlier models of stable isotope change in firn which are analytical (e.g. Whillans and Grootes, 1985), this is an iterative numerical model.

The isotope model requires estimates of the firn temperature and vapor density in the firn pore spaces. Both are calculated using a model similar to Albert (2002) described in detail in Chapter 3. Isotopic ratios of both the solid ice and the pore-space vapor are calculated on the same grid as the temperature and vapor density fields (Chapter 3). Throughout the paper, x refers to the horizontal coordinate and z is the vertical coordinate.

The isotopic composition of the ice matrix (δ_i) is modified by sublimation and condensation in the firn and isotopic exchange between the pore-space vapor and surrounding ice grains. The model neglects isotopic diffusion through the ice matrix (since diffusion through the solid is several orders of magnitude smaller than diffusion through the firn) or along quasi-liquid surface layers (since the thickness of this layer is very small (a monolayer) at temperatures typical on the Antarctic plateau (T <

-30°C)).

Three different mechanisms change the isotopic composition δ_v of the vapor: (a) firn ventilation, which includes advection of pore-space vapor and diffusion along isotopic gradients in the vapor, (b) isotopic equilibration between the vapor and the surrounding ice matrix, and (c)phase changes (both sublimation and condensation) in the firn.

Before describing the algorithm used to calculate the evolution of δ_v, I first present a brief outline of the procedure used to account for each of these distinct physical processes.

a. Firn Ventilation: Atmospheric vapor is advected through the firn as a result of firn ventilation. The subsurface air-flow fields are calculated following the methods of Colbeck (1989) and Waddington and others (1996), as described in Chapter 3. Air flow through the firn not only advects atmospheric vapor into the firn, but also provides a mechanism to transport pore-space vapor rapidly in the upper 1.5 m of the firn. I also assume that isotopes in the pore-space vapor diffuse along isotopic gradients in the vapor.

Following these assumptions, the change in the isotopic composition of the vapor is given by the conservation equation (Appendix F):

$$\frac{\partial}{\partial t}\delta_v^a + \nabla \cdot (\delta_v^a \vec{\mathbf{u}}) - \nabla \cdot (D_s \nabla \delta_v^a) = 0 \,, \tag{4.1}$$

where δ_v^a is the isotopic composition of the vapor under process 'a' (firn ventilation), D_s is the isotopic diffusivity of the pore-space vapor through snow and $\vec{\mathbf{u}}$ is the 2-dimensional subsurface air flux.

I use the assumptions of other investigators (Whillans and Grootes, 1985; Cuffey and Steig, 1998) and calculate the isotopic diffusivity in pore-space vapor D_s as:

$$D_s = D_a \left(1 - \frac{\rho_{snow}}{730}\right) \,, \tag{4.2}$$

where ρ_{snow} is the snow density expressed in kg m^{-3} and D_a is the diffusivity of water

vapor in air expressed in $m^2\ yr^{-1}$ and is given by (Geiger and Poirer, 1973)

$$D_a = 0.0371\, T^{1.75} \tag{4.3}$$

where T is the firn temperature expressed in K. Colbeck (1993) suggested that D_s is $\sim$ 5 times greater than D_a as a result of the so-called 'hand-to-hand diffusion' of water vapor, where snow grains act to reduce the path length for diffusion and increase temperature gradients across pore spaces. Cuffey and Steig (1998) argue that, in isotope studies, the ice matrix acts as a passive obstruction, and an enhancement to D_s is not warranted.

These assumptions allow isotopes to diffuse independently from the diffusion of water vapor along vapor-density gradients described in Chapter 3. I have not distinguished between the slightly different diffusivities of the heavy and light isotopes of either oxygen or hydrogen. I have also neglected the effect of air pressure on isotopic diffusivity in snow (Cuffey and Steig, 1998), which causes D_s to increase with decreasing air pressure.

b. Isotopic Equilibration: This model allows for isotopic exchange between the pore-space vapor and the surrounding ice matrix, unlike other studies (e.g. Whillans and Grootes, 1985; Johnsen and others, 2000) which assume the two phases are in isotopic equilibrium. The equilibration function I use assumes that the condensed phase is an essentially infinite reservoir of the minor isotope (Ingraham and Criss, 1998):

$$\delta_v^b(t) = \delta_{eq} + \left(\delta_v^{b\,0} - \delta_{eq}\right) e^{-kt}\,, \tag{4.4}$$

where k is the equilibration rate constant, t is time, the superscript 0 refers to an initial value at $t = 0$, the superscript b refers to isotopic composition as a result of process 'b' (isotopic equilibration) and δ_{eq}, the isotopic composition of the equilibrium vapor, is given by

$$\delta_{eq} = \frac{\delta_i}{\alpha} + 1000\left(\frac{1}{\alpha} - 1\right)\,, \tag{4.5}$$

where δ_i is the isotopic composition of the surrounding ice grains and α is the temperature-sensitive fractionation coefficient. The factor of 1000 is a result of the definition of the δ scale (Criss, 1999, p. 31).

Equation (4.4) is used to predict how the isotopic composition of the solid and vapor evolves in time steps of Δt. By comparing the initial and final isotopic composition of the vapor, and using information about control volume size, porosity and vapor density (an exponential function of temperature, Appendix E), I determine the number of heavy and light isotopes exchanged between phases in a given time step. This procedure calculates the changes in the isotopic composition of both the pore-space vapor and the surrounding ice matrix. This is similar to the approach outlined in Johnsen and others (2000) and is described in detail in Appendix G.

The equilibration constant k has not yet been measured for isotopic exchange between ice and water vapor at any temperature. This model assumes that the condensed phase represents an $\sim$ infinite reservoir of the minor isotope. Consequently, I assume that k is primarily related to the time required for the pore-space vapor to equilibrate, and so is determined by the water vapor diffusivity in snow. Epstein and Mayeda (1953) measured the isotopic equilibration between CO_2 gas and liquid water at 25°C. They found that k for this process was $\sim 2.85\ hr^{-1}$. Based on the ratio of the diffusivities for CO_2 gas and water vapor at 25°C (Massmann, 1998), I estimate that k for isotopic exchange between water vapor and liquid water may be $\sim 5\ hr^{-1}$. By assuming a linear relationship between k and saturation vapor pressure (where saturation vapor pressure and $k = 0$ at absolute zero), I estimate that k may be ~ 1. In the following calculations, I used a range of k from 0.1 to 5 hr^{-1}. This estimate neglects the effects of the geometry of the condensed phase (Ingraham and Criss, 1993), the ambient pressure and the impurity concentration of the condensed phase (Criss, 1999, p. 145) on the equilibration constant k. Laboratory measurements

are needed to determine an appropriate range of k for use in isotopic studies at low temperature.

c. Sublimation / Condensation: The model also includes the isotopic effects of sublimation and condensation in the firn. The phase-change field is calculated as described in Chapter 3 using the governing equations of Albert (2002). In short, sublimation and condensation in the firn are the result of the interaction between firn temperature and the local relative humidity in the firn. If air flow through the firn (ventilation) brings cool and relatively dry pore-space air into a warmer area, the pore space air will be under-saturated, and some of the surrounding ice will sublimate. Conversely, if vapor is advected from a warm area into a cooler area, the pore-space air will be super-saturated and some of the vapor condenses onto the surrounding snow grains.

In the isotope model, vapor derived from sublimating snow grains has the same isotopic composition as the solid. In this way, sublimation changes the isotopic composition of pore-space vapor, but does not change the composition of the remaining snow grains directly. However, condensation has isotopic implications for both the solid and the vapor phases. I assume that condensation in the firn follows a Rayleigh process and the condensate forms in isotopic equilibrium with the vapor as in Dansgaard (1961):

$$\delta_{\mathrm{c}}(\Delta t) = \left(\delta_{\mathrm{v}}^{\mathrm{c}\,0} + 1000\right) \frac{1-\beta(\Delta t)^{\alpha}}{1-\beta(\Delta t)} - 1000 \tag{4.6}$$

where δ_{c} is the isotopic composition of the condensate, the superscript 0 denotes an initial value at the beginning of the time step of Δt, the superscript c refers to the isotopic composition of the vapor as a result of process 'c' (sublimation or condensation) and β is the fraction of the vapor remaining at the end of the time step. δ_{i} is updated using a mass-weighted average of the isotopic composition of the pre-existing ice in the control volume and δ_{c}:

$$\delta_{\mathrm{i}}(\Delta t) = \frac{\delta_{\mathrm{i}}^{0} M_{\mathrm{i}} + \delta_{\mathrm{c}} M_{\mathrm{c}}(\Delta t)}{M_{\mathrm{i}} + M_{\mathrm{c}}(\Delta t)}\,, \tag{4.7}$$

where the superscript 0 denotes an initial value, M_{i} is the initial mass of the ice and M_{c} is the mass of the condensed vapor. The masses of both the ice matrix and vapor are updated accordingly. This model assumes fast diffusion in the ice grains (e.g. Whillans and Grootes, 1985; Chapter 2), such that grains have uniform δ_{i}. This is in contrast to the model of Rempel and Wettlaufer (in press), which tracks changes in the radial distribution of stable isotopes in individual snow grains. M_{c} is a function of the condensation rate and the time step Δ t. The time scale to radially equilibrate 500 μm grains during the summer ($T \sim$ -20°C) is $\sim$ 20 days (Whillans and Grootes, 1985), the time scale for equilibration in the winter is longer ($\sim$ 100 days). Consequently, the assumption of homogeneity is only valid during the summer.

Under these assumptions, the isotopic composition of the remaining vapor is found from (Dansgaard, 1961):

$$\delta_{\mathrm{v}}^{\mathrm{c}}(\Delta t) = \left(\delta_{\mathrm{v}}^{\mathrm{c}\,0} + 1000\right)\left(\beta(\Delta t)^{\alpha-1}\right) - 1000\,. \tag{4.8}$$

If pore-space vapor is in isotopic equilibrium with the surrounding snow grains, small amounts of condensation will not change the isotopic composition of the solid, as the initial condensate will have the same isotopic composition as the surrounding snow grains.

The isotopic change to $\delta_{\mathrm{v}}^{\mathrm{c}}$ as a result of sublimation and condensation can be summarized as:

$$\delta_{\mathrm{v}}^{\mathrm{c}\,1}(\Delta t) = \begin{cases} \left(\rho_{\mathrm{v}}^{0} + s\right)^{-1}\left(\delta_{\mathrm{v}}^{\mathrm{c}\,0}\rho_{\mathrm{v}}^{0} + \delta_{\mathrm{i}}^{0} s\right) & \text{if } s > 0\,(\text{sublimation}) \\ \left(\delta_{\mathrm{v}}^{\mathrm{c}\,0} + 1000\right)\left(1 + s\rho_{\mathrm{v}}^{-1}\right)^{\alpha-1} - 1000 & \text{if } s < 0\,(\text{condensation}) \end{cases} \tag{4.9}$$

where ρ_{v} is the vapor density in the pore space and s is the sublimation or condensation rate times the time step Δt. This model assumes that kinetic effects at the

grain surface (such as rapid condensation leading to large isotopic gradients within an individual grain) can be neglected. The condensation and sublimation rates predicted by my firn model (Chapter 3) cause very small changes in the grain radius.

Equation (4.1) is solved using the 2-D control-volume theory of Patankar (1982) on the same two-dimensional grid as was used to calculate the temperature and vapor-density fields. Since there are multiple processes that influence both δ_v and δ_i in a given time step, I iterate between each module to produce a self-consistent solution for a given time step.

I calculate an initial estimate (δ_v^1) of δ_v using Equations (4.1), (4.4) and (4.9) and the values of δ_v and δ_i from the prior time step (δ_v^0 and δ_i^0). Taking the difference between δ_v^0 and each estimate of δ_v^1, I generate a set of corrections to δ_v^0: δ_v^a, δ_v^b, δ_v^c). A second set of corrections is then found by replacing δ_v^0 with $\delta_v^0 + \delta_v^b + \delta_v^c$ in the solution algorithm for Equation(4.1); replacing δ_v^0 with $\delta_v^0 + \delta_v^a + \delta_v^c$ in Equation (4.4); and replacing δ_v^0 with $\delta_v^0 + \delta_v^a + \delta_v^b$ in Equation (4.9). By iterating in this fashion, I generate a final converged estimate of (δ_v^1) which is consistent among Equations (4.1), (4.4) and (4.9) over a single time step. The model converges rapidly, and using more than 3 iterations changes the estimate of δ_v^1 by less than 5×10^{-7} ‰.

The value of δ_i^1 is calculated in a similar fashion between the two processes outlined above for changes to δ_i (sublimation/condensation and isotopic equilibration). δ_i^1 is much less sensitive to errors than δ_v^1, and the value of δ_i^1 converges to similar accuracy after only 2 iterations.

This isotopic model requires several boundary conditions in addition to those needed for the heat and vapor-transport models described in Chapter 3. I assume that there is no isotopic exchange across the left, right or bottom boundaries of the solution domain. I also assume that the atmospheric vapor has a known isotopic composition and vapor density; these can either be constant or time dependent.

4.4 *Results*

The numerical model is run at 1 second temporal resolution until initial transients in δ_v have died out, which takes around 20,000 model seconds (around 5.5 model hours). Beyond this point, isotopic changes in both the vapor and the solid change in a uniform manner. The model is used primarily to calculate the isotopic composition of the solid as a function of time, although other ancillary parameters are calculated as well, such as δ_v, δ_c and the total mass exchanged between phases. Here I present model results for changes in $\delta^{18}O$. The model could also be used to calculate changes in δD by changing the appropriate parameters (fractionation coefficient α, and diffusivity D_s).

Other models (e.g. Cuffey and Steig, 1998) are analytical and generally make use of an effective isotopic diffusivity. The effective isotopic diffusivity D_f accounts for isotopic diffusion through the vapor phase and isotopic exchange between phases. This parameter describes how a stable isotope profile in the firn will diffuse as a result of several processes. In order to compare the results of my numerical model with analytical models I use a simple diffusion equation:

$$\frac{\partial \delta}{\partial t} = D_f \frac{\partial^2 \delta}{\partial z^2}\,, \tag{4.10}$$

where D_f is the effective isotopic diffusivity. This equation has a well-known solution:

$$\delta(z,t) = \bar{\delta} + \sum_{n=1}^{\infty} A_n \exp\left(-(n\pi)^2 D_f\, t\right) \sin(n\pi z) \tag{4.11}$$

where $\bar{\delta}$ is the mean isotopic composition and A_n are the Fourier coefficients for the initial profile. I use an initial sinusoidal $\delta^{18}O$ pattern in the firn with a 10 ‰ amplitude, mean $\delta^{18}O$ = -30 ‰ and a 0.25 m wavelength. This roughly corresponds to conditions on the Antarctic plateau. The snow density used in model runs presented here was 350 kg m^{-3}.

By using Equation (4.11) over the same total elapsed time t, and varying D_f until the analytical and numerical model results match, I determine the effective isotopic diffusivity of the numerical model.

4.4.1 Simplified Diffusion Model

I ran several simplified simulations to calculate the change in stable isotope ratios of the firn as a result of transport through the vapor phase and isotopic equilibration between solid and vapor. In these runs, firn temperature is uniform (= -30° C), air flow velocities in the firn are set to zero, and there is no exchange as a result of vapor density gradients (i.e. no condensation or sublimation in isothermal snow). The model was run with a time step of 1 second for 2×10^4 seconds, with 0.01 m vertical resolution, and 0.06 m horizontal resolution.

Using the best-guess value for the isotopic equilibration coefficient ($k = 3$ hr^{-1}) leads to an effective isotopic diffusivity D_f in the firn of 3×10^{-5} m^{2}yr^{-1}. This estimate is somewhat smaller than the isotopic diffusivity used by Johnsen and others (2000) for equivalent temperature and snow density ($D_f = 5.5 \times 10^{-5}$ m^2 yr-1).

As discussed above, there is considerable uncertainty in the value of k. Figure (4.1) shows the dependence of D_f on k. The solid line indicates the most likely range of k for isotopic equilibration between water vapor and snow. The isotopic diffusivity used by Johnsen and others (2000) corresponds to $k = 4.5$ hr^{-1} in the numerical model, at the large end of the scale of plausible values for k.

Diffusivity D_s of pore-space vapor is primarily a function of snow density ρ (Equation (4.2)). In these simplified model runs, I used a number of different values of ρ for a given temperature and k, and found that D_f can be expressed as a linear function of ρ ($r^2 = 0.98$):

$$D_f(\rho) = -8.29 \times 10^{-8} \times \rho + 5.84 \times 10^{-5} \quad (4.12)$$

Other studies (Cuffey and Steig, 1998; Johnsen and others, 2000) also use an air-pressure correction to D_s. I have not used one here. The effect of higher elevation (lower air pressure) is to increase D_s. This correction would improve agreement between D_f of my numerical model and the D_f used in the analytical model of Johnsen and others (2000).

4.4.2 Ventilation - Summer

The model used for calculating temperature, vapor density and mass transfer in the firn is similar to the model of Albert(2002), and is described in detail in Chapter 3. The model solves the coupled equations for heat and water-vapor motion in a 2-D cross-section of the firn. I used this model to determine an approximately steady-state temperature and mass-transfer pattern in the firn corresponding to midsummer conditions with strong winds (Section 3.8.2).

Air flow in the firn is the result of steady wind flow (10 m wind speed = 10 m s^{-1}) over a sinusoidal surface topography typical of the Antarctic interior (wavelength of surface topography = 3 m, surface amplitude = 0.1 m), as in Waddington and others (1996). Air flow velocity vectors are calculated as in Colbeck (1989) and are shown in Figure 4.2. Maximum air velocity is $\sim$ 1 cm s^{-1}.

Firn temperature is shown in Figure 4.3. In regions of air inflow (Fig. 4.2, note air flow is into the firn between 0:0.75 m and 2.25:3 m in the horizontal direction), the near-surface firn is isothermal as a result of the vertical advection of relatively warm air from the atmosphere ($T_{atm} \sim$ -20 °C). In regions of air outflow (Fig. 4.2, between 0.75:2.25 m in the horizontal direction), vertical advection carries relatively cold air from the firn interior towards the surface. Horizontal advection between these two regions helps to create the curved pattern of the isotherms in the upper few meters. Below about 3 m depth, advection is less important, and the temperature field is dominated by conduction, resulting in horizontal isotherms.

The phase-change field is shown in Figure 4.4. Advection of air through tempera-

ture gradients in the firn result in regions of super- and sub-saturated air in the pore spaces. In regions of air inflow, warm saturated air from the atmosphere is advected into the firn. This advected air is super-saturated relative to the cooler firn at depth, resulting in regions of condensation (mass transfer < 0 centered at ~ 1 m depth). In regions of air outflow, relatively cool and dry air from the firn interior is advected into progressively warmer firn near the surface. This air is sub-saturated, resulting in the sublimation of some of the surrounding snow grains. Lateral advection between regions of inflow and outflow coupled with the sinusoidal temperature pattern curves the locus of maximum sublimation toward the surface.

The temperature and phase-change fields are not recalculated in the isotopic diffusion model, but are treated as constant with respect to time. These fields provide an idealized 'snap-shot' of the firn during mid-summer. In order to generate an equivalent 'snap-shot' of isotopic changes in the firn during mid-summer, I ran the isotope model for 20,000 seconds (time step = 1 s, vertical resolution = 0.01 m to 5 m, horizontal resolution = 0.06 m to 4 m). At this point, initial transients in δ_v and δ_i have run their course; δ_v is essentially constant, and δ_i is changing in a uniform manner.

I assume that the isotopic composition of the near-surface atmospheric vapor δ_{atm} is constant and uniform, and is in isotopic equilibrium (Equation 4.5) with the surface snow (Massey, 1995). Air flowing into the firn reaches saturation vapor pressure in the upper few cm (Chapter 3); consequently, I neglect this near-surface mass transfer and assume that air flowing into the firn is at saturation vapor density. In fact, this near-surface sublimation (or condensation) may alter the δ_v of air entering the firn. Consequently, available data on atmospheric relative humidity should be used when applying this model to a specific site.

Air-flow velocities in the firn are negligible below ~ 2 m. Consequently, I expect that below the upper ~ 2 m, isotopic change in the firn will be well-described by a simple diffusion model, such as Equation (4.10).

Predictions of the isotopic change of the firn ($\delta_i^{final} - \delta_i^{initial}$) in regions of maximum

air inflow are shown by the solid line in Figure 4.5. In the lowest meter of the plot (2 to 3 meters depth), the model predicts that changes in δ_i follow a standard diffusion model: both summer and winter snow layers are modified equally, and the mean change is 0. The lower dotted line represents a fit of an analytical model (Equation (4.11)) to the numerical model results. At ~ 2.5 m depth, the effective diffusivity D_f of the numerical model is 3.4×10^{-5} m^2 yr^{-1}. D_f decreases with increasing depth, as shown from 2 to 3 meters in Figure 4.5, because of the effect of the reduced firn temperature on the vapor pressure.

It is apparent that other processes are active in the upper 1.5 m of the firn in Figure 4.5. In the upper 0.5 m, summer layers are not modified, while winter layers are strongly modified, producing an asymmetrical pattern. Investigating the isotopic composition of the pore-space vapor δ_v (Fig. 4.6) reveals that in regions of air inflow, δ_v is strongly influenced by δ_{atm}. δ_{atm} is in equilibrium with the summer layers, and by extension, far out of equilibrium with the winter layers. As this vapor is advected into the firn, isotopic equilibration causes a large change in the winter layers, but relatively small change in the summer layers.

In addition, condensation is an important component of δ_v in regions of air inflow. Condensation preferentially removes heavy isotopes from vapor and decreases δ_v (Equation(4.4)). In the firn, the maximum condensation rate in regions of air inflow (Fig. 4.4, centered at 0 and 3 m horizontal distance) is found at ~ 1 meter depth. The condensate is isotopically more similar to the winter layers than the summer layers, leading to greater changes in the summer layers. In addition, the remaining pore-space vapor is closer to equilibrium with the winter layers than the summer layers, leading to larger changes in the summer layers as a result of isotopic equilibration. However, these two effects are obscured by the effect of δ_{atm} and the large air-flow velocities in the upper 1 m. Gradually, the pore-space vapor becomes more like the vapor in diffusion-dominated systems (e.g. below ~ 2 m).

The equilibration between atmospheric vapor and the near-surface firn in the

upper 1.5 m in regions of inflowing air leads to relatively large values of D_f. The upper dashed line in Figure 4.5 represents the fit of an analytical model (Equation (4.11)) to the numerical model. At 0.5 m depth, the numerical model has an effective diffusivity of 1.2×10^{-4} m^2 yr^{-1}; this is 50% higher than D_f in a diffusion-only case at an equivalent temperature.

As air flow velocities decrease, these other effects become more important. The left panel of Figure 4.7 shows the model predictions for change in δ_i with the same environmental parameters as Figure 4.5, except the 10 m wind speed has been reduced to 5 m s^{-1}. The reduction in wind speed causes a reduction in sub-surface air flow and a corresponding reduced influence of δ_{atm}. The right panel of Figure 4.7 shows δ_v in regions of maximum air inflow (analogous to Figure 4.6). The influence of condensation on δ_i and δ_v can be seen between 0.75 m and 1.5 m depth in the right panel, and 1 m to 1.5 m in the left panel. In these regions, condensation of isotopically light pore space vapor causes greater changes to summer layers than winter layers. This effect was obscured in the strong wind case (Fig. 4.5 and 4.6) due to the advection of atmospheric vapor.

The solid line in Figure 4.8 shows the model prediction isotopic change ($\delta_i^{final} - \delta_i^{initial}$) in the firn in regions of maximum air outflow with 10 m wind speed again = 10 m s^{-1}. Below $\sim$ 2 m, these areas can be well-modelled by a standard diffusion equation; both summer and winter layers are modified equally, and the mean change is 0. The lower dotted line in Figure 4.8 represents the fit of an analytical model (Equation (4.11)) to the numerical results. At $\sim$ 2.75 m depth, the effective diffusivity D_f of the numerical model is 3×10^{-5} m^2 yr^{-1}. By $\sim$ 3.5 m depth, D_f is equivalent between regions of air inflow and outflow. This supports the idea that ventilation effects are not important below $\sim$ 2.5 meters, given the air-flow field in Figure (4.2).

In the upper 1 m, it is evident that winter layers are modified slightly more than summer layers. The reason for the asymmetry can be found by investigating the pore-space vapor (Fig. 4.9). Above 1.5 m, δ_v becomes progressively heavier as a result of the sublimation of surrounding snow grains (Fig. 4.4). Consequently, δ_v more closely resembles vapor in equilibrium with summer layers. Since δ_v is farther out of equilibrium with winter layers than with summer layers, winter layers are modified slightly more through isotopic equilibration. This effect intensifies towards the surface, where sublimation rates are highest. The upper dashed line in Figure 4.8 shows the fit of an analytical model to the numerical model results, and reveals that at $\sim$ 0.5 m depth, D_f is 7.7×10^{-5} m^2 yr^{-1}. Thus, ventilation increases D_f by $\sim$ 20% compared to modelled D_f without ventilation effects at an equivalent temperature.

The increase in the mean δ_v value between 3 m and 2 m in Figure 4.9 is due to the temperature sensitivity of the fractionation coefficient α (Majoube, 1971). This effect is present throughout the entire depth, as a result of the vertical temperature gradient (Fig. 4.3). Above 2 m, the influence of sublimating snow grains causes much greater changes in δ_v. The increase in mean δ_v as a result of the temperature dependence of α is also present in Figure 4.6 below 2.5 m, although condensation (which decreases δ_v) obscures this dependence above 2.5 m.

4.4.3 Ventilation - Winter

As a result of the non-linearity of water vapor pressure over ice, near-surface ρ_v is lower in winter by a factor of 25 compared with summer vapor density and mass transfer rates are as much as two orders of magnitude smaller in the winter than in the summer. Consequently, I expect that D_f is much smaller in winter than in summer.

I used the methods of Albert (2002) to predict temperature and sublimation and condensation rates in the firn using environmental parameters typical of the Antarctic plateau in winter (T_{atm} = -50 °C, δ_{atm} in equilibrium with winter layers). I used the same surface topography and wind speed as the summer case, and the sub-surface air flow velocity is identical to that shown in Figure 4.2. During winter, firn temperature is coldest at the surface and is progressively warmer with depth. Consequently, in

regions of air inflow, cold and relatively dry air from the atmosphere is advected into progressively warmer firn. The pore space air is sub-saturated and sublimation results. The situation is reversed in regions of air outflow, as relatively warm and moist air is advected into progressively colder firn, resulting in condensation. Note that this pattern of sublimation and condensation is the opposite of the pattern in summer (where condensation is associated with air inflow and sublimation is associated with air outflow).

By using an analytic model (Equation (4.11)) for isotopic diffusion, I determined D_f during the winter. In regions of air inflow, in the upper 0.5 m $D_f = 4 \times 10^{-6}$ m^2 yr^{-1}. Summer layers are modified more strongly than winter layers since the advected atmospheric vapor is initially in equilibrium with the winter layers. The pore-space vapor becomes gradually heavier, and by 1 m depth resembles typical pore-space vapor. D_f gradually increases with depth, as temperature increases with depth.

In regions of air outflow, D_f is larger due to condensation (Equation (4.7)), as large as 1×10^{-5} m^2 yr^{-1} in the upper 0.5 m. Condensation in these areas creates progressively lighter vapor. This causes more rapid modification of summer layers, as the remaining vapor is closer to equilibrium with winter layers than summer layers. D_f gradually decreases with depth as condensation rates decrease to $\sim$ 1.5 m depth, and then increase as firn temperature increases with depth.

4.5 Discussion

These results suggest that summer is the most important season for post-depositional isotopic exchange in the firn, as suggested by other investigators (e.g. Waddington and others, 2002). Since temperatures are higher in summer, isotopic exchange is more rapid. However, if the firn model of Albert (2002) and Chapter 3 generate realistic estimates of sub-surface mass transfer in the firn, isotopic exchange during winter and other seasons should not be ignored. In particular, condensation in the firn results in

potentially important isotopic exchange during any season. The condensation rates reported here are for relatively strong winds (10 m wind speed = 10 m s^{-1}) and modest surface topography. Slower winds will decrease condensation rates in the firn, as will flatter surface topography.

If we assume that the above model is representative of isotopic exchange during the summer months, we can estimate what the total change might be during the summer season. As noted above, winter layers are modified more rapidly than summer layers during the summer. In regions of air inflow at $\sim$ 0.5 m depth, this model predicts that winter layers change by 10×10^{-4} ‰ over 20,000 model seconds (0.23 model days). This rate of change would result in a $\sim$ 0.25 ‰ change over a 60 day period. In outflow regions, the rate of change is about 50 % smaller than in inflow regions, leading to a change of $\sim$ 0.1 ‰ during summer. This assumes that the isotopic composition of the atmospheric vapor is constant, which is a poor assumption. In fact, the isotopic composition of the atmosphere is strongly influenced by weather systems, and can change by $\sim$ 10 ‰ in a day (Grootes and Stuiver, 1997).

It is evident that for these environmental conditions, this model predicts that full isotopic equilibration between near-surface winter layers and atmospheric vapor will not be reached. This is supported by the model of Waddington and others (2002) which was based on the characteristic times of the isotopic exchange processes involved. For the environmental conditions used here (T $\sim$ -30°C, 10 meter wind speed = 10 m s^{-1}, accumulation rate 0.25 m yr^{-1}) the model of Waddington and others (2002) predicts that isotopic equilibrium between the firn and the atmospheric vapor will not be reached at any depth, but that some degree of equilibration may exist. As noted by Waddington and others (2002), firn will never actually reach isotopic equilibrium with atmospheric vapor since the δ_{atm} changes more rapidly than the firn can equilibrate, effectively changing the 'target' towards which the firn is equilibrating.

The rate-limiting step for isotopic exchange in the firn is isotopic equilibration

between the pore-space vapor and the surrounding ice grains. It is evident that this model predicts that δ_v is far from equilibrium with the surrounding snow grains (Figs. 4.6 and 4.9). Larger values of k in Equation (4.4) would promote more vigorous exchange between solid and vapor, leading to larger values of D_f. However, full isotopic equilibration between firn and the atmosphere would require unrealistically large values of k. Other models (e.g. Rempel and Wettlaufer, in press) assume isotopic equilibrium at the boundary between the solid and fluid phases (an essentially infinite k between the pore space vapor and the outer-most shell of the ice grain, but with Equation (4.4) modified to account for diffusion in the solid as the rate-limiting step). By considering (among other processes) equilibration with firn (an aggregate of grains with a variety of sizes and shapes), the model presented here obscures the importance of isotopic diffusion within individual grains in favor of a bulk equilibration factor k. In contrast, the model of Rempel and Wettlaufer (in press) considers exchange between the vapor and a grains of a single radius, and so retains grain-scale isotopic information. Consequently, I have limited k for an aggregate of grains, based on the limited data available.

This model represents a first step towards a physically-based model of post-depositional isotopic exchange in polar snow. However, there are a number of limitations that preclude broad application of the results. This is a static model that uses constant values of surface temperature, relative humidity of the atmosphere and δ_{atm}. In practice, all of these variables can vary widely on diurnal timescales or shorter. The model currently provides a 'snap-shot' of idealized changes in the firn at a single point in time.

Consequently, the model cannot accommodate the addition of new snow at the surface. As other investigators have shown (e.g. McConnell and others, 1997a; van der Veen and others, 1999) snow accumulation in Antarctica is episodic and can occur at any time of the year. As snow accumulates at the surface, near-surface layers will be advected down through zones of sublimation or condensation and equilibration in

the upper 1.5 m. Consequently, the accumulation of snow at the surface will change the spatial relationship between the isotopic profile in the snow (which is advected downwards relative to the snow surface) and regions of rapid phase change (which are a function of surface topography and wind speed, but remain at a fixed depth relative to the snow surface).

Modelling the ongoing compaction and densification in the firn will also be an important component of an improved model of post-depositional isotopic change in the firn. As noted by several investigators (e.g. Johnsen, 1977; Cuffey and Steig, 1998; Rempel and Wettlaufer, in press), strain decreases the wavelength of isotopic signals through time. Decreasing the wavelength of δ will increase D_f by increasing the spatial gradient of the pore-space vapor, leading to greater diffusive fluxes. In addition, metamorphic processes (such as grain boundary sliding and grain growth) act to increase firn density through time. The increased density will decrease D_f by decreasing diffusive vapor fluxes (Equation (4.2)). This model uses a uniform density profile in the firn and a uniform wavelength of δ.

There is also uncertainty in several of the model parameters. As discussed above, there is large uncertainty in appropriate values of k. In addition, uncertainty in D_s could arise from errors in D_a, which is ultimately based on the work of Geiger and Poirer (1973) and used by several studies, e.g. Whillans and Grootes (1985), Cuffey and Steig (1998) and Johnsen and others (2000). D_a is converted to diffusivity in snow (D_s) by considering the blocking effect of increasing density on water vapor motion in firn. Cuffey and Steig (1998) showed that, for their model, using a critical density of 730 kg m^{-3} in the denominator of Equation (4.2) provided the best match to observations. Other authors (e.g. Whillans and Grootes, 1985) use a larger value, 830 kg m^{-3}. In the model results presented here, I used the critical density of Cuffey and Steig, 1998. Using a larger value for the critical density would increase D_s for a given snow density, and therefore increase D_f. However, this is a fairly small effect and increasing the critical density from 730 kg m^{-3} to 830 kg m^{-3} increases D_f by $\sim$

5 %.

Although isotopic diffusion in the firn is a slow process, the cumulative effects are large. In low accumulation-rate areas, snow remains in the near-surface ventilated zone where isotopic exchange is relatively rapid for many years. It seems likely that winter snow will be modified more so than summer snow, leading to an apparent truncation of the winter portion of the annual δ cycle in snow. If this is correct, it may not be possible to distinguish this type of post-depositional isotope change from the wind-scour model proposed by Fisher and others (1983). Fisher noted that an isotope record from a windy divide site at Agassiz ice cap was apparently missing much of the winter precipitation, based on comparisons with the isotope record from the adjacent flank site, which is much less windy. In the isotope model presented here, stronger winds will lead to larger D_f by increasing the flux of water vapor from the atmosphere into the snow. Equilibration with atmospheric vapor will tend to reduce the amplitude of winter layers, which is also the effect of the wind scour model of Fisher and others (1983). Unless accounted for, either wind scour or the post-depositional asymmetric isotopic change suggested here could lead to erroneous reconstruction of the magnitude of seasonal precipitation or temperature variations.

4.6 Conclusions

This model represents a step towards a process-based understanding of post-depositional stable isotope change in the firn. The model results confirm what other investigators have suggested: that isotopic diffusion in the upper few meters is more rapid than can be explained by the Whillans and Grootes (1985) model, isotopic equilibration with atmospheric vapor is an important component of post-depositional isotopic change (Waddington and others, 2002) and that firn ventilation can enhance isotopic exchange (Neumann, 2001).

If ventilation effects are neglected (no air flow, sublimation or condensation), the

effective diffusivity D_f of this model broadly agrees with other models (e.g. Johnsen and others, 2000). This model suggests that isotopic equilibrium between the pore-space vapor and surrounding snow grains is rarely achieved, in contrast to the assumption of equilibrium in other parameter-based models (such as Cuffey and Steig, 1998). The proven success of these models may be due in part to tuneable parameters such as tortuosity (Johnsen and others, 2000) or critical density (Cuffey and Steig, 1998). This model may be lacking some mechanisms of vapor exchange (such as grain growth) that would increase D_f and improve agreement with Johnsen and others (2000). The disagreement could also be due in part to the large uncertainty in k (Equation (4.4)). It is unlikely that k is large enough to allow equilibrium between phases, but increasing k to 4.5 hr^{-1} would allow this model to match the effective diffusivity of Johnsen and others (2000). Another approach (taken by Rempel and Wettlaufer, in press) is to assume equilibrium between the ice grain surface and the surrounding pore-space vapor, and treat diffusion within the ice grains as the rate-limiting step.

Future model development will focus on reducing the uncertainty in k, and including model kinematics to account for the effects of snow accumulation, grain metamorphism and strain. In addition, isotopic inhomogeneities within individual snow grains may be important and their influence on isotopic diffusion in the firn should be examined further.

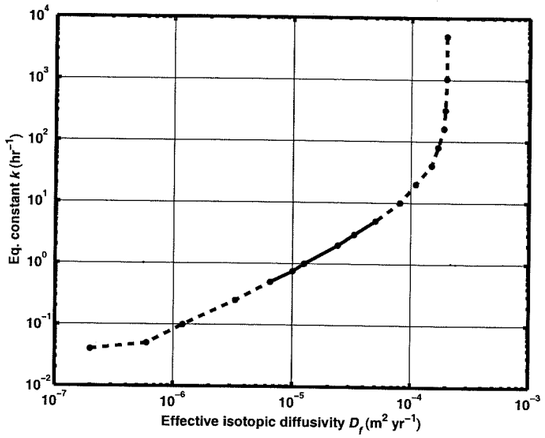


Figure 4.1: Effective isotopic diffusivity D_{f} (m^2 yr^{-1}) as a function of isotopic equilibration coefficient k (hr^{-1}). In this model run, firn temperature is uniform (= -30° C), ρ_{snow} = 600 kg m^{-3}, air-flow velocities in the firn are set to zero, and exchange as a result of vapor density gradients are neglected (i.e. no condensation or sublimation). Although the value of k between snow and water vapor is uncertain, I expect $0.1 \leq k \leq 5$ hr^{-1}; this range is indicated with the solid line.

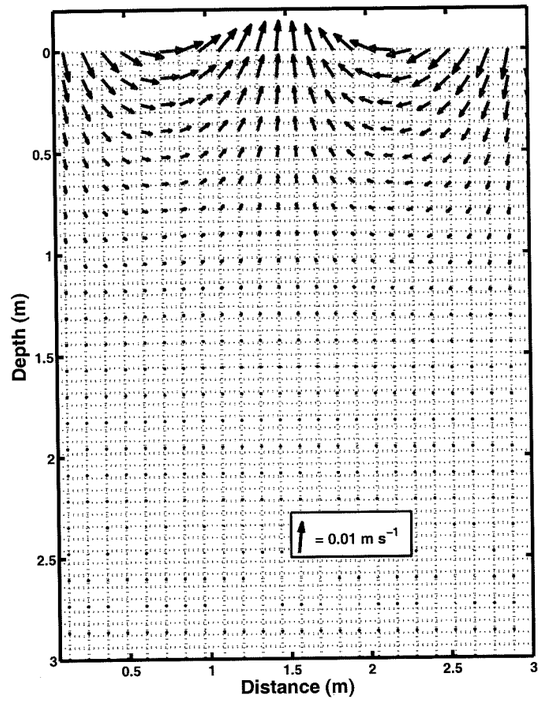


Figure 4.2: Air flow in the firn (ventilation) is the result of steady wind flow (10 m wind speed = 10 m s^{-1}) over a sinusoidal surface topography (wavelength of surface topography = 3 m, surface amplitude = 0.1 m). Air-flow velocity vectors are calculated as in Colbeck (1989) and Waddington and others (1996), and have a maximum value of 0.01 m s^{-1}. Air flows into the firn between 0:0.75 m and 2.25:3 m in the horizontal direction, and out of the firn between 0.75 and 2.25 m. Note that air-flow velocities are calculated on a rectangular grid, rather than along the actual sinusoidal snow surface. Cunningham and Waddington (1993) showed that this is a reasonable approximation as long as the aspect ratio of the bumps is < 1.

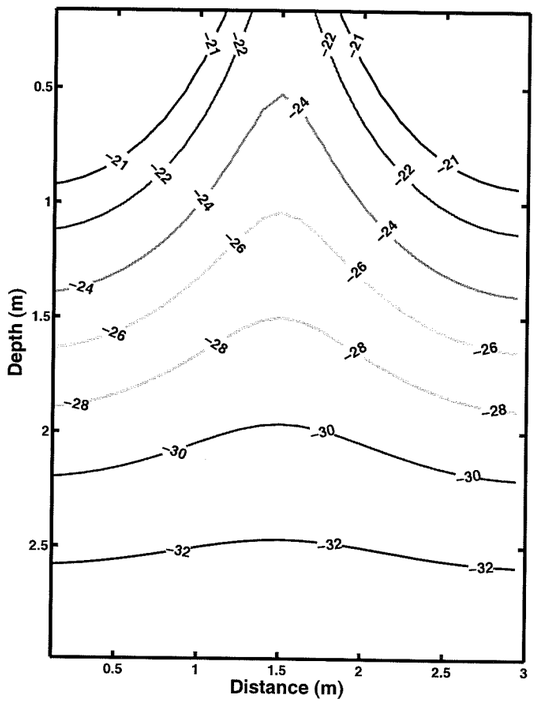


Figure 4.3: Contours of near-surface firn temperature (in °C) with sub-surface air flow as in Figure 4.2 calculated with environmental conditions typical of Antarctic summer. Firn temperature is calculated using a model similar Albert (2002). Near-surface isothermal zones exist in regions of inflowing air as a result of advection of relatively warm air from the atmosphere ($T_{\mathrm{atm}} \sim$ -20 °C). Cold air carried from at depth in the firn toward the surface in regions of outflowing air produces large lateral temperature gradients. Below 2.5 m, firn temperature is dominated by conduction, and isotherms are horizontal.

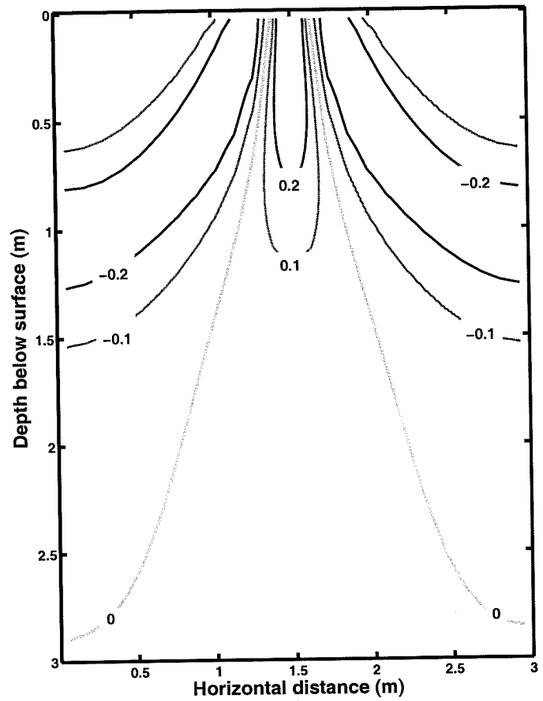


Figure 4.4: Contours of mass-transfer rate (given in 10^{-6} kg m^{-3} s^{-1}) calculated using environmental conditions typical of Antarctic summer with sub-surface air flow as in Figure 4.2. Contours of 0, $\pm$0.1 and $\pm$0.2 $\times$ 10^{-6} kg m^{-3} s^{-1} are plotted. Positive values indicate sublimation, negative values indicate condensation. Air flowing into the firn reaches saturation vapor pressure in the upper 0.05 m regardless of the initial relative humidity of the atmosphere (Chapter 3). Condensation in regions of inflowing air is a result of the advection of relatively warm and moist air from the atmosphere into progressively colder and drier regions. Regions of air outflow are marked by sublimation, as cold and dry air from the firn interior is advected into progressively warmer near-surface regions.

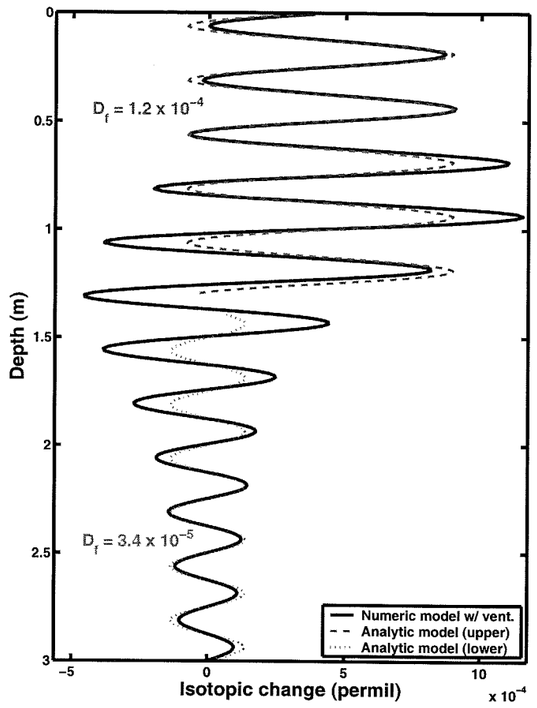


Figure 4.5: Numerical model predictions of isotopic change ($\delta_i^{\text{final}} - \delta_i^{\text{initial}}$) of firn in regions of air inflow with environmental conditions typical of Antarctic summer after 20,000 model seconds with 10 m wind speed = 10 m s^{-1}. Atmospheric vapor was assumed to be in equilibrium with the surface (summer) snow ($\delta_{\text{atm}} \sim$ = -43 ‰). Asymmetric changes in the near-surface layers (winter snow modified more strongly than summer layers) due to equilibration with atmospheric vapor. Below $\sim$ 2 m, isotopic changes are due to diffusion in the vapor phase and equilibration between solid and vapor. Dashed lines represent fit of analytical model (Equation (4.11)) to numerical model results in order to determine effective diffusivity D_f of numerical model. At $\sim$ 0.5 m depth, D_f = 1.2 $\times$ 10^{-4} m^2 yr^{-1}; at 2.5 m depth, D_f = 3.4 $\times$ 10^{-5} m^2 yr^{-1}.

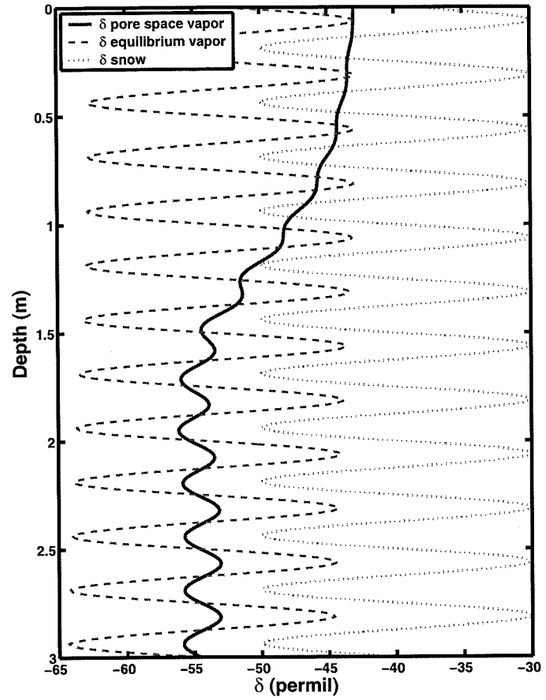


Figure 4.6: Numerical model prediction of pore-space vapor (δ_v, solid line), snow (δ_i, dotted line), and equilibrium vapor (from Equation (4.5), dashed line) during summer in regions of air inflow with 10 m wind speed = 10 m s^{-1}. The isotopic composition of the pore-space vapor is dominated by atmospheric vapor in the upper 1.5 m ($\delta_{\text{atm}} \sim$ -43 ‰). Condensation results in a depletion of δ_v between 1 m and 1.5 m. Below 1.5 m, δ_v is a balance between diffusion in the vapor phase and equilibration between solid and vapor. Note that this model predicts that the pore-space vapor is rarely in isotopic equilibrium with the surrounding snow grains, in contrast to the equilibrium assumption of Whillans and Grootes (1985). Vapor disequilibrium is a result of a rapid diffusion in the vapor phase, and relatively slow isotopic equilibration between solid and vapor (Equation (4.4)). The equilibration constant k must be $\sim$ 100 hr^{-1} in order to generate pore-space vapor in equilibrium with the solid, a value 2 orders of magnitude higher than our expected range of k (Fig. 4.1).

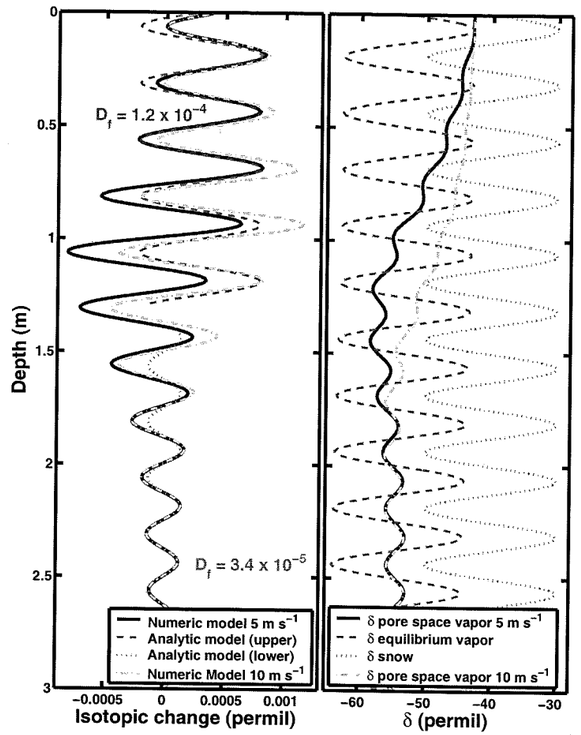


Figure 4.7: Left panel shows numerical model predictions of isotopic change ($\delta_i^{\text{final}} - \delta_i^{\text{initial}}$) in regions of maximum air inflow with environmental conditions as in Figure 4.5 except wind speed is reduced to 5 m s^{-1}. Asymmetric changes in the near-surface layers (winter snow modified more strongly than summer layers) due to equilibration with atmospheric vapor. Between 1 and 1.5 m, isotopically light condensation leads to greater changes in the summer layers than winter layers. In addition, δ_v is closer to equilibrium with winter layers than summer layers, leading to larger changes in summer layers through isotopic equilibration. Below $\sim$ 2 m, isotopic changes are due to diffusion in the vapor phase and equilibration between solid and vapor. At $\sim$ 0.5 m depth, $D_f = 1.2 \times 10^{-4}$ m^2 yr^{-1}; at 2.5 m depth, $D_f = 3.4 \times 10^{-5}$ m^2 yr^{-1}, as shown by dashed lines. Isotopic change under strong winds (10 m s^{-1}) is shown for comparison as dash-dot line. Right panel shows pore-space vapor (δ_v, solid line), snow (δ_i, dotted line), and equilibrium vapor (from Equation (4.5), dashed line). The isotopic composition of the pore-space vapor is dominated by atmospheric vapor in the upper 1.5 m, but to a lesser extent than in Figure 4.6. Condensation results in a depletion of δ_v between 1 m and 1.5 m. Pore space vapor under strong winds is shown for comparison as dash-dot line.

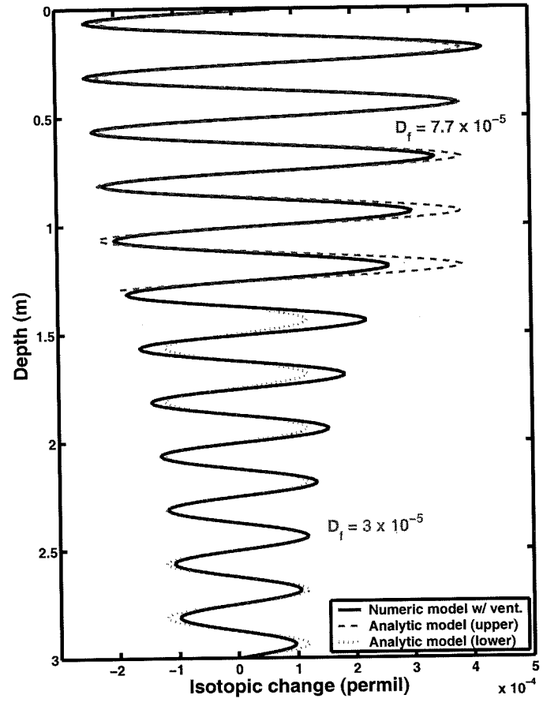


Figure 4.8: Numerical model predictions of isotopic change ($\delta_i^{\text{final}} - \delta_i^{\text{initial}}$) in regions of air outflow with environmental conditions typical of Antarctic summer after 20,000 model seconds and 10 m wind speed = 10 m s^{-1}. Asymmetric change in near-surface layers (winter modified slightly more than summer layers) due indirectly to sublimation. Sublimation makes δ_v heavier and closer to isotopic equilibrium with summer layers; consequently, isotopic equilibration changes winter layers more rapidly. Below $\sim$ 2 m, isotopic changes are due to diffusion in the vapor phase and equilibration between solid and vapor. Dashed lines represent fit of analytical model (Equation (4.11)) to numerical model results in order to determine effective diffusivity D_f of numerical model. At $\sim$ 0.5 m depth, $D_f = 7.7 \times 10^{-5}$ m^2 yr^{-1}; at 2.5 m depth, $D_f = 3 \times 10^{-5}$ m^2 yr^{-1}.

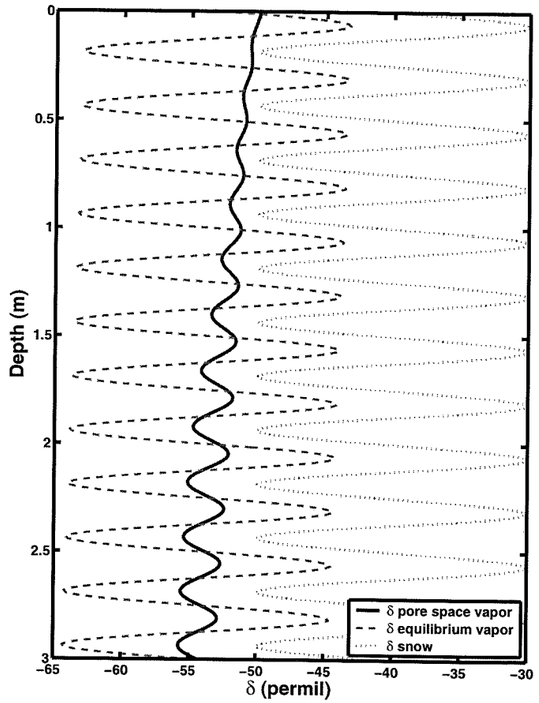


Figure 4.9: Numerical model prediction of pore-space vapor (δ_v, solid line), snow (δ_i, dotted line), and equilibrium vapor (from Equation (4.5), dashed line) during summer in regions of air outflow. The increase in the mean δ_v value between 3 m and 2 m is due to the temperature sensitivity of the fractionation coefficient α (Majoube, 1971). Above 2 m, the sublimation of surrounding snow grains (Fig. 4.4) becomes important. I assume that snow grains sublimate without fractionation. Consequently, sublimation of relatively heavy snow grains accelerates the increase in δ_v. The gradual decrease in amplitude towards the surface is due to increased air flow velocities near the surface, which act to smooth out large variations in δ_v.

Chapter 5

EFFECTS OF VENTILATION ON IRREVERSIBLY-DEPOSITED SPECIES

5.1 Summary

The vapor-transport model of Chapter 3 is used to quantify the effects of firn ventilation on irreversibly-deposited species. These species are not re-entrained after deposition at the snow surface. I assume that non-sea-salt (nss) sulfate is representative of these species. The bulk concentration of nss-sulfate is decreased by water vapor condensation in the firn and increased by sublimation of the surrounding ice grains. Concentration changes as a result of both seasonal and daily temperature cycles are presented. I also investigate the effects of enhanced water vapor diffusivity (hand-to-hand diffusion) in snow on concentrations of nss-sulfate. In all cases, the concentration change induced by water vapor redistribution in the firn is much smaller than the annual variability of nss-sulfate in surface snow.

5.2 Introduction

Temporal variations in chemical records obtained from polar snow and ice have been interpreted in terms of variations in atmospheric chemistry and transport (Legrand and Mayewski, 1997). For example, these records contain information about sea-salt loading in the atmosphere (Na^+), dust loading in the atmosphere (Al or Ca^{+2}), biological ocean productivity (methane sulfonate - MSA) and volcanic events (SO_4^{-2}). Much work has been done recently on the air-snow transfer function for many of these species (e.g. Wolff and others, 1998; Harder and others, 2000) in order to determine

how chemical concentrations of these species in surface snow relate to atmospheric concentrations. The extent to which concentrations of these species can be modified after deposition to the snow surface prior to deep burial has been characterized for some species (e.g. NO_3^-, H_2O_2), but has not been studied in detail for other species (e.g. SO_4^{-2}, MSA).

In this chapter, I examine the effect of firn ventilation on irreversibly-deposited (i.e. hydrophilic) species. As demonstrated in Chapter 3, firn ventilation coupled with seasonal temperature cycles can cause redistribution of water in firn. The concentration of irreversibly-deposited species in snow can be increased by sublimation of the surrounding ice grains, or decreased by condensation. In order to isolate the effect of the redistribution of water on chemical concentration, I avoid chemical species that have complex photochemistry (NO_3^-) or gaseous components (H_2O_2 or Cl^-), and focus on sulfate (SO_4^{-2}).

Sulfate concentration in the atmosphere changes seasonally. Sulfate is the product of the oxidation of biological, anthropogenic and volcanic sulfur emissions. Sulfate forms cloud condensation nuclei and is scavenged out of the atmosphere through both wet and dry deposition mechanisms (Bergin and others, 1995; Waddington and others, 1996). Prior work on sulfate and firn ventilation has focused on the filtering effect of snow (Gjessing, 1977; Cunningham and Waddington, 1993; Harder and others, 2000). These studies demonstrate that sulfate concentrations in snow can change either as a result of changes in the filtering efficiency or changes in atmospheric sulfate concentration. Total sulfate concentration is often converted to non-sea-salt sulfate (nss-sulfate) concentration by removing the fraction of sulfate attributable to sea spray (e.g. Harder and others, 2000). Total sulfate concentration is generally used when studying the record of volcanic events in ice (e.g. Hammer and others, 1980), while nss-sulfate concentration is generally used in studies of seasonal cycles or biological productivity. In this chapter, I use nss-sulfate concentrations, though the results presented here can be applied to total sulfate concentration.

In this chapter, I use the water-vapor motion model of Chapter 3 to determine how firn ventilation can affect the concentration of nss-sulfate in snow. I begin by reviewing a model for calculating water-vapor motion, and then show that firn ventilation can change nss-sulfate concentration by up to 3% for certain environmental conditions.

5.3 Model Details

The model used for calculating temperature, vapor density and sublimation or condensation rates in the firn is similar to the model of Albert (2002), and is described in detail in Chapter 3. The model solves the coupled equations for heat flow and water-vapor motion in a 2-D cross section of the firn. I used this model to determine an approximately steady-state temperature and mass-transfer pattern in the firn corresponding to midsummer conditions with strong winds (Section 3.8.2). The analysis is restricted to summer conditions since firn temperature, and consequently vapor density (through Equation (E.1)) and sublimation / condensation rates are two orders of magnitude larger in summer than winter (Chapter 3).

Air flow through the firn is the result of steady wind flow (10 m wind speed = 10 m s^{-1}) over a sinusoidal surface topography (wavelength of surface topography $\lambda = 3$ m, surface amplitude $h = 0.1$ m), as in Waddington and others (1996). Air flow velocity vectors are calculated as in Colbeck (1989) and Waddington and others (1996) as described in Chapter 3, and are shown in Figure 5.1. Here, I assumed a uniform firn microstructure (density and permeability), and that the 10 meter wind speed is constant. The magnitude of the modeled air flow vectors in Figure 5.1 are sensitive to the background wind speed; decreasing the wind speed from 10 m s^{-1} to 5 m s^{-1} reduces the maximum air flow velocity in the firn from $\sim$ 1 cm s^{-1} to 0.3 cm s^{-1}. Variations in surface microtopography (λ, h) primarily influence the ventilation depth (Waddington and others, 1996).

Calculations of firn temperature, shown in Figure 4.3, were made by assuming that

the surface temperature varies seasonally (mean T_{atm} = -40 °C; amplitude = 20 °C) and plotted after 10 model days starting in mid-summer. The surface temperature during this time period is $T_{\text{atm}} \sim$ -20 °C. In regions of air inflow (Fig. 5.1, between x = 0:0.75 m and 2.25:3 m in the horizontal direction), the near-surface firn is isothermal as a result of the vertical advection of relatively warm air from the atmosphere. In regions of air outflow (Fig. 4.2, x = 0.75:2.25 m), vertical advection carries relatively cold air from the firn interior towards the surface. Horizontal advection between these two regions helps to create a curved pattern of the isotherms in the upper few meters. Below about 2.5 m depth, advection is less important, and the temperature field is dominated by conduction, resulting in horizontal isotherms.

The phase-change field is calculated as described in Chapter 3 using the governing equations of Albert (2002) and is shown in Figure 4.4. Advection of air through temperature gradients in the firn results in regions of super- and sub-saturated air in the pore spaces. In regions of air inflow, warm saturated air from the atmosphere is advected into the firn. This advected air is super-saturated relative to the cooler firn at depth, resulting in regions of condensation (mass-transfer rate < 0 centered at ~ 1 m depth). In regions of air outflow, relatively cool and dry air from the firn interior is advected into progressively warmer firn near the surface. This air is under-saturated, resulting in sublimation of some surrounding snow. Lateral advection between regions of inflow and outflow coupled with the sinusoidal temperature pattern curves the locus of maximum sublimation toward the surface.

Sublimation and condensation rates presented here below $\sim$ 5cm depth in the firn are insensitive to the initial vapor density of the atmospheric air. Using these air flow velocities (Fig. 4.2), air advected into the firn reaches saturation vapor density in the upper few cm of the firn, regardless of initial vapor density (Section 3.8.1). In the model results presented here, I have assumed that the air advected into the firn is initially saturated.

The model results presented here use a uniform snow density (= 300 kg m^{-3}) and

permeability (= 5 $\times$ 10^{-9} m^2). The diffusivity of water vapor in snow is calculated following Cuffey and Steig (1998) as:

$$D_{\text{s}} = 0.0371\, T^{1.75} \left(1 - \frac{\rho_{\text{snow}}}{730}\right) \tag{5.1}$$

where T is firn temperature expressed in K and ρ_{snow} is the snow density expressed in kg m^{-3}. This combination of ρ_{snow} and T ($\sim$ 253 K) results in $D_{\text{s}} \simeq 1.2 \times 10^{-5}$ m^2 s^{-1}.

Prior research (e.g. Harder and others, 1996; Harder and others, 2000) has shown that snow acts as an excellent filter for sulfate aerosols. Virtually 100% of sulfate aerosol is removed in the upper 2 cm of the firn in regions of air inflow. Consequently, sulfate concentrations are relatively higher in the upper 2 cm in regions of air inflow compared with regions of air outflow as a result of firn ventilation. In this study, I am primarily interested in the magnitude of post-depositional change in sulfate concentrations, so I have assumed that sulfate is uniformly distributed throughout the firn initially.

5.4 Results and Discussion

5.4.1 Seasonal Cycles

Typical concentrations of nss-sulfate in surface snow are on the order of 100 ng g^{-1} of H_2O (e.g. Harder and others, 2000). Sulfate concentration in firn will be modified by the redistribution of water in the firn. In regions of sublimation (condensation) sulfate concentrations will increase (decrease).

By assuming that the calculated sublimation and condensation rates are representative of much of the summer, I estimated the cumulative effect of ventilation on sulfate concentration in the firn. I assumed that the temperature pattern and wind speed presented above are representative of the warmest 2 months of the year; the cumulative sublimation and condensation fields are shown in Figure (3.13).

Beneath regions of air inflow (Fig. 5.1; air enters the firn between x = 0:0.75 m and 2.25:3 m along the snow surface, where x is the lateral spatial coordinate) the maximum cumulative condensation over 60 days is $\sim$ 1 kg m^{-3} and is centered at $\sim$ 1 meter depth. Since I used a uniform snow density of 300 kg m^{-3}, this is a very small change, and will decrease sulfate concentration in the firn by $< 1\%$. The maximum cumulative sublimation is found beneath regions of air outflow (x = 0.75:2.25 m), and is also about 1 kg m^{-3}, leading to a sulfate concentration increase of < 1 %. Therefore, the effects of sublimation and condensation driven by seasonal temperature cycles on nss-sulfate are small.

5.4.2 Daily Cycles

Sublimation and condensation in the firn are caused by the advection of pore space vapor through temperature gradients in the firn. Firn temperature at 1 m depth is influenced primarily by the seasonal cycle. Consequently, these effects can be characterized as concentration changes due to the seasonal cycle. At that depth, typical temperature gradients are $\sim$ 5 °C m^{-1}. Much larger temperature gradients have been measured in the upper few decimeters of firn (Satow and Watanabe, 1975) as a result of diurnal temperature variations and synoptic weather systems. Surface temperature at a site is influenced by synoptic-scale weather systems and can vary by several tens of degrees in an hour. Rapid surface temperature changes, coupled with firn ventilation, can generate sublimation (and condensation) rates much larger than those produced as a result of the seasonal cycle.

The large and unknown variability of surface temperature on hourly timescales precludes calculating near-surface sublimation rates at a site, unless time series of surface temperature, wind speed and wind direction are available. However, in order to quantify the potential importance of daily temperature changes, I used the above model and allowed T_{atm} to vary sinusoidally with a 24 hour period and 5°C amplitude.

As expected, larger temperature gradients ($\sim$ 35 °C m^{-1}) can develop in the upper 1 m in regions of air inflow. Both the magnitude and the sign of the near-surface temperature gradient change throughout the daily cycle. During the warmest 12 hours of the day, the model predicts condensation rates as large as 8.5 $\times$ 10^{-6} kg m^{-3}s^{-1} in air-inflow regions, when warm and relatively moist air is advected into the colder firn. Regions of air outflow are largely unaffected by diurnal surface temperature changes, since firn temperature in these regions is dominated by advection of relatively cold air from the firn interior. Sublimation rates in air-outflow regions are lower, typically 2 $\times$ 10^{-7} kg m^{-3}s^{-1}, corresponding to a much smaller temperature gradient ($\sim$ 3 °C m^{-1}).

The daily cycle of sublimation and condensation in the upper meter of the firn is nearly symmetric; rapid sublimation during the cold parts of the day are balanced by rapid condensation during the warm parts of the day. However, since vapor density is a function of temperature, sublimation does not quite balance condensation. Figure 5.2 shows the total condensation in the upper 3 meters of the firn in a region of air inflow (solid line) and outflow (dashed line) integrated over the daily cycle. The model predicts that the net condensation rate in the upper 1 meter is $\sim$ a factor of 3 larger than the sublimation or condensation rates induced by the seasonal cycle. In regions of air inflow, the cumulative condensation rate is $\sim$ 20 g m^{-3} day^{-1} in the upper 1 m. The daily temperature cycle is most influential in the upper 50 cm, while the influence of the seasonal cycle is centered at 1.5 m depth. In regions of air outflow, the cumulative daily sublimation rate is $\sim$ 10 g m^{-3} day^{-1}. The maximum sublimation rate is centered at 40 cm depth. Above that level, the lateral advection of relatively moist air from regions of air inflow inhibits strong sublimation.

Note that these net changes are not much larger than the changes due to sublimation or condensation induced by the seasonal temperature cycle, which are also $\sim$ 20 g m^{-3} day^{-1}. However, the energy associated with phase changes induced by the daily temperature variation tends to reduce the influence of the seasonal temperature cycle in regions of air inflow. The daily temperature cycle does not allow a large nearly

Beneath regions of air inflow (Fig. 5.1; air enters the firn between x = 0:0.75 m and 2.25:3 m along the snow surface, where x is the lateral spatial coordinate) the maximum cumulative condensation over 60 days is $\sim$ 1 kg m^{-3} and is centered at $\sim$ 1 meter depth. Since I used a uniform snow density of 300 kg m^{-3}, this is a very small change, and will decrease sulfate concentration in the firn by $< 1\%$. The maximum cumulative sublimation is found beneath regions of air outflow (x = 0.75:2.25 m), and is also about 1 kg m^{-3}, leading to a sulfate concentration increase of < 1 %. Therefore, the effects of sublimation and condensation driven by seasonal temperature cycles on nss-sulfate are small.

5.4.2 Daily Cycles

Sublimation and condensation in the firn are caused by the advection of pore space vapor through temperature gradients in the firn. Firn temperature at 1 m depth is influenced primarily by the seasonal cycle. Consequently, these effects can be characterized as concentration changes due to the seasonal cycle. At that depth, typical temperature gradients are $\sim$ 5 °C m^{-1}. Much larger temperature gradients have been measured in the upper few decimeters of firn (Satow and Watanabe, 1975) as a result of diurnal temperature variations and synoptic weather systems. Surface temperature at a site is influenced by synoptic-scale weather systems and can vary by several tens of degrees in an hour. Rapid surface temperature changes, coupled with firn ventilation, can generate sublimation (and condensation) rates much larger than those produced as a result of the seasonal cycle.

The large and unknown variability of surface temperature on hourly timescales precludes calculating near-surface sublimation rates at a site, unless time series of surface temperature, wind speed and wind direction are available. However, in order to quantify the potential importance of daily temperature changes, I used the above model and allowed T_{atm} to vary sinusoidally with a 24 hour period and 5°C amplitude.

As expected, larger temperature gradients ($\sim$ 35 °C m^{-1}) can develop in the upper 1 m in regions of air inflow. Both the magnitude and the sign of the near-surface temperature gradient change throughout the daily cycle. During the warmest 12 hours of the day, the model predicts condensation rates as large as 8.5 $\times$ 10^{-6} kg m^{-3}s^{-1} in air-inflow regions, when warm and relatively moist air is advected into the colder firn. Regions of air outflow are largely unaffected by diurnal surface temperature changes, since firn temperature in these regions is dominated by advection of relatively cold air from the firn interior. Sublimation rates in air-outflow regions are lower, typically 2 $\times$ 10^{-7} kg m^{-3}s^{-1}, corresponding to a much smaller temperature gradient ($\sim$ 3 °C m^{-1}).

The daily cycle of sublimation and condensation in the upper meter of the firn is nearly symmetric; rapid sublimation during the cold parts of the day are balanced by rapid condensation during the warm parts of the day. However, since vapor density is a function of temperature, sublimation does not quite balance condensation. Figure 5.2 shows the total condensation in the upper 3 meters of the firn in a region of air inflow (solid line) and outflow (dashed line) integrated over the daily cycle. The model predicts that the net condensation rate in the upper 1 meter is $\sim$ a factor of 3 larger than the sublimation or condensation rates induced by the seasonal cycle. In regions of air inflow, the cumulative condensation rate is $\sim$ 20 g m^{-3} day^{-1} in the upper 1 m. The daily temperature cycle is most influential in the upper 50 cm, while the influence of the seasonal cycle is centered at 1.5 m depth. In regions of air outflow, the cumulative daily sublimation rate is $\sim$ 10 g m^{-3} day^{-1}. The maximum sublimation rate is centered at 40 cm depth. Above that level, the lateral advection of relatively moist air from regions of air inflow inhibits strong sublimation.

Note that these net changes are not much larger than the changes due to sublimation or condensation induced by the seasonal temperature cycle, which are also $\sim$ 20 g m^{-3} day^{-1}. However, the energy associated with phase changes induced by the daily temperature variation tends to reduce the influence of the seasonal temperature cycle in regions of air inflow. The daily temperature cycle does not allow a large nearly

isothermal region in the upper 75 cm to be created (c.f. Fig. 3.11). This isothermal zone is partially responsible for the large condensation rates centered at $\sim$ 1 m depth when only seasonal temperature forcing is used.

It should also be noted that these condensation rates are generated by using an idealized diurnal surface temperature cycle in the model; the actual surface temperature variations at a site could be quite different, leading to much different magnitudes in condensation or sublimation in the upper 1m of the firn. However, I expect that most sites will show net condensation in firn over a daily cycle as a result of the higher vapor densities in the firn during the warm part of the day.

Although the condensation rate due to the daily cycle is larger than the rates generated by the seasonal cycle, the impact on sulfate concentrations in the firn is still modest. If the results of Figure 5.2 are extrapolated over the summer season (60 days), the maximum cumulative condensation in the firn is $\sim$ 1.5 kg m^{-3}. For ρ_{snow} = 300 kg m^{-3}, this change corresponds to a sulfate concentration decrease of less than 1%. From this analysis, I conclude the sublimation and condensation in the firn driven by daily temperature cycles do not have a strong influence on nss-sulfate.

5.4.3 Hand-to-Hand Diffusion

The potential for firn ventilation-driven post-depositional sulfate concentration change is modest. Harder and others (2000) showed that nss-sulfate concentrations in snow pits at South Pole frequently vary by a factor of 2 in the upper meter. These measurements support theoretical work by Waddington and others (1996) that predicted that the variation is due to changes in both atmospheric concentration of nss-sulfate (varies by an order of magnitude) and filtering efficiency (due to changes in wind speed and microtopography). The total sulfate measurements of Stenberg (2000) from East Antarctica also show large variability with depth (factor of 3).

Several investigators (e.g. Yosida and others, 1955; Powers and others, 1985; Colbeck, 1993) suggest that water vapor diffuses more easily through snow than through

air. This so-called 'hand-to-hand' diffusion results from vapor diffusion through pore spaces as well as vapor transfer from particle to particle. Particle-to-particle vapor transport is a result of the large thermal conductivity differences between air and ice. This difference results in relatively large thermal gradients across pore spaces, and relatively small thermal gradients across ice grains. The net effect of this process is to allow water vapor to diffuse in snow as much as 5 times faster than in air.

I tested the influence of enhanced water vapor diffusivity in snow by increasing D_s by a factor of 5, from 1.2×10^{-5} m^2 s^{-1} to 6×10^{-5} m^2 s^{-1}. The primary result of this change is to decrease the Peclet number substantially. The Peclet number is a non-dimensional number that describes the relative strength of advection and diffusion (Appendix D). Figure 5.3 shows that increasing D_s decreases the range over which vapor transport is advection-dominated (Peclet number $>$ 1) considerably. With a large vapor diffusivity, diffusion is the dominant vapor transport process below the upper $\sim$ 25 cm, unlike in the low D_s case, where diffusion is dominant only below 1 m.

Increasing D_s also affects the net condensation and sublimation rates in the firn. Figure 5.4 compares the cumulative condensation (in kg m^{-3} day^{-1}) calculated with both values of D_s in regions of air inflow. Both show the same net condensation in the upper $\sim$ 75 cm as a result of the daily temperature cycle. Below this depth, the higher D_s case shows lower net condensation. In both cases, vapor transport below 1 meter is dominated by diffusion (Fig. 5.3). Increasing the diffusivity will lead to a decrease in the sublimation or condensation rate. As shown in Appendix E, the driving force for sublimation or condensation in the firn is a mismatch between the vapor density in pore spaces and the saturation vapor density. The net mobility of water vapor increases as D_s increases. With large values of D_s, large differences between vapor density and saturation vapor density do not develop, and so sublimation or condensation rates are smaller. Consequently, the cumulative condensation in regions of air inflow are about 25% lower with a factor of 5 enhancement to D_s.

Increasing D_s changes the net condensation rate at depth in the firn, but has little effect on condensation due to the diurnal cycle. Consequently, nss-sulfate concentrations in the snow is sensitive to changes in D_s only below ~ 1 m. This analysis suggests that water-vapor redistribution in firn has a small effect on nss-sulfate concentrations, whether D_s reflects hand-to-hand diffusion or not.

5.4.4 Cumulative Effects

The largest condensation and sublimation rates are found in the upper 2 meters of the firn. In low-accumulation rate areas, snow may remain in the near-surface ventilated zone for several years. If the surface topography is stationary, such that areas of air inflow and outflow are in the same place, the effects of firn ventilation on nss-sulfate concentration are cumulative. In this case, the total concentration change is a function of both accumulation rate (vertical velocity) and condensation/sublimation rate.

Several investigators (e.g. McConnell and others 1997a; van der Veen and others, 1999) have demonstrated the episodic nature of snowfall on the antarctic plateau. However, by assuming a constant accumulation rate of snow at the surface we can estimate the cumulative effect that firn ventilation may have on irreversibly-deposited species, such as nss-sulfate. Using an accumulation rate of snow of 20 cm yr^{-1} (ρ_{snow} = 300 kg m^{-3}, corresponds to 6.5 cm ice yr^{-1}), and neglecting strain, a packet of snow will move through the upper 3 m in 15 years. I further assume that the condensation and sublimation rates presented here are valid for the warmest 60 days of the year, and that water-vapor motion in other seasons can be neglected.

Figure 5.5 shows the cumulative condensation in the firn with these assumptions versus age in the firn. This age range (25 years) corresponds to the upper 5 meters of the firn, since I have neglected strain in the firn column. The solid line shows the cumulative mass change in regions of air inflow which have net condensation over the daily cycle, as shown above. Integrating the daily pattern of condensation shown

in Figure 5.2 over depth results in a total mass gain of ~ 7 kg m^{-3} in the upper 10 years (2 meters). For $\rho_{\text{snow}} = 300$ kg m^{-3}, this change corresponds to a sulfate concentration decrease of $\sim 2\%$.

Regions of air outflow are marked by sublimation, as cold air from the firn interior is advected into progressively warmer layers near the surface. The cumulative mass change in regions of air inflow is shown by the dashed line in Figure 5.5. As noted above, regions of air outflow are not affected by the diurnal temperature cycle, but are influenced most strongly by the seasonal cycle. With the assumptions presented above, the model predicts that snow will lose ~ 6 kg m^{-3} as it is advected down through the firn. For the snow density used in this study ($\rho_{\text{snow}} = 300$ kg m^{-3}), this mass loss due to sublimation will increase nss-sulfate concentration by about 3%.

5.5 Conclusions

Ventilation causes sublimation and condensation in the firn as a result of air flow through the firn, coupled with temperature gradients. The model for mass and energy conservation in the firn using only the seasonal temperature cycle predicts total mass transfer of ~ 1 kg m^{-3} of sublimation or condensation over the summer season. This water-vapor redistribution results in very modest changes (< 1 %) in the concentration of nss-sulfate and other irreversibly deposited species.

Firn temperature in the upper 1 meter is influenced by short-term variations in surface temperature, such as synoptic-scale weather or diurnal cycles. The short-term variations can generate larger temperature gradients, and consequently larger sublimation and condensation rates than seasonal temperature cycles. Using an idealized surface temperature cycle, this model predicts net condensation over a diurnal cycle in the upper 1 meter of the firn. Over the course of the summer season, the model predicts a maximum cumulative mass change of 2 kg, which causes a 1 % concentration change in nss-sulfate. The actual short-term surface temperature variation at

a site could generate much different sublimation or condensation rates. This model predicts temperature gradients as large as 35 ° C m^{-1}; larger temperature gradients have been observed (Satow and Watanabe, 1985). However, the results presented here (which use a 5 degree amplitude daily surface temperature cycle) may represent a plausible surface temperature variation.

The diffusivity of water vapor in snow is potentially five times larger than the diffusivity of water vapor in air (e.g. Yosida and others, 1955; Colbeck, 1993). Enhancing D_s by a factor of 5 leads to a decrease in the sublimation or condensation rate in the firn below the upper meter. Since the most rapid phase changes are in the upper meter, the concentrations of irreversibly-deposited species in the firn is largely insensitive to changes in D_s.

The concentration of many irreversibly-deposited species (such as nss-sulfate) vary seasonally. In the case of nss-sulfate, the atmospheric concentration varies by as much as 2 orders of magnitude and the concentration in firn varies by a factor of 2 or more (Harder, 2000; Stenberg, 2000) during the annual cycle. The predicted concentration change due to firn ventilation in a single season is much smaller than the annual variability in nss-sulfate. Consequently, it is unlikely that firn ventilation causes measurable changes in nss-sulfate. If surface topography is stationary in time, the effects of firn ventilation on nss-sulfate concentration may be cumulative. For a constant vertical velocity of 0.20 m yr^{-1}, the model presented here predicts total cumulative concentration change in nss-sulfate in regions of air inflow would be 3 %, still far less than the annual variability. It may be possible to detect post-depositional changes in other irreversibly-deposited species that have a relatively constant or well-characterized flux (e.g. ^{10}Be) to the snow surface throughout the year.

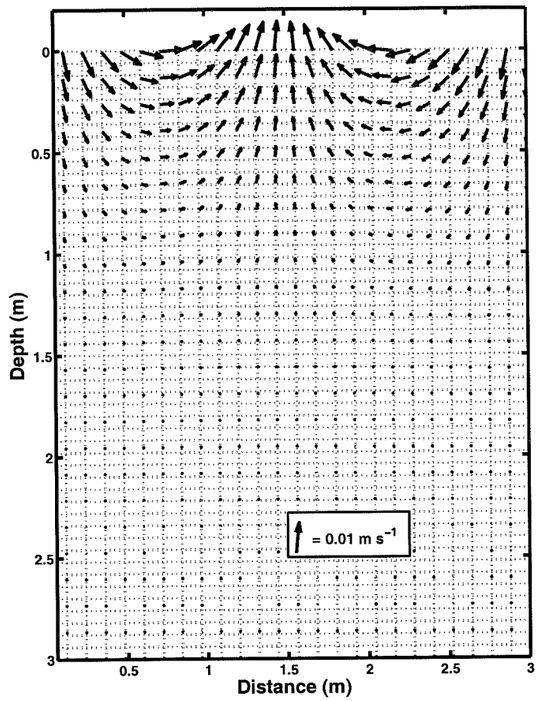


Figure 5.1: Air flow in the firn (ventilation) is the result of steady wind flow (10 m wind speed = 10 m s^{-1}) over a sinusoidal surface topography (wavelength of surface topography = 3 m, surface amplitude = 0.1 m). Air-flow velocity vectors are calculated as in Colbeck (1989) and Waddington and others (1996), and have a maximum value of 0.01 m s^{-1}. Air flows into the firn between 0:0.75 m and 2.25:3 m in the horizontal direction, and out of the firn between 0.75 and 2.25 m. Note that air-flow velocities are calculated on a rectangular grid, rather than along the actual sinusoidal snow surface. Cunningham and Waddington (1993) showed that this is a reasonable approximation as long as the aspect ratio of the bumps is < 1.

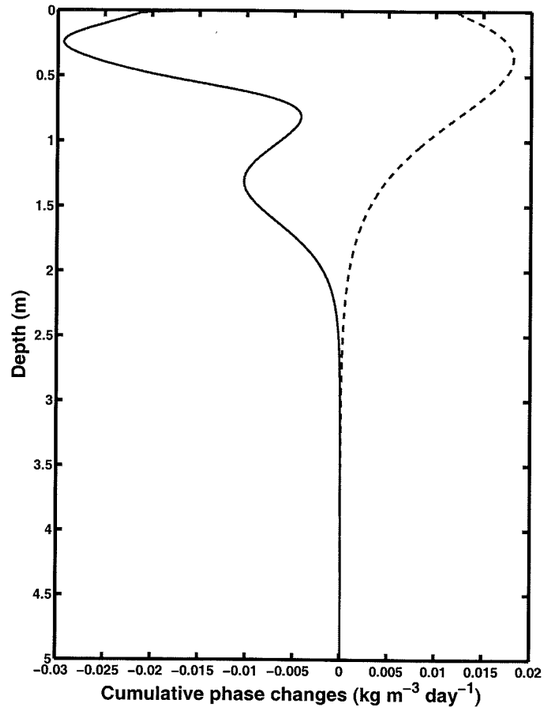


Figure 5.2: Cumulative daily mass-transfer of water (expressed as kg m^{-3} day^{-1}) as a result of diurnal surface temperature changes (amplitude = 5°C). Mass-transfer rates are calculated using environmental conditions typical of Antarctic summer with sub-surface air flow as in Figure 5.1. Negative mass-transfer rates indicate condensation. Solid (dashed) line represents cumulative change in regions of air inflow (outflow). Rapid condensation during warm parts of day in regions of air inflow (when relatively warm and moist air enters snow pack) is nearly balanced by rapid sublimation during the cold parts of the day (when cold air enters the firn). Integrating the mass transfer over the daily cycle yields net condensation in regions of air inflow (e.g. solid line at 0.4 m depth) as a result of higher vapor pressure during the warmer part of the day, which leads to larger mass-transfer rates during the warm part of the day. Influence of seasonal cycle is centered at 1.5 m in regions of air inflow. Regions of air outflow show sublimation throughout the daily temperature cycle. Lateral advection of warm, moist air from regions of air inflow inhibits strong sublimation in the upper 30 cm.

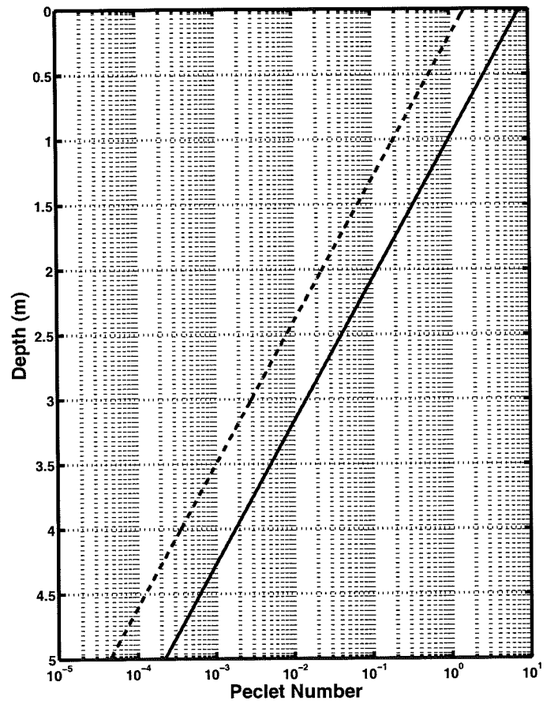


Figure 5.3: Change in Peclet number P in a region of air inflow as a result of enhanced water vapor diffusivity D_s. Solid line represents Peclet number with D_s calculated as in Equation 5.1. Dashed line represents Peclet number with D_s enhanced by a factor of 5. Increase in D_s reduces the depth of the firn dominated by vertical advection (P > 1) from upper 1 m to upper 20 cm.

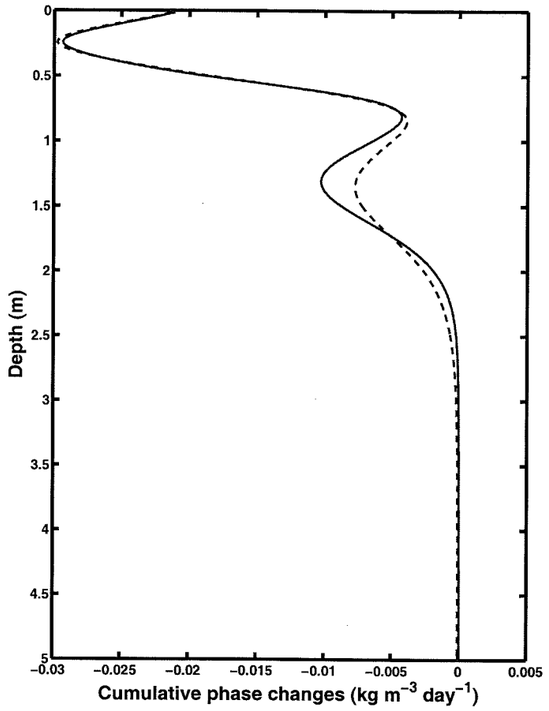


Figure 5.4: Comparison of cumulative daily condensation (expressed as kg m^{-3} day^{-1}) in region of air inflow. Solid (dashed) line represents cumulative daily condensation with normal (enhanced) water vapor diffusivity D_s. Both values of D_s show the same pattern in upper 75 cm due to daily temperature cycle (as in Fig. 5.2). Below that depth, enhanced D_s prevents large differences between vapor density and saturation vapor density in regions influenced by seasonal temperature cycles (centered at 1.5 m depth). This leads to lower condensation rates in regions with large temperature (and vapor density) gradients. Where temperature gradients are smaller (below $\sim$ 2m), enhanced D_s leads to increased condensation rates, as diffusion length scale is increased.

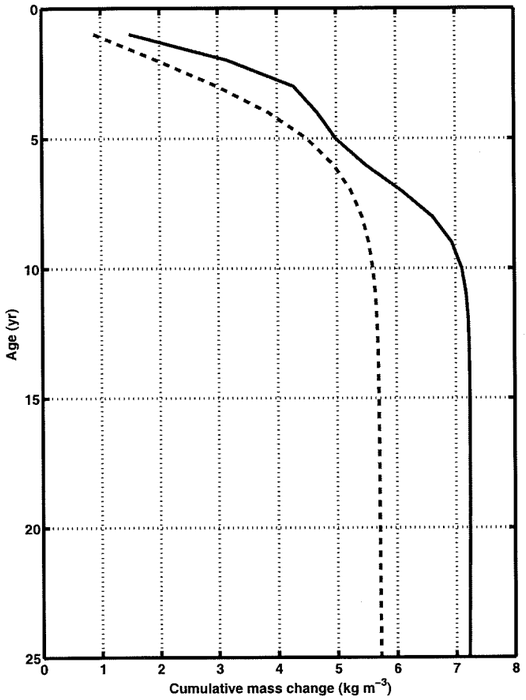


Figure 5.5: Cumulative change in firn mass (expressed as kg m^{-3}) as a result of diurnal surface temperature changes (amplitude = 5°C), assuming a constant vertical velocity of 0.2 m yr^{-1}. Solid line represents total condensation experienced by a parcel of snow advected through the firn column in a region of air inflow. Dashed line represents total sublimation experienced in a region of air outflow. Analysis assumes that daily condensation or sublimation rates (Fig. 5.2) are representative of the warmest 60 days of the year, and that other seasons have a minor influence on total condensation or sublimation.

Chapter 6

EFFECTS OF VENTILATION ON REVERSIBLY-DEPOSITED SPECIES

6.1 Summary

Modifications to the H_2O_2 preservation model of McConnell and others (1998) are made to account for the effects of sublimation and condensation induced by firn-ventilation on H_2O_2 concentration in the firn. I assume that H_2O_2 is representative of chemicals that cycle between the atmosphere and snow after deposition to the snow surface (reversibly-deposited species). Sublimation releases H_2O_2 from ice grains, decreasing the mean H_2O_2 concentration. Condensation increases H_2O_2 concentration through 2 processes: scavenging H_2O_2 from the pore space vapor (particularly important in the summer when atmospheric H_2O_2 concentrations are large) and increasing the grain radius, which lengthens the diffusion path in the solid particles. I use the vapor-transport model of Chapter 3 to predict sublimation and condensation rates in the firn, and to predict changes in average grain size. This analysis suggests that sublimation and condensation are of secondary importance to H_2O_2 concentration in firn, but may be more important to the preservation of other reversibly-deposited species. This study also suggests that it is likely that other mechanisms are responsible for grain size changes in addition to firn ventilation.

6.2 Introduction

Temporal variations in chemical records obtained from polar snow and ice have been interpreted in terms of variations in atmospheric chemistry and transport (Legrand

and Mayewski, 1997). These chemical records are composed of measurements of both aerosol species (which are relatively immobile after deposition to the ice sheet surface) and volatile species (which can be lost to the atmosphere after deposition). Volatile species generally exist as trace gasses in the polar atmosphere (e.g. HF, HCL, HNO_3, HCHO, H_2O_2) and are scavenged by ice grains growing in the atmosphere. Unlike irreversibly-deposited species, such as most aerosols, a fraction of the mass of volatile species in snow grains cycles between the atmosphere and snow through time. Consequently, volatile species are said to be 'reversibly deposited'.

In this chapter, I examine the effect of firn ventilation on reversibly-deposited (i.e. hydrophobic or volatile) species. As demonstrated in Chapter 3, firn ventilation coupled with seasonal temperature cycles can redistribute water in firn. Concentrations of reversibly-deposited species in snow are decreased by sublimation of the surrounding ice grain, as reversibly-deposited species can generally exist as gasses. The effect of condensation on reversibly-deposited species depends in part upon the chemical under consideration. Condensation increases the diffusion path length by increasing the grain radius. In addition, the process of condensation in the firn can scavenge trace gasses out of pore-spaces. In order to isolate the effect of the redistribution of water on chemical concentration, I avoid chemical species that have complex photochemistry (NO_x) or interact readily with snow (OH^-), and focus on H_2O_2 . I assume that H_2O_2 is representative of other reversibly-deposited species (e.g. Waddington and others, 1996).

Hydrogen peroxide is formed in the atmosphere through combination of two HO_2 (Christensen and others, 2002), and destroyed photochemically. H_2O_2 measurements in firn and ice cores are used to understand changes in the oxidizing capacity of the atmosphere (e.g. Thompson, 1995). Prior work (McConnell and others, 1997; McConnell and others, 1998) resulted in a model for H_2O_2 preservation in firn. The model captured the major mechanisms for post-depositional change of H_2O_2 and was able to match the magnitude of the variation of H_2O_2 in firn. Uncertainties in the

timing and magnitude of accumulation lead to errors in the depth of major H_2O_2 structure (such as seasonal cycles), while uncertainty in the H_2O_2 concentration in surface snow lead to errors in the estimates of H_2O_2 loss from the firn. In general, the model of McConnell and others (1998) demonstrates that preservation of H_2O_2 is primarily a function of grain size, ventilation rate and timing and magnitude of snow accumulation. Loss of H_2O_2 is a result of diffusion through the ice grain and equilibration of H_2O_2 in pore space vapor.

In this chapter, I modify the model of McConnell and others (1998) to include the effects of sublimation and condensation on H_2O_2 concentrations in snow. I calculate the sublimation and condensation rates using the water-vapor motion model of Chapter 3. I begin by reviewing the model of McConnell and others (1998) for calculating H_2O_2 concentration in firn, and describe my adaptations to it. This model allows me to also predict changes in average grain radius. Comparison of the predicted grain growth rates with the measurements of Gow (1969) and Sturm and Benson (1997) suggests that processes other than firn-ventilation-induced condensation control grain growth. This study supports the finding of McConnell and others (1998) that diffusion of H_2O_2 through ice grains and equilibration with pore space air are primarily responsible for H_2O_2 changes in firn, and that post-depositional water-vapor motion plays a secondary role.

6.3 Model Details

McConnell and others (1998) presented a model to calculate H_2O_2 changes within individual snow grains. I have modified this model to take into account H_2O_2 changes as a result of ventilation-driven sublimation and condensation on H_2O_2 concentration in the firn.

McConnell and others (1998) model snow using radially-symmetric spherical ice grains. In the following, temperature is T, the radial coordinate of the ice grain is r

and the ice grains have radius a. The time-dependent peroxide concentration C_r in the grains is given by a spherical diffusion equation:

$$\frac{\partial C_r}{\partial t} = \frac{1}{r^2}\left[\frac{\partial}{\partial r} D_i(T)\, r^2 \left(\frac{\partial C_r}{\partial r}\right)\right] \tag{6.1}$$

where $D_i(T)$ is the temperature-dependent diffusivity of H_2O_2 in an ice grain (Conklin and others, 1993). By assuming that D_i is uniform within an ice grain McConnell and others (1998) simplified Equation (6.1):

$$\frac{\partial C_r}{\partial t} = \frac{D_i(T)}{r^2}\frac{\partial}{\partial r}\left[r^2 \frac{\partial C_r}{\partial r}\right] \tag{6.2}$$

The H_2O_2 concentration on the grain surface $C_r(a,t)$ is determined by exchange of H_2O_2 with the pore space air through adsorption and desorption. I assume that the H_2O_2 exchange between the grain and the pore space air is instantaneous. $C_r(a,t)$ is determined by the concentration $C_{air}(t)$ in the firn pore space around the ice grain and by a partitioning coefficient K_D. This relationship takes the functional form of Henry's Law:

$$K_D(T(t)) = \frac{C_r(a,t)}{C_{air}(t)} \tag{6.3}$$

where C_r is expressed in moles per liter and C_{air} is expressed in atmospheres. The equilibrium partitioning coefficient K_D is temperature dependent, and has been estimated in lab studies (Conklin and others, 1993) and field-based studies (McConnell and others, 1997b). K_D increases with decreasing temperature (Conklin and others, 1993); thus, cold snow has a larger capacity to uptake H_2O_2. The model of McConnell and others (1998) uses values of K_D from McConnell and others (1997b) which are somewhat larger than those of Conklin and others (1993).

Initially, snow grains are assumed to have uniform H_2O_2 concentration throughout the grain. During ice grain formation in the atmosphere, hydrogen peroxide is incorporated into growing ice grains through co-deposition (Conklin and others, 1993;

Neftel and others, 1995)(i.e. same molar ratio in the ice grain and the atmosphere). Co-deposition results in supersaturation of H_2O_2 in the solid phase (Equation (6.3)) in newly-formed snow grains, since K_D is much smaller than the co-deposition partitioning coefficient. Consequently, snow grains release H_2O_2 after formation (Bales and others, 1995) as the H_2O_2 concentration in the ice grains returns toward equilibrium with the surrounding air.

McConnell and others (1998) solved Equation (6.2) with a two-dimensional finite-difference scheme. Earlier studies (McConnell and others, 1997b) used an analytical solution, but were limited by assuming a uniform concentration in the grain at the beginning of each weekly time-step. They assumed a uniform H_2O_2 concentration in the grain to avoid calculating the large number of Fourier coefficients necessary if a variable initial concentration is assumed. In this study, I have used an analytical solution to Equation (6.2) which assumes an arbitrary initial condition condition ($C_r(r,0) = f(r)$) at the start of each time step.

I assume a constant H_2O_2 concentration on the grain surface throughout the time step (i.e. $C_r(a,t) = C_r(a)$, and use the coordinate transformation $u(r,t) = r\,C_r(r,t)$ to transform Equation (6.2):

$$\frac{\partial u}{\partial t} = D_i(T)\frac{\partial^2 u}{\partial r^2} \tag{6.4}$$

with the transformed boundary conditions $u(0,t) = 0$ and $u(a,t) = u(a) = a\,C_r(a)$ and the initial condition $u(r,0) = rf(r)$. This equation can be solved in closed form and transformed back to the original coordinates (Haberman, 1987, p.246):

$$C_r(r,t) = C_r(a,t) + \frac{1}{r}\sum_{n=1}^{\infty} a_n \sin\frac{n\pi r}{a} \exp\left(-D_i\left(\frac{n\pi}{a}\right)^2 t\right) \tag{6.5}$$

where a_n are the Fourier coefficients, given by:

$$a_n = \frac{2}{a}\int_0^a [r'f(r') - r'C_r(a)]\sin\frac{n\pi r'}{a}dr' \tag{6.6}$$

In order to calculate $C_r(r,t)$ over long time periods, I update the surface boundary condition $C_r(a)$ (which is a function of temperature (Equation (6.3)) several times a day. The profile resulting from Equation (6.5) after a single time step is used as the initial profile in the following time step. This solution technique obviates the need for the high temporal-resolution finite-difference solution of McConnell and others (1998), which was solved every 6 seconds.

However, this solution technique relies upon the Fourier expansion of the H_2O_2 concentration in the grain at the beginning of each time step. I retained as many Fourier coefficients as necessary to insure that the Fourier expansion of the initial profile differed from the real initial profile by less than 1% in all cases ($\sim 10^3$ Fourier coefficients were typically required).

I include the effects of ventilation-driven sublimation and condensation of water on the H_2O_2 concentration at the end of each time step. For a given snow density and grain radius, I calculate the number of snow grains and total surface area of the grains per cubic meter of firn. The average sublimation or condensation rate in the firn (expressed in kg $m^{-3}s^{-1}$ and determined using the methods of Chapter 3) is then converted to a change in snow grain radius by assuming that sublimation (or condensation) occurs evenly over all snow grains.

This analysis assumes that the total number of grains in a given volume (number density) is constant. In seasonal snow packs, Sturm and Benson (1997) have demonstrated the the number of grains per volume decreases by as much as 2 orders of magnitude during the winter season as a result of local water-vapor redistribution between grains. This decrease in the number of grains is associated with a factor of 3 increase in average grain radius. Gow (1969) measured rapid grain growth in the upper 4 m at South Pole, and slower growth below that depth, but did not report a decrease in the number density of snow grains with depth. Rapid grain growth and changes in the number density of grains could change the surface area to volume ratio of the snow pack, depending on the growth habit of the ice grains (Colbeck, 1983b).

Clearly, the effects of grain growth and changes in the number density of grains in polar snow warrants further study. In this preliminary analysis, I have assumed that ice grains can be approximated by ice spheres, that the grains remain spherical during periods of crystal growth, and that number density of grains is constant.

I assume that H_2O_2 does not fractionate during ice grain sublimation, and that the outer layers of the grain and all of the H_2O_2 within the layer is removed during sublimation. Consequently, sublimation does not affect H_2O_2 concentration directly, but decreases the snow grain radius. The decrease in radius facilitates the exchange of H_2O_2 between the ice grain and the surrounding pore space by shortening the diffusion path length.

The condensation of water vapor in firn has two effects on H_2O_2 in an ice grain. First, water vapor condensation increases the grain radius and increases the diffusion path length of H_2O_2. Second, I assume that water vapor and H_2O_2 are incorporated into the new ice layers in the same manner as ice grains grow in the atmosphere, that is through co-deposition (Conklin and others, 1993; Neftel and others, 1995). Consequently, ice layers added through condensation in the firn have a H_2O_2 concentration much higher than the equilibrium concentration for solid ice (Equation (6.3)).

This model assumes that C_{air} is known. McConnell and others (1998) used a one-dimensional advection-dispersion equation to calculate the evolution of C_{air} in the pore space air. In this simplified model, I use a prescribed value for C_{air} in order to demonstrate the effect of condensation and sublimation on the evolution of H_2O_2 concentrations in ice grains.

It should be pointed out that this model lacks several features that a complete model of H_2O_2 concentrations in firn should have. It needs a model for the evolution of C_{air} as air moves through the firn and H_2O_2 is exchanged with surrounding snow grains. Other mechanisms should also be included, such as downward advection of snow grains due to snow accumulation (e.g McConnell and others 1997b, 1998), other mechanisms for grain growth (e.g. radius-of-curvature effect (Colbeck, 1980); temperature-gradient grain growth (Sommerfeld and LaChapelle, 1970)) and vertical strain. The model presented in this chapter is designed to be applied at a point in the 2-D section of firn described in Chapter 3.

6.4 Results

I tested the output of the model presented here against results presented in McConnell and others (1997b) and McConnell and others (1998). In McConnell and others (1997b), the response of the H_2O_2 concentration in a 200 μm grain to a step change in surface H_2O_2 concentration at a specified temperature was presented. At -40 °C, the H_2O_2 concentration reached a new steady-state concentration after 20 weeks; at -30 °C, a new steady-state was reached after 15 weeks. My model was able to replicate these results, which suggests that Equation (6.5) is appropriate, and that my parameterization of the temperature-dependent diffusivity D_{i} is also approximately correct. I was able to improve agreement with the McConnell and others (1997b) results by decreasing my diffusivity by $\sim$ 50 %.

I also verified my model performance using the results presented in McConnell and others (1998) as a second benchmark. McConnell and others (1998) showed that the H_2O_2 concentration of the center of an 80 μm grain lagged almost 5 weeks behind the mean concentration of the grain, reflecting the time-scale of diffusion into the center of the grain. They modelled the radial H_2O_2 concentration of the grain over the course of a year using the surface temperature and atmospheric H_2O_2 record from South Pole station. I calculated the radial concentration with my model using estimates for the atmospheric H_2O_2 concentration as a function of temperature. My results indicate that H_2O_2 concentration at the center of the grain lag the mean concentration by only 2 weeks. The difference could again be a result of a slightly higher diffusivity D_{i} in my model, or differences in the temperature and atmospheric H_2O_2 histories I have used.

The numerical solution of McConnell and others (1998) subdivided individual grains into 10 concentric shells. My solution technique uses numerical integration (Equation (6.6)) over the grain radius to calculate the Fourier coefficients. Consequently, this model is susceptible to errors induced through the discretization of the grain radius. Figure 6.1 shows the sensitivity of my numerical solution to the number of concentric shells in each grain. In this figure, I tracked the H_2O_2 concentration changes for a given set of environmental conditions and varied only the number of shells in the grain. It is evident that the modelled grain concentration is sensitive to the number of shells used for fewer than $\sim$ 75 shells. In the following results, I have used 80 shells in each model run.

Sublimation and condensation rates are calculated using the methods described in Chapter 3, which follows the governing equations of Albert (2002). In short, sublimation and condensation in the firn are the result of the interaction between firn temperature and the local relative humidity. If air flow through the firn (ventilation) brings cool and relatively dry pore-space air into a warmer area, the pore space air will be under-saturated, and some of the surrounding ice grains will sublimate. Conversely, if vapor is advected from a warm area into a cooler area, the pore-space air will be super-saturated and some of the vapor condenses onto the surrounding snow grains. Using this model, I estimated that sublimation or condensation rates may be as large as $\pm$ 7 $\times$ 10^{-6} kg $m^{-3}s^{-1}$ in regions or air inflow during the summer season. The model predicts that sublimation and condensation rates are as much as 2 orders of magnitude higher during the summer season, primarily as a result of the exponential relationship between vapor pressure and temperature (Appendix E).

In order to isolate the effects of water vapor motion on H_2O_2 concentration, I conducted a series of tests on a single grain both with and without sublimation or condensation effects. For all results presented below, I used a 1 mm grain size.

The H_2O_2 model ran for 14 model days. Grain temperature was calculated assuming a daily temperature cycle (5°C amplitude), as in Chapter 5. The sublimation and condensation rates used here also reflect the daily cycle (as in Section 5.4.2). I assumed that the grain was located at 25 cm depth in a region of air inflow. The temperature and sublimation/condensation time series used are shown in Figure 6.2.

The upper panel of Figure 6.3 shows the model prediction of radially averaged H_2O_2 concentration without sublimation/condensation effects. Hydrogen peroxide is initially incorporated into the grain through co-deposition, which results in H_2O_2 super-saturation in the grain (initial concentration $\sim$ 22.8 μM l^{-1}), relative to equilibrium concentration. Consequently, the H_2O_2 concentration in the grain decreases through time toward equilibrium values ($\sim$ 6 μM l^{-1}). The surface H_2O_2 concentration (shown in the lower panel of Figure 6.3) reflects the temperature-dependence of the equilibrium coefficient K_D (Equation 6.3). The diurnal temperature cycle in the firn causes surface H_2O_2 concentration to vary between 3 and 10 μM l^{-1}. The decrease in average surface H_2O_2 concentration due to increasing temperature (Fig. 6.2) is evident.

Model results with sublimation and condensation effects included are shown in Figure 6.4. When sublimation and condensation effects are included, the ice grain radius changes through time, as described above. Figure 6.2 shows that the cycle of sublimation and condensation in the firn does not quite balance over a day, and the grain experiences net condensation (Section 5.4.2). In the upper panel of Figure 6.4, the gradual increase in the grain radius over the 14 day model run is apparent. The radius change is modest, reflecting a $\sim$ 1 μm growth in a two-week span.

Sublimation decreases the grain radius, promoting more rapid equilibration by shortening the diffusion path length. Condensation inhibits equilibration in two ways: by increasing the diffusion path length and by increasing the surface concentration of H_2O_2 through co-deposition. Since condensation predominates over the daily cycle, the rate of equilibration is expected to be slower when sublimation and condensation effects are included. However, the magnitude of these effects are small, owing to the small sublimation and condensation rates. The lower panel of Figure 6.4 shows the

difference between the radial concentration profiles when sublimation and condensation effects are included and when they are neglected. Positive values indicate regions where the H_2O_2 concentration is higher when sublimation and condensation effects are included. Over the 14 day model run, most of the changes are in the outer-most half of the grain. The concentration difference in the outermost part of the grain show the effects of the condensation during the last few hours of the model run (Fig. 6.2). Through time, these effects result in higher average H_2O_2 concentrations in the grain during the summer than if condensation/sublimation are neglected, although the magnitude of the effect is small ($< 1\%$ change in H_2O_2 concentration).

Currently, the length of the model run is limited by the temperature and sublimation/condensation time series, which are computationally intensive (Chapter 3). I generated longer time series of these parameters by using the existing time series several times in succession, such that the patterns shown in Figure 6.2 repeat after 14 days. Figure 6.5 shows model predictions for H_2O_2 change over a 90 day period (the summer season). The upper panel shows changes in grain radius over 90 days, and the lower panel shows the effect of including sublimation/condensation on radial H_2O_2 concentration as in Figure 6.4. This analysis predicts that including the effects of sublimation and condensation will change H_2O_2 concentration by up to 0.035 μM l^{-1}.

6.5 Discussion

In the above analysis, I have restricted the calculation to include only changes during the summer season. During the winter season temperatures are lower (leading to much smaller H_2O_2 diffusivity (Conklin and others, 1993)), atmospheric H_2O_2 concentrations are much lower (McConnell and others, 1998) and sublimation/condensation rates are much smaller. Consequently, the effects of firn ventilation on H_2O_2 concentrations will be reduced further in winter. Further work will be used to analyze the impact of neglecting other seasons, as longer temperature and sublimation/condensation

time series become available.

As shown in Figures 6.4 and 6.5, firn ventilation likely has a very small effect on H_2O_2 concentrations in firn. Several investigators (e.g. McConnell and others, 1998) have demonstrated that H_2O_2 concentrations in firn vary between $\sim$ 2 and 20 μM l^{-1}. These changes are primarily due to H_2O_2 equilibration between the ice grain and pore space vapor, and the subsequent spherical diffusion within the ice grain. The model of McConnell and others (1998) matches the major features of H_2O_2 concentration in the upper few meters at the South Pole. Although the model replicated the amplitude of the H_2O_2 record, there was disagreement between the modelled and measured depth of the major structure of the H_2O_2 profile. This disagreement was likely a result of the difficulty in determining the timing and magnitude of accumulation events. Some of the disagreement between the model and measurements in McConnell and others (1998) may also be due to variability in the type of accumulation. Some of the accumulated snow was new accumulation, in which H_2O_2 concentration is governed by co-deposition. However, an unknown fraction was likely wind-blown snow, which should have H_2O_2 concentration between that of co-deposition and full equilibrium with the atmosphere.

This model predicts very slow grain growth due to firn ventilation, on the order of 3 μm per year. Measurements by Gow (1969) at the South Pole showed that snow grain radius increases by $\sim$ 200 μm in the upper 1.5 meters of the firn, which was attributed to large near-surface temperature gradients. If we assume an accumulation rate of snow of 0.25 m of snow per year (McConnell and others 1997a), this translates to a grain growth rate of $\sim$ 35 μm per year in the upper 1.5 meters. Sturm and Benson (1997) suggest that an inter-particle water-vapor flux is largely responsible for grain growth. The results of both Gow (1969) and Sturm and Benson (1997) suggest that the present analysis under-predicts grain growth rates (perhaps by an order of magnitude), and that additional processes are active in upper few meters, although neither Gow (1969) nor Sturm and Benson (1997) identify these additional

processes. Additional mechanisms for water-vapor transport (such as radius of curvature grain growth, described by Colbeck, 1980) in the firn should enhance the effect of condensation on H_2O_2 concentration in snow grains. However, unless the above analysis underestimates the water-vapor flux by several orders of magnitude, water-vapor motion will have a small effect on H_2O_2 concentration in the firn. Initial estimates of the inter-particle vapor flux by Sturm and Benson (1997) suggest that it is $\sim$ an order of magnitude less than the vapor flux due to wind-ventilation.

Other investigators have suggested that wind-ventilation effects are responsible for the loss of volatile species in ice. Lal and others (2001) attributed the deficiency of in situ ^{14}C in samples from Vostok and Taylor Dome, Antarctica to wind-ventilation processes. ^{14}C is produced by spallation of oxygen atoms in ice grains, and exists as either CO or CO_2 in snow grains. Sublimation releases ^{14}C, and it is lost irretrievably to the atmosphere.

Similarly, Wagnon and others (1999) reported rapid loss of volatile species (Cl, F, NO_3, MSA) in the upper 5 meters of the firn at Vostok, Antarctica. Although methane sulphonate (MSA) is generally considered a hydrophilic species (Chapter 5), data of Wagnon and others (1999) from Vostok and data from the Antarctica Peninsula of Pasteur and Mulvaney (2000) suggest that MSA may exist partially in the vapor phase. The authors suggest that firn metamorphic processes are responsible for the loss of volatile species, but do not identify which processes are most likely responsible.

The model results presented here suggest that the main loss mechanism for H_2O_2 is not sublimation induced by firn ventilation. It is also unlikely that inter-particle water-vapor transport can modify H_2O_2 concentrations in firn, unless the above analysis underestimates the water-vapor flux by several orders of magnitude. However, for other reversibly-deposited (hydrophobic) species with much lower solid-state diffusivities (such that spherical diffusion is slower) post-depositional water-vapor motion may be more important. Depending on the environmental conditions, either firn-ventilation induced or inter-particle water-vapor motion may be the dominant

mechanism for the release of volatile species from the firn. Ultimately, a coupled model that combines aspects of the firn ventilation model reported here with a model for grain growth (such as Colbeck, 1983a, 1983b or Gubler, 1985) will be required to quantitatively address the issue of preservation and release of volatile species in firn.

6.6 Conclusions

McConnell and others (1998) showed that preservation of H_2O_2 is largely a function of grain size, ventilation rate and timing, and magnitude and timing of snow accumulation. The most important component for release of H_2O_2 from snow grains are spherical diffusion within the grain and equilibration with H_2O_2 in the pore space vapor. This study has shown that these processes account for a much larger fraction of post-depositional H_2O_2 concentration change than H_2O_2 change due to sublimation or condensation in the firn.

The model presented here predicts that sublimation and condensation induced by firn ventilation increases grain radius by $\sim$3 μm per year, which is approximately an order of magnitude slower than the grain growth measured by Gow (1969), and that H_2O_2 concentration in the firn can increase by up to 0.35 μM l^{-1} during the summer season. Given that the seasonal variability of H_2O_2 in surface firn is $\sim$ 20 μM l^{-1}, firn-ventilation induced changes must be considered a secondary effect.

Other mechanisms for water vapor redistribution are active in the firn, such as inter-particle water-vapor flow. These processes may be more efficient at moving water vapor than firn ventilation. However, unless these processes redistribute several orders of magnitude more water vapor than firn ventilation, this study suggests that post-depositional water-vapor redistribution will have a minimal effect on H_2O_2 concentrations in the firn.

However, this study also suggests that post-depositional water-vapor flow may be important in the preservation of species with a smaller diffusivity in the ice matrix

than H_2O_2 , or species which are generated within the ice matrix, such as ^{14}C. In these cases sublimation will release the species, and spherical diffusion will have a minor role. A quantitative process-based model for the release of other volatile species in the firn should include both inter-particle and firn-ventilation induced water-vapor fluxes, as well as spherical diffusion and equilibration.

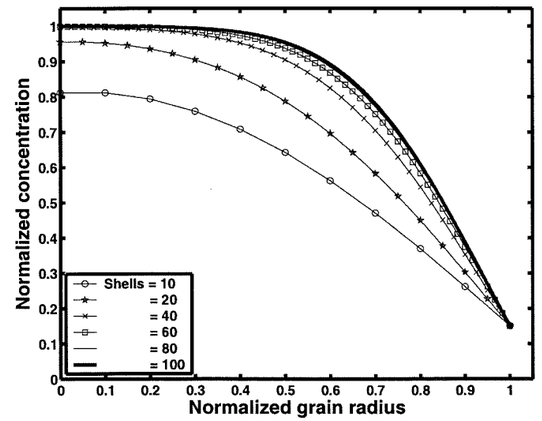


Figure 6.1: Sensitivity to grain discretization for model for reversible species. In these results, I ran the models with the same environmental parameters (no sublimation/condensation, temperature = -20°C) and same initial and surface boundary conditions; varying only the number of concentric shells in the grain. Differences arise due to numerical integration in calculating Fourier coefficients (Equation (6.6)). Differences are small when the number of shells is > 75.

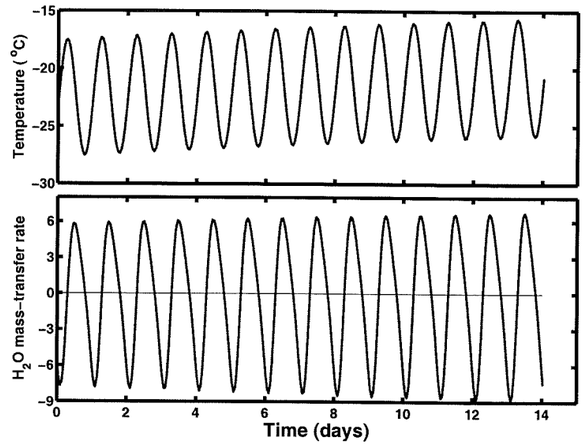


Figure 6.2: Upper panel shows temperature (in °C) time series used in model for H_2O_2 concentration changes. Lower panel shows sublimation/condensation rate (expressed in 10^{-6} kg m^{-3} s^{-1}) time series used in test of firn ventilation on H_2O_2 concentration. Temperature and sublimation/condensation rates calculated at 25 cm depth, using the methods described in Chapter 3 and Section 5.4.2. Positive (negative) values in lower panel indicate sublimation (condensation). Note that over the daily cycle, the grain will experience net condensation since condensation occurs during the warm part of the day when vapor densities are highest.

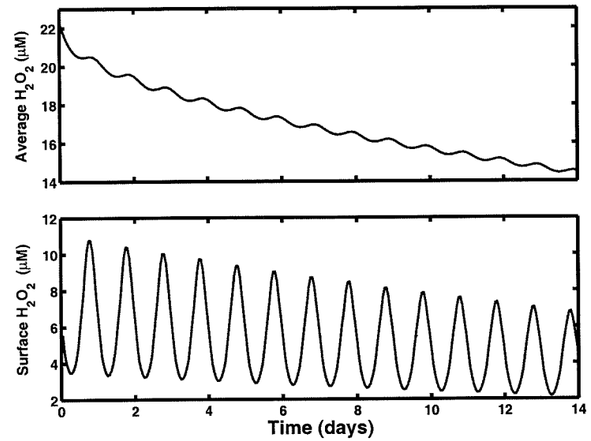


Figure 6.3: Upper panel shows radially-averaged H_2O_2 concentration (expressed in μM l^{-1}) during 14 day model run. Concentrations are initially super-saturated because of co-deposition. Lower panel shows surface concentration of H_2O_2 (expressed in μM l^{-1}) during 14 model days. Surface H_2O_2 concentration is sensitive to changes in the atmospheric H_2O_2 concentration and temperature (Fig. 6.2, Equation (6.3)).

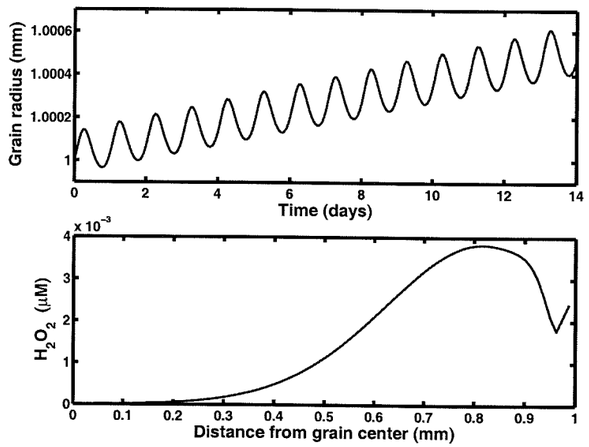


Figure 6.4: Upper panel shows changes in the grain radius r due to sublimation (radius decreases) and condensation (radius increases) during 14 model days. Since condensation predominated, grain grows by ~ 0.5 μm in the two-week span. Lower panel shows effect of sublimation/condensation on H_2O_2 concentration (expressed in μM l^{-1}). Line indicates concentration difference (with sublimation/condensation - without sublimation/condensation) as a function of the radius at the end of 14 model days. Positive values indicate higher H_2O_2 concentration when sublimation/condensation effects are included.

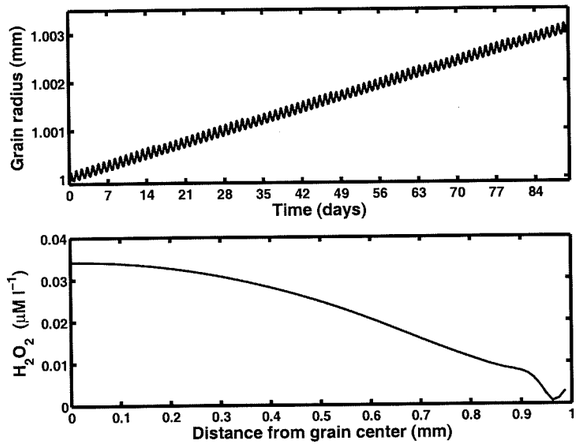


Figure 6.5: Upper panel shows changes in the grain radius r due to sublimation (which decreases the radius) and condensation (which increases the radius) during a 90 day model run. Lower panel shows cumulative effect of sublimation/condensation on H_2O_2 concentration (expressed in μM l^{-1}). Line indicates concentration difference (with sublimation/condensation - without sublimation/condensation) as a function of the radius at the end of 90 model days. Positive values indicate larger H_2O_2 concentration when sublimation/condensation effects are included.

Chapter 7

CONCLUSION AND SUMMARY

In this chapter, I summarize conclusions from previous chapters regarding the magnitude of water-vapor motion induced by firn ventilation, and the implications for snow geochemistry.

7.1 Vapor Motion in Firn

My model of subsurface water-vapor motion induced by firn ventilation is ideal for generating initial estimates under a wide variety of environmental conditions. I have applied the model to estimate sublimation and condensation rates in the firn for environmental conditions typical on the Antarctic plateau. In order to obtain realistic results for a specific site, local measurements of surface temperature, wind speed, surface topography, accumulation rate, grain size as a function of depth and the permeability of the firn are needed for model input.

Subsurface mass-exchange rates are exponentially proportional to temperature gradients. Firn temperature in the upper meter is influenced by short-term variations in surface temperature caused by synoptic-scale weather or diurnal cycles, while firn temperature below the upper meter is influenced by seasonal temperature variations. Short-term variations can generate larger temperature gradients, and consequently larger sublimation and condensation rates in firn than seasonal temperature cycles. Using an idealized surface temperature cycle (sinusoidal with 24 hour period and 5°C amplitude), the model predicts a daily cycle of sublimation and condensation in the upper meter that is nearly symmetric: rapid sublimation during the cold parts of the

day are balanced by rapid condensation during the warm parts of the day. However, since vapor density is an exponential function of temperature, sublimation does not quite balance condensation, and the model predicts net condensation over a diurnal cycle in the upper 1 meter of the firn in regions of air inflow.

Short-term surface temperature variations at a site could generate much different sublimation or condensation rates. The model predicts temperature gradients as large as 35°C m^{-1} as a result of the daily cycle, while seasonal temperature variations generate more moderate temperature gradients (typically 5°C m^{-1}).

Air flow into the firn usually reaches local saturation vapor density in the upper 1 cm of the firn. Consequently, atmospheric relative humidity has a negligible effect on mass-exchange rates below the upper centimeter. The primary importance of firn ventilation is to increase temperature gradients in the firn, rather than to carry large (or small) vapor density from the atmosphere into the firn.

In general, the model predicts that mass-exchange rates are much larger during summer than winter. This is primarily due to the strong temperature dependence of water vapor pressure over ice (Equation (E.1)). Consequently, winter can be ignored when studying the cumulative effects of subsurface water-vapor motion on time scales longer than 1 year. However, if the amplitude of the snow surface topography or the mean wind speed change throughout the year (as suggested by Albert and Hawley, 2002), mass exchange during all seasons could be important.

The predicted mass-exchange rate is strongly influenced by the mean size of snow grains in the firn. Large grains have lower instantaneous mass-exchange rates, which allow differences between local vapor pressure and saturation vapor pressure to persist. Hence, larger mean mass-exchange rates occur with larger grains. Small grains exchange water vapor rapidly, causing air in firn pore spaces to essentially always be saturated.

Some investigators have suggested that the diffusivity of water vapor in snow D_s is up to five times larger than the diffusivity of water vapor in air as a result of

hand-to-hand diffusion (e.g. Yosida and others, 1955; Colbeck, 1993). In hand-to-hand diffusion, the large contrast in thermal conductivity between air and ice leads to large temperature and vapor density gradients in the pore spaces, and nearly isothermal ice grains. On the grain scale, hand-to-hand diffusion may accelerate grain metamorphism, as water vapor is condensed onto one side of the grain, and sublimated from the other side. However, on a multi-grain scale, high D_s leads to a decrease in the sublimation or condensation rate in the firn below the upper meter. Rapid diffusion of water vapor due to large values of D_s reduce the difference between local vapor density and saturation vapor density as a result of rapid diffusion of water vapor. Since phase changes are driven by the difference between local vapor density and saturation vapor density, increasing D_s leads to a decrease in mass-exchange rate.

My model for water-vapor transport is focused on the influence of firn ventilation. However, other mechanisms for water-vapor redistribution are active in the firn. These include inter-particle water-vapor flow (Sturm and Benson, 1997) or hand-to-hand diffusion (Yosida and others, 1955; Colbeck, 1993) which may also be important. Together, these processes have been described as firn diagenesis (Alley, 1988) or metamorphism (Colbeck, 1983a), and may contribute to the formation of depth hoar layers in firn and the increase in grain size with depth noted by Gow (1969) and other investigators. These processes may be more efficient than firn ventilation at moving water vapor on the grain scale. Both the vapor flux (Sturm and Benson, 1997) and the growth habit (Colbeck, 1983b) may be important for the preservation of some geochemical species, as well as for sub-surface air flow velocities (Colbeck, 1997). Ultimately, a coupled model that combines firn ventilation and grain growth (e.g. Colbeck, 1983a, 1983b or Gubler, 1985) should be developed to generate a complete model of water-vapor motion in firn, but this is outside the scope of this dissertation.

7.2 Implications for Geochemistry

7.2.1 Stable Isotopes

My two-dimensional isotope model is a step towards a process-based understanding of post-depositional stable isotope change in firn. The model tracks the evolution of the isotopic composition of both the pore-space vapor and the firn in a two-dimensional cross-section of the firn. Isotopes are redistributed in the firn as a result of: (a) advection of atmospheric vapor (with a specified isotopic composition) as a result of forced air flow through the firn (ventilation or wind pumping; Clarke and others, 1987), (b) diffusion along isotopic gradients in the pore-space vapor, (c) isotopic equilibration between vapor and solid and (d) sublimation and condensation in the firn.

Model results confirm what other investigators have suggested: isotopic diffusion in the upper few meters is more rapid than can be explained by the Whillans and Grootes (1985) model (or variations thereof); isotopic equilibration with atmospheric vapor is an important component of post-depositional isotopic change (Waddington and others, 2002); and firn ventilation can enhance isotopic exchange (Neumann, 2001). In comparison with the models of Whillans and Grootes (1985) or Johnsen and others (2000), firn ventilation increases the effective isotopic diffusivity by up to 50% in regions of air inflow and by 20% in regions of air outflow.

Future development of the isotopic model will focus on reducing the uncertainty in the isotopic equilibration coefficient and including model kinematics to account for the effects of snow accumulation and strain. In addition, isotopic inhomogeneities within individual snow grains may be important (e.g. Rempel and Wettlaufer, in press) and their influence on isotopic diffusion in the firn should be examined further.

7.2.2 *Irreversibly-Deposited Species*

The concentration of irreversibly-deposited species in snow can be increased by sublimation of the surrounding ice grains, or decreased by water condensation around impurities. In order to isolate the effect of firn ventilation on chemical concentration, I avoid chemical species that have complex photochemistry or gaseous components, and focus on non sea salt (nss-) sulfate. I assume that the behavior of nss-sulfate is representative of other irreversibly-deposited (i.e. hydrophilic) species.

Using only the seasonal temperature cycle, the model predicts total mass exchange of ~ 1 kg m^{-3} of sublimation or condensation over the summer season. The magnitude of mass exchange in the firn due to the daily temperature cycle is similar to those due to the seasonal cycle. This water-vapor redistribution results in very modest changes ($< 1\%$) in the concentration of nss-sulfate and other irreversibly deposited species.

The concentrations of many irreversibly-deposited species vary seasonally. In the case of nss-sulfate, the atmospheric concentration varies up to 2 orders of magnitude and the concentration in firn varies by a factor of 2 or more (Harder, 2000; Stenberg, 2000) during the annual cycle. The predicted concentration change due to firn ventilation in a single season is much smaller than the annual variability in nss-sulfate; it is unlikely that firn ventilation causes measurable changes in nss-sulfate. If surface topography is stationary in time, the effects of firn ventilation on nss-sulfate concentration may be cumulative. For a constant vertical velocity of 0.20 m yr^{-1}, my model estimates total cumulative concentration change in nss-sulfate in regions of air inflow of 3%, which is still far less than the annual variability in the firn. Post-depositional changes may be measurable in other irreversibly-deposited species that have a relatively constant or well-characterized flux to the snow surface throughout the year.

7.2.3 *Reversibly-Deposited Species*

Reversibly-deposited, or volatile species generally exist as trace gasses in the polar atmosphere (e.g. HF, HCL, HNO_3, HCHO, H_2O_2) and are scavenged by ice grains growing in the atmosphere. Unlike irreversibly-deposited species, such as most aerosols, a fraction of the mass of volatile species in a snow grain cycles between the atmosphere and snow through time. The concentration of reversibly-deposited species in snow is decreased by sublimation of the surrounding ice grain, as reversibly-deposited species generally exist as gasses. The effect of condensation on reversibly-deposited species depends in part on the species. However in general, condensation increases the diffusion path length by increasing the grain radius. In addition, the process of condensation in the firn can scavenge trace gasses out of pore-space air. In order to isolate the effect of the redistribution of water on chemical concentration, I avoid chemical species that have complex photochemistry (NO_x) or interact readily with snow (OH^-), and focus on H_2O_2 . I assume that the behavior of H_2O_2 is representative of other reversibly-deposited species (e.g. Waddington and others, 1996).

My model for reversibly-deposited species predicts that sublimation and condensation induced by firn ventilation increases grain radius by ~ 3 μm per year, which is approximately an order of magnitude slower than the grain growth measured by Gow (1969), and that H_2O_2 concentration in the firn can increase by up to 0.35 μm l^{-1} during the summer season. Given that the seasonal variability of H_2O_2 in surface firn is ~ 20 μm l^{-1}, firn-ventilation induced changes must be considered a secondary effect.

As described above, other mechanisms for water vapor redistribution are active in the firn, such as inter-particle water-vapor flow. These processes may be more efficient at moving water vapor than firn ventilation on the grain-scale (~ 1 mm). However, unless these processes redistribute several orders of magnitude more water vapor than

firn ventilation, this study suggests that post-depositional water-vapor redistribution will have a minimal effect on H_2O_2 concentrations in the firn.

However, this study also suggests that post-depositional water-vapor redistribution may be important in the preservation of species with a smaller diffusivity in the ice matrix than H_2O_2 , or species that are generated within the ice matrix, such as ^{14}C. In these cases sublimation will release the species, and diffusion with the snow grain will have a minor role. A quantitative process-based model for the release of other volatile species in the firn may need to include water-vapor fluxes induced by both inter-particle exchange and firn ventilation, as well as spherical diffusion and chemical equilibration between snow grains and pore space vapor.

7.3 Future Research

Including other processes responsible for water-vapor motion in the firn is an important next step in the development of a process-based model for post-depositional changes in firn. In particular, the grain-scale process of inter-particle water-vapor flux (Sturm and Benson, 1997) and the effects of hand-to-hand diffusion should be incorporated. These processes could be important for releasing volatile species from the firn, and contributing to isotopic fractionation in the firn.

In addition, the model should be adapted to accommodate the accumulation of new snow at the snow surface, and strain within the firn. Accounting for these processes would permit the study of seasonal cycles in firn microstructure, and a more realistic estimate of condensation and sublimation at different times during the year. In addition, accounting for accumulation and strain would allow comparison of the relative importance of this model of isotopic diffusion (which reduces the amplitude of seasonal isotopic cycles) and strain (which reduces the wavelength of isotopic cycles). Strain is less important in the upper 3 meters than ventilation-driven diffusion of stable isotopes, but more important below that depth. Including strain would allow

me to use this model to analyze isotopic change to a much greater depth.

7.3.1 An Inverse Problem

As demonstrated in detail throughout this dissertation, different geochemical indicators respond in different ways to post-depositional redistribution and loss of water. This opens the possibility of determining the fractional loss of H_2O by sublimation and any subsequent redeposition by measuring an appropriate suite of geochemical species. The key to the success of this idea is to choose geochemical species that respond differently enough to sublimation and condensation (i.e. are orthogonal functions with respect to sublimation and condensation) to be able to use geophysical inverse techniques (e.g. Menke, 1989) to solve for the sublimation and condensation rates in the firn. Here I present some thoughts on the inversion, and identify geochemical species that may be good candidates for the inverse problem.

As shown in Chapter 4, stable isotopic ratios in the firn are sensitive to both sublimation and condensation in the firn. Sublimation does not affect the isotopic composition of ice grains directly, but changes the composition of the pore space vapor. Condensation affects the isotopic composition of both the pore space vapor and the solid ice grains. Sublimation and condensation should affect stable isotope ratios in the upper 2 meters of the firn. Separating the effects of sublimation and condensation from isotopic equilibration between the firn and the atmosphere will be difficult, and may require measurements of the isotopic composition of the atmospheric vapor at a site over several years. If these measurements are available, or can be characterized to a high degree of accuracy, stable isotope ratios can be used in an inversion to determine sublimation and condensation rates.

Chapter 5 demonstrated that concentrations of irreversibly-deposited species are largely insensitive to sublimation or condensation in the firn. For example, the estimated magnitude of the change in nss-sulfate concentration due to firn ventilation was several orders of magnitude less than the seasonal cycle of nss-sulfate in the firn. This

suggests that, unless the initial concentration of an irreversibly-deposited geochemical species at the snow surface is known with a high degree of accuracy throughout the year, it will not be possible to measure concentration changes due to firn ventilation. A possible candidate species is ^{10}Be. The concentration of ^{10}Be in the atmosphere and the deposition of ^{10}Be to the snow surface throughout the year have been studied. Although, given the low sensitivity of irreversibly-deposited species to sublimation and condensation in the firn, even ^{10}Be will likely not be useful in the inverse problem.

It is possible that reversibly-deposited species may be useful. The concentration of species that have an appreciable solid-state diffusivity in solid ice grains (such as H_2O_2) are primarily influenced by diffusion through ice grains and equilibration with gas-phase species in the atmosphere (McConnell and others, 1998). Other species with lower solid-state diffusivities will be more strongly influenced by sublimation and condensation in the firn. As discussed above, sublimation releases volatile species from the ice matrix, while the influence of condensation is species-specific.

An additional requirement of using a volatile species in the inverse problem is a known (or know-able) initial concentration at the snow surface. Species like H_2O_2 have large seasonal fluctuations in atmospheric concentration, which leads to large variations in H_2O_2 concentration at the snow surface throughout the year. Other gas-phase species (such as HF) have not been measured in either the snow surface or the atmosphere, and so their seasonal variability is unknown. An alternative is to use ^{14}C, which is produced by spallation of oxygen atoms in the ice grain, and exists as either CO or CO_2 in snow grains. The production rate of ^{14}C in polar snow has been well-studied (Lal and others, 2001). If the mobility of CO and CO_2 within ice grains is small (less than that of H_2O_2), ^{14}C could be used in the inverse problem. However, volatile species are released as a result of both ventilation-driven sublimation and condensation in the firn and grain metamorphism, and these effects on ^{14}C would need to be quantified and separated in order to determine the sensitivity of ^{14}C to sublimation and condensation in the firn. This result points toward the need for a

quantitative process-based model for grain metamorphism in polar snow.

A field program could be used to validate both the predictions of firn-ventilation induced geochemical change in firn and use these measurements to infer precipitation and evaporation components of net accumulation. Ideally, the study should be conducted at sites with large spatial gradients of accumulation rate. Large spatial gradients make it possible to measure changes at both a 'control' location (where a high accumulation rate minimizes post-depositional changes) and a 'sample' location (where a lower accumulation rate makes post-depositional changes larger). Since post-depositional changes at the 'control' site will be small, it is possible to extrapolate these measurements to estimate the initial concentration of snow at the 'sample' site. At Taylor Dome, Antarctica, the net accumulation rate varies by an order of magnitude over 40km (Morse and others, 1999), making it an attractive site for field measurements of post-depositional geochemical changes.

In conclusion, it may be possible to use geochemical measurements to separate the net accumulation of snow into precipitation and evaporation components through an inverse model. Irreversibly-deposited species are probably not useful in this inversion, but both stable isotopes and reversibly-deposited species should be diagnostic. In order to reach that goal, the model for water-vapor redistribution in the firn presented here should be expanded to include grain-scale processes. Furthermore, a campaign to measure temporal variations of both the isotopic composition of atmospheric vapor and the isotopic composition of the firn should be conducted.

BIBLIOGRAPHY

Albert, M.R., Modeling heat, mass, and species transport in polar firn, *Annals of Glaciology*, *23*, 138-143, 1996.

Albert, M.R., Effects of snow and firn ventilation on sublimation rates, *Annals of Glaciology*, *35*, 52-56, 2002.

Albert, M.R., E.M. Arons and R.E. Davis, Firn properties affecting gas exchange at Summit, Greenland: Ventilation possibilities, In Wolff, E.W. and R.C. Bales (Ed.), *Chemical Exchange Between the Atmosphere and Polar Snow*, NATO Advanced Science Institutes Series, vol. 43, Springer-Verlag, 561-565, 1996.

Albert, M.R. and R.L. Hawley, Seasonal changes in snow surface roughness characteristics at Summit, Greenland: implications for snow and firn ventilation, *Annals of Glaciology*, *35*, 510-514, 2002.

Albert, M.R. and W.R. McGilvary, Thermal effects due to air flow and vapor transport in dry snow, *Journal of Glaciology*, *38*(129), 273-281, 1992.

Albert, M.R. and E.F. Shultz, Snow and firn properties and air-snow transport processes at Summit, Greenland, *Atmospheric Environment*, *36*(15-16), 2789-2797, 2002.

Albert, M.R., E.F. Schultz and F.E. Perron, Jr., Snow and firn permeability at Siple Dome, Antarctica, *Annals of Glaciology*, *31*, 353-356, 2000.

Alley, R.B., Concerning the deposition and diagenesis of strata in polar firn, *Journal of Glaciology*, *34*(118), 283-290, 1988.

Bales, R.C., M.V. Losleben, J.R. McConnell, K. Fuhrer and A. Neftel, H_2O_2 in snow, air and open pore space in firn at Summit, Greenland, *Geophysical Research Letters*, *22*(10), 1261-1264, 1995.

Benfield, A.E., The temperature distribution in an accumulating snowfield, *Monthly Notices of the Royal Astronomical Society Geophysical Supplement*, *6*(3), 139-147, 1951.

Benoist, J.P., J. Jouzel, C. Lorius, L. Merlivat and M. Pourchet, Isotope climatic record over the last 2.5 ka from Dome C, Antarctica, ice cores, *Annals of Glaciology*, *3*, 17-22, 1982.

Benson, C.S., Stratigraphic studies in the snow at Byrd Station, Antarctica, compared with similar studies in Greenland, In Crary (Ed.), *Antarctic Snow and Ice Studies II*, Antarctic Research Series Vol. 16, American Geophysical Union, USA, 333-353, 1971.

Bergin, M.H., J.-L. Jaffrezo, C.I. Davidson, J.E. Dibb, S.N. Pandis, R. Hillamo, W. Maenhaut, H.O. Kuhns and T. Makela, The contributions of snow, fog, and dry deposition to the summer flux of anions and cations at Summit, Greenland, *Journal of Geophysical Research*, *100*, 16,275-16,288, 1995.

Bintanja, R., Snowdrift sublimation in a katabatic wind region of the Antarctic ice sheet, *Journal of Applied Meteorology*, *40*(11), 1952-1966, 2001.

Bolzan, J.F. and V.A. Pohjola, Reconstruction of the undiffused seasonal oxygen isotope signal in central Greenland ice cores, *Journal of Geophysical Research*, *105*(C9), 22,095-22,106, 2000.

Chu, J.C., J. Kalil and W. Wetteroth, Mass transfer in a fluidized bed, *Chemical Engineering Progress*, *49*(3), 141-149, 1953.

Christensen, L.E., M. Okumura, S.P. Sander, R.J. Salawitch, G.C. Toon, B. Sen, J.-F. Blavier, and K.W. Jucks, Kinetics of $HO_2 + HO_2 \rightarrow H_2O_2 + O_2$: Implications for stratospheric H_2O_2, *Geophysical Research Letters*, *29*(9), 1299, doi:10.1029/2001GL014525, 2002.

Ciais, P., J.W.C. White, J. Jouzel, J.R. Petit, The origin of present-day Antarctic precipitation from surface snow deuterium excess data, *Journal of Geophysical Research*, *100*(D9), 18,917-18,927, 1995.

Clarke, G.K.C., D.A. Fisher and E.D. Waddington, Wind pumping: a potentially significant heat source in ice sheets, In Waddington and Walder (Eds.), *The Physical Basis of Ice Sheet Modelling*, IAHS-AISH Publication No. 170, 169-180, 1987.

Clow, G.D., Generation of liquid water on Mars through the melting of a dusty snowpack, *Icarus*, *72*, 95-127, 1987.

Colbeck, S.C., Thermodynamics of snow metamorphism due to variations in curvature, *Journal of Glaciology*, *26*(94), 291-301, 1980.

Colbeck, S.C., Growth of faceted crystals in snow cover, *CRREL Report 82-29*, 1982.

Colbeck, S.C., Theory of metamorphism of dry snow, *Journal of Geophysical Research*, *88*(C9), 5475-5482, 1983a.

Colbeck, S.C., Ice crystal morphology and growth rates at low supersaturations and high temperatures, *Journal of Applied Physics*, *54*(5), 2677-2682, 1983b.

Colbeck, S.C., Air movement in snow due to windpumping, *Journal of Glaciology*, *35*(120), 209-213, 1989.

Colbeck, S.C., Vapor-pressure dependence on temperature in models of snow metamorphism, *Journal of Glaciology*, *36*(124), 351-353, 1990.

Colbeck, S.C., The vapor diffusion coefficient for snow, *Water Resources Research*, *29*(1), 109-115, 1993.

Colbeck, S.C., Model of wind pumping for layered snow, *Journal of Glaciology*, *43*(143), 60-65, 1997.

Conklin, M.H., E. Sigg, A. Neftel and R.C Bales, Atmosphere-snow transfer function for H_2O_2: Microphysical considerations, *Journal of Geophysical Research*, *98*(D10), 18-367-18,376, 1993.

Criss, R.E., *Principles of Stable Isotope Distribution*, Oxford University Press, Oxford, 1999.

Cuffey, K.M. and E.J. Steig, Isotopic diffusion in polar firn: implications for interpretation of seasonal climate parameters in ice-core records, with emphasis on central Greenland, *Journal of Glaciology*, *44*(147), 273-284, 1998.

Cunningham, J. and E.D. Waddington, Air flow and dry deposition of non-sea salt sulfate in polar firn: paleoclimatic implications, *Atmospheric Environment*, *27A*(17/18), 2943-2956, 1993.

Dansgaard, W., The isotopic composition of natural waters, *Meddelelser om Grφnland*, *165*(2), 1-120, 1961.

Dansgaard, W., Stable isotopes in precipitation, *Tellus*, *16*(4), 436-468, 1964.

Dansgaard, W., S.J. Johnsen, H.B. Clausen and N. Gundestrup, Stable Isotope Glaciology, *Meddelelser om Grφnland*, *197*(2), 1-153, 1973.

Davis, R.E., E.M. Arons and M.R. Albert, Metamorphism of polar firn: significance of microstructure in mass, energy, and chemical species transfer, In Wolff, E.W. and R.C. Bales (Ed.), *Chemical Exchange Between the Atmosphere and Polar Snow*, NATO ASI Series I, "Global Environmental Change" Vol. 43, Springer Verlag, Berlin, 379-402, 1996.

de Quervain, M.R., On the metamorphism of snow, In W.D. Kingery (Ed.) *Ice and Snow*, MIT Press, Cambridge, MA, 377-390, 1973.

Epstein, S. and T.K. Mayeda, Variations of O^{18} content of waters from natural sources, *Geochemica et Cosmochemica Acta*, *4*, 213-224, 1953.

Fisher, D.A., R.M. Koerner, W.S.B. Paterson, W. Dansgaard, N. Gundestrup and N. Reeh, Effect of wind scouring on climatic records from ice-core oxygen-isotope profiles, *Nature*, *301*(5897), 205-209, 1983.

Friedman, I., C. Benson and J. Gleason, Isotopic changes during snow metamorphism, In *Stable Isotope Geochemistry: A tribute to Samuel Epstein*, The Geochemical Society, Special Publication, No. 3., 211-221, 1991.

Fujii, Y. and K. Kusunoki, The role of sublimation and condensation in the formation of ice sheet surface at Mizuho Station, Antarctica, *Journal of Geophysical Research*, *87*(C6), 4293-4300, 1980.

Geiger, G.H. and D.R. Poirer, *Transport Phenomena in Metallurgy*, Addison-Wesley, 1973.

Gjessing, Y.T., The filtering effect of snow, In *Isotopes and impurities in snow and ice*, IAHS-AISH Publication No. 118, 199-203, 1977.

Gow, A.J., On the accumulation and seasonal stratification of snow at the South Pole,

Journal of Glaciology, *5*(40), 467-477, 1965.

Gow, A.J., On the rates of growth of grains and crystals in south polar firn, *Journal of Glaciology*, *8*(53), 241-252, 1969.

Grenfell, T.C., S.G. Warren and P.C. Mullen, Reflection of solar radiation by the Antarctic snow surface at ultraviolet, visible and near-infrared wavelengths, *Journal of Geophysical Research*, *99*(D9), 18,669-18,684, 1994.

Grootes, P.M. and E.J. Steig, Taylor ice-dome study, *Antarctic Journal of the U.S.*, *27*(5), 57-58, 1992.

Grootes, P.M., E.J. Steig and M. Stuiver, Taylor Ice-Dome study 1993-1994: An ice core to bedrock, *Antarctic Journal of the U.S.*, *29*(5), 79-81, 1994.

Grootes, P.M. and M. Stuiver, Oxygen 18/16 variability in Greenland snow and ice with 10^{-3}- to 10^{5}-year resolution, *Journal of Geophysical Research*, *102*(C12), 26,455-26,470, 1997.

Grootes, P.M., E.J. Steig, M. Stuiver, E.D. Waddington, D.L. Morse and M.-J. Nadeau, Long Taylor Dome Antarctic ^{18}O record indicates global synchroneity of glacial climate fluctuations, *Quaternary Research*, *56*(3), 289-298, 2001.

Gubler, H., Model for dry snow metamorphism by interparticle vapor flux, *Journal of Geophysical Research*, *90*(D5), 8081-8092, 1985.

Haberman, R., *Elementary Applied Partial Differential Equations*, Prentice-Hall, 2nd edition, 1987.

Hammer, C.U., H.B. Clausen and W. Dansgaard, Greenland ice sheet evidence of post-glacial volcanism and its climatic impact, *Nature*, *288*, 230-235, 1980.

Harder, S. L., S.G. Warren and R.J. Charlson, Sulfate in air and snow at the South Pole: Implications for transport and deposition at sites with low snow accumulation, *Journal of Geophysical Research*, *105*(D18), 22,825-22,832, 2000.

Harder, S.L., S.G. Warren, R.J. Charlson and D. S. Covert, Filtering of air through snow as a mechanism for aerosol deposition to the Antarctic ice sheet, *Journal of Geophysical Research*, *101*(D13), 18,729-18,743, 1996.

Hawley, R.L., E.D. Waddington, D. L. Morse, N.W. Dunbar and G.A. Zielinski, Dating firn cores by vertical strain measurements, *Journal of Glaciology*, *48*(162), 401-406, 2002.

Hyland, R.W. and A. Wexler, Formulations for the thermodynamics properties of the saturated phases of H_2O from 173.15 K to 473.15 K, *ASHRAE Transactions*, *89*(2A), 500-519, 1983.

Indermuhle, A., E. Monnin, B. Stauffer, T. Stocker, M. Wahlen, Atmospheric CO_2 concentration from 60 to 20 kyr BP from the Taylor Dome ice core, Antarctica, *Geophysical Research Letters*, *27*(5), 735-738, 2000.

Ingraham, N.L. and R.E. Criss, The effects of surface area and volume on the rate of isotopic exchange between water and water vapor, *Journal of Geophysical Research, Atmospheres*, *98*(D11), 20,547-20,553, 1993.

Ingraham, N.L. and R.E. Criss, The effect of vapor pressure on the rate of isotopic exchange between water and water vapor, *Chemical Geology*, *150*, 287-292, 1998.

Johnsen, S.J., Stable isotope homogenization of polar firn and ice, In *Isotopes and impurities in snow and ice*, IAHS-AISH Publication No. 118, 210-219, 1977.

Johnsen S.J., H.B. Clausen, K.M. Cuffey, G. Hoffmann, J. Schwander and T. Creyts, Diffusion of stable isotopes in polar firn and ice: the isotope effect in firn diffusion, In Hondoh (Ed.), *Physics of ice core records*, Hokkaido University Press, Sapporo, Japan, 121-140, 2000.

Jouzel, J. and L. Merlivat, Deuterium and Oxygen 18 in Precipitation: Modeling of the isotopic effects during snow formation, *Journal of Geophysical Research*, *89*(D7), 11,749-11,757, 1984.

Jouzel, J., R.B. Alley, K.M. Cuffey, W. Dansgaard, P. Grootes, G. Hoffmann, S.J. Johnsen, R.D. Koster, D. Peel, C.A. Shuman, M. Stievenard, M. Stuiver and J. White, Validity of the temperature reconstruction from water isotopes in ice cores, *Journal of Geophysical Research*, *102*(C12), 26,471-26,487, 1997.

Lal, D., A.J.T. Jull, D.J. Donahue, G.S. Burr, D. Beck, J. Jouzel, E. Steig, Record of

cosmogenic in situ produced ^{14}C in Vostok and Taylor Dome ice samples: implications for strong role of wind ventilation processes, *Journal of Geophysical Research*, *106*(D23), 31,933-31,941, 2001.

Legrand, M. and P.A. Mayewski, Glaciochemistry of polar ice cores: a review, *Reviews of Geophysics*, *35*(3), 219-243, 1997.

Majoube, M. Fractionnement en ^{18}O entre la glace et la vapeur d'eau, *Journal de Chimice Physique*, *68*(4), 625-636, 1971.

Marti, J. and K. Mauersberger, A survey and new measurements of ice vapor pressure at temperatures between 170 and 250K, *Geophysical Research Letters*, *20*(5), 363-366, 1993.

Massman, W.J., A review of the molecular diffusivities of H_2O, CO_2, CH_4, CO, O_3, SO_2, NH_2, N_2O, NO and NO_2 in air, O_2 and N_2 near STP, *Atmospheric Environment*, *32A*(6), 1111-1127, 1998.

Massey, C.A., Development of hydrogen Mass Spectrometry Methods for Testing Stable Isotopic Interactions of Water Vapor at the Snowpack-Air Interface, Summit, Greenland, *M.S. Thesis*, *University of Washington*, 1995.

McConnell, J.R., R.C. Bales and D.R. Davis, Recent intra-annual snow accumulation at South Pole: Implications for ice core interpretation, *Journal of Geophysical Research*, *102*(D18), 21,947-21,954, 1997a.

McConnell, J.R. J.R. Winterle, R.C. Bales, A.M. Thompson and R.W. Stewart, Physically based inversion of surface snow concentrations of H_2O_2 to atmospheric concentrations at South Pole, *Geophysical Research Letters*, *24*(4), 441-444, 1997b.

McConnell, J.R., R.C. Bales, R.W. Stewart, A.M. Thompson, M.R. Albert and R. Ramos, Physically based modeling of atmosphere-to-snow-to-firn transfer of H_2O_2 at South Pole, *Journal of Geophysical Research*, *103*(D9), 10,561-10,570, 1998.

Menke, W., *Geophysical Data Analysis: Discrete Inverse Theory*, Academic Press, revised edition, 1989.

Merlivat, L., Molecular diffusivities of $H_2^{16}O$, $HD^{16}O$, and $H_2^{18}O$ in gases, *Journal of*

Chemical Physics, *69*(6), 2864-2871, 1978.

Morse, D.L., Glacier geophysics at Taylor Dome, Antarctica, *Ph.D. Thesis*, *University of Washington*, 1997.

Morse, D.L., E.D. Waddington and E.J. Steig, Ice age storm trajectories inferred from radar stratigraphy at Taylor Dome, Antarctica, *Geophysical Research Letters*, *25*(17), 3383-3386, 1998.

Morse, D.L., E.D. Waddington, H.P. Marshall, T.A. Neumann, E.J. Steig, J.E. Dibb, D.P. Winebrenner and R.J. Arthern, Accumulation rate measurements at Taylor Dome, East Antarctica: Techniques and strategies for mass balance measurements in polar environments, *Geografiska Annaler*, *81A*(4), 683-694, 1999.

Neftel, A., R.C. Bales and D.J. Jacob, H_2O_2 and HCHO in polar snow and their relation to atmospheric chemistry, In Delmas, R. (Ed.), *Ice Core Studies of Global Biogeochemical Cycles*, NATO ASI Series I, "Global Environmental Change" Vol. 30, Springer Verlag, Berlin, 249-264, 1995.

Neumann, T.A., Post-depositional changes in stable isotope ratios, *Eos*, *82*(20), Spring Meeting Supplement, Abstract OS51B-04, 2001.

Neumann, T.A. and E.D. Waddington, A two-dimensional model of post-depositional changes in stable isotope ratios in polar firn. *Eos*, *83*(47), Fall Meeting Supplement, Abstract C61A-11, 2002.

Neumann, T.A., E.D. Waddington, H.P. Marshall, D.L. Morse and M. Koutnik, Inference of accumulation rate pattern from deep radar layers, in preparation.

Nield, D.A., Onset of thermohaline convection, *Water Resources Research*, *4*(3), 553-560, 1968.

Pasteur, E.C. and R. Mulvaney, Migration of methane sulphonate in Antarctic firn and ice, *Journal of Geophysical Research*, *105*(D9), 11,525-11,534, 2000.

Patankar, S.V., *Numerical Heat Transfer and Fluid Flow*, Taylor and Francis, Hemisphere Publishing Corporation, 1980.

Paterson, W.S.B., *The Physics of Glaciers*, Pergamon Press, Third Edition, 1994.

Picciotto, E., G. Crozaz and W. DeBreuck, Accumulation on the South Pole - Queen Maud Land Traverse, 1964-1968, In Crary (Ed.), *Antarctic Snow and Ice Studies II*, Antarctic Research Series Vol. 16, American Geophysical Union, USA, 257-315, 1971.

Powers, D., K. O'Neill and S.C. Colbeck, Theory of natural convection in snow, *Journal of Geophysical Research*, *90*(D6), 10,641-10,649, 1985.

Reif, F., *Fundamentals of Statistical and Thermal Physics*, McGraw-Hill, 1965.

Rempel, A.W. and J.S. Wettlaufer, Isotopic diffusion in polycrystalline ice, in press *Journal of Glaciology.*

Robin, G. de Q., Ice cores and climatic changes, *Philosophical Transactions of the Royal Society, London, Series B*, *280*, 143-168, 1977.

Satake, H. and K. Kawada, The quantitative evaluation of sublimation and the estimation of original hydrogen and oxygen isotope ratios of a firn core at East Queen Maud Land Antarctica, *Bulletin of Glacier Research*, 15, 93-97, 1997.

Satow, K. and O. Watanabe, Net accumulation and oxygen isotope composition of snow on Mizuho Plateau, Antarctica, *Annals of Glaciology*, *6*, 300-302, 1985.

Severinghaus, J.P., A. Grachev and M. Battle, Thermal fractionation of air in polar firn by seasonal temperature gradients, *Geochemistry, Geophysics, Geosystems*, *2*(7), 2000GC000146, 2001.

Sommerfeld, R.A. and E.R. LaChapelle, The classification of snow metamorphism, *Journal of Glaciology*, *9*(55), 3-17, 1970.

Steig, E.J., P.M. Grootes and M. Stuiver, Seasonal precipitation timing and ice core records, *Science*, *266*(5192), 1885-1886, 1994.

Steig, E.J., E.J. Brook, J.W.C. White, C.M. Sucher, M.L. Bender, S.J. Lehman, D.L. Morse, E.D. Waddington and G.D. Clow, Synchronous Climate Changes in Antarctica and the North Atlantic, *Science*, *282*, 92-95, 1998.

Steig, E.J., D.L. Morse, E.D. Waddington, M. Stuiver, P.M. Mayewski, S.I. Whitlow and M. S. Twickler, Wisconsinan and Holocene climate history from an ice core at Taylor Dome, western Ross Embayment, Antarctica, *Geografiska Annaler*, *82A*, 213-235, 2000.

Stenberg, M., Spatial varibility and temporal changes in snow chemistry, Dronning Maud Land, Antarctica, *Ph.D. Thesis, Stockholm University*, 2000.

Sturm M. and C.S. Benson, Vapor transport, grain growth and depth-hoar development in the subarctic snow, *Journal of Glaciology*, 43(143) 42-59, 1997.

Sturm, M., J. Holmgren, M. König and K. Morris, The thermal conductivity of seasonal snow, *Journal of Glaciology*, *43*(143), 26-41, 1997.

Taylor, L.D., Glaciological studies on the South Pole Traverse, 1962-1963, In Crary (Ed.), *Antarctic Snow and Ice Studies II*, Antarctic Research Series Vol. 16, American Geophysical Union, USA, 209-224, 1971.

Thompson, A.M., Photochemical modeling of chemical cycles: Issues related to the interpretation of ice core data, In R. Delmas (Ed.), *Biogeochemical Cycles in Ice Cores*, NATO ASI Series I, "Global Environmental Change" Vol. 30, Springer Verlag, Berlin, 265-297, 1995.

Trim, D.W., *Applied Partial Differential Equations*, PWS-Kent, Wadsworth, 1990.

van den Broeke, M.R., Spatial and temporal variations of sublimation on Antarctica: Results of a high-resolution general circulation model, *Journal of Geophysical Research*, *102*(D25), 29,765-29,777, 1997.

van der Veen, C.J., I.M. Whillans and A.J. Gow, On the frequency distribution of net annual snow accumulation at the South Pole, *Geophysical Research Letters*, *26*(2), 239-242, 1999.

Vimeux, F., V. Masson, J. Jouzel, J.R. Petit, E.J. Steig, M. Stievenard, R. Vaikmae and J.W.C. White, Holocene hydrological cycle changes in the Southern Hemisphere documented in East Antarctic deuterium excess records, *Climate Dynamics*, *17*, 509-513, 2001.

Waddington, E.D., J. Cunningham and S.L. Harder, The effects of snow ventilation on chemical concentrations, In Wolff, E.W. and R.C. Bales (Ed.), *Chemical Ex-*

change Between the Atmosphere and Polar Snow, NATO ASI Series I, "Global Environmental Change" Vol. 43, Springer Verlag, Berlin, 403-451, 1996.

Waddington, E.D., E.J. Steig and T.A. Neumann, Using characteristic times to assess whether stable isotopes in polar snow can be reversibly deposited, *Annals of Glaciology, 35*, 118-124, 2002.

Wagnon, P., R.J. Delmas and M. Legrand, Loss of volatile acid species from upper firn layers at Vostok, Antarctica, *Journal of Geophysical Research, 104*(D3), 3423-3431, 1999.

Wallace, J.M. and P.V. Hobbs, *Atmospheric Science*, Academic Press, 1977.

Weast, R.C. and S.M. Selby (Ed.), *Handbook of Chemistry and Physics*, 46th Edition, Chemical Rubber Co., 1966.

Weller, G., The heat and mass balance of snow dunes on the central antarctic plateau, *Journal of Glaciology, 8*(53), 277-284, 1969.

Whillans I.M. and P.M. Grootes, Isotopic diffusion in cold snow and firn, *Journal of Geophysical Research, 90*(D2), 3910-3917, 1985.

Wolff, E.W., J.S Hall, E.C Pasteur, D. Wagenbach, M. Legrand, Relationship between chemistry of air, fresh snow and firn cores for aerosol species in coastal Antarctica, *Journal of Geophysical Research, 103*(D9), 11,057-11,070, 1998.

Yosida, Z. and others, Physical studies on deposited snow, *Contributions from the Institute of Low Temperature Science, 7*, 19-74, 1955.

Appendix A

ANALYTIC MODEL FOR POST-DEPOSITIONAL ISOTOPIC CHANGE

We can create closed-form solutions to predict the evolution of the remaining solid mass of firn $m_{\mathrm{v}}(t)$, the isotopic content of the condensate $\delta^{18}\mathrm{O_c}(t)$, and the bulk isotopic content of the remaining firn $\delta^{18}\mathrm{O_f}(t)$. We begin with the equations of Dansgaard (1961) for condensation of vapor over an ice surface:

$$R_{\mathrm{v}} = R_{\mathrm{vo}}\, \beta^{\,\alpha-1} \tag{A.1}$$

$$R_{\mathrm{c}} = R_{\mathrm{vo}}\, \frac{1-\beta^{\,\alpha}}{1-\beta}\,, \tag{A.2}$$

where R denotes the ratio of $^{18}\mathrm{O}$ to $^{16}\mathrm{O}$ in a sample of water and the subscript refers to the type of sample. In this nomenclature R_{v} denotes the ratio in water vapor, R_{c} is the ratio in the condensate, and R_{vo} is the initial ratio in the vapor. β is the fraction of the initial mass of vapor remaining and α is an isothermal isotopic fractionation coefficient.

Since isotopic composition is more commonly expressed on the $\delta^{18}\mathrm{O}$ scale, we convert (A.1) and (A.2) to this scale. The $\delta^{18}\mathrm{O}$ of a sample is defined as:

$$\delta^{18}\mathrm{O}_{\mathrm{sample}} = \frac{R_{\mathrm{sample}} - R_{\mathrm{std}}}{R_{\mathrm{std}}} \times 10^{3}\,, \tag{A.3}$$

where R refers to oxygen isotope ratio, and the standard is commonly Standard Mean Ocean Water (SMOW). We can manipulate Equation (A.3) to find that:

$$R_{\mathrm{sample}} = \frac{\delta^{18}\mathrm{O}_{\mathrm{sample}}\, R_{\mathrm{std}}}{10^{3}} + R_{\mathrm{std}}\,. \tag{A.4}$$

We use Equations (A.2) and (A.3) to find an expression for $\delta^{18}O_c$, the $\delta^{18}O$ of the condensate from water vapor (Equation (2.7)):

$$\delta^{18}O_c = \left(1000 + \delta^{18}O_{vo}\right) \frac{1-\beta^{\alpha}}{1-\beta} - 1000\,. \tag{A.5}$$

We model the pore-space vapor as a mix of atmospheric vapor, which we assume is in isotopic equilibrium with the average $\delta^{18}O$ of the snowpack, and vapor derived locally through grain sublimation. The mixing ratio between these two sources is $(1 - RH)$, and the equation for $\delta^{18}O_{vo}$ is Equation (2.9).

We now construct a model for the changes in remaining firn mass m_f and isotopic content $\delta^{18}O_f$ with time. By dividing the remaining firn mass m_f by a reference mass $m_o = 1\text{kg}$, we non-dimensionalize the expressions involving mass. If we assume that the time required for mass transfer between the solid and vapor phases in the firn (i.e. the mass-transfer time scale) is short relative to the residence time τ of air in the firn, then the normalized mass of firn decreases by the fraction $\mathcal{R}\tau$ in time τ, where $\mathcal{R}$ is the fractional rate at which the firn sublimates. The mass also increases due to redeposition. We assume that air in the snowpack is always saturated. The normalized mass of vapor in the pore space is m_v. The amount of mass redeposited in time τ is $(1-\beta)m_v$, and the remaining mass of the firn $m_f(t)$ changes through time as:

$$m_f(t+\tau) = m_f(t) - \mathcal{R}\tau\, m_f(t) + (1-\beta)m_v\,. \tag{A.6}$$

Assuming that the temporal derivative of m_f can be written as:

$$\frac{d}{dt}m_f(t) = \frac{m_f(t+\tau) - m_f(t)}{\tau}\,, \tag{A.7}$$

Equation (A.6) can be written as a first order differential equation for $m_f(t)$:

$$\frac{d}{dt}m_f(t) + \mathcal{R}\, m_f(t) = \frac{1-\beta}{\tau}m_v\,. \tag{A.8}$$

τ is the characteristic residence time of air in the firn, which is a function of depth (Colbeck, 1989). In this analysis, we treat τ as constant. A closed-form solution for the mass of the sample (Equation (2.6)) follows after an integration.

The $\delta^{18}O$ of the remaining firn ($\delta^{18}O_f$) is a weighted average of the $\delta^{18}O$ of the condensate and the $\delta^{18}O$ of the remaining mass:

$$\delta^{18}O_f(t+\tau) = \frac{\delta^{18}O_f(t)\;[m_f(t) - m_f(t)\mathcal{R}\tau] + \delta^{18}O_c(t)\,(1-\beta)\,m_v}{m_f(t) - m_f(t)\,\mathcal{R}\tau + m_v\,(1-\beta)}\,. \tag{A.9}$$

By substituting Equations (A.5) and (2.9) into (A.9), we get a differential equation for the isotopic content $\delta^{18}O_f$ of the remaining snow mass:

$$\begin{aligned}\frac{d}{dt}\delta^{18}O_f(t) + \delta^{18}O_f(t)\left(\frac{(1-\beta)\,m_v}{\tau\, m_f(t)}\right)(Fa-1) = \ldots \\ \frac{(1-\beta)\,m_v}{\tau\, m_f(t)}\,(Fb - 1000)\;,\end{aligned} \tag{A.10}$$

where F, a and b are defined in Equations (2.10), (2.11) and (2.12). The solution to this first order linear ordinary differential equation is presented as Equation (2.8).

Given appropriate choices for β and $\mathcal{R}$, these equations can be used to calculate the changes in an idealized snow sample as a function of time. The assumptions made in this analysis are discussed in the text.

Appendix B

ENERGY-CONSERVATION MODEL

B.1 Mass and Energy Conservation in Firn

My model for tracking vapor motion in firn solves the coupled equations for mass and energy conservation in 2 dimensions. The vapor transport model is described in Appendix D. Both models use the same coordinate system where x is positive to the right, y is positive down, u is flow velocity in the positive x direction, and v is flow velocity in the positive y direction (see figure B.1). In this appendix, I outline the energy-conservation model. This model captures energy changes in the firn as a result of heat conduction, the advection of heat by air flowing through firn, and sources / sinks of heat from phase changes of water. I began with a statement of energy conservation per unit volume for a given continuous material:

$$\frac{\partial}{\partial t}(\rho H) + \frac{\partial}{\partial x}(\rho u H) + \frac{\partial}{\partial y}(\rho v H) - \frac{\partial}{\partial x}\left(K\frac{\partial T}{\partial x}\right) - \frac{\partial}{\partial y}\left(K\frac{\partial T}{\partial y}\right) - Q = 0 \qquad \text{(B.1)}$$

where ρ is the firn density, H is the specific enthalpy of the firn, and the product ρH describes energy per unit volume. K is the bulk thermal conductivity and Q describes sources of heat. The first term in equation(B.1) is the unsteady term, which represents the rate of change of energy per unit volume. The second and third terms represent energy advected through the system per unit volume due to flow, per unit time. The third and fourth terms describe energy conduction per unit volume due to temperature gradients in the material. The final term accounts for sources or sinks of energy per unit volume per time. I do not include the additional kinetic energy contribution from air flow through the firn. For air flow rates encountered in

the firn (less than 1 m s^{-1}), the contribution of air motion to the total energy of the system is negligible.

Traditionally, thermal studies of firn have treated firn as a composite material (e.g. Yosida and others, 1955; Sturm and others, 1997). These studies have generally not considered the thermal properties of each component individually (solid ice, water vapor and air), but rather measure and report the thermal characteristics of the aggregate material. In part, this simplification has been made in the past due to the difficulty in determining importance of each component in heat transfer. For example, quantifying the extent to which the bulk conductivity is due to heat conduction through the ice versus the latent heat transfer of water vapor sublimation and condensation across pore spaces has been studied in detail for a variety of snow types (Sturm and others, 1997) yet remains an open question. I follow these earlier investigators and treat firn as a composite material composed of air, water vapor and solid ice. I transformed Equation (B.1) into an equation for temperature T in the firn, treating firn as a macroscopic system.

Specific-enthalpy change (ΔH) at constant pressure is defined as the sum of change in stored energy E and pressure-volume PV work done on the system:

$$\Delta H = \Delta(E + PV) \qquad \text{(B.2)}$$

Energy changes in the firn happen at a relatively constant atmospheric pressure, so we can make the approximation that P is constant:

$$\Delta H = \Delta E + P\Delta V \qquad \text{(B.3)}$$

Using the approximation that P is constant, I can write the First Law of Thermodynamics as:

$$\Delta Q = \Delta E + P\Delta V \qquad \text{(B.4)}$$

where ΔQ is the total change in heat. I define the specific heat capacity at a constant pressure c_p for a macroscopic system as (Reif, 1965):

$$c_p = \frac{\Delta Q}{\Delta T} \tag{B.5}$$

Using the above three relations, I then equate the enthalpy change in the system with temperature change as:

$$\Delta H = c_{\mathrm{p}} \Delta T \tag{B.6}$$

This shows that all energy changes in the firn can be related to temperature changes using the specific heat capacity of firn. I used this result to rewrite equation (B.1) using T as the dependent variable:

$$\frac{\partial}{\partial t}\left(\rho c_{\mathrm{p}} T\right) + \nabla \cdot \left(\rho c_{\mathrm{p}} \vec{\mathbf{u}} T\right) - \nabla \cdot \left(K \nabla T\right) - Q = 0 \tag{B.7}$$

where $\vec{\mathbf{u}}$ is the velocity vector (u, v). Firn is a composite material which consists of ice, air and water vapor, as discussed above. I am concerned with capturing the temperature change of the mixture through time. Consequently, I made a number of assumptions about the meaning of the terms in the conservation equation (B.7):

- The unsteady term represents temperature changes in the composite snow and moist-air mixture. Therefore, in the first term of equation (B.7), I replaced ρc_{p} with:

$$\phi \left(\rho c_{\mathrm{p}}\right)_{\mathrm{a}} + (1 - \phi) \left(\rho c_{\mathrm{p}}\right)_{\mathrm{i}}. \tag{B.8}$$

  where the subscripts a and i represent *air* and *ice*, respectively. This formula represents a volume-weighted average of air and ice (Albert and McGilvary, 1992). The term $\left(\rho c_{\mathrm{p}}\right)_{\mathrm{a}}$ represents values for moist air (rather than dry air) and ϕ is the porosity of the firn.

- The advection term accounts only for air flow through firn. Any heat advected by motion of the firn (compaction) is not considered. Consequently, any strain heating as a result of firn compaction is also not considered. Benfield (1951) studied the advection of heat due to snow accumulation and found that this is a first order effect for high accumulation rates of snow (8 m yr^{-1}). This model will be applied to much lower accumulation rates of snow (1 m yr^{-1} or less). For low accumulation rates, air flow moves several orders of magnitude more heat than snow accumulation in the upper 2 meters of the firn. Consequently, I can safely neglect the advection of heat by snow accumulation. Therefore, in the second term, ρc_{p} is replaced by $\phi \left(\rho c_{\mathrm{p}}\right)_{\mathrm{a}}$, and $\vec{u}$ refers only to the two-dimensional air-flow velocity through the firn.

- The conduction term represents conduction through the composite material. Therefore, the conductivity K refers to firn conductivity. Firn conductivity depends on two main properties: temperature and microstructure (Sturm and others, 1997). There have been many studies (both theoretical and experimental) of the thermal conductivity of snow for a variety of snow types, densities and temperatures. Based on these studies, Sturm and others (1997) conclude that the temperature dependence of thermal conductivity arises as a result of vapor transport in snow. Above -40 C in well-bonded, dense snow ($\rho_{\mathrm{firn}} > 300$ kg m$^{-}3$), the temperature effect is of secondary importance, and may be safely neglected. Below -40 C, the thermal conductivity increases, as a result of the increasing thermal conductivity of the ice matrix. Since I intend to use this model to study relatively high density polar firn, I neglect the temperature dependence of the thermal conductivity.

  However, the microstructure is of first-order importance, and its effect on conductivity may be parameterized using the firn density for a variety of snow types. In this study, I use the quadratic equation presented by Sturm and others (1997) to calculate the effective thermal conductivity of the firn for a given density:

$$K = 0.138 - 1.01\rho_{\mathrm{f}} + 3.233\rho_{\mathrm{f}}^2 \ , \tag{B.9}$$

where ρ_{f} is the *firn* density, which I assume is constant. Sturm and others (1997) note that this relation is only valid near -14.6 C. For other temperatures (particularly higher temperatures), a slight correction may be needed, although there is not sufficient data to determine the magnitude of the correction. This equation produces slightly lower values of K than the more common Van Dusen formula (Paterson, 1994, p. 205).

With these substitutions, the equation of energy conservation in the firn is given by:

$$\frac{\partial}{\partial t}\left[T\left(\phi\left(\rho c_{\mathrm{p}}\right)_{\mathrm{a}} + (1-\phi)\left(\rho c_{\mathrm{p}}\right)_{\mathrm{i}}\right)\right] + \nabla\cdot\left(\phi\left(T\rho c_{\mathrm{p}}\right)_{\mathrm{a}}\vec{\mathbf{u}}\right) - \nabla\cdot\left(K\nabla T\right) - Q = 0 \tag{B.10}$$

In addition, I required that the air flow field satisfy the continuity equation:

$$\frac{\partial}{\partial t}\left(\phi\rho_{\mathrm{a}}\right) + \nabla\cdot\left(\phi\rho_{\mathrm{a}}\vec{\mathbf{u}}\right) = 0 \tag{B.11}$$

Several investigators (e.g. Patankar 1982) divide the conservation equation (equation B.10) by $\rho\, c_{\mathrm{p}}$ in order to simplify the equation and to facilitate discretizing the equation. However, since firn is a composite material, my expression for energy conservation is more complicated than the basic case. Consequently, my solution technique differs from published solutions. I have made an effort to highlight these differences in the following description of my derivation of the discretization equations used to solve the coupled equations (B.10) and (B.11).

B.2 Discretization Technique

I solve this system of equations using control-volume theory, closely following the technique presented in Patankar (1982), chapter 5. My grid scheme uses x positive

to the right and y positive down. Grid points are placed at the centers of the control volumes (Patankar, 1982, p.69). See figure B.1 for the grid set-up and indicial notation. Upper-case subscripts refer to values at the centers of control volumes. The subscripts P, E, W, S and N refer to values at the center of the control volume of interest, and the centers of neighboring control volumes to the east, west, south and north, respectively. Lower case subscripts e, w, s and n refer to values at the east, west, south and north interfaces. I replaced the specific heat capacity c_{p} with the simpler c to avoid future confusion. The solution begins by regrouping terms:

$$\begin{aligned}
&\frac{\partial}{\partial t}\left[\left(\phi\left(\rho c\right)_{\mathrm{a}} + (1-\phi)\left(\rho c\right)_{\mathrm{i}}\right)T\right] \ + \\
&\quad\frac{\partial}{\partial x}\left[\phi\left(\rho c\right)_{\mathrm{a}} uT - K\frac{\partial T}{\partial x}\right] \ + \\
&\quad\frac{\partial}{\partial y}\left[\phi\left(\rho c\right)_{\mathrm{a}} vT - K\frac{\partial T}{\partial y}\right] \ = \ Q
\end{aligned} \tag{B.12}$$

The source term Q accounts for latent heat effects due to the condensation or sublimation of water in the firn. The mass of water per unit volume that changes phase (S) is calculated in the vapor transport model (described in Appendix D). I multiplied this mass per volume per time by the latent heat of the phase change L to calculate the energy source or sink (such that $Q = LS$). I defined two new terms, J_x and J_y as the total flux (advection and diffusion terms) in the positive x and y directions, respectively:

$$\begin{aligned}
J_x &= \phi\left(\rho c\right)_{\mathrm{a}} uT - K\frac{\partial T}{\partial x} \\
J_y &= \phi\left(\rho c\right)_{\mathrm{a}} vT - K\frac{\partial T}{\partial y}
\end{aligned}$$

which simplifies equation (B.12) to:

$$\frac{\partial}{\partial t}\left[T\left(\phi\left(\rho c\right)_{\mathrm{a}} + (1-\phi)\left(\rho c\right)_{\mathrm{i}}\right)\right] + \frac{\partial}{\partial x}J_x + \frac{\partial}{\partial y}J_y = Q \tag{B.13}$$

I integrated this equation with respect to x, y and t over a control volume (see figure B.1):

$$\frac{\Delta x \Delta y}{\Delta t}\left[T_{\mathrm{P}}\left(\phi_{\mathrm{P}}\left(\rho c\right)_{\mathrm{a}}+\left(1-\phi_{\mathrm{P}}\right)\left(\rho c\right)_{\mathrm{i}}\right)-T_{\mathrm{P}}^{0}\left(\phi_{\mathrm{P}}^{0}\left(\rho c\right)_{\mathrm{a}}+\left(1-\phi_{\mathrm{P}}^{0}\right)\left(\rho c\right)_{\mathrm{i}}\right)\right]+$$
$$J_{\mathrm{e}}-J_{\mathrm{w}}+J_{\mathrm{s}}-J_{\mathrm{n}}=Q\Delta x\Delta y \quad \text{(B.14)}$$

where the terms J_{e}, J_{w}, J_{s} and J_{n} refer to total integrated fluxes over the east, west, south and north faces, respectively. The superscript 0 refers to values at the beginning of the time step, i.e. the "old" values.

I have assumed that the density of air ρ_{a} is constant with respect to both space and time. In reality, ρ_{a} varies as a function of temperature (Wallace and Hobbs, p.48). Accounting for variations in ρ_{a} would allow for free convection (Benard convection) of air through firn pore spaces, since the density of air decreases with increasing temperature. The possibility of Benard convection in the firn can be estimated with the dimensionless Rayleigh number for a porous media (Powers and others 1985):

$$Ra=\frac{\rho g\beta\Delta THK}{\mu\kappa}, \quad \text{(B.15)}$$

where ρ is the density of air, g is the gravitational acceleration, β is the thermal expansion coefficient ($= 3.5\times10^{-3}$ K^{-1} for air), H is the thickness of the layer, ΔT is the temperature difference across the layer, K is the permeability, μ is the air viscosity and κ is the thermal diffusivity ($= 2.2\times10^{-5}$ m^2 s^{-1} for air). Typical values in the firn are $\Delta T = 10$ K, $H = 5$ m, $K = 5\times10^{-9}$ m^2, which lead to $Ra \sim 5$. Critical values for the onset of Benard convection in porous media are between 15 and 40 (Nield, 1968).

Although my calculated Rayleigh number is somewhat less than the critical values, inhomogeneities in firn permeability or large local temperature gradients could result in the onset of convection. Convecting air in the firn pore spaces would enhance the transport of heat and water vapor in the firn.

However, neglecting variations in ρ_{a} (and the possibility of convection) is a reasonable assumption for three reasons. First, close to the surface where temperature

gradients are large (and associated Rayleigh numbers are large), advective velocities (u, v) are much larger than free-convection velocities. Second, where advective velocities are small (below the top two meters), temperature gradients are small; this results in small convection velocities. Third, Bernard convection is most likely during the winter months when cold surface air overlies warmer air at depth in the firn. If convection were active in the winter, a greatly attenuated isotopic thermal fractionation signal would be expected (Severinghaus, and others 2001). In fact, the winter thermal fractionation signal is well-developed and not destroyed by vigorous Benard convection.

The heat capacity of the air c_{a} is also assumed to be constant. The value of this parameter is a function of relative humidity, and will vary slightly with space and time. However, although the amount of heat carried by the air is larger than the amount of heat carried by the compaction of the snow (due to the low advective velocity of the snow), the heat carried by both of these transport terms are small compared to the amount of heat stored in the ice. Consequently, variations in c_{a} will have a negligible impact on the temperature profile of the firn.

I multiplied the continuity equation (B.11) by a constant, c_{a}, since I did not divide the heat capacity out of the conservation equation (B.14). This insured that the dimensions between the conservation equation and the continuity equation would be consistent. I again assumed that the density of air is constant with respect to both time and space, and integrated the continuity equation with respect to x, y, and t:

$$\begin{aligned}&\left[\left(\rho c\right)_{\mathrm{a}}\phi_{\mathrm{P}}-\left(\rho c\right)_{\mathrm{a}}\phi_{\mathrm{P}}^{0}\right]\Delta x\Delta y+\\&\left[\left(\left(\rho c\right)_{\mathrm{a}}\phi u\right)_{\mathrm{e}}-\left(\left(\rho c\right)_{\mathrm{a}}\phi u\right)_{\mathrm{w}}\right]\Delta y\Delta t+\\&\left[\left(\left(\rho c\right)_{\mathrm{a}}\phi v\right)_{\mathrm{s}}-\left(\left(\rho c\right)_{\mathrm{a}}\phi v\right)_{\mathrm{n}}\right]\Delta x\Delta t=0\,.\end{aligned} \quad \text{(B.16)}$$

I simplified the above expression by creating a term similar to the mass flow rates used by Patankar (1982):

$$F_{\mathrm{e}} \;=\; \left(\phi\left(\rho c\right)_{\mathrm{a}}u\right)_{\mathrm{e}}\Delta y$$

$$
\begin{aligned}
F_{\mathrm{w}} &= \left(\phi\left(\rho c\right)_{\mathrm{a}} u\right)_{\mathrm{w}} \Delta y \\
F_{\mathrm{s}} &= \left(\phi\left(\rho c\right)_{\mathrm{a}} v\right)_{\mathrm{s}} \Delta x \\
F_{\mathrm{n}} &= \left(\phi\left(\rho c\right)_{\mathrm{a}} v\right)_{\mathrm{n}} \Delta x
\end{aligned}
$$

These terms are identical to Patankar's, except for the additional presence of the specific heat capacity. I used these substitutions, and multiplied each term of equation (B.16) by $T_{\mathrm{P}}/\Delta t$:

$$
T_{\mathrm{P}} \frac{\Delta x \Delta y}{\Delta t}\left[\phi_{\mathrm{P}}\left(\rho c\right)_{\mathrm{a}} - \phi_{\mathrm{P}}^{0}\left(\rho c\right)_{\mathrm{a}}\right] + F_{\mathrm{e}} T_{\mathrm{P}} - F_{\mathrm{w}} T_{\mathrm{P}} + F_{\mathrm{s}} T_{\mathrm{P}} - F_{\mathrm{n}} T_{\mathrm{P}} = 0 \,. \tag{B.17}
$$

Then I combined the equations for energy conservation (equation B.14) and continuity (equation B.17) by subtracting equation (B.17) from equation (B.14) and simplifying:

$$
\begin{aligned}
&T_{\mathrm{P}} \frac{\Delta x \Delta y}{\Delta t}\left[\left(1-\phi_{\mathrm{P}}\right)\left(\rho c\right)_{\mathrm{i}} + \phi_{\mathrm{P}}^{0}\left(\rho c\right)_{\mathrm{a}}\right] - \\
&T_{\mathrm{P}}^{0} \frac{\Delta x \Delta y}{\Delta t}\left[\phi_{\mathrm{P}}^{0}\left(\rho c\right)_{\mathrm{a}} + \left(1-\phi_{\mathrm{P}}^{0}\right)\left(\rho c\right)_{\mathrm{i}}\right] + \left(J_{\mathrm{e}} - F_{\mathrm{e}} T_{\mathrm{P}}\right) - \\
&\left(J_{\mathrm{w}} - F_{\mathrm{w}} T_{\mathrm{P}}\right) + \left(J_{\mathrm{s}} - F_{\mathrm{s}} T_{\mathrm{P}}\right) - \left(J_{\mathrm{n}} - F_{\mathrm{n}} T_{\mathrm{P}}\right) = Q \Delta x \Delta y \,.
\end{aligned} \tag{B.18}
$$

In order to simplify the above expression, I introduced a new factor D, which is similar to the diffusion conductance defined by Patankar (1982):

$$
\begin{aligned}
D_{\mathrm{e}} &= \frac{K_{\mathrm{e}} \Delta y}{\left(\delta x\right)_{\mathrm{e}}} \\
D_{\mathrm{w}} &= \frac{K_{\mathrm{w}} \Delta y}{\left(\delta x\right)_{\mathrm{w}}} \\
D_{\mathrm{s}} &= \frac{K_{\mathrm{s}} \Delta x}{\left(\delta y\right)_{\mathrm{s}}} \\
D_{\mathrm{n}} &= \frac{K_{\mathrm{n}} \Delta x}{\left(\delta y\right)_{\mathrm{n}}} \,,
\end{aligned}
$$

where K_{e} is the interface conductivity. Using the above expressions for D along with the expressions for F, I generated the Peclet number. This non-dimensional number is a ratio of the strengths of advection and diffusion:

$$
P = \frac{F}{D} \,, \tag{B.19}
$$

where F and D are as defined above. In Appendix C, I used the factors D, F and P to show that:

$$
\begin{aligned}
J_{\mathrm{e}} - F_{\mathrm{e}} T_{\mathrm{P}} = \left[D_{\mathrm{e}} A\left(|P_{\mathrm{e}}|\right) + \max\left(-F_{\mathrm{e}}, 0\right)\right]\left(T_{\mathrm{P}} - T_{\mathrm{E}}\right) &= a_{\mathrm{E}}\left(T_{\mathrm{P}} - T_{\mathrm{E}}\right) \\
J_{\mathrm{w}} - F_{\mathrm{w}} T_{\mathrm{P}} = \left[D_{\mathrm{w}} A\left(|P_{\mathrm{w}}|\right) + \max\left(F_{\mathrm{w}}, 0\right)\right]\left(T_{\mathrm{W}} - T_{\mathrm{P}}\right) &= a_{\mathrm{W}}\left(T_{\mathrm{W}} - T_{\mathrm{P}}\right) \\
J_{\mathrm{s}} - F_{\mathrm{s}} T_{\mathrm{P}} = \left[D_{\mathrm{s}} A\left(|P_{\mathrm{s}}|\right) + \max\left(-F_{\mathrm{s}}, 0\right)\right]\left(T_{\mathrm{P}} - T_{\mathrm{S}}\right) &= a_{\mathrm{S}}\left(T_{\mathrm{P}} - T_{\mathrm{S}}\right) \\
J_{\mathrm{n}} - F_{\mathrm{n}} T_{\mathrm{P}} = \left[D_{\mathrm{n}} A\left(|P_{\mathrm{n}}|\right) + \max\left(F_{\mathrm{n}}, 0\right)\right]\left(T_{\mathrm{N}} - T_{\mathrm{P}}\right) &= a_{\mathrm{N}}\left(T_{\mathrm{N}} - T_{\mathrm{P}}\right)
\end{aligned}
$$

where:

$$
\begin{aligned}
a_{\mathrm{E}} &= D_{\mathrm{e}} A\left(|P_{\mathrm{e}}|\right) + \max\left(-F_{\mathrm{e}}, 0\right) \\
a_{\mathrm{W}} &= D_{\mathrm{w}} A\left(|P_{\mathrm{w}}|\right) + \max\left(F_{\mathrm{w}}, 0\right) \\
a_{\mathrm{S}} &= D_{\mathrm{s}} A\left(|P_{\mathrm{s}}|\right) + \max\left(-F_{\mathrm{s}}, 0\right) \\
a_{\mathrm{N}} &= D_{\mathrm{n}} A\left(|P_{\mathrm{n}}|\right) + \max\left(F_{\mathrm{n}}, 0\right) \,,
\end{aligned} \tag{B.20}
$$

and where the function max(...) selects the largest quantity contained in the parenthesis. The function $A\left(|P|\right)$ is a weighting function which determines the relative importance of advection and conduction terms in determining the temperatures at the centers of control volumes. Both conduction and advection terms are calculated at control volume boundaries, while temperatures are only known at control volume centers. The function $A\left(|P|\right)$ partitions the influence of the interface flux (both advection and conduction) on the temperature T at the control volume centers. I chose to use the power law approximation for $A\left(|P|\right)$ (Patakar, 1982, p. 80-99). (see Appendix C for discussion):

$$
A\left(|P|\right) = \max\left(0, \left(1 - 0.1|P|\right)^{5}\right) \,. \tag{B.21}
$$

Using the above substitutions, I simplified equation (B.19), and proceeded directly to the final discretization of the energy conservation equation:

$$a_{\mathrm{P}}T_{\mathrm{P}} = a_{\mathrm{E}}T_{\mathrm{E}} + a_{\mathrm{W}}T_{\mathrm{W}} + a_{\mathrm{S}}T_{\mathrm{S}} + a_{\mathrm{N}}T_{\mathrm{N}} + b \tag{B.22}$$

where:

$$a_{\mathrm{P}} = a_{\mathrm{E}} + a_{\mathrm{W}} + a_{\mathrm{S}} + a_{\mathrm{N}} + a_{\mathrm{P}}^{0} \tag{B.23}$$

$$b = T_{\mathrm{P}}^{0}a_{\mathrm{P}}^{0} + Q \tag{B.24}$$

and

$$a_{\mathrm{P}}^{0} = \frac{\Delta x \Delta y}{\Delta t}\left[\phi_{\mathrm{P}}^{0}\left(\rho c\right)_{\mathrm{a}} + \left(1-\phi_{\mathrm{P}}\right)\left(\rho c\right)_{\mathrm{i}}\right] \tag{B.25}$$

This equation is coupled to a similar equation for vapor transport in the firn (described in Appendix D) through the source term $Q = SL$, where S is the mass of water which changes phase per unit volume. These equations are solved iteratively using Matlab software to calculate temperature changes in the firn through time as a result of advection of sensible heat by air through the firn, latent heat sources and sinks and heat conduction.

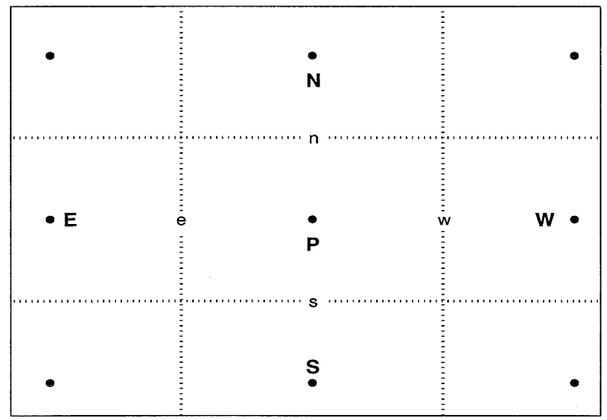


Figure B.1: Control volume centers are placed at the center of control volumes. The subscript P denotes values calculated at the center of the control volume of interest. Neighboring control volume centers are denoted by capital letters. Lower case letters denote the interfaces of the control volume of interest.

Appendix C

DERIVATION OF PARTITIONING FUNCTION

In the control volumes that I used to model vapor transport and energy conservation in firn, the values of the dependent variable (such as temperature or vapor density) are defined at control volume centers, while fluxes (both advective and diffusive) are defined at control volume interfaces. This pattern is reminiscent of the use of staggered grids in finite difference methods. Here, I develop an interpolation scheme to determine the relative importance of advection and diffusion to the values of the dependent variable Ψ (either temperature or vapor density). My approach closely follows Patankar (1982, Chapter 5).

The goal is to transform expressions for flux at interfaces into a difference equation involving values of Ψ at adjacent control volume centers. The weighting between adjacent values of Ψ will be given by an expression involving the Peclet number $\mathcal{P}$, which expresses the relative strengths of advective and diffusive transport. Patankar (1982) derived these weighting functions by solving the one-dimensional steady-state advection-diffusion equation for a general dependent variable Ψ. Patankar (1982) then used these weighting functions in the linear, two-dimensional models used to calculate temperature and vapor density (presented in Appendices B and D). The extension from one to two dimensions is warranted since in control volume models based on volumes aligned with the coordinate axes, values of interface fluxes in the y direction are independent of interface fluxes in the x direction. Consequently, I can study the expressions for flux at interfaces in each dimension independently. In the following, I present the derivation in the x direction; the solution for the y direction follows similarly.

I also extend this analysis of a steady-state case to the non-steady case in Appendices B and D. In the implicit scheme, the new value of Ψ is used throughout the entire time step, which means that the interface fluxes depend only on values of Ψ for a single time step (rather than a weighted average of past and present values). Therefore, the same weighting functions calculated from analysis of the interface fluxes in the steady case can also be applied in the non-steady case.

I began by considering the steady-state one-dimensional advective-diffusive equation for an arbitrary dependent variable Ψ, as in Patankar (1982), chapter 5:

$$\frac{d}{dx}\left(\rho u \Psi\right) = \frac{d}{dx}\left(\Gamma \frac{d\Psi}{dx}\right), \tag{C.1}$$

where the general diffusion coefficient is given by Γ, the density of Ψ is ρ, the horizontal velocity in the positive x direction is u. The solution between points P and E (see figure C.1 for grid and indicial notation) is:

$$\Psi = \Psi_{\mathrm{P}} + \left(\Psi_{\mathrm{E}} - \Psi_{\mathrm{P}}\right)\left[\frac{\exp\left(\frac{\mathcal{P}_{\mathrm{e}} x}{(\delta x)_{\mathrm{e}}}\right) - 1}{\exp\left(\mathcal{P}_{\mathrm{e}}\right) - 1}\right]. \tag{C.2}$$

where $(\delta x)_{\mathrm{e}}$ is the distance between the control volume center of interest, and the control volume center to the right (East). $\mathcal{P}$ is the Peclet number, defined as:

$$\mathcal{P}_{\mathrm{e}} = \frac{(\rho u)_{\mathrm{e}}}{\Gamma_{\mathrm{e}} / (\delta x)_{\mathrm{e}}} = \frac{F_{\mathrm{e}}}{D_{\mathrm{e}}}. \tag{C.3}$$

$\mathcal{P}$ is defined only at control volume interfaces (e.g. $\mathcal{P}_{\mathrm{e}}$ is the Peclet number at the *east* interface), where the velocity u and the diffusivity Γ are defined. This solution is strictly valid only when control volume interfaces are located midway between grid points. I chose to place grid points at control volume centers, which means that interfaces will not always be equidistant from adjacent grid points (Patankar, 1982, p.69). However, provided changes in grid spacing are gradual (i.e. $(\delta x)_{\mathrm{e}} / (\delta x)_{\mathrm{w}} \simeq 1$), Equation (C.2) is still approximately valid. Patankar (1982) defined the total flux J to be the combination of the advection term, and the diffusion term:

$$J = \rho u \Psi - \Gamma \frac{d\Psi}{dx}. \tag{C.4}$$

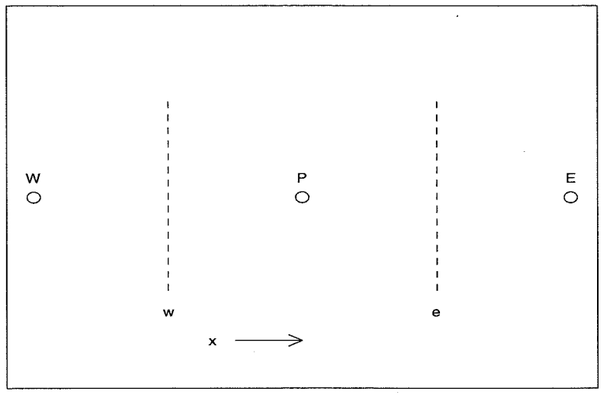


Figure C.1: Grid used for one-dimensional steady-state model in this appendix. Control volume centers are denoted by circles and are labelled with roman upper-case letters: P for the control volume center of interest (not to be confused with the Peclet number $\mathcal{P}$, which is known only at interfaces), E for the control volume to the east, and W for the control volume to the west. Lower-case letters and vertical dashed lines indicate the interfaces of the control volume of interest. Values of the dependent variable Ψ are calculated only at grid points, while fluxes are calculated at interfaces.

Substituting the definition of J into Equation (C.1) yields:

$$\frac{dJ}{dx} = 0 \,. \tag{C.5}$$

This equation can be integrated over the control volume (see figure C.1) to yield:

$$J_\mathrm{e} - J_\mathrm{w} = 0 \,. \tag{C.6}$$

J_e is the total integrated flux at the *east* interface, and J_w is the total integrated flux at the *west* interface. I use the exact solution (Equation (C.2)) to the conservation equation (C.1) to determine the interface fluxes J_e and J_w in terms of the values of Ψ at the adjacent grid points and the Peclet number. The first derivative of Ψ is given by:

$$\frac{d\Psi}{dx} = \frac{(\rho u)_\mathrm{e}}{\Gamma_\mathrm{e}} \frac{\Psi_\mathrm{E} - \Psi_\mathrm{P}}{\exp(\mathcal{P}_\mathrm{e}) - 1} \exp\left(\frac{\mathcal{P}_\mathrm{e} x}{(\delta x)_\mathrm{e}}\right) \,. \tag{C.7}$$

I substituted the values for Ψ and $d\Psi/dx$ into Equation (C.4) and reduced the resulting expression to get:

$$J_\mathrm{e} = F_\mathrm{e}\left(\Psi_\mathrm{P} + \frac{\Psi_\mathrm{P} - \Psi_\mathrm{E}}{\exp(\mathcal{P}_\mathrm{e}) - 1}\right), \tag{C.8}$$

and

$$J_\mathrm{w} = F_\mathrm{w}\left(\Psi_\mathrm{W} + \frac{\Psi_\mathrm{W} - \Psi_\mathrm{P}}{\exp(\mathcal{P}_\mathrm{w}) - 1}\right) \,. \tag{C.9}$$

At this point, Patankar (1982) introduced a new function J^*, which is the normalized flux:

$$J^* = \frac{J\delta x}{\Gamma} = \frac{J}{D} \,. \tag{C.10}$$

I used this substitution to convert the expressions for J into J^*. I also collected the factors of $\mathcal{P}$ to express J^* as a function of Ψ:

$$J^*_\mathrm{e} = \Psi_\mathrm{P}\frac{\mathcal{P}_\mathrm{e}\exp(\mathcal{P}_\mathrm{e})}{\exp(\mathcal{P}_\mathrm{e}) - 1} - \Psi_\mathrm{E}\frac{\mathcal{P}_\mathrm{e}}{\exp(\mathcal{P}_\mathrm{e}) - 1}, \tag{C.11}$$

and

$$J^*_\mathrm{w} = \Psi_\mathrm{W}\frac{\mathcal{P}_\mathrm{w}\exp(\mathcal{P}_\mathrm{w})}{\exp(\mathcal{P}_\mathrm{w}) - 1} - \Psi_\mathrm{P}\frac{\mathcal{P}_\mathrm{w}}{\exp(\mathcal{P}_\mathrm{w}) - 1} \,. \tag{C.12}$$

Note that the equality of Equation (C.6) is still preserved through these substitutions, i.e. $J^*_\mathrm{e} - J^*_\mathrm{w} = 0$. The similarity between the two sets of coefficients lead Patankar (1982) to define:

$$A = \frac{\mathcal{P}}{\exp(\mathcal{P}) - 1} \,, \tag{C.13}$$

and

$$B = \frac{\mathcal{P}\exp(\mathcal{P})}{\exp(\mathcal{P}) - 1} \,, \tag{C.14}$$

where A represents the coefficient for the value of Ψ *ahead* of the interface, and B represents the coefficient for the value of Ψ *behind* the interface. A and B define how the values of the dependent variable in adjacent control volumes are weighted by a function of the Peclet number at the interface to determine the flux of Ψ at the interface. These are the weighting functions that I used in the non-steady temperature and vapor density models. It remains now to manipulate the expressions for normalized flux (J^*) into a form that can be substituted into the models for energy conservation

and vapor transport (Appendices B and D). Using these weighting functions, we can simplify the expressions for J^*:

$$J_e^* = B\Psi_P - A\Psi_E \tag{C.15}$$

$$J_w^* = B\Psi_w - A\Psi_P \, . \tag{C.16}$$

Patankar (1982) points out that the functions A and B have a number of useful relationships between them, which are used in later manipulations:

$$\begin{aligned} A(-\mathcal{P}) &= B(\mathcal{P}) \\ A(\mathcal{P}) &= B(-\mathcal{P}) \\ B &= A + \mathcal{P} \\ A(\mathcal{P}) &= A(|\mathcal{P}|) + \max(-\mathcal{P}, 0) \\ B(\mathcal{P}) &= A(|\mathcal{P}|) + \max(\mathcal{P}, 0) \, , \end{aligned} \tag{C.17}$$

The last two relations allowed me to again rewrite the expressions for J^*:

$$J_e^* - \mathcal{P}_e\Psi_P = A\left(\Psi_P - \Psi_E\right) \tag{C.18}$$

$$J_w^* - \mathcal{P}_w\Psi_P = B\left(\Psi_W - \Psi_P\right) \, , \tag{C.19}$$

substituting back in the definitions of J^* (Equation (C.10)) and $\mathcal{P}$ (Equation (C.3)):

$$J_e - F_e\Psi_P = A\, D_e\left(\Psi_P - \Psi_E\right) \tag{C.20}$$

$$J_w - F_w\Psi_P = B\, D_w\left(\Psi_W - \Psi_P\right) \, . \tag{C.21}$$

Using Equations (C.18) and the definition of $\mathcal{P}$, Patankar (1982) again rewrote the expressions for $J - F\Psi$ into their final form:

$$J_e - F_e\Psi_P = \left[D_e A(|\mathcal{P}_e|) + \max(-F_e, 0)\right]\left(\Psi_P - \Psi_E\right) \tag{C.22}$$

$$J_w - F_w\Psi_P = \left[D_w A(|\mathcal{P}_w|) + \max(F_w, 0)\right]\left(\Psi_W - \Psi_P\right) \, , \tag{C.23}$$

and similar expressions for the n and s terms. These forms of the interface flux are substituted directly into the models for temperature and vapor transport in the firn in Appendices B and D.

Patankar (1982) advocates using a power law approximation to A, rather than the exponential form (Equation (C.13)) in the interest of computational efficiency. I have found that the exponential form uses the same number of machine cycles as the power law approximation when using Matlab software. Furthermore, the exponential form computes almost twice as fast as the power law approximation. However, the exponential form of A is numerically unstable for small values of $\mathcal{P}$. Since $\mathcal{P}$ in the firn ranges from large values near the surface, where air flow velocities are large, to $\sim$0 at depth, where are flow is negligible, I use Patakar's power law approximation:

$$A\left(|\mathcal{P}|\right) = \max\left(0, (1 - 0.1|\mathcal{P}|)^5\right) \, , \tag{C.24}$$

in place of the exact form of Equation (C.13).

Appendix D

VAPOR TRANSPORT MODEL

Water vapor moves through the firn as a result of both advection and diffusion. Moist air flowing through firn as a result of surface-pressure variations (e.g. Colbeck, 1989; Waddington and others, 1996) redistributes water vapor. Water vapor can also diffuse through pore spaces in the firn as the result of temperature gradients, which cause vapor density gradients. Water vapor is added to the air in firn pore spaces through sublimation of snow grains, and removed by condensation of vapor onto snow grains. The vapor transport model that I used models the transport of vapor due to both advection and diffusion. It also incorporates phase changes. The vapor transport model is coupled to the energy conservation model (see Appendix B) through the latent heat released by the phase changes. I expressed the changes in vapor density ρ_v as a conservation law:

$$\frac{\partial}{\partial t}\rho_v + \nabla \cdot (\rho_v \vec{\mathbf{u}}) - \nabla \cdot (\kappa \nabla \rho_v) - S = 0 \,, \tag{D.1}$$

where $\vec{\mathbf{u}}$ is the two-dimensional velocity vector (u, v), x is positive to the right, y is positive down and κ is the diffusivity of water vapor in firn. This is the same vapor transport model used by Albert and McGilvary (1992). The source term S couples vapor transport to energy conservation, and is described in detail in Appendix E. As in Appendix B, the flow field $\vec{\mathbf{u}}$ must satisfy mass continuity:

$$\frac{\partial}{\partial t}(\phi \rho_a) + \nabla \cdot (\phi \rho_a \vec{\mathbf{u}}) = 0 \,, \tag{D.2}$$

where the subscript a represents values for *air* in the firn pore spaces and ϕ is firn porosity. I discretized Equations (D.1) and (D.2) following a solution technique similar to the method in Appendix B. Since the source term depends in part on ρ_v (Appendix E), I separated S into two parts; a constant term S_c that does not depend on ρ_v and a second term S_v that is multiplied by ρ_v. A brief summary of the discretization technique follows.

I defined two new factors J_x and J_y that describe the total flux in the x and y directions:

$$\begin{aligned} J_x &= u\rho_v - \kappa \frac{\partial \rho_v}{\partial x} \\ J_y &= v\rho_v - \kappa \frac{\partial \rho_v}{\partial y} \,, \end{aligned} \tag{D.3}$$

and used these two factors to simplify Equation (D.1):

$$\frac{\partial}{\partial t}\rho_v + \frac{\partial}{\partial x}J_x + \frac{\partial}{\partial y}J_y = S_\mathrm{c} + S_\mathrm{v}\rho_v \,. \tag{D.4}$$

I integrated this equation with respect to x, y and t:

$$\frac{\Delta x \Delta y}{\Delta t}\left(\rho_{v\mathrm{P}} - \rho^0_{v\mathrm{P}}\right) + J_\mathrm{e} - J_\mathrm{w} + J_\mathrm{s} - J_\mathrm{n} = \left(S_c + S_v \rho_{v\mathrm{P}}\right)\Delta x \Delta y \,, \tag{D.5}$$

where the subscript P refers to values at the control volume center, the superscript 0 refers to values at the beginning of the time step (i.e. the "old" values), and J_e, J_w, J_s and J_n refer to the integrated total flux through the east, west, south and north interfaces, respectively. See Figure D.1 for indicial notation and grid set-up.

I assume that ρ_a is constant in the continuity equation (Equation (D.2)), as in Appendix B. In reality, ρ_a varies as a function of temperature (Wallace and Hobbs, p. 48). Variations in ρ_a would allow for free convection (Benard convection) of air through firn pore spaces. See Appendix B for discussion of the motivation for neglecting variation in ρ_a. Essentially, neglting variations in ρ_a is a reasonable assumption for three reasons. First, close to the surface where temperature gradients are large (and associated Rayleigh numbers are large), advective velocities (u, v) are much larger than free-convection velocities. Second, where advective velocities are small (below the top two meters), temperature gradients are small; this results in small convection velocities. Third, Bernard convection is most likely during the winter months when cold surface air overlies warmer air at depth in the firn. If convection were active in the

winter, a greatly attenuated isotopic thermal fractionation signal would be expected (Severinghaus, and others 2001). In fact, the winter thermal fractionation signal is well-developed and not destroyed by vigorous Benard convection. Consequently, I divided ρ_a out of Equation (D.2):

$$\frac{\partial}{\partial t}\phi + \nabla \cdot (\phi \vec{u}) = 0 \,. \tag{D.6}$$

Integrating this equation with respect to space and time yielded:

$$\Delta x \Delta y \left(\phi_P - \phi_P^0\right) + \Delta y \Delta t \left((\phi u)_e - (\phi u)_w\right) + \Delta x \Delta t \left((\phi v)_s - (\phi v)_n\right) = 0 \,, \tag{D.7}$$

where subscripts refer to values on control volume faces (Fig. 1). I simplified this expression by defining flux terms F_j similar to the mass flow rate used by Patankar (1982, p. 98):

$$\begin{aligned} F_e &= (\phi u)_e \Delta y \\ F_w &= (\phi u)_w \Delta y \\ F_s &= (\phi v)_s \Delta x \\ F_n &= (\phi v)_n \Delta x \,, \end{aligned} \tag{D.8}$$

Using this simplification and multiplying through by the vapor density at control volume centers, ρ_{vP}, Equation (D.6) becomes:

$$\frac{\Delta x \Delta y}{\Delta t}\left(\rho_{vP}\phi_P - \rho_{vP}\phi_P^0\right) + F_e\rho_{vP} - F_w\rho_{vP} + F_s\rho_{vP} - F_n\rho_{vP} = 0 \,. \tag{D.9}$$

Then I subtracted this form of the continuity equation from Equation (D.5) and simplified the expression to yield:

$$\begin{aligned} \rho_{vP}\frac{\Delta x \Delta y}{\Delta t}\left(1 - \phi_P + \phi_P^0\right) &+ \rho_{vP}^0\frac{\Delta x \Delta y}{\Delta t} + \\ (J_e - F_e\rho_{vP}) - (J_w - F_w\rho_{vP}) &+ (J_s - F_s\rho_{vP}) - (J_n - F_n\rho_{vP}) = \\ & (S_c + S_v\rho_{vP})\,\Delta x \Delta y \,, \end{aligned} \tag{D.10}$$

To simplify the above expression, I defined a term similar to Patankar's (1982) diffusion conductance (p. 100):

$$\begin{aligned} D_e &= \frac{(\phi\kappa)_e \Delta y}{\delta x} \\ D_w &= \frac{(\phi\kappa)_w \Delta y}{\delta x} \\ D_s &= \frac{(\phi\kappa)_s \Delta x}{\delta y} \\ D_n &= \frac{(\phi\kappa)_n \Delta x}{\delta y} \,, \end{aligned} \tag{D.11}$$

where the subscripts on κ refer to the diffusivity at the interface. Using the above relations for D and F, I defined the Peclet number for vapor transport in the firn:

$$P = \frac{F}{D} \,, \tag{D.12}$$

which describes the relative strength of advection and diffusion at redistributing water vapor across each interface. Following the methods of Appendix C, I used the relationships between J, P, F and D to generate:

$$\begin{aligned} J_e - F_e\rho_{vP} = \left[D_e A\left(|P_e|\right) + \max\left(-F_e, 0\right)\right]\left(\rho_{vP} - \rho_{vE}\right) &= a_E(\rho_{vP} - \rho_{vE}) \\ J_w - F_w\rho_{vP} = \left[D_w A\left(|P_w|\right) + \max\left(F_w, 0\right)\right]\left(\rho_{vW} - \rho_{vP}\right) &= a_W(\rho_{vW} - \rho_{vP}) \\ J_s - F_s\rho_{vP} = \left[D_s A\left(|P_s|\right) + \max\left(-F_s, 0\right)\right]\left(\rho_{vP} - \rho_{vS}\right) &= a_S(\rho_{vP} - \rho_{vS}) \\ J_n - F_n\rho_{vP} = \left[D_n A\left(|P_n|\right) + \max\left(F_n, 0\right)\right]\left(\rho_{vN} - \rho_{vP}\right) &= a_N(\rho_{vN} - \rho_{vP}) \,, \end{aligned}$$

where:

$$a_E = D_e\left(A|P_e|\right) + \max(-F_e, 0) \tag{D.13}$$

$$a_W = D_w\left(A|P_w|\right) + \max(F_w, 0) \tag{D.14}$$

$$a_S = D_s\left(A|P_s|\right) + \max(-F_s, 0) \tag{D.15}$$

$$a_N = D_n\left(A|P_n|\right) + \max(F_n, 0) \,, \tag{D.16}$$

where the function max(...) selects the largest quantity in the parentheses. The function A is a function of the Peclet number and determines the relative importance of

conduction and advection to vapor transport in the firn. Appendix C presents the background and derivation of A. I chose to define A using Patankar's exponential scheme (Patankar 1982, p. 90):

$$A\left(|P|\right) = \max\left(0, (1 - 0.1|P|)^5\right) . \tag{D.17}$$

Using the above substitutions, I generated the final form of the discretization equations for the vapor transport model:

$$a_{\mathrm{P}}\rho_{v\mathrm{P}} = a_{\mathrm{E}}\rho_{v\mathrm{E}} + a_{\mathrm{W}}\rho_{v\mathrm{W}} + a_{\mathrm{S}}\rho_{v\mathrm{S}} + a_{\mathrm{N}}\rho_{v\mathrm{N}} + b\,, \tag{D.18}$$

where:

$$a_{\mathrm{P}} = a_{\mathrm{E}} + a_{\mathrm{W}} + a_{\mathrm{S}} + a_{\mathrm{N}} + \frac{\Delta x\Delta y}{\Delta t}\left(1 - \phi + \phi^0\right) - S_{\mathrm{v}}\Delta x\Delta y \tag{D.19}$$

$$b = \rho^0_{v\mathrm{P}}\frac{\Delta x\Delta y}{\Delta t} + S_{\mathrm{c}}\Delta x\Delta y\,, \tag{D.20}$$

and D and F are as defined in Equations (D.12) and (D.9), respectively. This model of vapor transport in the firn is solved iteratively using Matlab software. The new vapor density at each point $\rho_{v\mathrm{P}}$ is calculated according to the above relationships. Since the vapor model is coupled to the energy conservation model (Appendix B) through the source term S, I iterated between these two models (vapor transport and energy conservation) to produce a mutually consistent set of temperatures T_{p} and vapor densities $\rho_{v\mathrm{P}}$ at each time step.

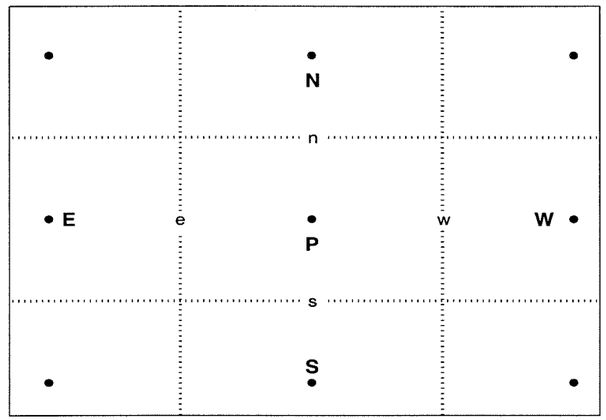


Figure D.1: Control volume centers are placed at the geometric centers of control volumes. The subscript P denotes values calculated at the center of the control volume of interest. Neighboring control volume centers are denoted by upper case roman letters. Lower case letters denote the interfaces of the control volume of interest.

Appendix E

TRANSFER OF WATER BETWEEN PHASES

Water molecules in the firn may change phases between solid and vapor. Ultimately, the reason for the phase change is a mismatch between the vapor density of the air in firn pore spaces, and the saturation vapor density of air in contact with the snow grains. If the vapor density in the air is lower than the saturation density, some of the snow will sublimate to move the local vapor density towards equilibrium. If the vapor density exceeds the saturation value, some water vapor will condense out of the air onto the ice grains. Both processes influence the temperature of the firn through latent heat effects.

In general, the saturation vapor density over ice is a function of both temperature and the radius of curvature of ice grains. For ice grains larger than about 1 μm, the temperature effect dominates, and the radius-of-curvature effect can be neglected (Colbeck, 1983a).

Many investigators use measurements and estimates of vapor pressure, rather than vapor density. In this model, I converted all measurements of vapor pressure into vapor density using the ideal gas law, since I am interested in the mass of water changing phase per volume of firn in a given time step.

There are several published equations for calculating the saturation vapor pressure over ice (e.g. Hyland and Wexler, 1983; Colbeck, 1990; Marti and Mauersberger, 1993; Albert, 2001) which give slightly different results. Hyland and Wexler (1983) fit a six-term polynomial to measurements of vapor pressure over ice for different temperatures. Several other estimates are based on a form of the Clapeyron equation (also known as the Van't Hoff equation):

$$\ln\left(\frac{P_1}{P_2}\right) = \frac{-\Delta H^0}{R}\left(\frac{1}{T_1} - \frac{1}{T_2}\right) \tag{E.1}$$

where P denotes vapor pressure, R is the gas constant, ΔH^0 is the enthalpy change between solid and vapor phases for water, and T is the temperature. Given a reference point where both P and T are known, Equation (E.1) can be used to calculate saturation vapor pressure. I found that by using values for ΔH^0 from Wallace and Hobbs (1982) and reference values at the triple point ($P_1 = 6.1165$ mbar, $T_1 = 273.15$ K), Equation (E.1) replicated the results of both Hyland and Wexler (1983) and mea-

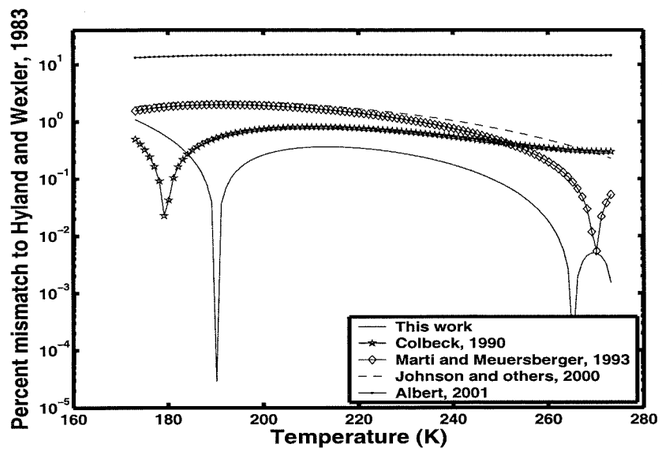


Figure E.1: Fit of several published estimates for saturation vapor pressure to measurements by Hyland and Wexler (1983). Hyland and Wexler (1983) developed a six-term polynomial in temperature to fit their observations. Colbeck (1990) uses a similar derivation as that presented here, although uses different values of saturation vapor density at the triple point. Marti and Mauersberger (1993) use a least squares fit to observational data to generate a logarithmic equation. Albert (2001) uses ΔH^0 = 2838.3 J g^{-1} and a reference temperature of 263 K in Equation (E.1). Johnson and others (2000) do not specify values of ΔH^0 or the reference temperature and pressure used. This work uses $\Delta H^0 = 2834$ J g^{-1}, $P_1 = 6.1165$ mbar and $T_1 = 273.15$ K in Equation (E.1).

surements in the Handbook of Chemistry and Physics (Weast and Selby, 1966) to 1% or better. Figure E.1 shows how the estimate of saturation vapor density given by Equation (E.1) compares with other published estimates. Marti and Mauersberger (1993) show that their data replicate that of Hyland and Wexler (1983) to $\sim$ 2%, and suggest that 2% is the total uncertainty in each measurement. Consequently, the equations of Johnson and others (2000), Marti and Mauersberger (1993), Colbeck (1990), and Equation (E.1) (with $\Delta H^0 = 2834$ J g^{-1}, $P_1 = 6.1165$ mbar and $T_1 = 273.15$ K) all provide an equivalent fit to the available measurements.

If water could move between phases infinitely fast, the expression for the source term in Equation (D.1) of Appendix D would simply be the difference between the local vapor density and saturation vapor density. However, since some time is required for the change, a slightly more complicated expression is required (Albert and McGilvary 1992):

$$S = h_{\mathrm{m}} a_{\mathrm{s}} \left(\rho_v^{\mathrm{sat}} - \rho_v \right) \tag{E.2}$$

where h_{m} is the mass transfer coefficient, and a_{s} is the surface area per unit bulk volume in snow. The mass transfer coefficient describes the speed with which the surface can move as a result of phase change; it has not been well-studied for snow. I use the value suggested by Albert and McGilvary (1992) ($h_{\mathrm{m}} = 0.09$ m s^{-1}), which is based on a correlation of characteristic numbers developed by Chu and others (1953) for a variety of materials.

Equation (E.2) is used by both the energy conservation model and the vapor transport model. In the energy conservation model, I calculate the total latent heat release Q from the mass of water changing phase S. Then $Q = LS$, where L is the latent heat released or absorbed by the phase change per unit mass. Since Q depends only weakly on temperature (through Equations (E.1) and (E.2)), I used the above relation for Q (Equation (E.2)) directly in the energy conservation model described in Appendix B (Equation (B.10) in Appendix B).

However, the vapor transport model uses S directly, and Equation (E.2) depends linearly on the local vapor density ρ_v, which is the dependent variable in the vapor transport model. Consequently, I separated S into a constant part S_{c} that does not depend on ρ_{v} and a variable part, that depends on ρ_{v}:

$$S_{\mathrm{c}} = h_{\mathrm{m}} a_{\mathrm{s}} \rho_v^{\mathrm{sat}} \tag{E.3}$$

$$S_{\mathrm{v}} = -h_{\mathrm{m}} a_{\mathrm{s}} \,, \tag{E.4}$$

so that:

$$S = S_{\mathrm{c}} + S_{\mathrm{v}} \rho_v \,. \tag{E.5}$$

This relationship replaced Equation (E.2), and is used in the vapor transport model (Equation (D.1)) in Appendix D).

Appendix F

ISOTOPIC CONSERVATION IN PORE SPACE VAPOR

This appendix contains a derivation for the evolution of the isotopic profile in the pore space vapor as a result of advection from firn ventilation and diffusion along isotopic gradients in the vapor. The end result of the derivation is Equation (4.1), which is an isotope conservation equation in terms of δ. I begin by defining the number concentration per unit volume of the minor isotope (e.g. O^{18} or D) in the pore space vapor as N' and the major isotope (e.g. O^{16} or H) as N. I assume a single diffusivity D for both the minor and major species.

A conservation equation for N' as a result of advection and diffusion in the vapor phase is given as (assuming a uniform density of air in firn pore spaces):

$$\frac{\partial}{\partial t}N' + \nabla \cdot (N'\vec{u}) - \nabla \cdot (D\nabla N') = 0 \tag{F.1}$$

where $\vec{u}$ is the two-dimensional air-flow velocity in the firn (in practice, I use the air-flow field described in Section 3.3), and ∇ is the two-dimensional spatial derivative. Similarly, a conservation equation for the major isotope can be written as:

$$\frac{\partial}{\partial t}N + \nabla \cdot (N\vec{u}) - \nabla \cdot (D\nabla N) = 0 \tag{F.2}$$

The second term in this conservation equation can be expanded to yield:

$$\frac{\partial}{\partial t}N + N\nabla \cdot \vec{u} + \vec{u} \cdot \nabla N - \nabla \cdot (D\nabla N) = 0 \tag{F.3}$$

The goal of the derivation is to generate a similar conservation equation in terms of δ, which is defined as:

$$\delta = \frac{\frac{N'}{N} - s}{s} * 1000 \tag{F.4}$$

where s refers to a standard isotopic ratio, often taken as the isotopic ratio of Standard Mean Ocean Water, and the factor of 1000 is used to express δ values as parts per thousand. We can define N' in terms of N and δ using Equation (F.4):

$$N' = Ns(1 + \frac{\delta}{1000}) \tag{F.5}$$

I define a temporary parameter Λ as:

$$\Lambda = s(1 + \frac{\delta}{1000}) \tag{F.6}$$

and use a change of variables $N' = N\Lambda$ in Equation (F.1):

$$\frac{\partial}{\partial t}[N\Lambda] + \nabla \cdot ([N\Lambda]\vec{u}) - \nabla \cdot (D\nabla[N\Lambda]) = 0 \tag{F.7}$$

The unsteady term expands as:

$$\frac{\partial}{\partial t}[N\Lambda] = N\frac{\partial}{\partial t}\Lambda + \Lambda\frac{\partial}{\partial t}N \tag{F.8}$$

The advection term expands as:

$$\nabla \cdot ([N\Lambda]\vec{u}) = N\Lambda\nabla \cdot \vec{u} + \vec{u}\Lambda \cdot \nabla N + \vec{u}N \cdot \nabla\Lambda \tag{F.9}$$

The diffusion term expands as:

$$-\nabla \cdot (D\nabla[N\Lambda]) = -(\nabla \cdot (ND\nabla\Lambda) + \nabla \cdot (\Lambda D\nabla N)) \tag{F.10}$$

$$= -N\nabla \cdot (D\nabla\Lambda) - \Lambda\nabla \cdot (D\nabla N) - 2D\nabla N\nabla\Lambda \tag{F.11}$$

I collect terms which can be combined as $\Lambda \times$ Equation (F.3):

$$\Lambda\frac{\partial}{\partial t}N + N\Lambda\nabla\cdot\vec{u} + \vec{u}\Lambda\cdot\nabla N - \Lambda\nabla\cdot(D\nabla N) \tag{F.12}$$

Because of Equation (F.3), these terms sum to zero and are dropped from the analysis, leaving:

$$N\frac{\partial}{\partial t}\Lambda + \vec{u}N\cdot\nabla\Lambda - N\nabla\cdot(D\nabla\Lambda) - 2D\nabla N\nabla\Lambda \tag{F.13}$$

Division by N yields:

$$\frac{\partial}{\partial t}\Lambda + \vec{u}\cdot\nabla\Lambda - \nabla\cdot(D\nabla\Lambda) - 2\frac{D}{N}\nabla N\nabla\Lambda = 0 \tag{F.14}$$

If $\frac{\Delta N}{N} \ll 1$, then the last term can be eliminated. N is approximately equivalent to the density of the pore space air (i.e. the number of H_2O^16 molecules per m^{-3}) and air density is not significantly affected by small changes in the isotopic content. Consequently, the last term may be safely neglected as it is $\ll 1$. Substituting the definition of Λ back into the remainder of Equation (F.14) and dividing out the constant s yields:

$$\frac{\partial}{\partial t}\frac{\delta}{1000} + \vec{u}\cdot\nabla\frac{\delta}{1000} - \nabla\cdot(D\nabla\frac{\delta}{1000}) = 0 \tag{F.15}$$

Multiplying out the factor of 1000 yields:

$$\frac{\partial}{\partial t}\delta + \vec{u}\cdot\nabla\delta - \nabla\cdot(D\nabla\delta) = 0 \tag{F.16}$$

Adding in the assumption that the air-flow field conserves volume ($\nabla\cdot\vec{u} = 0$), this equation can be written in the form of Equation (4.1). The extent to which my calculated air-flow field conserves mass is discussed in Section 3.7.1.

Appendix G

EFFECTS OF ISOTOPIC EQUILIBRATION ON ICE GRAINS

The effect of isotopic equilibration on δ_i is determined by calculating the number of moles of the major and minor isotopes which change phases during a given time step as a result of isotopic equilibration. This is achieved by first calculating the isotopic ratios R in the vapor phase initially and after equilibration:

$$R_v^0 = S\left(\frac{1}{1000}\delta_v^0 + 1\right) \tag{G.1}$$

$$R_v^1 = S\left(\frac{1}{1000}\left(\delta_{eq} + \left(\delta_v^0 - \delta_{eq}\right)\exp\left(-k\Delta t\right)\right) + 1\right)\,, \tag{G.2}$$

where S is a standard isotopic ratio (usually that of Standard Mean Ocean Water), δ_{eq} is given by Equation (4.5) and k is the equilibration rate constant. The superscript 0 reflects an initial value at the beginning of the time step and 1 reflects a final value at the end of the time step. The total number of water molecules in the vapor phase N_{tv} is given by:

$$N_{tv} = \frac{1}{m}\rho_v\Delta x\Delta y\,, \tag{G.3}$$

where m is the molar mass of water, $\rho_m athrmv$ is the vapor density in the control volume and $\Delta x\Delta y$ is the control volume area. I calculate the number of moles of major and minor water molecules at the beginning and end of the time step as:

$$N_v'^0 = N_{tv} - \frac{N_{tv}}{R_v^0 + 1} \tag{G.4}$$

$$N_{\mathrm{v}}^{0} = \frac{N_{\mathrm{tv}}}{R_{\mathrm{v}}^{0}+1} \tag{G.5}$$

$$N_{\mathrm{v}}^{\prime 1} = N_{\mathrm{tv}} - \frac{N_{\mathrm{tv}}}{R_{\mathrm{v}}^{1}+1} \tag{G.6}$$

$$N_{\mathrm{v}}^{1} = \frac{N_{\mathrm{tv}}}{R_{\mathrm{v}}^{1}+1}\,, \tag{G.7}$$

where N' denotes the number of models of the minor isotope and R_{v}^{0} and R_{v}^{1} are given by Equation (G.2) and (G.2) respectively. Note that the total number of isotopes is conserved, i.e. $N_{\mathrm{v}}^{\prime 0} + N_{\mathrm{v}}^{0} = N_{\mathrm{v}}^{\prime 1} + N_{\mathrm{v}}^{1} = N_{\mathrm{tv}}$. I now calculate number of heavy and light isotopes changing phase as:

$$dN' = N_{\mathrm{v}}^{\prime 1} - N_{\mathrm{v}}^{\prime 0} \tag{G.8}$$

$$dN = N_{\mathrm{v}}^{1} - N_{\mathrm{v}}^{0}\,. \tag{G.9}$$

Note that $dN > 0$ reflects a transfer to the vapor phase, and $dN < 0$ indicates a transfer to the solid. In a similar manner, I calculate the initial isotopic ratio in the ice R_{i}^{0} as:

$$R_{\mathrm{i}}^{0} = S\left(\frac{1}{1000}\delta_{\mathrm{i}}^{0}+1\right)\,. \tag{G.10}$$

The total number of moles of water in the snow is:

$$N_{\mathrm{ts}} = \frac{1}{m}M_{\mathrm{i}}\,, \tag{G.11}$$

where M_{i} is the total mass of snow in the control volume. The initial number of major and minor isotopes in the snow are given by:

$$N_{\mathrm{i}}^{\prime 0} = N_{\mathrm{ts}} - \frac{N_{\mathrm{ts}}}{R_{\mathrm{i}}^{0}+1} \tag{G.12}$$

$$N_{\mathrm{i}} = \frac{N_{\mathrm{ts}}}{R_{\mathrm{i}}^{0}+1}\,. \tag{G.13}$$

The isotopic ratio of the snow at the end of the time step is then given by:

$$R_{\mathrm{i}}^{1} = \frac{N_{\mathrm{i}}^{\prime 0} - dN'}{N_{\mathrm{i}} - dN}\,. \tag{G.14}$$

Finally, the isotopic composition of the snow at the end of the time step is given as:

$$\delta_{\mathrm{i}}^{1} = 1000\left(\frac{R_{\mathrm{i}}^{1}-S}{S}\right)\,. \tag{G.15}$$

Note that Equation (4.4) assumes that the solid is an infinite reservoir of the minor isotope. In fact, the number of light isotopes in the solid phase is limited, although $N_i^{'} \gg N_v^{'}$ in any given control volume.

VITA

Name: Thomas A. Neumann

Date: June 2, 2003

Education

B. A.: Geophysical Science, University of Chicago, 1996

Ph. D.: University of Washington, 2003

Dissertation Title

Ph. D.: Effects of firn ventilation on geochemistry of polar snow.

Publications

A. F. Fountain, T. A. Neumann, P. L. Glenn, and T. Chinn. Can climate warming induce glacier advance in Taylor Valley, Antarctica? *Journal of Glaciology*, submitted.

D. L. Morse, D. D. Blankenship, E. D. Waddington, and T. A. Neumann. A site for deep coring in West Antarctica: Results from aerogeophysical surveys and thermo-kinematic modeling. *Annals of Glaciology*, 35, 2002, 36-44.

E. D. Waddington, E. J. Steig, and T. A. Neumann. Using characteristic times to assess whether stable isotopes can be reversibly deposited. *Annals of Glaciology*, 35, 2002, 118-124.

D. L. Morse, E. D. Waddington, H. P. Marshall, T. A. Neumann, E. J. Steig, J. E. Dibb, D. P. Winebrenner, and R. J. Arthern. Accumulation rate measurements

at Taylor Dome, East Antarctica: Techniques and strategies for mass balance measurements in polar environments. *Geografiska Annaler*, 81A(4): 683-694, 1999.

Abstracts and Research Summaries

T. A. Neumann, and E. D. Waddington. A two-dimensional model of post-depositional changes in stable isotope ratios in polar firn. *Eos Transactions AGU, 2002 Fall Meeting Supplement*, 83(47): C61A-11, 2002. abstract.

E. D. Waddington, T. A. Neumann, D. L. Morse, and H. P. Marshall. Spatial accumulation-rate pattern inferred from radar internal layers and point measurements of velocity and accumulation near Taylor Mouth, Victoria Land. *Eos Transactions AGU, 2002 Fall Meeting Supplement*, 83(47): C12A-0998, 2002. abstract.

T. A. Neumann. Post-depositional changes in stable isotope ratios. *Eos Transactions AGU, 2001 Spring Meeting Supplement*, 82(20): OS51B-04, 2001. abstract.

T. A. Neumann, E. D. Waddington, H. P. Marshall, D. L. Morse and P. M. Grootes. From the dome to the flank: Relating two stable isotope records. *Eos Transactions AGU, 2000 Fall Meeting Supplement*, 81(48): H52C-09, 2000. abstract.

C. F. Raymond, T. A. Neumann, E. Rignot, A. Rivera, G. Casassa. Retreat of Tyndall Glacier, Patagonia, Chile. *Eos Transactions AGU, 2000 Fall Meeting Supplement*, 81(48): H61G-02, 2000. abstract.

T. A. Neumann, E. D. Waddington, H. P. Marshall, D. L. Morse, G. Clow and J. E. Dibb. A wrinkle in time: The impact of spatial gradients on ice core timescales. *Eos Transactions AGU, 1998 Fall Meeting Supplement*, 79(45): H21D-11, 1998. abstract.